A quantum optical microphone in the audio band based on nonlinear interferometry and a fiber-optical interface for nanophotonic devices

Von der Fakultät 8 Mathematik und Physik der Universität Stuttgart
zur Erlangung der Würde eines Doktors der Naturwissenschaften
(Dr. rer. nat.) genehmigte Abhandlung

Vorgelegt von

Raphael Nold

aus Tübingen

Hauptberichter:	Prof. Dr. Jörg Wrachtrup
Mitberichter:	Prof. Dr. Tilman Pfau
Tag der mündlichen Prüfung:	07.12.2022

3. Physikalisches Institut
Universität Stuttgart

2022

For my Family,
For Sabine Kleinhansl-Nold and Siegfried Nold for teaching me everything about life...besides quantum physics.
For Andreas Nold my most favorite brother.
And last but not least for my Grandmother Monika Kleinhansl for bringing joy into my life from the beginning of my birth until now and hopefully continuing for a long long time.

"... Science is constantly proved all the time. You see, if we take something like any fiction, any holy book ... and destroyed it, in a thousand years' time, that wouldn't come back just as it was. Whereas if we took every science book, and every fact, and destroyed them all, in a thousand years they'd all be back, because all the same tests would [produce] the same result."
—Ricky Gervais

Contents

List of Figures

Acknowledgments

Before setting out the past years of my Ph.D. life in this manuscript, I want to thank many people who contributed directly or indirectly to its success and made my life over all these years easier.

First, I want to thank all jury members, namely Prof. Dr. Jörg Wrachtrup, Prof. Dr. Tilman Pfau, and Prof. Dr. Hans Peter Büchler, for accompanying this last step as a Ph.D. student and taking the time to read the thesis manuscript carefully.

I am incredibly grateful to Prof. Dr. Jörg Wrachtrup, who welcomed me into this group nearly four years ago and allowed me to do my research in this fantastic research group. Furthermore, I want to thank Dr. Florian Kaiser and Prof. Dr. Christof M. Gebhardt, who both were part of the project leading to the development of a quantum optical microphone. Additionally, I want to thank Prof. Dr. Stefanie Barz for providing me laboratory space for performing the measurements concerning the development of the quantum optical microphone. Dr. Florian Kaiser additionally directly supervised me over the entire time of my Ph.D., stood out as one of the brightest minds I got to know so far, and has been a great support, including fruitful discussions, 'magical' adjustments in the laboratory whenever challenges appeared and his overall knowledge from which I was able to learn a lot.

To come to the less formal part of my acknowledgments, I want to point out my Family, who made these, often not easy, years lighter and supported me unconditionally. First, I want to thank my Mother, Sabine Kleinhansl-Nold, and my Father, Siegfried Nold, for all the support not only during my Ph.D. but also for always giving me a rock-solid basis I could always count on no matter the occasion. Also, my grandparents Ernst and Monika Kleinhansl and Mina and Franz Nold have played a large part in my life. Their happiness, kindness, and, especially in the case of Monika, their wit I will never forget and hold dearly. Last but not least, I want to thank my super-smart brother Andreas Nold, my obviously favorite brother, for all the years growing up. You were always a role model to me. Of course, I can't finish this part without thanking my godchild and niece Emilia Nold, who, especially in the last year of my Ph.D., brought me a sh**load of fun.

Before no one reads any further and skips this part bored, I want to mention some collaborators who do not appear as authors in my publications but played a crucial role in finalizing the experiments this thesis is about. Maybe they will never read this,

but I still want to say thank you this way. First, I want to start with Annette Zechmeister and Barbara Baum from the Max Planck Institute for Solid State Research in Stuttgart for giving me an insight into the world of crystal and glass processing enabling the final design of a mirror membrane for the quantum microphone. Furthermore, I want to give Rüdiger Boppert a big thank you for allowing me to perform speech recognition tests in his facilities. Without your help, this project could never have been realized. Last but not least, I want to thank Marion Hagel for fabricating the tapered fibers in the Max Planck Institute for Solid State Research in Stuttgart. You were always fast and reliable; without your help, I would have never been able to finish my thesis.

As a short inset, I want to thank the Center for Integrated Quantum Science and Technology (IQST), which supported my Ph.D. financially. Mainly I want to give you guys credit because it happens way too rarely, so you stay as a silent contributor behind a variety of exciting experiments in quantum science.

Time to get real. I want to thank all current and past members of the Kaiser Squad, Di Liu, Jonah Heiler, Jonathan Körber, Dzhavid Dzhavadzade, Timo Steidl, Lukas Niechziol, Erik Hesselmeier, Arthur Bouamra, Marcel Krumrein, Raphael Wörnle, Joel Schmidt, Tobias Linkewitz, Dr. Charles Babin and whoever I might missed. You all made my Ph.D. thesis at the 3rd Institute of Physics a delightful time. All of you were always supportive at work, happy to discuss things, and equally excited to share after-work activities.
Primarily, I want to thank Joel Schmidt, Tobias Linkewitz, and Dr. Charles Babin for contributing to the quantum microphone. Each of you was a crucial part of the development; without any of you, it would not have been possible to realize.
Mainly because I promised to do so, I want to thank Jonah Heiler extraordinary for a constant supply of snacks during my writing period. Without you, I would be much thinner but also unhappier, so thank you for your kind support.
Additionally, I want to thank Charles Babin, Erik Hesselmeier, Jonah Heiler, Di Liu, Timo Steidl, Lukas Niechziol, Lukas R. Gussmann, Katharina V. Wutz, Jonathan Körber, Raphael (2) Wörnle and Marcel Krumrein for the incredible precise proofreading of this manuscript.
Furthermore, I want to thank Charles Babin, Jonah Heiler, Marcel Krumrein, Jonathan Körber, and Fiametta Sardi for almost weekly compensating side projects, aka climbing and bouldering. And, of course, special thanks to Fiametta Sardi for introducing me to this incredibly lovely sport in the first place.

Because I think your name did not appear even slightly often enough, again in a private paragraph, I want to thank you Dr. Charlieboii for your never-ending support, generally admirable lightness, and friendship. You made my Ph.D. life inside and outside the work environment much more enjoyable. You were in some sense the light of Eärendil's star during the harder times of my Ph.D.

Also, I want to send some special thanks to my Roommates, Lukas R. Gussmann and Katharina V. Wutz, for enduring me through the stressful time of my Ph.D. and

for your general support.

Additionally, thanks to my amazing other friends, in which I want to point out Maximilian Reinert, being my best friend since the eighth grade, with whom I already went through thick and thin...probably a lot of thick. I will always answer your calls and follow your fast decisions blindly, no matter where we are heading, as long as we head together. Thank you, Nathalie Jashinski, for being pretty much the same but with another pronoun. And, of course, thanks to Jonas Kuhls. Your balanced personality, friendliness, kindness, and humor make you a very dear person to me.

So finally, there is not much to say but thank you all guys for supporting me more or less directly. Each of you has been an essential part of my long, long journey as a Ph.D. student.

Scientific publications

1 R. Nold, C. Babin, J. Schmidt, T. Linkewitz, M. Zaballos, *et al.*, "A Quantum Optical Microphone in the Audio Band", *PRX Quantum* **3**, 020358 (2022) [1]

2 P. Vergyris, C. Babin, R. Nold, E. Gouzien, H. Herrmann, *et al.*, "Two-photon phase-sensing with single-photon detection", *Appl. Phys. Lett.* **117**, 024001 (2020) [7]

3 M. Stecker, R. Nold, L.M. Steinert, J. Grimmel, D. Petrosyan, *et al.*, "Controlling the dipole blockade and ionization rate of Rydberg atoms in strong electric fields", *Phys. Rev. Lett.* **125**, 103602 (2020) [8]

General introduction

This thesis is dealing with the manipulation of light in nanophotonic structures and the manipulation of single and multi-photon states as a direct step towards the realization of applications based on quantum optics.
Science can look back on a rich history in classical optics of more than one hundred years. In this regard, the formulation of the famous Maxwell's equations can be seen as a highlight [9, 10]. However, the field of experimental quantum optics emerged only in the past decades and its origins lie in the discovery of quantum mechanics. At the turn of the 20th century Max Planck first introduced the novel idea of energy quantization in absorption and emission of light in atoms [11]. This, at this time, entirely new concept would lead to a groundbreaking new field of physics: the quantum mechanics. Not many years later, in 1905, Einstein introduced the light quantization in the photo-electric effect [12] entirely independent of atoms and already proposed the wave-particle duality as a concluding remark of the 1909 paper [13]:
"... the next stage of the development of theoretical physics will bring us a theory of light which can be regarded as a kind of fusion of the wave theory and the emission theory ... a profound change in our views of the nature and constitution of light is indispensable."
Not long after that, Dirac introduced a theoretical description of the quantization of the light field in 1927 laying the foundations of modern quantum mechanics and quantum optics [14]. Altogether, this lead to a variety of theoretical descriptions of the quantum properties of light: Dirac in quantum field theory and furthermore by George Sudarshan, Roy J. Glauber, and Leonard Mandel in the field of applied quantum theory to the electromagnetic field in the 1950s and 1960s [15–19].
Simultaneously, first experiments on the correlation of the intensity of the light of stars had been performed by Hanbury Brown and Twiss [20]. With the development of the Laser in 1960 [21] the experimental investigation of the theory of light gained momentum, resulting in the first experimental investigation of antibunching by Kimble, Dagenais and Mandel [22]. Subsequently in 1985 Slusher demonstrated the first realization of squeezing [23], followed by the performance of the well known Hong-Ou-Mandel effect in 1987 [24]. All these developments in the field of quantum mechanics and quantum optics are commonly summarized in the single term: the **first quantum revolution**, describing the understanding and first realization of fundamental experiments in these fields.
However, today the **second quantum revolution** arises, where scientist all around the globe use the power of quantum mechanics and quantum optics for practical applications. For example building large-scale quantum computers, for enhanced computa-

tional power in certain fields [25] or in quantum sensing, recently realized by the usage of squeezed states of light in the new generation of gravitational wave detectors in LIGO [26], in the field of quantum cryptography [27–29] or biological sensing [30–32]. My thesis is placed in this emerging fields and covers two main parts. The first part is about a novel concept in nonlinear interferometry pushing toward reasonable applications by introducing a quantum optical microphone while the second part is about the efficient collection of light emitted from defects in SiC into optical fibers to overcome low photon collection rates of color centers in solid-states, representing an important step towards the miniaturization of quantum systems and associated scalability.

First chapter: Nonlinear interferometry

The first chapter gives a general overview of different approaches in nonlinear interferometry, focusing solely on phase-sensitive measurements. Starting with a short introduction of the textbook example of a classical interferometer, essential parameters like coherence, visibility, the standard quantum limit, etc. will be introduced.
In the following, three approaches to overcome the boundaries of this classical concept are presented; multi-photon interferometry, squeezed state interferometry, and SU(1,1) interferometry. The general operation concept, the reachable and realized enhancement, and current state challenges are outlined for each approach.

Second chapter: Novel concept of a nonlinear interferometer

This chapter introduces our novel approach to nonlinear interferometry. It starts with a small recap of the basic principles of photon-pair generation in nonlinear crystals. Here, the concept of parametric down-conversion and the quasi-phase matching in periodically poled crystals will be introduced. Furthermore, a detailed description of our experimental setup will be presented, covering the solution to two main challenges; the verification of temporal indistinguishability and the path-polarization quantum state engineering using a wavelength-selective waveplate.
After introducing the general concept of our novel quantum sensor, it is benchmarked against an almost perfect classical Michelson interferometer. Here, the enhancement over this experimentally realized classical interferometer and a perfect theoretical interferometer is shown. Additionally, the measurement speed in terms of the sampling rate is characterized. Covering the entire audio band, this characterization introduces the development of a quantum optical enhanced microphone, as shown in the next chapter.
As an auxiliary section, the extension to higher photon-pair fluxes of several hundreds of nanowatts will be discussed by measuring the noise performance of commercially available InGaAs cameras. Here, the sub-shot noise performance of fluxes of hundreds of nanowatts is characterized, and the sub-shot-noise detection is verified.

Third chapter: Quantum microphone in the audio band

Building up on the last chapter, the development of a quantum optical microphone in the audio band is presented. While not outperforming every arbitrary chosen classical microphone, the easy applicability of our concept is presented in this chapter. Further-

more, an enhancement over a classical microphone of the same type will be presented. This includes conceptual challenges like finding a suitable speaker and the development of a mirror membrane. The complete characterization of this mirror membrane will be presented in the following. As a next step, two medically approved speech recognition tests will be shown: the Freiburger speech test and the Oldenburger sentence test. Those tests will be compared, and their unique advantages and disadvantages discussed. Capitalizing on these features, the speech recognition test used in this work, the Oldenburger sentence test, will be further outlined. This part ends with introducing a single value number defining the threshold in dB sound pressure level, where people can understand 50% of the words played: the speech recognition threshold.
After having found a suitable speech recognition test, the classical and quantum microphone recordings will be characterized, and the enhancement performance between the two compared. Here, an enhancement factor in the signal-to-noise ratio of 1.10 ± 0.04 can already be presented. Additionally, a study containing 45 test subjects performing two Oldenburger sentence tests (quantum and classical) will be discussed. This study shows an enhanced understanding of the recorded words of the quantum microphone with a reduction of a speech recognition value of $0.57\,\mathrm{dB_{SPL}}$ with a standard deviation under the square root law of $0.22\,\mathrm{dB_{SPL}}$. Furthermore, the significance of the study is investigated using a standard statistical t-test with the hypothesis: "The quantum microphone does not lead to an improvement.".

Fourth chapter: Theoretical Framework

This chapter introduces a theoretical framework describing our novel quantum sensor. Here, the experimental setup will be reduced to a single operator in the Heisenberg picture $\hat{O}_{\mathrm{Qu.Sens.}}$. Following this representation, the possible enhancement and the performance under loss will be investigated for two regimes: the low squeezing regime $r \ll 1$ and the high squeezing regime $r \gg 1$. The results are discussed and in case of a small squeezing parameter related to the experimental findings.

Fifth chapter: Nanophotonic tapered-fiber-tapered-waveguide interface

This chapter investigates the coupling between nanophotonic waveguides and optical single-mode fibers. First, the goal to integrate single defects into silicon carbide waveguides will be introduced by presenting the silicon carbide platform in general. As a second step, a short theoretical description of nanophotonic waveguides will be presented. The fundamental wave propagation in dielectric media will be introduced as well as Yee's finite difference algorithm, an algorithm to numerically compute arbitrary nanophotonic structures and the light propagation in them. Additionally, a short principal description of waveguide coupling using Bragg gratings will be discussed.
This theoretical part presents strategies to increase the coupling efficiency between single-mode fibers and nanophotonic waveguides. Here, three main approaches will be presented: using diffraction gratings, edge couplers, and tapered fibers. Furthermore, different concepts of the fabrication of tapered fibers will be introduced: CO_2-laser heating, thermal heating, and chemical etching using hydrofluoric acid (HF).
As a next step, the tapered-fiber-tapered-waveguide interface is investigated theoretically using the commercially available software Lumerical based on Yee's algorithm.

First, the choice of the waveguide design will be discussed, leading to single-mode waveguides with a triangular cross-section. Secondly, the in- and outcoupling between these waveguides and tapered fibers will be discussed separately. The coupling efficiency is investigated for the free parameters of the waveguide and the fiber; fiber taper angle, fiber taper-end diameter, and waveguide taper length.
Capitalizing on that, the fabrication process (HF etching), carried out in our institute and the Max Planck Institute for Solid State Research in Stuttgart, will be described in detail. Following this fabrication process, the characterization of the fiber taper angle is presented using an optical and a scanning electron microscope. Subsequently, the characterization of the complete coupling interface will be outlined. First, a single frequency coupling for different waveguide parameters shows coupling efficiencies of approximately 80%. Furthermore, the incoupling efficiency as a function of the taper-taper overlap is characterized, showing the same behavior as predicted by theory. Following these measurements, the coupling efficiency as a function of the wavelength is investigated. Here, a transmission spectrum is collected and discussed, leading to an average coupling efficiency of approximately 83% at 917 nm .
As an auxiliary section, I will present an expansion of our characterization setup toward detecting single V_2 centers in SiC. In addition to the previous setup we will introduce an expansion of the setup with a self-built imaging system, allowing an excitation from the top. A proof of principle confocal image of the waveguides, where the excitation is taking place from the top, while the collection is done via the tapered-fiber-tapered-waveguide interface, will be presented. Furthermore, preliminary results, showing distinct single bright spots, which we assigned to optically active defects in SiC will be presented. A subsequent study of the emission behavior and a resulting second order correlation value of $g^{(2)}(0) = 0.24$ confirms additionally the existence of single emitters inside the waveguides, while its typification is still left unclassified.

Allgemeine Einleitung

Diese Arbeit befasst sich mit der Manipulation von Licht in nanophotonischen Strukturen und der Manipulation von Ein- und Mehrphotonenzuständen als direktem Schritt zur Realisierung sinnvoller Anwendungen auf der Grundlage der Quantenoptik.
Die Wissenschaft kann auf eine reiche, mehr als hundertjährige Geschichte der klassischen Optik zurückblicken. In dieser Hinsicht kann die Formulierung der berühmten Maxwellschen Gleichungen als ein Höhepunkt angesehen werden [9,10]. Das Gebiet der experimentellen Quantenoptik ist jedoch erst in den letzten Jahrzehnten entstanden, und seine Ursprünge liegen in der Entdeckung der Quantenmechanik. Um die Wende zum 20. Jahrhundert führte Max Planck erstmals die neuartige Idee der Energiequantisierung bei der Absorption und Emission von Licht in Atomen ein. Dieses zu diesem Zeitpunkt völlig neue Konzept sollte zu einem bahnbrechenden neuen Gebiet der Physik führen: der Quantenmechanik. Nicht viele Jahre später, 1905, führte Einstein die Lichtquantisierung im photoelektrischen Effekt [12] völlig unabhängig von Atomen ein und schlug bereits den Welle-Teilchen-Dualismus als Schlussbemerkung der 1909 erschienenen Arbeit [13] vor:
"... die nächste Stufe der Entwicklung der theoretischen Physik wird uns eine Theorie des Lichts bringen, die als eine Art Verschmelzung der Wellentheorie und der Emissionstheorie angesehen werden kann ... eine tiefgreifende Änderung unserer Ansichten über die Natur und Beschaffenheit des Lichts ist unabdingbar."
Nicht lange danach stellte Dirac 1927 eine theoretische Beschreibung der Quantisierung des Lichtfeldes vor und legte damit den Grundstein für die moderne Quantenmechanik und Quantenoptik [14]. Insgesamt führte dies zu einer Vielzahl von theoretischen Beschreibungen der Quanteneigenschaften des Lichts: Dirac in der Quantenfeldtheorie und darüber hinaus durch George Sudarshan, Roy J. Glauber und Leonard Mandel im Bereich der angewandten Quantentheorie auf das elektromagnetische Feld in den 1950er und 1960er Jahren [15–19].
Gleichzeitig wurden von Hanbury Brown und Twiss erste Experimente zur Korrelation der Intensität des Lichts von Sternen durchgeführt. Mit der Entwicklung des Lasers im Jahr 1960 [21] gewann die experimentelle Untersuchung der Lichttheorie an Schwung, was zur ersten experimentellen Untersuchung des Antibunching durch Kimble, Dagenais und Mandel führte [22]. Anschließend demonstrierte Slusher 1985 die erste Realisierung von gequetschtem Licht [23], gefolgt von der Durchführung des bekannten Hong-Ou-Mandel-Effekts im Jahr 1987 [24]. All diese Entwicklungen auf dem Gebiet der Quantenmechanik und Quantenoptik werden gemeinhin unter dem Begriff der ersten Quantenrevolution zusammengefasst, der das Verständnis und die erste Durchführung grundlegender Experimente auf diesen Gebieten beschreibt. Heute jedoch

befinden wir uns in Zeiten der **zweiten Quantenrevolution**, in denen Wissenschaftler rund um den Globus die Macht der Quantenmechanik und Quantenoptik für praktische Anwendungen nutzen. Zum Beispiel beim Bau von Quantencomputern zur Steigerung der Rechenleistung in bestimmten Bereichen [25] oder bei der Quantensensorik, die zum Beispiel kürzlich durch die Verwendung von gequetschten Lichtzuständen in der neuen Generation von Gravitationswellendetektoren in LIGO [26] realisiert wurde, auf dem Gebiet der Quantenkryptographie [27–29] oder der biologischen Sensorik [30–32]. Meine Dissertation ist in diesem aufstrebenden Bereich angesiedelt und umfasst zwei Hauptteile. Im ersten Teil geht es um ein neuartiges Konzept in der nichtlinearen Interferometrie. Die Entwicklung eines quantenoptischen Mikrofons, beweist die einfache Anwendbarkeit unseres Konzeptes, und ebnet dadurch den Weg für sinnvolle Anwendungen. Der zweite Teil befasst sich mit der effizienten Kopplung von Wellenleitern in Siliziumkarbid an optische Fasern. Hier wird die Sammeleffizienz von Licht, das von Defekten in Siliziumkarbid emittiert wird drastisch erhöht, um die niedrigen Photonensammelraten von Farbzentren in Festkörpern zu überwinden. Dies stellt einen bedeutenden Schritt in Richtung Miniaturisierung von Quantensystemen und der damit verbundenen Skalierbarkeit dar.

Erstes Kapitel: Nichtlineare Interferometrie

Das erste Kapitel gibt einen allgemeinen Überblick über die verschiedenen Ansätze in der nichtlinearen Interferometrie und konzentriert sich dabei ausschließlich auf phasenempfindliche Messungen. Beginnend mit einer kurzen Einführung in das Lehrbuchbeispiel eines klassischen Interferometers werden wesentliche Parameter wie Kohärenz, Kontrast, das Standard-Quantenlimit, etc. vorgestellt.
Im Folgenden werden drei Ansätze zur Überwindung der Grenzen dieses klassischen Konzepts vorgestellt: Multiphotonen-Interferometrie, Squeezed State Interferometrie und SU(1,1)-Interferometrie. Für jeden Ansatz werden das allgemeine Betriebskonzept, die erreichbare und realisierte Verbesserung sowie die aktuellen Herausforderungen skizziert.

Zweites Kapitel: Neuartiges Konzept eines nichtlinearen Interferometers

In diesem Kapitel wird unser neuartiger Ansatz zur nichtlinearen Interferometrie vorgestellt. Es beginnt mit einer kurzen Rekapitulation der Grundprinzipien der Erzeugung von Photonenpaaren in nichtlinearen Kristallen. Hier werden das Konzept der parametrischen Abwärtskonversion und die Quasi-Phasenanpassung in periodisch gepolten Kristallen vorgestellt. Darüber hinaus wird eine detaillierte Beschreibung unseres experimentellen Aufbaus vorgestellt, der die Lösung zweier wichtiger Herausforderungen umfasst: die Verifizierung der zeitlichen Ununterscheidbarkeit und das Pfadpolarisations-Engineering der Quantenzustände unter Verwendung einer wellenlängenselektiven Wellenplatte.
Nach der Vorstellung des allgemeinen Konzepts unseres neuartigen Quantensensors wird dieser mit einem nahezu perfekten realen klassischen Michelson-Interferometer verglichen. Hier wird die Verbesserung gegenüber diesem experimentell realisierten klassischen Interferometer und einem perfekten theoretischen Interferometer gezeigt. Zusätzlich wird die Messgeschwindigkeit in Bezug auf die Abtastrate charakterisiert.

Diese Charakterisierung, die das gesamte Audioband abdeckt, leitet die Entwicklung eines quantenoptisch verbesserten Mikrofons ein, wie im nächsten Kapitel gezeigt wird. Als Zusatzkapitel wird die Ausweitung auf höhere Photonenpaarflüsse von mehreren hundert Nanowatt durch Messung des Rauschverhaltens von kommerziell erhältlichen InGaAs-Kameras diskutiert. Hier wird das Sub-Shot-Rauschverhalten bei Flüssen von Hunderten von Nanowatt charakterisiert und die detektion mit geringerem Rauschen als das photonische Schrotrauschen verifiziert.

Drittes Kapitel: Quantenmikrofon im Audioband

Aufbauend auf dem letzten Kapitel wird hier die Entwicklung eines quantenoptischen Mikrofons im Audioband vorgestellt. Obwohl es nicht jedes beliebige klassische Mikrofon übertrifft, wird in diesem Kapitel die einfache Anwendbarkeit unseres Konzepts vorgestellt. Weiterhin wird eine Verbesserung gegenüber einem klassischen Mikrofon desselben Typs vorgestellt, beginnend mit konzeptionellen Herausforderungen wie der Suche nach einem geeigneten Lautsprecher und der Entwicklung einer Spiegelmembran. Die vollständige Charakterisierung dieser Spiegelmembran wird im Folgenden vorgestellt. In einem nächsten Schritt werden zwei medizinisch anerkannte Spracherkennungstests vorgestellt: der Freiburger Sprachtest und der Oldenburger Satztest. Diese Tests werden miteinander verglichen und ihre jeweiligen Vor- und Nachteile diskutiert. Ausgehend von diesen Merkmalen wird der in dieser Arbeit verwendete Spracherkennungstest, der Oldenburger Satztest, näher erläutert. Dieser Teil endet mit der Einführung einer einzigen Zahl, die den Schwellenwert in dB Schalldruckpegel definiert, bei dem Menschen 50% der gespielten Wörter verstehen können, die Spracherkennungsschwelle.
Nachdem ein geeigneter Spracherkennungstest gefunden wurde, werden die klassischen und die quantenmechanischen Mikrofonaufnahmen charakterisiert und die Sensitivität zwischen beiden verglichen. Hier kann bereits ein Verbesserungsfaktor im Signal-Rausch-Verhältnis von $1,10 \pm 0,04$ präsentiert werden. Zusätzlich wird eine Studie mit 45 Versuchspersonen vorgestellt, die zwei Oldenburger Satztests (quantenmechanisch und klassisch) durchführten. Diese Studie zeigt ein verbessertes Verständnis der aufgenommenen Wörter des Quantenmikrofons mit einer Reduktion der Spracherkennungsschwelle um $0,57\,\mathrm{dB_{SPL}}$ bei einer Standardabweichung unter dem Quadratwurzelgesetz von $0,22\,\mathrm{dB_{SPL}}$. Darüber hinaus wird die Signifikanz der Studie mit Hilfe eines statistischen Standard-t-Tests mit der Hypothese: "Das Quantenmikrofon führt nicht zu einer Verbesserung." untersucht.

Viertes Kapitel: Theoretischer Rahmen

In diesem Kapitel wird ein theoretischer Rahmen zur Beschreibung unseres neuartigen Quantensensors vorgestellt. Hier wird der experimentelle Aufbau auf einen einzelnen Operator im Heisenberg-Bild $\hat{O}_{\mathrm{Qu.Sens.}}$ reduziert. Anhand dieser Darstellung werden der mögliche Verbesserungsfaktor und der Einfluss von Verlusten für zwei Regime untersucht: das Regime mit kleinem Quetschungsparameter $r \ll 1$ und das Regime mit großem Quetschungsparameter $r \gg 1$. Die Ergebnisse werden diskutiert und im Falle eines kleinen Quetschungsparameter mit den experimentellen Ergebnissen vergleicht.

Fünftes Kapitel: Nanophotonische Schnittstelle unter der Verwendung von konischen Fasern und spitz zulaufenden Wellenleitern

In diesem Kapitel wird die Kopplung zwischen nanophotonischen Wellenleitern und optischen Singlemode-Fasern untersucht. Zunächst wird das Ziel, einzelne Defekte in Siliziumkarbid-Wellenleiter zu integrieren, eingeführt, indem die Siliziumkarbid-Plattform im Allgemeinen vorgestellt wird. In einem zweiten Schritt wird eine kurze theoretische Beschreibung von nanophotonischen Wellenleitern vorgestellt. Die grundlegende Wellenausbreitung in dielektrischen Medien wird ebenso vorgestellt wie der Endliche-Differenzen-Algorithmus von Yee, ein Algorithmus zur numerischen Berechnung beliebiger nanophotonischer Strukturen und der Lichtausbreitung in ihnen. Zusätzlich wird eine kurze prinzipielle Beschreibung der Wellenleiterkopplung mit Bragg-Gittern diskutiert.
In diesem theoretischen Teil werden Strategien zur Steigerung der Kopplungseffizienz zwischen Singlemode-Fasern und nanophotonischen Wellenleitern vorgestellt. Dabei werden drei Hauptansätze vorgestellt: die Verwendung von Beugungsgittern, Kantenkopplern und konischen Fasern. Darüber hinaus werden verschiedene Konzepte für die Herstellung von konischen Fasern vorgestellt: CO_2-Lasererwärmung, thermische Erwärmung und chemisches Ätzen unter Verwendung von Flusssäure.
In einem nächsten Schritt wird die Schnittstelle zwischen spitz zulaufender Faser und spitz zulaufendem Wellenleiter mit Hilfe der kommerziell erhältlichen Software Lumerical, die auf dem Algorithmus von Yee basiert, theoretisch untersucht. Zunächst wird die Wahl des Wellenleiterdesigns diskutiert, das zu Einzelmodenwellenleitern mit dreieckigem Querschnitt führt. Zweitens werden die Ein- und Auskopplung zwischen diesen Wellenleitern und konischen Fasern separat diskutiert. Die Kopplungseffizienz wird für die freien Parameter der Wellenleiter und der Faser untersucht: Faseröffnungswinkel, Durchmesser der Faserspitze und Länge der Wellenleiterspitze.
Darauf aufbauend wird der in unserem Institut durchgeführte Herstellungsprozess (HF-Ätzen) im Detail beschrieben. Im Anschluss an den Herstellungsprozess wird die Charakterisierung des Faseröffnungswinkels unter Verwendung eines optischen und eines Rasterelektronenmikroskops vorgestellt. Anschließend wird die Charakterisierung der gesamten Kopplungsschnittstelle skizziert. Zunächst zeigt eine Einzelfrequenzkopplung für verschiedene Wellenleiterparameter Kopplungseffizienzen von etwa 80%. Darüber hinaus wird die Einkopplungseffizienz als Funktion der Überlappung von Faserkonus und Wellenleiterkonus charakterisiert, wobei sich das gleiche Verhalten, wie in der Theorie vorhergesagt, zeigt. Im Anschluss an diese Messungen wird die Kopplungseffizienz in Abhängigkeit von der Wellenlänge untersucht. Hier wird ein Transmissionsspektrum gemessen und diskutiert, das zu einer durchschnittlichen Kopplungseffizienz bei 917 nm von etwa 83% führt.
In einem zusätzlichen Abschnitt wird eine Erweiterung unseres Charakterisierungsaufbaus zum Nachweis einzelner V_2-Zentren in SiC vorgestellt. Zusätzlich zum bisherigen Aufbau wird eine Erweiterung präsentiert, die ein selbstgebautes Abbildungssystem umfasst, das eine Anregung von oben ermöglicht. Anschließend werden erste Ergebnisse, ein konfokales Bild des Wellenleiters präsentiert, bei dem die Anregung von oben erfolgt, während die Sammlung über die Schnittstelle zwischen konischer Faser und spitz zulaufendem Wellenleiter durchgeführt wird. Als Ergebnis werden deutliche einzelne helle Punkte sichtbar, die wir optisch aktiven Defekten im SiC zuordnen.

Eine anschließende Untersuchung des Emissionsverhaltens und ein daraus resultierender Korrelationswert zweiter Ordnung von $g^{(2)}(0) = 0,24$ bestätigt die Existenz von Einzelemittern in den Wellenleitern.

Chapter 1

Nonlinear interferometry

In the last century, the ability to perform high-precision optical measurements has proved to be paramount. In many fields of engineering or physics, interferometric measurements emerged as the gold standard, to measure small displacements [33], refractive indices [30, 34] or surface properties [35, 36]. In recent years, quantum optical sensing has quickened interest in many fields of physics. New generations of quantum sensors promise to reach resolutions and sensitivities unfathomable for classical sensors.
This, often associated with the second quantum revolution, has already led to a foray toward enhanced sensing in optical coherence tomography [37], in the measurement of dichromatic dispersion [38], quantum microscopy [31] and Raman microscopy [39] or maybe the most popular field the gravitational wave detection at LIGO [26]. The interferometric sensor at LIGO, with its classical optical path length difference sensitivity of 1/10,000th of a proton's width, even further increases its sensitivity using squeezed states of light [40]. Another exciting field to utilize quantum phenomena for sensing is biological imaging. Advances in this field have recently led to the award of the Nobel Prize in Chemistry (2014) for Eric Betzig, Stefan W. Hell, and William E. Moerner for the development of super-resolved fluorescence microscopy [41–43]. Microscopy based on interferometric measurements without the disposition of fluorescent markers or molecules is often limited due to the sensitivity of biological samples to light exposure and short wavelength photons [32, 44–48], limiting the amount of light and therefore the sensitivity of an optical measurement. Here, an enhancement of the sensitivity per resource/photon is of utmost interest [32] and proves to be a niche field of application for the first generations of quantum sensors.
In this chapter, we will solely focus on phase-sensitive measurements in interferometers. In the first section, I will briefly introduce the textbook example of a classical interferometer and its intrinsic boundaries. Here we will use the plane wave approach and single-photon one to introduce the emerging interferometer signal and the correlation between the interferometer's coherence and the visibility. Furthermore, as a resource, I will introduce the maximum sensitivity to a phase estimation measurement using single photons (which enter the interferometer). This maximum sensitivity is also known as the standard quantum limit (SQL), which is only limited by the classical photonic shot noise.
In the subsequently following three sections, I will introduce different approaches in

nonlinear interferometry, which promise to overcome this classical limit and thus outperform classical interferometers. As a first example, nonlinear interferometry using squeezed states of light will be introduced. This approach promises large enhancement factors and high absolute sensitivities for phase estimation measurements. Further challenges like a loss dependency of the enhancement factor over the complete experimental system, including the detection, will be discussed.
A second example of nonlinear interferometry presents a straightforward approach to saturate the Heisenberg limit using maximally entangled multi-photon states. Again, challenges like low repetition rates and a complex multi-photon state generation, will be discussed.
The relatively novel concept of SU(1,1) interferometers is introduced in the last section. These nonlinear interferometers use parametric amplification of a signal without amplifying the noise as a primary source of enhancement. While promising to overcome the loss dependency of the enhancement outside of the interferometer itself, this approach shows so far low enhancement factors. Also, it does not offer suppression of common-mode noise as in classical interferometry.

1.1 The Mach-Zehnder interferometer

This section consists of a short recap of classical interferometry. As a representative example, we will focus solely on the Mach-Zehnder interferometer. I will introduce several parameters, which will prove relevant for comparison with nonlinear interferometry later.

1.1.1 Interference and coherence

The textbook example of a classical interferometer is the Mach-Zehnder interferometer [49, 50]. A schematic of this sensor is shown in Fig. 1.1. Here, a plane wave is entering the sensor from the left side. A 50:50 beam splitter defines two optical paths (a and b). A phase-altering object (depicted by ϕ) introduces a phase difference between the two paths. After recombination at a second 50:50 beam splitter, the intensity is measured at each output port D_1 and D_2.
To understand how this interferometer measures the phase ϕ, we will assume that a plane wave $E(r,t) = E_{\mathrm{in}} e^{-i(\omega t - \vec{k_i} n \vec{r})}$ is entering the interferometer at the input port of the first beam splitter. The beam splitter splits this plane wave into two waves of amplitude $E_{\mathrm{a,b}} = E_{\mathrm{in}}/\sqrt{2}$. After the second beam splitter, these two waves are recombined, leading to signals at the output ports of this beam splitter of [51]:

$$E_{\mathrm{c}}(r,t) = \frac{E_{\mathrm{in}}}{\sqrt{2}} e^{-i(\omega t - \vec{k_c}\vec{r})} \cdot (e^{-i\vec{k}\vec{r}_{\mathrm{a}}} e^{-i\Delta\phi} + e^{-i\vec{k}\vec{r}_{\mathrm{b}}}) \tag{1.1}$$

$$E_{\mathrm{d}}(r,t) = \frac{E_{\mathrm{in}}}{\sqrt{2}} e^{-i(\omega t - \vec{k_d}\vec{r})} \cdot (e^{-i\vec{k}\vec{r}_{\mathrm{a}}} e^{-i\Delta\phi} - e^{-i\vec{k}\vec{r}_{\mathrm{b}}}), \tag{1.2}$$

where $\vec{r}_{\mathrm{a}}$ and $\vec{r}_{\mathrm{b}}$ resemble different path lengths (or an otherwise introduced phase difference $\Delta\phi$) between path a and b.

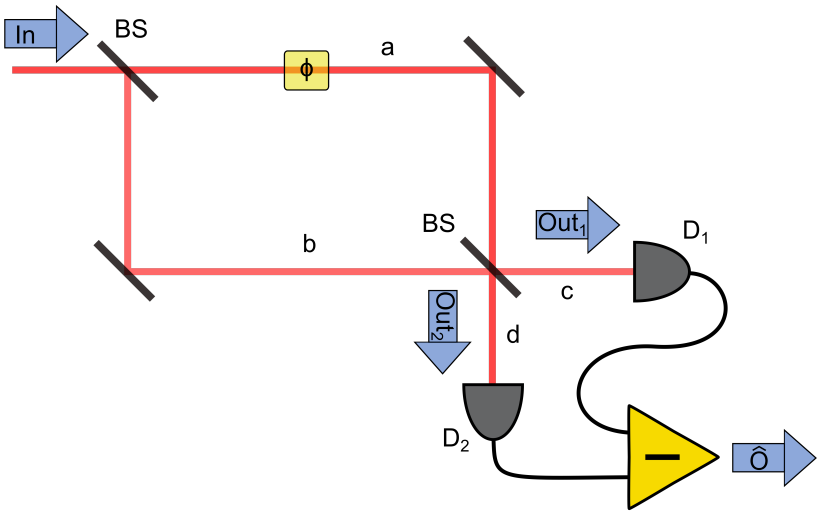

Figure 1.1: **Schematic of a Mach-Zehnder interferometer.** A plane wave enters the Mach-Zehnder interferometer through a 50:50 beam splitter, which defines two paths. A path length difference, or an object with a different refractive index than its environment, introduces a phase difference between the paths a and b. The output ports c and d of a second beam splitter give rise to a phase difference estimation measurement via intensity detection (detectors D_1 and D_2), depicted as operator $\hat{O}$. A standard approach to collect a maximum of information is the subtraction of both output intensity signals. Adapted from [1].

The resulting intensity signal measured at the detectors D_1 and D_2 is thus:

$$I_1(\Delta r, \Delta\phi) = \frac{1}{2} I_0 (1 + \cos(k\Delta r + \Delta\phi)) \tag{1.3}$$

$$I_2(\Delta r, \Delta\phi) = \frac{1}{2} I_0 (1 - \cos(k\Delta r + \Delta\phi)) \tag{1.4}$$

As a standard approach to reach the highest sensitivity to a phase difference between paths a and b, and to not lose information by measuring only a single output port, the signals are subtracted, leading to a single intensity signal of:

$$I_{1-2}(\Delta r, \Delta\phi) = I_0 \cos(k\Delta r + \Delta\phi). \tag{1.5}$$

Out of convenience, we will focus solely on the temporal coherence in the next part. Note that spatial coherence also plays a role in terms of a non-perfect mode overlap. By employing the coherence, we will finally introduce the visibility of a classical interferometer which, as I will show in chapter 4, influences the maximum reachable phase sensitivity.
The temporal coherence introduces a value for the time τ_c, after which the phases of two electromagnetic waves are not correlated anymore [52]. In other words this temporal difference can be directly translated into a so-called coherence length $L_c = \frac{c}{n}\tau_c$. By using the first-order correlation function [51]

$$g^{(1)}(\tau) = \frac{\langle E^*(t) E(t+\tau) \rangle}{\langle |E(t)|^2 \rangle}, \tag{1.6}$$

the coherence time can be defined as:

$$\tau_c = \int_{-\infty}^{\infty} |g^{(1)}(\tau)|^2 d\tau. \tag{1.7}$$

Ultimately the coherence time is linked to the spectral width of the light and, therefore to the spectral shape. For example, for a Lorentzian shape, the coherence time can be defined as:

$$\tau_c \approx \frac{1}{\pi\Delta\nu}, \tag{1.8}$$

with $\Delta\nu$ the full width at half maximum (FWHM) spectral linewidth. Thus, sources with narrow linewidth promise to reach longer coherence times and vice versa.
If we follow the common definition of the visibility:

$$\text{visibility} = \frac{I_{\max} - I_{\min}}{I_{\max} + I_{\min}} \tag{1.9}$$

we can connect the visibility with the first-order correlation function. If we consider a Mach-Zehnder interferometer with a constant average intensity and a temporal path length difference of τ, the output field can be described simply as [52]:

$$E_{\text{out}}(t) = \frac{1}{\sqrt{2}} (E(t) - E(t+\tau)). \tag{1.10}$$

Using equation (1.6), the average output intensity ($I_{\text{out}}(\tau) = \frac{c\,\epsilon_0}{2}\langle E_{\text{out}}(t)^* E_{\text{out}}(t)\rangle$) can be written as:

$$I_{\text{out}}(\tau) = I_0\Big(1 - \text{Re}(|g^{(1)}(\tau)|)\Big), \tag{1.11}$$

with $I_0 = \frac{c\,\epsilon_0}{2}\langle E(t)^* E(t)\rangle$ and ϵ_0 the vacuum permittivity.
With equation 1.9 it can be seen, that the visibility resembles the absolute value of the first-order correlation function:

$$\text{visibility} = |g^{(1)}(\tau)|. \tag{1.12}$$

Thus, there is an immanent connection between the coherence of an interferometer and the intensity detector signal. Combined with loss-induced decoherence, this effect will be our quantum sensor's primary suppression of the enhancement factor.

1.1.2 The standard quantum limit

For deriving the phase estimation sensitivity limit in classical interferometry, I will focus in this section on the case where distinct photons travel through the interferometer. This solely changes the description of the amplitude from intensity to a photon number and therefore does not lose generality.
In direct analogy, the scheme mentioned above can be reduced to the single photon level, in which instead of a plane wave, N distinct single photons are entering the Mach-Zehnder interferometer. Thus the equations (1.3), (1.4) and (1.5) solely change to:

$$S_1(\Delta r, \Delta\phi) = \frac{1}{2}\,N\,(\,1 + \cos\,(k\Delta r + \Delta\phi)\,) \tag{1.13}$$

$$S_2(\Delta r, \Delta\phi) = \frac{1}{2}\,N\,(\,1 - \cos\,(k\Delta r + \Delta\phi)\,) \tag{1.14}$$

and

$$S_{1-2}(\Delta r, \Delta\phi) = N\,\cos\,(\,k\Delta r + \Delta\phi\,). \tag{1.15}$$

In the following the parameters $k\Delta r + \Delta\phi$ will be, for convenience only, combined to an absolute phase difference $\Delta\phi_{\text{tot}}$. In Fig. 1.2 this subtracted single photon interferometer signal is illustrated as a function of the phase difference between the paths a and b.
Sensitivity is the signal intensity difference for a given phase shift. In our case, the sensitivity is maximal if the initial phase difference is odd multiples of $\pi/2$. Around this point, for sufficiently small phase changes, the first order Taylor expansion [53] can be performed, leading to a difference signal of:

$$S_{1-2}(\Delta\phi_{\text{tot}}) \overset{\phi_0=\frac{\pi}{2}}{\approx} N\,\Delta\phi_{\text{tot}}. \tag{1.16}$$

As the smallest resolvable phase shift, the phase shift equal to or above the noise level can be defined. With recalling that N photons entered the interferometer, external loss sources are neglected, and N photons arrive at the detectors, the total noise in the system solely consists of the intrinsic shot noise of the photons itself ($\sqrt{N}$ [54]).
With photonic shot noise as the only source of noise, this leads to:

$$S_{1-2}(\Delta\phi_{\text{tot}}) \overset{\phi_0=\frac{\pi}{2}}{\approx} N\,\Delta\phi_{\text{tot}} \geq \sqrt{N}. \tag{1.17}$$

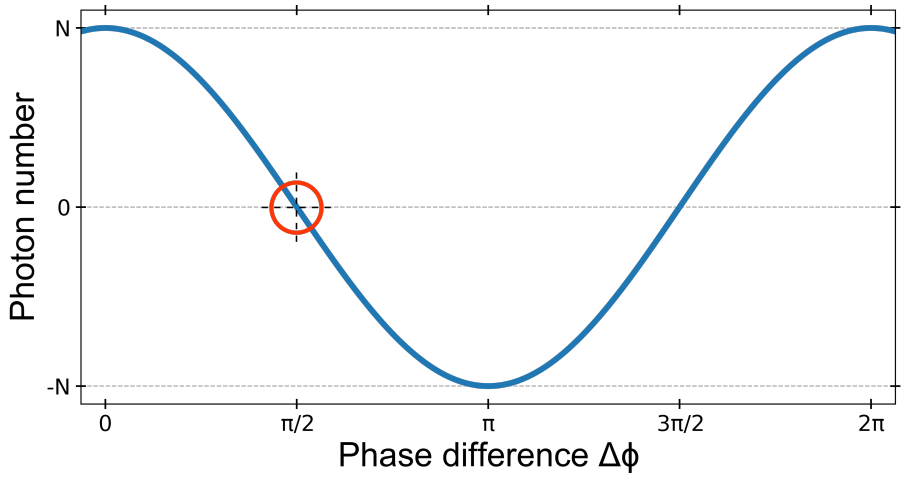

Figure 1.2: **Subtracted interferometer signal of the Mach-Zehnder interferometer.** The subtracted interferometer signal $S_{1-2}(\Delta\phi_{\mathrm{tot}}) = N\cos(\Delta\phi_{\mathrm{tot}})$ as a function of the absolute phase difference $\Delta\phi_{\mathrm{tot}}$. The red circle depicts the point of the highest sensitivity to a change in the phase difference. Interestingly, it corresponds to the point, where the intensities measured at both detectors are perfectly balanced.

If the equation is solved for the phase shift $\Delta\phi_{\mathrm{tot}}$, we obtain a lower bound for a minimal resolvable phase shift. This equation is well known as the standard quantum limit (SQL) [55]:

$$\Delta\phi_{\mathrm{tot}} \geq \frac{1}{\sqrt{N}}. \tag{1.18}$$

The main goal in nonlinear interferometry is to use different states of light to overcome these fundamental limits and outperform classical interferometers. So far, various nonlinear interferometers have been realized with the primary goal to show phase estimation sensitivities beyond the classical standard quantum limit without setting limitations to absolute sensitivities, measurement speed, or else. Thus only very few experimental schemes have shown enhanced sensing in appropriate fields of application.

1.2 Multi-photon interferometry

Already in the 20th century, Milburn [56] and Ou [57] presented an approach to overcome the fundamental limit of classical interferometry and improve the sensitivity from $1/\sqrt{N}$ to $1/N$ using correlated Fock-states.
Later it was discovered that the usage of maximally entangled states [58] of the form

$$|\Psi_N\rangle = \frac{1}{\sqrt{N}}\left(|N,0\rangle + |0,N\rangle\right) \tag{1.19}$$

proved optimal for a maximal improvement of the phase sensitivity [59]. Note, that in the following only a perfect N00N state is discussed, omitting states with nonzero pair-components. The name N00N state derives from this typical description of a maximally entangled state.

A pictorial representation of the source of enhancement using N00N states brings us back to the Mach-Zehnder interferometer (Fig. 1.1). Instead of sending N distinct single photons separately through the interferometer representing N single phase estimation measurements, it could be considered that either N indistinguishable photons travel simultaneously along path a and zero photons along path b or vice versa.
A common way to represent the N00N state from equation (1.19) is [60–63]:

$$|\Psi_N\rangle = \frac{1}{\sqrt{N}} \left(|N,0\rangle + |0,N\rangle \right) = \frac{1}{\sqrt{2}} \left(\frac{\hat{a}_{\mathrm{a}}^{\dagger N}}{\sqrt{N!}} + \frac{\hat{a}_{\mathrm{b}}^{\dagger N}}{\sqrt{N!}} \right) |\mathrm{vac}\rangle \tag{1.20}$$

with $|\mathrm{vac}\rangle$ the vacuum state and $\hat{a}_i^{\dagger N}$, $i = \mathrm{a}, \mathrm{b}$ the creation operator for each interferometer arm. The phase shift in the interferometer arm a can be characterized by the effect on the filed operator $\hat{a}_{\mathrm{a}}^{\dagger N}$:

$$\hat{a}_{\mathrm{a}}^{\dagger N} \rightarrow \mathrm{e}^{-i\phi}\, \hat{a}_{\mathrm{a}}^{\dagger N}. \tag{1.21}$$

Thus, a phase shifted N00N state:

$$|\Psi_{N,\phi}\rangle = \frac{1}{\sqrt{2}} \left(\mathrm{e}^{-iN\phi} \frac{\hat{a}_{\mathrm{a}}^{\dagger N}}{\sqrt{N!}} + \frac{\hat{a}_{\mathrm{b}}^{\dagger N}}{\sqrt{N!}} \right) |\mathrm{vac}\rangle = \frac{1}{\sqrt{N}} (\mathrm{e}^{-iN\phi} |N,0\rangle + |0,N\rangle), \tag{1.22}$$

can be introduced. To estimate the phase difference between the paths a and b the observable

$$\hat{O}_{\mathrm{N00N}} = |N,0\rangle \langle N,0| + |0,N\rangle \langle 0,N| \tag{1.23}$$

can be defined. When this observable is measured we obtain a similar result as for the classical Mach-Zehnder interferometer:

$$\langle \Psi_{N,\phi}|\, \hat{O}_{\mathrm{N00N}}\, |\Psi_{N,\phi}\rangle = \cos(N\,\phi). \tag{1.24}$$

For an arbitrary detection operator, the variance can be calculated as $\Delta\hat{U}^2 = \langle \hat{U}^2 \rangle - \langle \hat{U} \rangle^2$. With $\hat{O}_{\mathrm{N00N}}^2 = \mathbb{1}$ the variance resembles:

$$\Delta\hat{O}_{\mathrm{N00N}}^2 = 1 - \cos^2(N\,\phi) = \sin^2(N\,\phi). \tag{1.25}$$

Using the variance and the signal strength of an infinitesimal phase change $|\partial_\Phi \langle \hat{O}_{\mathrm{N00N}} \rangle|$ additionally the maximum sensitivity to a relative phase change can be calculated as:

$$\Delta\Phi = \frac{\Delta\hat{O}_{\mathrm{N00N}}}{|\partial_\Phi \langle \hat{O}_{\mathrm{N00N}} \rangle|} = \frac{1}{N}. \tag{1.26}$$

Consequently, the N00N state interferometry promises a saturation of the Heisenberg limit under lossless conditions.
A figurative way to explain N00N state interferometry is that instead of N single measurements estimating each time a phase difference of $e^{i\Delta\phi}$, in a single measurement, the phase information $e^{iN\Delta\phi}$ can be collected. This results in the reduction of the intrinsic noise, leading to an enhanced phase sensitivity:

$$\Delta\phi_{\mathrm{classical}} = \frac{1}{\sqrt{N}} \rightarrow \Delta\phi_{\mathrm{N00N}} = \frac{1}{N}. \tag{1.27}$$

N00N state interferometry has already been successfully demonstrated in application-oriented experiments [30,31,64]. Nevertheless, besides its promising huge advantage in phase estimation measurements, the price to pay for this quantum feature is significant. The realization of a measurement of the observable $\hat{O}_{\mathrm{N00N}}$ has been realized in previous approaches via time coincidence, N-photon detection [65–67] or photonic parity detection of even or odd number of photons at each interferometer output [68,69]. These detection schemes require the simultaneous detection of multiple photons of the order of N. The associated measurement rates tend to be slow as these detectors show low optical saturation levels [70], and complex coincidence counting is involved [71]. Low optical saturation levels limit the absolute amount of photons per time and thus the absolute sensitivity. Coincidence or multi-photon detection, on the other hand, is prone to losses. Here, only N-photon events are considered, while every other measurement is discarded. Thus each loss of a photon reduces the count rate and thus the sensitivity and the sampling rate. Based on the same argument for apparent decoherence (or loss) in the system, non-perfect N00N states prove to be superior [72].
Furthermore, so far a probabilistic superposition in the generation of higher-order N00N states ($N \geq 2$) proves to limits the application of N00N states to few photons per mode (in the lower two-digit regime) and/or very low measurement speed or sampling rates [73–75].

1.3 Squeezed state interferometry

In this section, I will introduce the probably most prominent concept of surpassing the standard quantum limit; the use of squeezed states of light [76,77].
Squeezed states are based on the variation of the Heisenberg uncertainty principle of quadrature operators for quantized electromagnetic field states. These quadrature operators can be associated with the photon number and the phase for phase-sensitive measurements. In a first step, I will introduce the derivation of field quadratures via the quantum mechanical description of a harmonic oscillator and introduce the squeezing parameter e^{-2r}. In a second section, I introduce the squeeze operator, which describes, for example, down-conversion processes. Furthermore, I will briefly introduce the visualization of squeezed states of light using the Wigner distribution as a schematic format. Next, I will introduce different approaches to generate squeezed states of light, their use in nonlinear interferometry, and a detection scheme to measure squeezing: the balanced homodyne detection. In the last step, I present a short recap of the sections and give a perspective of using squeezed states of light in nonlinear interferometry.

Quantization of the electromagnetic field

As a result of the quantization of the electromagnetic field, the electric field amplitudes can be described as a combination of independent harmonic oscillators. The Hamiltonian for the electromagnetic field then reduces to [78]:

$$\hat{H} = \sum_k \hbar\omega_k(\,\hat{n}_k + \frac{1}{2}\,) = \hbar\omega(\,\hat{a}_k^\dagger \hat{a}_k + \frac{1}{2}\,), \tag{1.28}$$

which represents the sum over all photons in each mode k with the energy of the vacuum fluctuations being $1/2\ \hbar\omega_k$. Another way to write this Hamiltonian is, to use the quadrature amplitude operators defined by [79]:

$$\hat{a}^\dagger = \hat{X} - i\hat{Y}, \tag{1.29}$$

$$\hat{a} = \hat{X} + i\hat{Y}, \tag{1.30}$$

$$\hat{X} = \frac{1}{2}(\,\hat{a} + \hat{a}^\dagger\,) \tag{1.31}$$

$$\hat{Y} = \frac{1}{2i}(\,\hat{a} - \hat{a}^\dagger\,). \tag{1.32}$$

With these operators the Hamilton operator (equation (1.28)) can be rewritten as:

$$\hat{H} = \hbar\omega\,(\,\hat{X}^2 + \hat{Y}^2\,). \tag{1.33}$$

The quadrature operators satisfy the commutation relation $[\hat{X}, \hat{Y}] = i/2$ and thus, the variances follow the Heisenberg uncertainty principle:

$$\Delta^2\hat{X}\,\Delta^2\hat{Y} \geq \frac{1}{16}. \tag{1.34}$$

For classical states of light, the variances satisfy the inequalities $\Delta^2\hat{X} \geq 1/4$ and $\Delta^2\hat{Y} \geq 1/4$. Squeezed states of light are now defined as states, which either $\Delta^2\hat{X}$ or $\Delta^2\hat{Y}$ violate their inequality [80]. Note that for squeezing one quadrature operator due to the generality of the Heisenberg uncertainty principle, the other quadrature operator is anti-squeezed by the same amount.
To quantify the amount of squeezing, a squeezing parameter can be defined, which displays the squeezing of the variance of the quadrature operator compared to its vacuum value [79]:

$$e^{-2r} = \frac{\Delta^2\hat{X}}{\Delta^2\hat{X}_{\text{vac}}}. \tag{1.35}$$

For introduced optical loss in the system, the squeezing parameter is reduced. This results in an increase in the variance of the quadrature operator's product above the minimum value [79]. The new equation of the squeezing parameter under the influence of optical loss in the system is then given by:

$$e^{-2r} = \frac{\Delta^2\hat{X}'}{\Delta^2\hat{X}_{\text{vac}}}, \tag{1.36}$$

with $\Delta^2\hat{X}' = \eta^2\,\Delta^2\,\hat{X} + (\,1-\eta^2\,)\,\Delta^2\hat{X}_{\text{vac}}$ and $(\,1-\eta^2\,)$ the relative energy loss [79]. The main challenge of squeezed states of light is, thus, the reduction of any optical loss in the system. Dissimilar to classical interferometry, or our approach (introduced in chapter 2), this applies to the entire experimental setup and not only to the interferometer itself.

Squeeze operator

Compared to the un-squeezed vacuum state, the squeezed vacuum state can be linked to a photon number excitation [79]. Squeezed states of light are generated via interactions

in a nonlinear medium, like parametric down-conversion.
Thus, it is appropriate to introduce the "squeeze operator" that we meet again for the theoretical framework of our novel quantum sensor (chapter 4) [80]. This operator creates and annihilates photon pairs in the following manner:

$$\hat{S}(\xi) = \exp\left(\frac{1}{2}(\xi^* \hat{a}^2 - \xi \hat{a}^{\dagger 2}) \right), \tag{1.37}$$

where $\xi = re^{i\theta}$ and r resembles the squeezing parameter from equation (1.35), with $0 \leq r \leq \infty$ and a squeeze angle $0 \leq \theta \leq 2\pi$ [80]. This operator resembles some kind of two-photon operator which annihilates and creates a coherent two-photon state [80]. Note that the two photons do not necessarily be generated in the same mode, so the operator can be represented by $\hat{S}(\xi) = \exp\left(\frac{1}{2}(\xi^* \hat{a}_1 \hat{a}_2 - \xi \hat{a}_1^\dagger \hat{a}_2^\dagger)\right)$, where $\hat{a}_i$, $i = 1, 2$ represents two different modes. In the following, we will focus on the degenerate case of a single mode squeeze operator without loss of generality. Thanks to the Baker-Campbell-Hausdorff formula [81–84], it can be shown that:

$$\hat{S}^\dagger(\xi)\, \hat{a}\, \hat{S}(\xi) = \hat{a}\, \cosh(r) - \mathrm{e}^{i\theta}\, \hat{a}^\dagger\, \sinh(r) \tag{1.38}$$

$$\hat{S}^\dagger(\xi)\, \hat{a}^\dagger\, \hat{S}(\xi) = \hat{a}^\dagger\, \cosh(r) - \mathrm{e}^{i\theta}\, \hat{a}\, \sinh(r). \tag{1.39}$$

Taking the identity $\hat{S}\hat{S}^\dagger$ and equations (1.38) and (1.39) results in [79]:

$$\Delta^2 \hat{X} = \frac{1}{4} \left(\cosh^2(r) - \cosh(r) \sinh(r) + \sinh^2(r) \right) = \frac{1}{4}\, \mathrm{e}^{-2r} \tag{1.40}$$

$$\Delta^2 \hat{Y} = \frac{1}{4} \left(\cosh^2(r) + \cosh(r) \sinh(r) + \sinh^2(r) \right) = \frac{1}{4}\, \mathrm{e}^{2r} \tag{1.41}$$

$$\tag{1.42}$$

The squeeze operator can further be applied to any kind of state. Applied to the vacuum state, this leads, for example, to vacuum squeezed light.
A link to a phase estimation measurement is a consequence of the definition of the coherent state (α) using the quadrature operators $\hat{X}_1$ and $\hat{X}_2$ [52]:

$$\hat{\alpha} = \hat{X} + i\hat{Y} \tag{1.43}$$

and separating α into photon number and phase dependency:

$$\hat{\alpha} = |\hat{\alpha}|\, e^{i\phi}. \tag{1.44}$$

Phase space representation

A figurative way to visualize squeezed states of light is the representation in phase space. A possible motivation is the introduction of the Wigner distribution. The Wigner distribution was introduced in 1932 by Wigner [85], to characterize a state $|\Psi\rangle$ of a quantum system in phase space [86]. In one dimension the Wigner distribution is defined as [86]:

$$W(q,p) = \frac{1}{2\pi} \int_{-\infty}^{+\infty} \left\langle q + \frac{1}{2}\hbar x \right| \hat{\rho} \left| p - \frac{1}{2}\hbar x \right\rangle \mathrm{e}^{ixp}\, \mathrm{d}x, \tag{1.45}$$

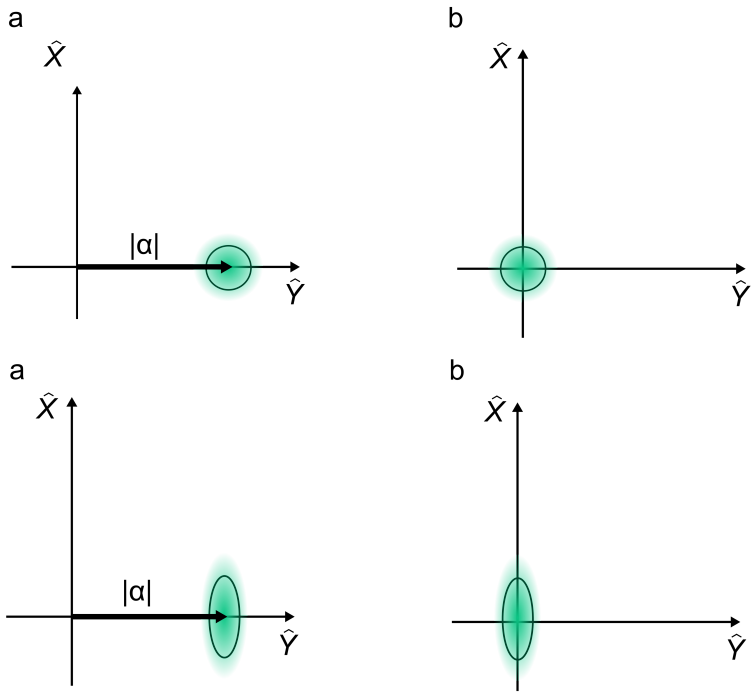

Figure 1.3: **Simplified picture of the Wigner distribution for different states.** **a**, Wigner distribution of a coherent state. **b**, Wigner function of the vacuum state. **c**, Schematic representation of a displaced squeezed state. **d**, Schematic representation of a squeezed vacuum state.

with $|q\rangle$, $|p\rangle$ the position and momentum state and $\hat{\rho}$ the density operator of the system. Integrating the Wigner distribution over q or p shows the probability density $p(q)$ and $p(p)$ of measurement results of the observables. [79]:

$$\int_{-\infty}^{+\infty} W(q,p)\,\mathrm{d}q = p(q) \tag{1.46}$$

$$\int_{-\infty}^{+\infty} W(q,p)\,\mathrm{d}p = p(p). \tag{1.47}$$

The Wigner distribution is a quasi-probabilistic distribution, that contains the entire information of a state, including its quantum statistic [79]. Two characteristics of the Wigner distribution show a nonclassicality of a state:

- ❖ The Wigner distribution can contain negative values, that have no equivalent in classical mechanics.
- ❖ The Wigner distribution can show a "squeezed" width in the probability compared to the ground state.

Fig. 1.3 shows a schematic representation of the Wigner function for different states. On the axes $\hat{X}$ and $\hat{Y}$ the quasi-probabilities $p(X)$ and $p(Y)$ are drawn. Here, the phase-space quasi-probability is depicted by the darkness of the shaded areas. In Fig. 1.3a and b, a classical coherent state with amplitude $|\alpha|$ and the vacuum state is presented. In Fig. 1.3c and d, a displaced squeezed state and a squeezed vacuum state

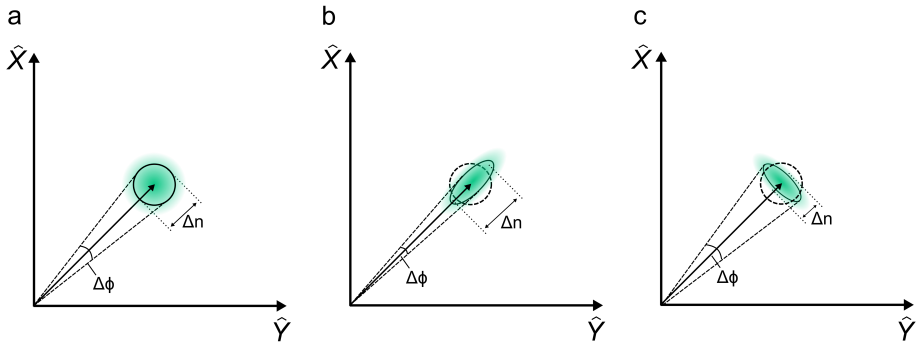

Figure 1.4: **Schematic of quadrature squeezed states of light.** **a**, Phasor diagram for coherent state $|\alpha\rangle$. **b**, Schematic representation of phase-squeezed light and **c**, amplitude-squeezed light.

are shown. In both cases, the variance of one quadrature operator is squeezed while the other is anti-squeezed. Thus, Fig. 1.3c and d show a steeper distribution in one direction than the classical counterpart.
By linking the classical electromagnetic energy $E_{\text{classical}} = \hbar\omega|\alpha|^2$ and the quantum theory of the electromagnetic harmonic oscillator $E_{\text{quantum}} = \hbar\omega\bar{n} + \frac{1}{2}\hbar\omega$ [52] the equity of $\Delta n = |\alpha| = \sqrt{\bar{n}}$ can be shown. Thus, using the correlation $\delta\phi = \frac{1/2}{\sqrt{\bar{n}}}$ we can find the number-phase uncertainty in the following manner [52]:

$$\Delta\hat{\phi}\,\Delta\hat{n} \geq \frac{1}{2}. \tag{1.48}$$

This inequality gives a preliminary hint of the possibility of changing the uncertainty of either the phase or the photon number without violating the Heisenberg uncertainty principle (equation (1.48)).
A schematic representation is shown in Fig. 1.4. Here dependent on the axis of squeezing, these different squeezed states are named phase-squeezed (Fig. 1.4b) and amplitude-squeezed light (Fig. 1.4c). For comparison, a classical coherent state is illustrated in Fig. 1.4a.

Generation of squeezed states

In this section, I will focus solely on the generation of squeezed states in nonlinear crystals and only shortly introduce other systems. In principle, every system showing a nonlinear susceptibility can be used to generate squeezed states of light. Thus not only nonlinear crystals but also, for example, atomic ensembles can be used [23]. Here, in a Λ-shaped atomic energy level, a strong pump beam can create two photons that are either degenerate or non-degenerate dependent on the energy difference of the ground states. In the non-degenerate case, these two modes are known as Stokes and Anti-Stokes. Those two modes form a (two-)mode squeezed state. Even though facing especially in the early years challenges, squeezed state generation using atomic ensembles can reach up to 9 dB squeezing [87].

However, the generation of squeezed states of light using nonlinear crystals has a long history. Already in 1986 first experiments were realized using parametric down-conversion [88]. In principle, there are three main processes in nonlinear crystals commonly used for the generation of squeezed states of light:

- ❖ Parametric down-conversion (PDC),
- ❖ Optical parametric oscillation (OPO),
- ❖ Parametric up-conversion.

In degenerate PDC, where the signal and idler modes are indistinguishable in terms of frequency ($\omega_i = \omega_s$) and polarization, the system Hamiltonian can be written as [89]:

$$H = g\,(a^2 + a^{\dagger 2}), \tag{1.49}$$

with g the nonlinear coupling parameter proportional to the medium's nonlinear susceptibility and the pump field's amplitude (see Appendix E). The unitary evolution of this Hamilton $U = \exp(-ig(a^2 + a^{\dagger 2}))$ resembles exactly the form of the squeeze operator introduced in section 1.3.
In OPO, PDC is performed inside of a cavity. As detailed in Appendix E, a medium with a nonlinear susceptibility can be represented as a phase-sensitive amplifier. Thus dependent on the initial phase of the pump photons, field quadratures can either be amplified or deamplified. In the case of degenerate parametric down-conversion, following the conservation of energy $\omega_p = \omega_i + \omega_s$, with no initial signal field entering the media, the signal mode is taken from the always present vacuum modes. As seen in Appendix E also for vacuum modes, the same phase-sensitive amplification exists, which leads to an amplification or deamplification of the field quadratures of the vacuum modes. This approach showed so far up to 15 dB squeezing [90].
In principle, the up-conversion process is the inverse process of PDC. This process, thus, also can show squeezing. However, there is a figurative way to explain (amplitude-) squeezing in an up-conversion process.
If we consider the case of parametric up-conversion, e.g., frequency doubling, we face a process where two pump photons of the energy $\omega_p = \omega$ create with a certain probability a photon of the energy $\omega_{\mathrm{SHG}} = 2\omega$. The pump beam follows Poissonian photon statistics, so the arrival of photons at the nonlinear crystal is random. For an up-conversion process, two pump photons must arrive at a certain time to be converted to an up-converted photon. Therefore, there will be instances where two photons arrive closer to each other, increasing the chance of a conversion process. Thus above-average fluctuations of the pump beam will be automatically filtered out, leaving the up-converted beam with a more regular flow than before.

Squeezed states in interferometry

In general, the use of squeezed states of light promise to provide a light source with reduced noise or photonic fluctuations in either the phase or the amplitude. If we consider the textbook example of a Michelson interferometer (schematically presented in Fig. 1.5a), coherent light enters the interferometer at one input port of a 50:50 beam splitter leaving one "open" port. This port allows a vacuum field to enter the

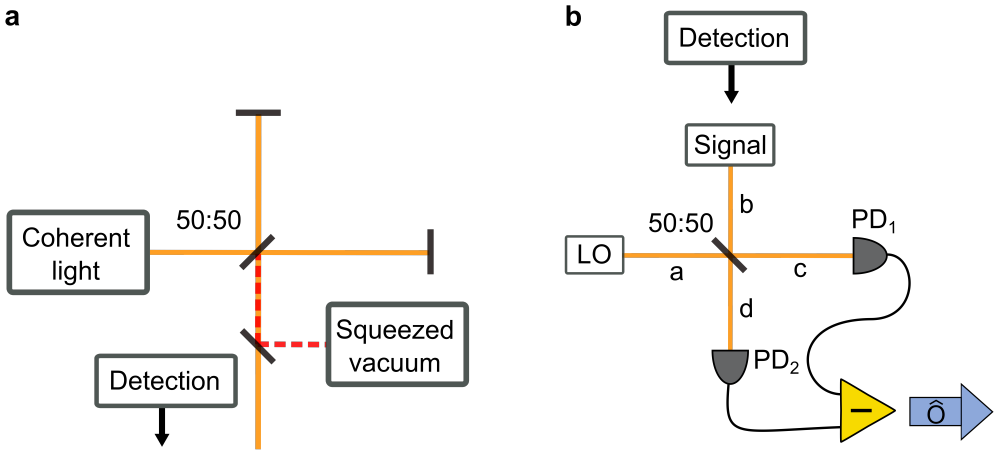

Figure 1.5: **Simplified picture of a Michelson interferometer and balanced homodyne detection.** **a**, Coherent light enters a Michelson interferometer through one port of a 50:50 beam splitter. In the absence of a squeezed light source a vacuum state is seeded into the second input port of this beam splitter. Introducing squeezed vacuum into this port leads to a reduction of noise. **b**, The balanced homodyne detector consists of a 50:50 beam splitter and two photodiodes (PD_1 and PD_2). A signal field and a local oscillator are incident on both input ports a and b of the 50:50 beam splitter. To create the balanced homodyne detector signal the signals of both photodiodes (c and d) are subtracted, depicted here as operator $\hat{O}$.

interferometer. By injecting squeezed vacuum instead, the noise can be reduced and the interferometer's sensitivity to a phase (or amplitude) change can be increased [91]. This approach is not limited to the Michelson interferometer and can be transferred to various experimental setups. Even though in most cases, an increase of the light power might be an easier way to enhance the sensitivity in certain fields, the introduction of squeezed states of light proves to be paramount.

Detection of squeezed light

A common detection strategy to observe squeezed light is balanced detection. In this context, photocurrents of two balanced detectors are subtracted to cancel out classical noise sources, enabling measurements at or below the shot noise limit. A standard method, especially for squeezed states of light, is balanced homodyne detection. In Fig. 1.5b a schematic of a balanced homodyne detector is shown. In principle, balanced homodyne detection is based on the overlap of a signal beam with a large-amplitude light wave of the same frequency, commonly known as the local oscillator (LO). In Fig. 1.5b, the squeezed signal beam enters one input port of a 50:50 beam splitter, while the LO enters the second. An illustrative way to treat this detection scheme is a semi-classical approach, in which the LO is treated classically while the signal field is treated quantum mechanically. We introduce the signal field at the input port b (in Fig. 1.5b) as E_s and the local oscillator field at the input port a as E_{LO}. At the output

ports, c and d, the fields are given by:

$$E_c = \frac{1}{\sqrt{2}} \left(E_{\mathrm{LO}} \mathrm{e}^{i\phi_{\mathrm{LO}}} + E_s \right) \tag{1.50}$$

$$E_d = \frac{1}{\sqrt{2}} \left(E_{\mathrm{LO}} \mathrm{e}^{i\phi_{\mathrm{LO}}} - E_s \right), \tag{1.51}$$

with ϕ_{LO} a phase relative to the signal field. As we treat the signal field quantum mechanically, we use the same argument as in section 1.3 and split the signal field into its field field quadrature components:

$$E_S = E_s^{X_1} + i\, E_s^{X_2} \tag{1.52}$$

with $i = \mathrm{e}^{i\pi/2}$ representing the 90° phase difference between the quadratures. Equation (1.50) then can be written as:

$$E_c = \frac{1}{\sqrt{2}} \left((E_{\mathrm{LO}} \cos(\phi_{\mathrm{LO}}) + E_s^{X_1}) + i(E_{\mathrm{LO}} \sin(\phi_{\mathrm{LO}}) + E_s^{X_2}) \right) \tag{1.53}$$

$$E_d = \frac{1}{\sqrt{2}} \left((E_{\mathrm{LO}} \cos(\phi_{\mathrm{LO}}) - E_s^{X_1}) - i(E_{\mathrm{LO}} \sin(\phi_{\mathrm{LO}}) - E_s^{X_2}) \right) \tag{1.54}$$

The photocurrent measured at PD_1 and PD_2 corresponds to $I_i = \frac{c\epsilon_0}{2} |E_i|^2 \propto |E_i|^2$, with $i = c, d$ and $|E_i|^2 = E\, E^*$. Thus the subtracted detector signal $I_{\mathrm{sub}} = I_c - I_d$ results in:

$$I_{\mathrm{sub}} = I_c - I_d \tag{1.55}$$

$$I_{\mathrm{sub}} = \frac{c\epsilon_0}{2} \left(E_c E_c^* - E_d E_d^* \right) \tag{1.56}$$

$$I_{\mathrm{sub}} = c\epsilon_0\, E_{\mathrm{LO}} \left[E_s^{X_1} \cos(\phi_{\mathrm{LO}}) + E_s^{X_2} \sin(\phi_{\mathrm{LO}}) \right] \tag{1.57}$$

Interestingly the subtracted detector signal is phase sensitive. For $\phi_{\mathrm{LO}} = 0, \pi, 2\pi...$ the output photocurrent is proportional to $E_{\mathrm{LO}} E_s^{X_1}$ and for $\phi_{\mathrm{LO}} = \pi/2, 3\pi/2...$ the signal is proportional to $E_{\mathrm{LO}} E_s^{X_2}$. Different field quadratures can be detected, dependent on the phase of the local oscillator relative to the signal field. Even though this signal proves to be proportional to either $E_s^{X_1}$ or $E_s^{X_2}$, also the local oscillator field is measured. To make a statement about the shot noise level of the signal field, an additional measurement in the absence of any signal field has to be done. By leaving the signal port b "open", a vacuum field is inserted generating an output signal proportional to $E_{\mathrm{LO}} E_{\mathrm{vac}}$. This is commonly interpreted as the shot noice limit of the local oscillator. The detection of phase-dependent noise below this limit is thus a clear sign of squeezed vacuum. In the case of amplitude squeezed light, the reduced photon number uncertainty can be directly observed using single photon counters or PIN photodiodes.

Perspective

Quite early, squeezed states of light already have quickened the interest in interferometric setups [92,93]. Proof-of-principle experiments followed soon [94–97], indicating the benefit of enhancing the sensitivity of a phase estimation measurement.
This led probably to the most popular application in the gravitational wave detector LIGO, which was able to recently detect the space-time curvature of two black

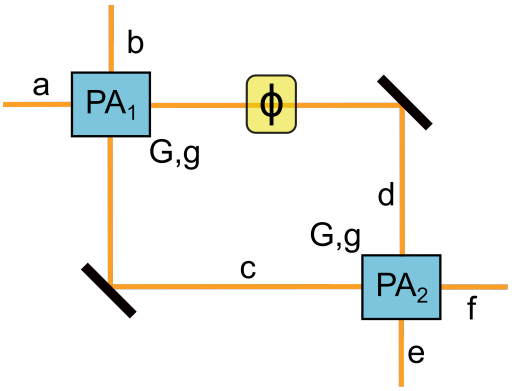

Figure 1.6: **Schematic of a SU(1,1) interferometer.** The SU(1,1) interferometer resembles a Mach-Zehnder Interferometer, in which both 50:50 beam splitter are replaced by parametric amplifiers (PA_1 and PA_2). In path d a phase difference is depicted by ϕ.

holes merging [98]. Since then, new detector generations have been introduced using squeezed states of light [99, 100].
Also, in other fields, squeezed states of light already show application relevant advances [101–103]. Nevertheless, even with huge squeezing factors of above 15 dB [90] and thus possible enhancement factors in a phase estimation measurement of approximately 5.6 times, the implementation of squeezing comes at the cost of the often complex interferometer or cavity setups [90, 104] and instabilities at high pump powers [105, 106]. Additionally, squeezed states of light are susceptible to losses inside and outside the interferometers, including the detection [44, 79, 89, 107], which makes highly efficient detectors necessary. The dependency of the variance of the measured squeezed state quadratures $\Delta\hat{X}(\theta)$ is particularly apparent in the equation [105, 108]:

$$\Delta\hat{X}(\theta) = \eta\,(\,e^{2r}\cos(\theta) + e^{-2r}\sin(\theta)\,) + 1 - \eta, \tag{1.58}$$

where η represents the detection efficiency. Furthermore, approaches based on pulsed squeezed of light typically show very low duty cycles, thus limiting the overall sampling rate [109–111].

1.4 SU(1,1) interferometry

The relatively novel SU(1,1) interferometry promises to tackle the main challenge of approaches using squeezed states of light. SU(1,1) interferometers are less sensitive to noise outside of the interferometer part itself and thus promise to be easier applicable or scalable [112, 113]. In principle, the original concept of SU(1,1) interferometers resembles a simple Mach-Zehnder interferometer, in which both 50:50 beam splitters are replaced by two parametric amplifiers (Fig. 1.6, [114]). In analogy to the squeeze operator, the interaction Hamiltonian for parametric amplification can be written as

[115]:

$$\hat{H}_{\mathrm{PA}} = i\,\hbar\,\xi\,\hat{a}_1^\dagger\,\hat{a}_2^\dagger - i\,\hbar\,\xi^*\,\hat{a}_1\,\hat{a}_2, \tag{1.59}$$

with ξ a parameter dependent on the pump field's amplitude and the medium's nonlinear susceptibility. In the non-degenerate case two fields $\hat{a}_1$ and $\hat{a}_2$ are generated. Similar to section 1.3 we can transfer the system in the Heisenberg picture and investigate the system with the operator evolution:

$$\hat{a}_c = G\,\hat{a}_b + g\,\hat{a}_a^\dagger \tag{1.60}$$

$$\hat{a}_d = G\,\hat{a}_a + g\,\hat{a}_b^\dagger, \tag{1.61}$$

with $G = \cosh(r)$ and $g = \sinh(r)$. Note that for convenience only we set the phase of r ($\xi = r\mathrm{e}^{i\theta}$) to zero, without loss of generality [115]. We assume for the second parametric amplifier PA_2 again for convenience only, the same values for G and g. Thus the interaction with the second parametric amplifier results in:

$$\hat{a}_e = G\,\mathrm{e}^{i\phi}\,\hat{a}_d + g\,\hat{a}_c^\dagger \tag{1.62}$$

$$\hat{a}_f = G\,\hat{a}_c + g\,\mathrm{e}^{-i\phi}\,\hat{a}_d^\dagger, \tag{1.63}$$

with ϕ a collected phase difference in path d. Together with equation (1.60) this results in:

$$\hat{a}_e = (\,G^2\,\mathrm{e}^{i\phi} + g^2\,)\,\hat{a}_a + G\,g\,(\,\mathrm{e}^{i\phi} + 1\,)\,\hat{a}_b^\dagger \tag{1.64}$$

$$\hat{a}_f = (\,G^2 + g^2\,\mathrm{e}^{-i\phi}\,)\,\hat{a}_b + G\,g\,(\,\mathrm{e}^{-i\phi} + 1\,)\,\hat{a}_a^\dagger. \tag{1.65}$$

Introducing $G_{\mathrm{tot}}(\phi) = (G^2\mathrm{e}^{i\phi} + g^2)$ and $g_{\mathrm{tot}}(\phi) = Gg(\mathrm{e}^{i\phi} + 1)$ this equation reduces to:

$$\hat{a}_e = G_{\mathrm{tot}}(\phi)\,\hat{a}_a + g_{\mathrm{tot}}(\phi)\,\hat{a}_b^\dagger \tag{1.66}$$

$$\hat{a}_f = G_{\mathrm{tot}}(\phi)\,\hat{a}_b + g_{\mathrm{tot}}(\phi)\,\hat{a}_a^\dagger. \tag{1.67}$$

For a coherent input in path b ($|\Psi\rangle_b = |\alpha\rangle$ and $\langle\Psi|_b\,\hat{a}_b^\dagger\hat{a}_b\,|\Psi\rangle_b = |\alpha|^2$) and vacuum in path a the output intensity at the output path e can thus be calculated as:

$$\langle\hat{a}_e^\dagger\hat{a}_e\rangle = |g_{\mathrm{tot}}|^2\,(\,1 + |\alpha|^2\,) \tag{1.68}$$

$$= 2G^2\,g^2\,(\,|\alpha|^2{+}1\,)(\,1 + \cos(\phi)\,) \tag{1.69}$$

Furthermore, another interesting value is the phase sensing intensity I_{PS}, the amount of light traveling through the phase-changing object ϕ. This intensity can be calculated in the same way as equation (1.68):

$$I_{\mathrm{PS}} = \langle\,\hat{a}_d^\dagger\,\hat{a}_d\,\rangle = g^2\,(\,|\alpha|^2{+}1\,) \tag{1.70}$$

A classical Mach-Zehnder interferometer with a coherent input $|\alpha\rangle$ has a phase sensing intensity of $|\alpha|^2/2$. Thus equation (1.69) and (1.70) shows for large values of $|\alpha|^2$ a by $2G^2$ increased fringe size [116].
However, larger fringes do not necessarily correspond to a higher phase sensitivity. But, if we consider the SU(1,1) interferometer with an initial phase shift of $\phi = (2n+1)\pi$,

leaving output path e at a dark fringe, $G_{\mathrm{tot}}(\phi) = 1$ and $g_{\mathrm{tot}}(\phi) = 0$ applies. Therefore, equation (1.66) reduces to:

$$\hat{a}_e = \hat{a}_a. \tag{1.71}$$

If we recall that no input (or vacuum) is inserted in path a, the noise resembles the vacuum noise. Thus theoretically, an enhancement of the sensitivity of a phase-sensitive measurement can also be expected to be by a factor of $2G^2$ times higher compared to classical interferometry [113, 115, 116].
Another exciting aspect of the SU(1,1) interferometry appears if we focus on the second output of PA_2, path f:

$$\begin{aligned}
\langle \hat{a}_f^\dagger \, \hat{a}_f \rangle =& |G_{\mathrm{tot}}|^2 \, |\alpha|^2 + |g_{\mathrm{tot}}|^2 && (1.72)\\
=& |\alpha|^2 \, (\, G^4 + g^4 + 2g^2 G^2 \cos(\phi) \,) + 2G^2 g^2 \, (\, 1 + \cos(\phi) \,) && (1.73)\\
=& |\alpha|^2 + 2G^2 g^2 \, (\, 1 + |\alpha|^2 \,) (\, 1 + \cos(\phi) \,). && (1.74)
\end{aligned}$$

Equations (1.69) and (1.74) show that both output ports of PA_2 are in phase, in contrast to 180° out of phase for a Mach-Zehnder interferometer [112]. Therefore canceling out common-mode noise like in classical interferometry is not possible.
In case of loss inside of the interferometer part (paths c and d), where loss L is modeled by a beam splitter with transmissivity $1-L$ the signal to noise ratio (SNR) enhancement is also modeled by $(1-L)/L$ [112]. However, for large G the SNR is almost not affected by loss outside of the interferometer (paths e and f) [112, 117, 118].
The detection signal of the SU(1,1) interferometers can be detected by simple intensity measurements or, as well as squeezed states of light, by balanced homodyne detection. So far, I only introduced the case of a bright coherent state input. This kind of SU(1,1) interferometer is known as coherent state-boosted or bright seed SU(1,1) interferometer [119–121]. However, there are different amended SU(1,1) interferometers, which still show an enhancement over a classical counterpart, but are, in some cases, easier to realize:

- Coherent state-boosted or bright seed SU(1,1) interferometer as described above.
- Vacuum seed SU(1,1) interferometer, in which the first parametric amplifier is seeded with vacuum instead of a coherent state. This interferometer still shows an enhancement over a classical interferometer but a worse performance for a phase estimation measurement than the coherent state-boosted SU(1,1) interferometer [122].
- A SU(2) interferometer nested in a SU(1,1) interferometer, in which a classical Mach-Zehnder interferometer is nested in between both parametric amplifiers. This approach promises an accuracy beating the standard quantum limit by simultaneously realizing dense quantum metrology, where joint estimates of two conjugate quantities (like amplitude and phase) can be made [123].
- A SU(1,1) interferometer, where the second parametric amplifier is exchanged by a beamsplitter [124, 125]. This interferometer promises to show the same enhancement as the coherent state-boosted SU(1,1) interferometer but is in the same way as squeezed state interferometry sensitive to loss outside of the interferometer [112].

- ❖ The truncated SU(1,1) interferometer [126, 127]. In this approach the second parametric amplifier is replaced by homodyne detection paths and a post-detection current mixer [112]. This approach promises the same enhancement as the coherent state-boosted SU(1,1) interferometer but, as well as the previous approach, the same loss sensitivity outside of the interferometer as squeezed state interferometry.

- ❖ An approach, where both interferometer paths interact with a phase-changing object [128, 129]. This approach promises an increased sensitivity to a phase change by, at the same time, the same advantages as the coherent state-boosted SU(1,1) interferometer.

Of course, not only optical waves can interact in SU(1,1) interferometry. Also, atomic waves in a Bose-Einstein condensate [130–132] or microwaves [133] can be used in SU(1,1) setups.

Perspective

Yurke et al. [114] could prove in 1986 that the SU(1,1) interferometer in principle, as well as maximally entangled states, can saturate the Heisenberg limit ($\Delta\phi \geq 1/N$) of a phase estimation measurement.
A first measurement characterizing the noise dependencies of the SU(1,1) interferometry has been done by Hudelist et al. [116]. Even though proving to be robust to noise outside of the interferometer part, losses inside of the interferometer itself can still introduce uncorrelated vacuum noise, which cannot be canceled out [112].
Additionally, in the introduction of the SU(1,1) interferometer scheme in 1986 by Yurke et al. [114], it was designed to use vacuum as an input. This limited the experimentally accessible regime to low photon numbers.
Later the use of different states of light, like coherent states [119, 134] led to increased overall photon fluxes. Since then several different states of light and different measurement schemes where implemented in the SU(1,1) interferometry [123, 135–137]. So far the enhancement factors for a phase-sensitive measurement can reach up to approximately 1.6 times by a signal to noise increase of up to 4.3 dB [116, 123, 138, 139].
Additionally to these proof-of-principle experiments, application-oriented developments, mainly in the field of imaging, have been realized [123, 140–142].
Even though SU(1,1) interferometry offers a significant enhancement in phase estimation measurements and avoids sensitivities to losses outside of the interferometer itself, it comes with certain challenges. As well as the approach using squeezed states of light, the SU(1,1) interferometers often suffer from complex experimental systems [116]. Further, the output ports of the SU(1,1) interferometer are in phase, in contrast to 180° out of phase for a Mach-Zehnder interferometer [112]. This excludes the possibility of canceling out common-mode noise like laser power fluctuations etc., which severely limits the stability. Furthermore, the gain dependency of the enhancement factor limits, so far, the enhancement to values way below approaches using squeezed states of light [116, 123, 138, 139].

1.5 Conclusion

In this chapter, I introduced the limits for phase estimation measurements in classical interferometry with the Mach-Zehnder interferometer as a representative example. I introduced the maximum phase sensitivity as the standard quantum limit $\Delta\phi = 1/\sqrt{N}$ and further summarized three different approaches in nonlinear interferometry: squeezed states of light, multi-photon entanglement, and SU(1,1) interferometry.

Multi-photon interferometry:
Multi-photon entangled states promise a brute force technique to saturate the Heisenberg limit but suffer from low repetition rates due to the necessity of single or multi-photon detection. Further, the problematic generation of multi-photon states above $N = 2$ limits the enhancement and applicability so far.

Advantages

- ❖ Can saturate the Heisenberg limit.
- ❖ Straight forward to approach.

Challenges

- ❖ Requires single- or multi-photon detection.
- ❖ Limited in sampling rate and absolute sensitivity.
- ❖ Multi-photon states difficult to generate (above $N \geq 2$).

Squeezed state interferometry:
Squeezed state interferometry is maybe the most advanced approach to this day, which is also represented by the implementation into the interferometer with the highest sensitivity on earth LIGO [99, 100]. The usage of squeezed states of light offers with approximately 5.6 times, the highest enhancement factor so far. This applicability, combined with the introduced high enhancement factors, comes at the cost of a high loss sensitivity in the complete system (including the detectors) and sometimes highly complex experimental apparatuses.

Advantages

- ❖ Can saturate the Heisenberg limit.
- ❖ High and low sampling rates.
- ❖ Achieved already high enhancement factors up to 5.6 times for phase sensing.
- ❖ Application relevant for specific applications.

Challenges

- ❖ Complex interferometer and cavity setups.
- ❖ Sensitivity to loss outside of the interferometer itself.
- ❖ Highly efficient detectors necessary.

SU(1,1) interferometry:
The SU(1,1) interferometry seems to be one of the most exciting approaches using quantum interference to reduce the noise in an amplification process. This approach so far has only shown enhancement factors of approximately 1.6 times and suffers, like squeezed states of light, often from complex experimental setups. Additionally, the convenient suppression of common-mode noise in classical interferometry could so far not be implemented in SU(1,1) interferometry.
In the next chapter, I will introduce our novel concept in nonlinear interferometry. This approach will, in theory, be able to saturate the Heisenberg limit. In addition, our approach allows simple intensity measurements and common-mode noise cancellation by, at the same time, high sampling rates and immunity of the sensitivity to losses outside of the interferometer.

Advantages

- Can saturate the Heisenberg limit.
- Mainly high sampling rates.
- Resilience to losses outside the interferometer.

Challenges

- Complex interferometer and cavity setups.
- No cancellation of common-mode noise possible.
- So far only low enhancement factors realized (up to 1.6 times).

Chapter 2

Novel concept of a nonlinear interferometer

In the previous chapter, I presented different concepts in nonlinear interferometry with their advantages and current state issues. In this chapter, I will detail our novel approach and where it differs from these concepts. In particular, I will present:

- ❖ the ability to perform measurements over a large sampling rate regime simultaneously (so far 200 Hz − 100 kHz),
- ❖ the use of standard intensity detection schemes,
- ❖ the simplicity of the experimental setup,
- ❖ robustness of the enhancement to losses outside of the interferometer,
- ❖ and the ability of common mode noise rejection.

In the first part, I will introduce basic principles of photon-pair generation in nonlinear crystals, such as the origin of three-photon processes and the particularity of periodic poling with the intertwined definition of quasi-phase-matching. The second section shows the experimental realization in detail. It covers the solution to two main challenges: the verification of temporal indistinguishability and path-polarization quantum state engineering with a wavelength-selective waveplate (WSWP).
Additionally, this section presents a benchmarking against an almost ideal classical sensor of similar built. This classical sensor resembles a simple Michelson interferometer with the same phase sensing properties but no losses inside the interferometer itself and almost unity visibility. From this comparison, we will infer a phase sensing enhancement factor of our sensor.
Finally, I present the current enhancement of the quantum sensor with a value of 1.13 ± 0.02 beyond the standard quantum limit for sampling rates between 200 Hz and 100 kHz. The enhancement over the entire audio band ($200 - 20,000$ Hz) paves the way for developing a quantum optical microphone.
Further, an extension to higher photon-pair fluxes up to several hundred nanowatts will be discussed as an auxiliary section. On that basis, noise measurements of commercially available InGaAs cameras will be presented, allowing the sub-shot noise measurement

of these fluxes. These measurements are used as a compelling argument for the extension to higher photon-pair fluxes of several hundreds of nanowatts and, therefore, the possibility to reach higher absolute sensitivities and achieve even higher sampling rates.

2.1 Basics of photon-pair generation in nonlinear crystals

This section starts with a short motivation for generating two-photon states via Type 0 down-conversion as used in our novel quantum sensor. A more detailed quantum mechanical description of this novel nonlinear interferometer is given in chapter 4. Therefore, only necessary parts will be discussed in this chapter.
For this, we start with the famous Maxwell's equations, formulated first in 1861 by James Clerk Maxwell, which describe the propagation of light in any medium [9, 10]. These equations are derived from the foundation of classical electromagnetism and are composed of a set of four differential equations (here presented in the SI convention):

$$\nabla \cdot \vec{D}(r,t) = \rho \tag{2.1}$$

$$\nabla \cdot \vec{B}(r,t) = 0 \tag{2.2}$$

$$\nabla \times \vec{E}(r,t) = -\frac{\partial \vec{B}(r,t)}{\partial t} \tag{2.3}$$

$$\nabla \times \vec{H}(r,t) = \vec{j} + \frac{\partial \vec{D}(r,t)}{\partial t}. \tag{2.4}$$

$$\tag{2.5}$$

These equations represent the relation between electric and magnetic fields (and their changes), currents, charges, and electric and magnetic susceptibilities. These susceptibilities are hidden in this representation in the magnetic field strength $\vec{H}$ and the electric displacement field $\vec{D}$ which are usually defined in the case of linear optics by the relations:

$$\vec{B}(r,t) = \mu_0 \left(1 + \chi_{\mathrm{M}}\right) \vec{H}(r,t) \tag{2.6}$$

$$\vec{D}(r,t) = \epsilon_0 \vec{E}(r,t) + \vec{P}(r,t), \tag{2.7}$$

with $\vec{P}(r,t) = \chi_{\mathrm{E}(r,t)} \epsilon_0 \vec{E}(r,t)$ the polarization, χ_{M} the magnetic susceptibility and $\chi_{\mathrm{E}(r,t)}$ the electric susceptibility. However, the dependency of the polarization on the electric susceptibility does not have to be necessarily linear. The description of this nonlinear dependency or a nonlinear susceptibility is defined as nonlinear optics.

2.1.1 Parametric down-conversion

To introduce the parametric down-conversion process, I will shortly present the concept of the nonlinear electric susceptibility of dielectric media. Here, I will give an overview of different frequency conversion processes and motivate the conversion of energy and momentum. Further details are found in chapter 4 and appendix D.

In nonlinear optics, the relation between the electric field $\vec{E}$ and the polarization $\vec{P}$ is not necessarily linear but assembles as a linear combination of susceptibilities of different order [143]:

$$\vec{P}(r,t) \;=\; \chi^{(1)}_{\mathrm{E}(r,t)}\,\epsilon_0\,\vec{E}(r,t) + \chi^{(2)}_{\mathrm{E}(r,t)}\,\epsilon_0\,\vec{E}^2(r,t) + \chi^{(3)}_{\mathrm{E}(r,t)}\,\epsilon_0\,\vec{E}^3(r,t) + ... \tag{2.8}$$

For the down-conversion process, only the second-order nonlinear susceptibility plays a role. Thus, in the following we will only focus on the case of second-order nonlinear susceptibilities ($\chi^{(i)}_{\mathrm{E}(r,t)} = 0$, for $i > 2$). As a result equation (2.8) reduces to:

$$\vec{P}(r,t) \;=\; \chi^{(1)}_{\mathrm{E}(r,t)}\,\epsilon_0\,\vec{E}(r,t) + \chi^{(2)}_{\mathrm{E}(r,t)}\,\epsilon_0\,\vec{E}^2(r,t) \tag{2.9}$$

If a medium with a non-vanishing second-order nonlinear susceptibility is excited by two cosinusoidal waves of different frequency ω_1 and ω_2 and electric field amplitudes $\vec{E}_1$ and $\vec{E}_2$ the second order polarization $\vec{P}(r,t)^{(2)} = \chi^{(2)}_{\mathrm{E}(r,t)}\,\epsilon_0\,\vec{E}^2(r,t)$ can be written as:

$$\vec{P}(r,t)^{(2)} \;= \vec{E}_1\,\vec{E}_2\,\epsilon_0\,\chi^{(2)}_{\mathrm{E}(r,t)}\,\cos(\omega_1\,t)\,\cos(\omega_2\,t) \tag{2.10}$$

$$\vec{P}(r,t)^{(2)} \;= \frac{1}{2}\,\vec{E}_1\,\vec{E}_2\,\epsilon_0\,\chi^{(2)}_{\mathrm{E}(r,t)}\,\cos((\omega_1 + \omega_2)\,t)\,\cos((\omega_1 - \omega_2)\,t) \tag{2.11}$$

As a result, a nonlinear medium excited by two electric fields of frequencies ω_1 and ω_2 can introduce an oscillating polarization at frequencies of $\omega_1 + \omega_2$ and $\omega_1 - \omega_2$ [52].
In standard nomenclature, these processes are called sum frequency conversion ($\omega = \omega_1 + \omega_2$) and difference frequency conversion, ($\omega_1 - \omega_2$) respectively. These processes can also reverse in which, for example, a photon of frequency $\omega_1 + \omega_2$ splits into two photons of frequency ω_1 and ω_2. A very appealing way to illustrate these processes is the use of Feynman diagrams [144]. In Fig. 2.1 the conversion of either two photons into one photon (Fig. 2.1a and b, sum frequency conversion and as a special case frequency doubling) or the conversion of a single photon into two photons (Fig. 2.1c, parametric down-conversion) is illustrated.
For our novel approach in nonlinear interferometry, only the case of spontaneous parametric down-conversion (Fig. 2.1c) is of interest. In this special case the photons ω_1, ω_2 and ω_3 are often provided with the names "pump", "signal" and "idler" photon (ω_p, ω_s and ω_i). A pump photon generates, in the case of parametric down-conversion, a photon-pair consisting of the signal and idler photon following the energy conservation:

$$\omega_p = \omega_s + \omega_i. \tag{2.12}$$

As already depicted in these diagrams, not only the conversion of energy has to be satisfied but also the conservation of momentum, represented by the equation $\vec{k}_p = \vec{k}_s + \vec{k}_i$. Especially in the path-degenerate case, where $\vec{k}_s/|\vec{k}_s| = \vec{k}_i/|\vec{k}_i|$, the conservation of momentum can also be represented by:

$$\frac{n_p\omega_p}{c} = \frac{n_s\omega_s}{c} + \frac{n_i\omega_i}{c}, \tag{2.13}$$

using the identity $|\vec{k}| = n\omega/c$. Further, this equation can be rearranged to:

$$n_p - n_s = (n_i - n_s)\frac{\omega_i}{\omega_p}. \tag{2.14}$$

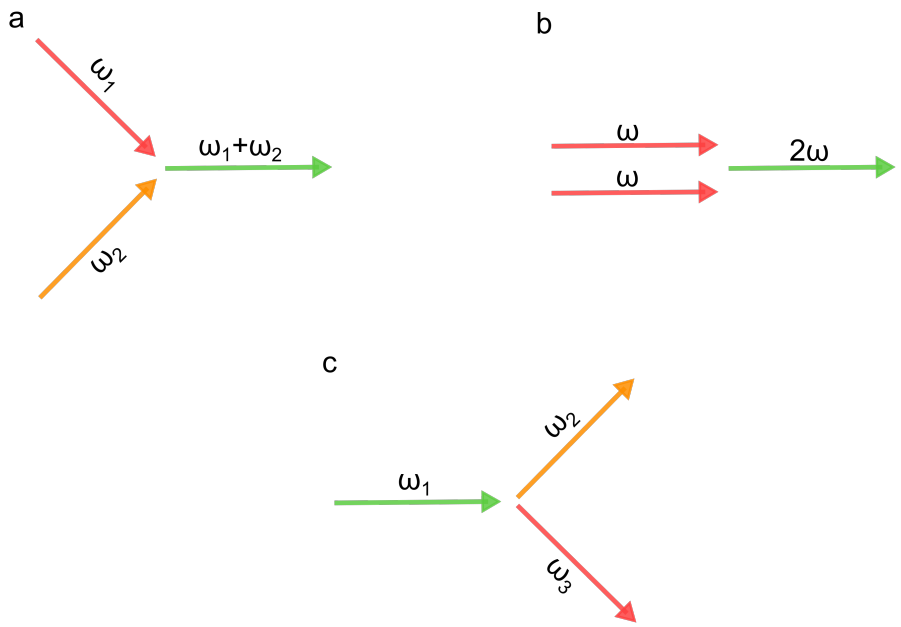

Figure 2.1: **Feynman diagrams of various three wave mixing types.** **a**, sum frequency conversion. **b**, frequency doubling **c**, parametric down conversion.

This equation is not necessarily satisfied for normal dispersion, where the refractive index n_p is larger than n_s (especially for the case of energy-degenerate parametric down-conversion ($\omega_s = \omega_i$)). Hence, the left side of the equation is negative, and the right side equals zero. This usually also applies to the non-path-degenerate case of different frequencies and non-parallel $\vec{k}_{s,i}$.
However, a possibility to still fulfill the conservation of momentum is anomalous dispersion. Here, contrary to normal dispersion, the refractive index increases with decreasing frequency. Alternatively, the birefringence of many crystalline materials can be used to change the refractive index for different polarization angles. Another technique is to locally violate equation (2.14) but globally conserve it by a well-engineered process called periodic poling. In this case, the conservation of momentum (2.14) is slightly adapted and called quasi-phase-matching. This concept will be described in more detail in the next section.
A more detailed description of the general nonlinear conversion is given in chapter 4 and appendix D.

2.1.2 Quasi-phase-matching

In this section, I will introduce the concept of periodic poling and quasi-phase-matching. As mentioned above, in case of spontaneous parametric down-conversion (SPDC, Fig. 2.1c) ,the photons ω_1, ω_2, and ω_3 are provided with the names "pump", "signal" and "idler" photon (ω_p, ω_s and ω_i).
If we consider a nonlinear crystalline medium of length l, an analytic solution for the intensity of the down-converted photons can be found. This solution is represented as a function, dependent on the phase-matching (or the wavevector mismatch $\Delta k = k_1 - k_2 - k_3$) and the length of the nonlinear media l [145] (see also appendix

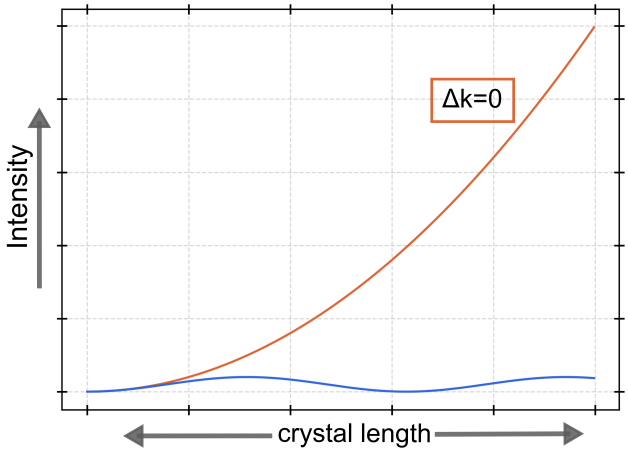

Figure 2.2: **Schematic of the parametric down-conversion intensity as a function of $l$for fixed values of Δk.** For a perfect phase-matching the down-conversion intensity increases quadratically with the crystal length. However for a non-perfect wavevector mismatch the down-conversion intensity undergoes oscillations.

D):

$$I_{\mathrm{SPDC}}(\Delta k, l) = \Gamma I_{\mathrm{P}} l^2 \,\mathrm{sinc}^2\left(\frac{\Delta k\, l}{2}\right), \tag{2.15}$$

with I_{P} the power of the pump photons and $\Gamma = \frac{4d_{\mathrm{eff}}^2 \omega_p^3}{c^3 n(\omega_p) n(\omega_i) n(\omega_s)}$ an additional parameter containing dependencies on other parameters (see appendix D). For a change in the wavevector mismatch Δk the down-conversion intensity can change quite dramatically. Further, if the wavevector mismatch Δk is fixed, the intensity of the down-converted light can be illustrated as a function of the crystal length l (Fig. 2.2). For a perfect phase-matching ($\Delta k = 0$), the term in the sinc function becomes zero and, thus, the sinc function becomes one. The down- conversion intensity then solely depends on the square of the crystal length ($I_{\mathrm{SPDC}} \propto l^2$). In this figure, for $\Delta k \neq 0$ an oscillatory behavior of the $I_{\mathrm{SPDC}}(\Delta k, l)$ as a function of the crystal length is visible. The reason for this behavior lies in the spatial coherence of the involved signal, idler, and pump photons. For $\Delta k \neq 0$ after a certain distance, the involved fields are out of phase and thus interfere destructively. Therefore, as a function of the crystal length l, I_{SPDC} will excite and de-excite the signal, and idler modes periodically [51].
The reason for this decoherence is the dispersion in the nonlinear medium. Here different wavelengths experience different refractive indices, introducing a phase difference between pump, idler, and signal photons. Thus this phase mismatch leads to a shortened coherence length ($l_{\mathrm{coh}} = \pi/\Delta k$) inside of the crystal, which inhibits an increasing down conversion intensity for an increasing crystal length l.
In reality, a perfect phase-matching ($\Delta k = 0$) is difficult to realize; thus, different approaches to overcome this oscillatory behavior have been developed.
An (at least in theory) simple solution to that problem is illustrated in Fig. 2.3. Here, the orientation of the ferroelectric domains of a nonlinear crystal is flipped at multiples of the coherence length l_{coh}. This leads to a change of the sign of the nonlinear coefficients d, which creates a phase jump that balances the phase mismatch [143]. This

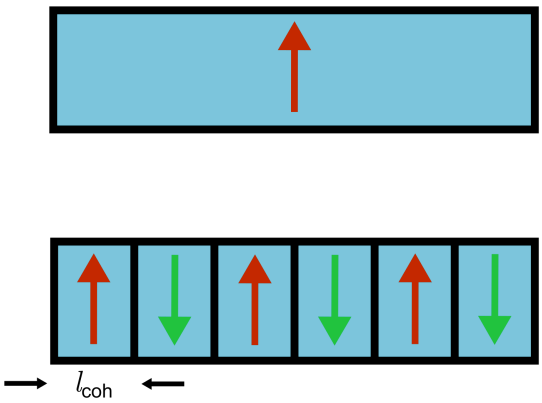

Figure 2.3: **Schematic of the periodically poling of a nonlinear crystal.** The orientation of the ferroelectric crystal domains is rotated by 180° at multiples of the coherence length l_{coh}.

flip of the ferroelectric domains is commonly known as periodic poling.
Even though this effect was already theoretically described quite early in 1962 [146] only way later could reproducible realizations be demonstrated (1990; [147]). The influence of periodic poling is apparent in the change of the perfect wavevector mismatch ($\Delta k = 0$) to:

$$\Delta k = \frac{\pi}{\Lambda}, \tag{2.16}$$

with Λ the spacing between poles in the crystal.
With this approach, a linear increase of the down-conversion intensity can be achieved even with non-perfect phase-matching (Fig. 2.4). Thus, periodically poled nonlinear crystals promise to reach higher down-conversion intensities for $\Delta k \neq 0$ than simple bulk material. In our experiment, a 1x1x10mm periodically poled potassium titanyl phosphate (PPKTP) crystal for Type 0 down-conversion with a grating period of 9 µm from the company "Raicol Crystals" has been used. These crystals are commonly used for prostatectomy using green light [148] or in laser pointers.
In birefringent nonlinear crystals, a distinction between different phase-matching types, dependent on the polarization of the pump, signal, and idler photon, can be made.

Polarization			Type
Pump	Signal	Idler	
o	o	o	Type 0 (Type V)
e	o	o	Type I
e	o	e	Type II
e	e	o	Type III
e	e	e	Type IV
o	o	e	Type VI
o	o	e	Type VII
o	e	e	Type VIII

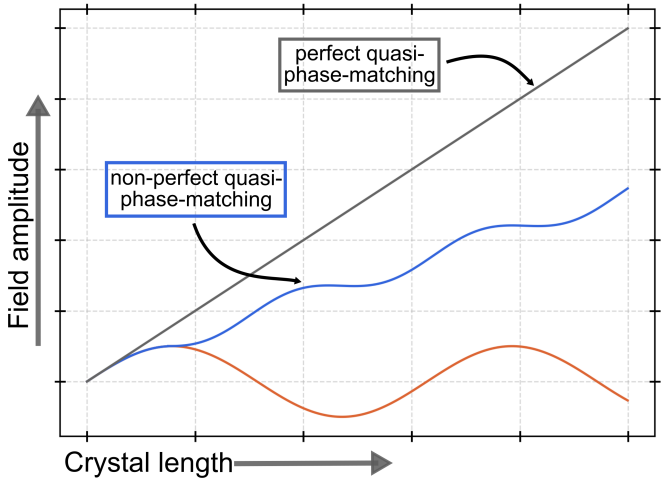

Figure 2.4: **Schematic of the down-conversion intensity for periodically poling of a nonlinear crystal.** With the periodically poling of the nonlinear crystal, even for non perfect quasi-phase-matching a linear increase of the down-conversion intensity can be restored.

Because nonlinear crystals are mostly negative uniaxial, e depicts a polarization along the axis of the smaller refractive index and vice versa for the o axis.
Our novel nonlinear interferometer is based on Type 0 spontaneous parametric down-conversion, where the polarization for the pump, signal, and idler photons is the same, resulting in a vertical polarization of the photons with respect to the experimental setup plane.

2.2 Development of a high-speed quantum optical phase sensor

In this section, I will present our novel quantum sensor. First, the detailed experimental realization will be shown, followed by a characterization against an almost perfect classical counterpart. Finally, an auxiliary section will discuss the sub-shot noise detection of high photon-pair fluxes (approximately 100 nW) using commercially available InGaAs cameras.
Our novel nonlinear interferometer is based on Type 0 spontaneous parametric down-conversion. The general principle of our nonlinear interferometer is that an entangled two-photon state is used to collect information about the phase difference between the two paths of the nonlinear interferometer. After that, we use path-polarizing quantum state engineering to transfer the phase information of this entangled two-photon state onto a single photon state. This state shows sub-shot noise phase sensing under a simple intensity measurement at high and low sampling rates.
Thus, the main features of this novel quantum sensor are:

- ❖ With higher order multi-photon states (of the order of N), a saturation of the Heisenberg limit is possible. In this work, we restrict ourselves to a two-photon state which results in a maximum enhancement factor of $\sqrt{2}$.

- ❖ Can be operated at an arbitrary sampling rate (here presented up to 100 kHz).
- ❖ Basic intensity measurements (no expensive single photon or photon-number resolving detectors are necessary, which are required to saturate the Heisenberg limit in other multi-photon state schemes).
- ❖ A simple experimental setup compared to squeezed states of light and SU(1,1) interferometry (see Fig. 2.5 and [90, 116])
- ❖ Robustness to losses outside of the interferometer (① in Fig. 2.5).
- ❖ The same ability of common mode noise rejection as in classical interferometry.

2.2.1 Experimental setup

In principle, our experimental setup can be split up into four different parts. These parts are depicted in Fig. 2.5 with the numbers ①-④.

① The first part represents the interferometer itself.

② The second part is a filtering stage that transfers the two-photon phase information onto a single photon state.

③ The third part is a variable polarization delay stage which allows us to adjust the temporal indistinguishability arbitrarily.

④ Finally, the last part mirrors the detection scheme of a classical interferometer, where a PBS and two intensity detectors are used for a common mode noise rejecting intensity measurement.

By going into detail about each part, we analyze how a gain of $\sqrt{2}$ is achievable.

① The interferometer

A 532 nm vertically polarized pump laser creates in the forward (f) direction (in Fig. 2.5 depicted as a red arrow) via Type 0 parametric down-conversion in a PPKTP nonlinear crystal a photon-pair contribution which can be described as:

$$|\Psi\rangle_{\mathrm{N}} = |\mathrm{V}_1, \mathrm{V}_2\rangle_f \,. \tag{2.17}$$

Here V stands for vertical polarization, and the index f for forward direction generated photon-pair contribution. The nonlinear crystal temperature was adjusted to 323 K with a simple heat element. This affects the refractive indices of the birefringent material, so that the quasi-phase-matching supports the creation of signal and idler photons with center frequencies of 1109.3 nm (index 2) and 1022.6 nm (index 1) and bandwidths (full width at half maximum) of 10.8 nm (3.1 THz) and 12.6 nm (3.6 THz) respectively. A spectrum of this photon-pair can be seen in Fig. 2.6.
The forward-generated photon-pair contribution travels through a dichroic mirror (DM_2) towards a retro-reflecting sample mirror (SM). The pump beam, reflected at the dichroic mirror (DM_2), defines the reference path and is retro-reflected at the reference mirror (RM). In the sample path the photon-pair contribution collects (compared to the reference path) a phase difference of $\Delta\phi = \Delta\phi_1 + \Delta\phi_2$. This is depicted in Fig. 2.5 by

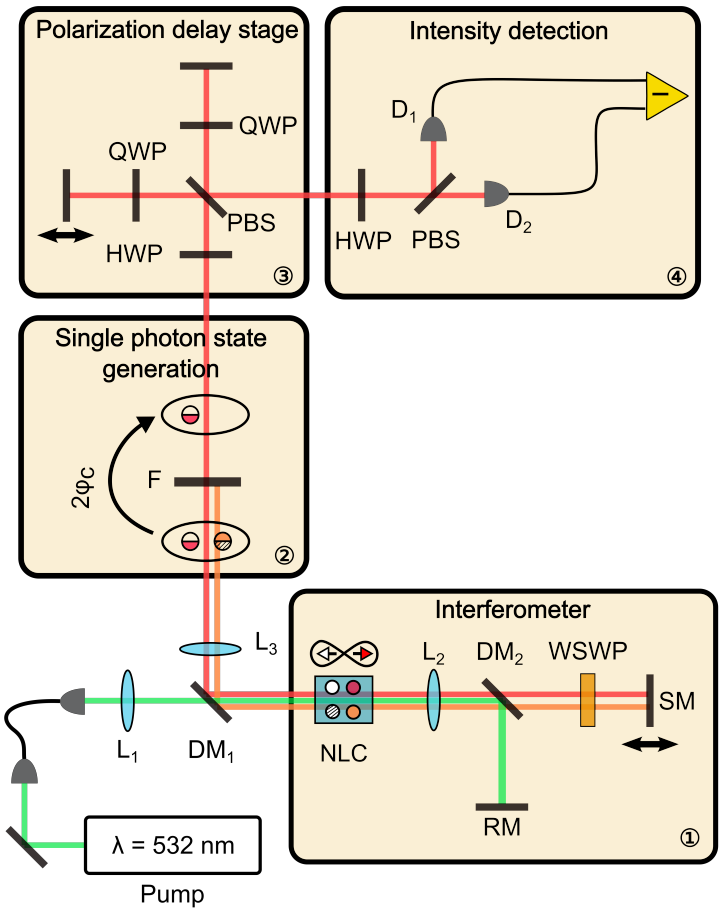

Figure 2.5: **Detailed experimental setup.** The quantum sensor resembles a Michelson interferometer, however modified to use photon-pair states. It consists of four parts. ① The interferometer itself, where via Type 0 down-conversion photon-pair contributions are generated in a nonlinear crystal (NLC). A phase difference $\Delta\phi = \Delta\phi_1 + \Delta\phi_2$ between the reference (enclosed by the reference mirror RM) and the sample path (enclosed by the sample mirror SM) is accumulated by the in forward and backward generated photon-pair contributions. A wavelength-selective waveplate (WSWP) leads for a double pass to a polarization rotation of the signal photon $|V_1, V_2\rangle \rightarrow |V_1, H_2\rangle$. ② A filter stage filters out the idler photon, thus reducing the photon-pair state to a single photon state. ③ A polarization delay stage consisting of a half-wave plate (HWP), a polarizing beam splitter (PBS), and two quarter-wave plates (QWP). Here the temporal indistinguishability can be adjusted arbitrarily. And ④ the detection. A Hadamard gate consisting of a HWP and a PBS is implemented, allowing the intensity detection at both output ports of the PBS with the intensity detectors D_1 and D_2. Further optical elements: L: Lens, DM: Dichroic mirror, F: Filter.

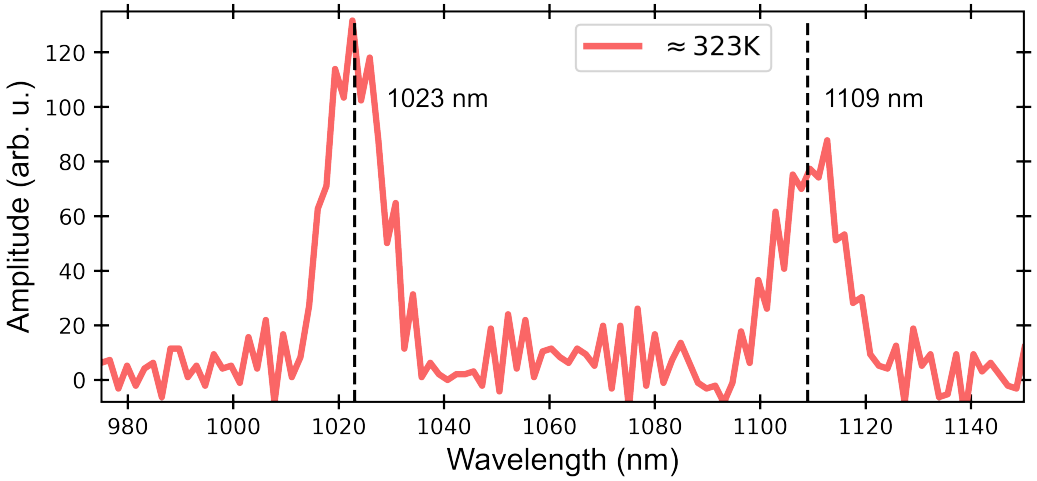

Figure 2.6: **Spectrum of the photon-pair contributions generated for the quantum sensor.** Photon pair spectrum of the PPKTP crystal heated up to a temperature of 323 K. The idler photon shows a center wavelength of 1022.6 nm and the signal photon 1109.3 nm. The bandwidths (full width at half maximum; FWHM) are 10.8 nm and 12.6 nm respectively [1].

a displacement of the retro-reflecting sample mirror (SM). $\Delta\phi_1$ and $\Delta\phi_2$ represent the wavelength-dependent phase difference for each photon of the two-photon state. This can be illustrated in the quantum state representation in equation (2.17) as

$$|\Psi\rangle_{\mathrm{N}} = e^{i(\Delta\phi_1+\Delta\phi_2)}\,|\mathrm{V}_1,\mathrm{V}_2\rangle_{\mathrm{f}}\,. \tag{2.18}$$

A double pass through a wavelength-selective waveplate (WSWP) creates a 90° polarization rotation of the signal photon (1109.3 nm) which leads to

$$|\Psi\rangle_{\mathrm{N}} = e^{i(\Delta\phi_1+\Delta\phi_2)}\,|\mathrm{V}_1,\mathrm{H}_2\rangle_{\mathrm{f}}\,. \tag{2.19}$$

The pump photons, retro-reflected from the reference mirror (RM), create on their way back through the nonlinear crystal again via Type 0 down-conversion a second photon-pair contribution $|\mathrm{V}_1,\mathrm{V}_2\rangle_{\mathrm{b}}$ (now with an index b indicating a photon-pair contribution generated in backward direction). In Fig. 2.5 the backward generated photon-pair contribution is depicted by a white arrow. This results in the entangled two-photon state:

$$|\Psi\rangle_{\mathrm{N}} = \frac{1}{\sqrt{2}}(e^{i(\Delta\phi_1+\Delta\phi_2)}\,|\mathrm{V}_1,\mathrm{H}_2\rangle_{\mathrm{f}} + |\mathrm{V}_1,\mathrm{V}_2\rangle_{\mathrm{b}}\,). \tag{2.20}$$

This state already shows some interesting features. First, this state contains the phase information of a photon-pair ($\Delta\phi_1 + \Delta\phi_2$). Second, the perpendicular polarization of the signal photon contributions allows easy handling of a possible temporal mismatch between the photon-pair contributions caused by the birefringence of the nonlinear crystal by implementing a polarization delay stage (see section 2.2.2).

② Single-photon state generation

A measurement of a single photon cannot reveal its origin (forward or backward generated) if both photon-pair contributions are indistinguishable. In this case, the indices

f and b become obsolete, which can be represented as:

$$|\Psi\rangle_{\mathrm{N}} = \frac{1}{\sqrt{2}} |V_1\rangle \left(e^{i(\Delta\phi_1+\Delta\phi_2)} |\mathrm{H}_2\rangle + |\mathrm{V}_2\rangle \right). \tag{2.21}$$

Interestingly, then the entangled superposition state (equation (2.20)) is transformed to a superposed pure state (equation (2.21)). A measurement of the idler photon $|\mathrm{V}\rangle_1$ does not reveal any information about the phase difference or even about the origin of the photon (backward or forward direction). Thus an implemented spectral filter (a narrow bandpass filter, Omega Optical, LLC NB1109/2), filtering out the idler photon (1022.6 nm) does not collapse the entangled state and does not reveal any phase information. Therefore the entangled two-photon state reduces to a superposed pure single-photon state:

$$|\Psi\rangle_{\mathrm{N}} = \frac{1}{\sqrt{2}} \left(e^{i(\Delta\phi_1+\Delta\phi_2)} |\mathrm{H}_2\rangle + |\mathrm{V}_2\rangle \right). \tag{2.22}$$

Fascinatingly this state represents a single-photon state in the same way as in classical interferometry but containing still the two-photon phase information $\Delta\phi_1 + \Delta\phi_2$. In contrast, a classical counterpart would only carry phase information of $(\Delta\phi_1 + \Delta\phi_2)/2$. Thus, creating this single photon state allows further treatment similar to classical interferometry.

③ Polarization delay stage

To adjust the indistinguishability mentioned above, we used a polarization delay stage. A separate section (section 2.2.2) will present a more detailed description of the cause of distinguishability and countermeasures.
In this delay stage, photons of different polarization travel through different ports of a polarizing beam splitter (PBS), defining two paths. After a retro-reflection (and passing a quarter-wave plate), both paths are overlapped at a single output port of the PBS. Due to their perpendicular polarization (equation (2.22)), the signal photon contributions travel along different paths inside of the polarization delay stage. By adjusting one path length, the optical path length of one signal-photon contribution can be extended or reduced so that the temporal mismatch between both photon pair contributions can be arbitrarily adjusted. Note that quantum mechanics allows us to perform this adjustment even after we have already measured (filtered out) the idler photon (more details in section 2.2.2).

④ Intensity detection

Identically to standard detection schemes in classical interferometry a Hadamard gate (in Fig. 2.5 implemented as a half-wave plate and a polarizing beam splitter) can be applied to the single-photon state of equation (2.22).
This Hadamard gate (operator) can be represented as a 2D matrix:

$$\hat{H} = \frac{1}{\sqrt{2}} \begin{pmatrix} 1 & 1 \\ 1 & -1 \end{pmatrix}, \tag{2.23}$$

where

$$|\mathrm{H}\rangle = \begin{pmatrix} 1 \\ 0 \end{pmatrix} \quad \text{and} \quad |\mathrm{V}\rangle = \begin{pmatrix} 0 \\ 1 \end{pmatrix}. \tag{2.24}$$

Thus the Hadamard gate operation transfers the single photon state from equation (equation (2.22)) to:

$$|\Psi\rangle_{\mathrm{N}} = \frac{1}{2}\left((1 + e^{i(\Delta\phi_1+\Delta\phi_2)})\,|\mathrm{H}_2\rangle + (e^{i(\Delta\phi_1+\Delta\phi_2)} - 1)\,|\mathrm{V}_2\rangle \right). \tag{2.25}$$

Additionally, this implementation of a Hadamard gate as a half-wave plate and a polarizing beam splitter already separates horizontally and vertically polarized photon contributions. Note that this state is still a single photon state, so single-photon, coincidence, or multi-photon detection schemes are obsolete, and a simple intensity measurement scheme is sufficient. If we repeat this process with N photons entering the quantum sensor, we find an intensity signal for both detectors D_1 and D_2 as:

$$\mathrm{D}_1(\phi, N) = \frac{N}{2}\cos^2\left(\frac{\Delta\phi_1 + \Delta\phi_2}{2}\right) \quad \text{and} \quad \mathrm{D}_2(\phi, N) = \frac{N}{2}\sin^2\left(\frac{\Delta\phi_1 + \Delta\phi_2}{2}\right) \tag{2.26}$$

Note that indeed N photons enter the sensor, but half of the photons (idler photons) are filtered out, leaving $N/2$ photons being measured at the detectors D_1 and D_2. Following the same approach as in section 1.1.2 of chapter 1 the resulting difference signal reduces to:

$$\mathrm{D}_{1-2}(\phi, N) = \frac{N}{2}\cos(\Delta\phi_1 + \Delta\phi_2). \tag{2.27}$$

This intensity signal provides a couple of advantages over previous realizations. First, the two-photon phase information can be obtained by only measuring single photons (or half of the photons ($N/2$) entering the interferometer). As a result, we can profit from simple, inexpensive intensity detection at the output port of the beam splitter. Second, we also profit from a difference signal, which cancels out common mode fluctuations like laser power instabilities and promises high stability. Additionally, losses in each part of the sensor beside of the interferometer (① in Fig. 2.5) does not decrease the enhancement factor. Losses outside the interferometer only lead to the loss of a photon and thus only to a reduced amplitude (or photon number) of the intensity signals.

2.2.2 Preliminary adjustments

This section will detail some crucial features of the experimental setup described above. We will focus on two parts: the adjustment of a temporal mismatch between the photon pair contributions, which we counteract with an arbitrary path polarization delay stage, and the path polarization quantum state engineering using a wavelength-selective waveplate.

Temporal indistinguishability

In our quantum sensor, the two possible causes of temporal mismatch between the two photon-pair contributions are the wavelength-dependent velocity in media (dispersion)

and the birefringence of the PPKTP crystal. Due to the probabilistic generation of photon-pair states via spontaneous parametric down-conversion, it takes place on average at the center of the nonlinear crystal (PPKTP). Therefore the forward-created photon-pair contribution travels on its way back additionally through the whole crystal, whereas its backward counterpart does not.
To guide the eye, we will focus on the temporal spacing between the photons of each photon-pair contribution (forward and backward generated). To reach temporal indistinguishability, the temporal spacing between both photon pair contributions has to be equal. Usually, for a temporal mismatch smaller or equal to the coherence time τ, electromagnetic waves are considered coherent. However, the temporal mismatch Δt is ideally kept as small as possible ($\Delta t \ll \tau$). For a Gaussian shaped spectrum the coherence time is defined as $\tau = 2\ln(2)/(\pi\Delta f) \approx 0.44/\Delta f \approx 0.90\,\mathrm{ps}$.
In the following, the dispersion of the nonlinear crystal has been calculated using the Sellmeier dispersion formulas for KTP [149]. Taking solely dispersion into account, the temporal mismatch between forward and backward direction generated photon-pair contributions is $\Delta t = 0.11\,\mathrm{ps}$ and therefore by almost one magnitude lower than the coherence time.
But due to a polarization rotation of the signal photon from $|\mathrm{V}\rangle_2 \rightarrow |\mathrm{H}\rangle_2$, before re-entering the nonlinear crystal, the birefringence causes an additional temporal mismatch of $\Delta t = 2.9\,\mathrm{ps}$, which exceeds the coherence time and thus leads to decoherence and therefore a collapse of the entangled state (equation (2.20)). Thus the temporal distinguishability introduced by the birefringence of the PPKTP nonlinear crystal has to be adjusted to provide the highest possible enhancement factors.
For this adjustment, we took advantage of the feature which originally also caused the mismatch to appear, the perpendicularity of the polarization of the signal photon contributions $|\mathrm{V}_2\rangle$ and $|\mathrm{H}_2\rangle$. A polarization delay stage (③ in Fig. 2.5) has been implemented, which splits up both photon contributions $|\mathrm{V}_2\rangle$ and $|\mathrm{H}_2\rangle$ into different paths. The retro-reflecting mirrors in these paths could be arbitrarily adjusted to compensate for the introduced temporal mismatch by extending or reducing the path lengths for the photon contributions. Note that the beauty of quantum mechanics allows us to first measure or filter out the idler photon $|\mathrm{V}_1\rangle$ and afterward adjust the temporal spacing between its partner photon without collapsing the entangled state. This is possible because only the temporal spacing between each photon-pair contribution defines its origin. Thus if the temporal indistinguishability is adapted before the detection of the single photon state, no statement of the origin of the photon-pair contribution can be made (after detection).

Path-polarization quantum state engineering with a wavelength-selective waveplate (WSWP)

Another crucial component of our quantum sensor is the wavelength-dependent waveplate (WSWP). To successfully transfer the phase information from the two-photon state onto a single-photon state a perpendicular polarization of the in forward direction generated photon-pair contribution ($|\mathrm{V}_1, \mathrm{V}_2\rangle \rightarrow |\mathrm{V}_1, \mathrm{H}_2\rangle$) is necessary. For this purpose, a multi-order half-wave plate from Thorlabs was considered (Thorlabs WPMH05M-980). A previous check of its specifications indicated that this waveplate represents for a double pass for signal photons a half-wave plate and for idler pho-

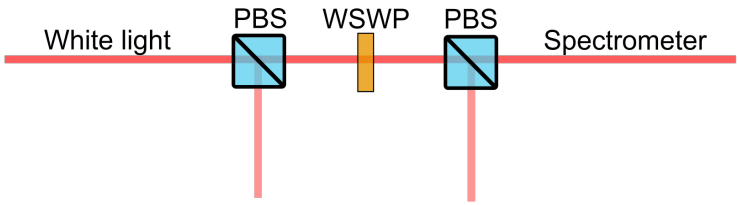

Figure 2.7: **Wavelength dependent retardance setup.** For the characterization of the WSWP, white light was sent first through a polarizing beam splitter (PBS), then through the WSWP, and afterward again through a PBS. The light exiting the second PBS is detected with a spectrometer. The first PBS polarizes the light linearly, and the second PBS translates the polarization rotation angle onto the intensity. Adapted from [1].

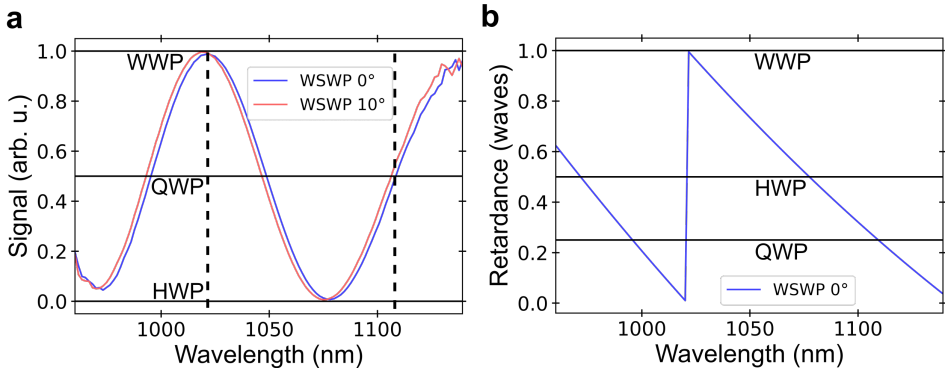

Figure 2.8: **Retardance.** **a**, Intensity signal of the retardance measurement for the waveplate put at normal beam incidence and tilted by 10°. The black lines show the idler levels, which correspond to a quarter-wave plate (QWP), a half-wave plate (HWP), and a whole waveplate (WWP). The WSWP is equivalent to a WWP at a wavelength of 1023 nm and to a QWP for a wavelength of 1109 nm. **b**, Calculated retardance of the WSWP. The retardance corresponds to 0.995 ± 0.001 (1023 nm) and 0.250 ± 0.001 (1109 nm). Adapted from [1].

tons a whole-waveplate, thus meeting the requirement to fulfill the transformation $|V_1, V_2\rangle \rightarrow |V_1, H_2\rangle$. To characterize the actual retardance of the WSWP, we developed a simple white light spectrometer (Fig. 2.7). Here the WSWP has been inserted at angles of 0° and 45° between two PBS. A white light source in the wavelength range of $960 - 1140$ nm has been sent into the input port of the first PBS. After the second PBS, the wavelength-dependent intensity at one output port of the second PBS was measured with a spectrometer. With the measured background I_{bg} and the values at 0° ($I_{0°}$) and 45° ($I_{45°}$) an interference function:

$$f(\lambda) = \frac{I_{45°} - I_{\mathrm{bg}}}{I_{0°} - I_{\mathrm{bg}}} \tag{2.28}$$

can be calculated. Additionally to perfect perpendicular placement of the WSWP, we checked the influence of a non-perfect placement of the WSWP in terms of a small tilting angle of 10°. Both results are shown in Fig. 2.8a. To extract the retardance

from this wavelength-dependent intensity signal, a fit function in the form of:

$$f(\lambda) = a\,\sin^2(b\lambda^2 + c\lambda + d) + e \tag{2.29}$$

has been used. From the obtained parameters $a - e$ of the wavelength-dependent intensity function, we could further calculate the retardance of the WSWP using the equation:

$$r(\lambda) = \Big((b\lambda^2 + c\lambda + d)\pi + 0.5\Big) \bmod 1. \tag{2.30}$$

The WSWP resembles at normal incidence for a single pass, a retardance of 0.995 ± 0.001 (1023 nm) and 0.250 ± 0.001 (1109 nm). This means that for a double pass with 0.500 ± 0.002 the WSWP acts for the signal photon (1109 nm) like a half-wave plate and for the idler photon (1023 nm) with a retardance of 1.990 ± 0.002 like a whole-waveplate.
Due to the non-perfect performance of the WSWP for the idler photon, we calculated its influence on the visibility and therefore the enhancement factor of our quantum sensor as a further step. For this purpose, we treated the WSWP as an arbitrary birefringent material phase retarder in the form of a Jones matrix [150]:

$$\hat{J}_{\mathrm{WSWP}} \equiv \mathrm{e}^{-i\frac{\eta}{2}} \begin{pmatrix} \cos^2(\Theta) + \mathrm{e}^{i\eta}\cdot\sin^2(\Theta) & (1-\mathrm{e}^{i\eta})\cdot\cos(\Theta)\sin(\Theta) \\ (1-\mathrm{e}^{i\eta})\cdot\cos(\Theta)\sin(\Theta) & \sin^2(\Theta) + \mathrm{e}^{i\eta}\cdot\cos^2(\Theta) \end{pmatrix}. \tag{2.31}$$

Note that we used here the value $\eta = (0.995 \pm 0.001)\cdot 2\pi$ for the WSWP because the value 0.250 ± 0.001 is already quite perfect. Thus calculating the double passage of the idler photon $\hat{J}_{\mathrm{WSWP}}(-\Theta)\hat{J}_{\mathrm{WSWP}}(\Theta)|\mathrm{V,s}\rangle$ leads to the polarization state $|\mathrm{V,s}\rangle \rightarrow \alpha|\mathrm{H,s}\rangle + \beta|\mathrm{V,s}\rangle$ with $\alpha = 0.063$ and $\beta = 0.998$. To calculate the effect of this non-perfect retardance on the quantum enhancement, we further calculated the detection probability of this state in the σ_x basis. We define the density matrix of the state exiting the interferometer as $\rho = |\Psi\rangle\langle\Psi|$, with $|\Psi\rangle = (|\mathrm{V,i}\rangle|\mathrm{V,s}\rangle + \mathrm{e}^{i\phi}|\mathrm{V,i}\rangle(\alpha|\mathrm{H,s}\rangle + \beta|\mathrm{V,s}\rangle)/\sqrt{2}$.
Furthermore, we separate the idler as done in the experiment by a spectral filter (Fig. 2.5).

$$\rho_{\mathrm{exc}} = \langle \mathrm{H},s|\rho|\mathrm{H},s\rangle + \langle \mathrm{V},s|\rho|\mathrm{V},s\rangle = \frac{1}{2}\begin{pmatrix} 1 & \beta^*\mathrm{e}^{-i\cdot\Phi} \\ \beta\mathrm{e}^{i\cdot\Phi} & 1 \end{pmatrix}. \tag{2.32}$$

Again as described above, we apply a Hadamard gate consisting of a half-wave plate and a polarizing beam splitter for a detection in the σ_x basis:

$$\hat{H}\rho_{\mathrm{exc}}\hat{H} = \begin{pmatrix} 2 + \beta^*\mathrm{e}^{-i\cdot\Phi} + \beta\mathrm{e}^{i\cdot\Phi} & \beta\mathrm{e}^{i\cdot\Phi} - \beta^*\mathrm{e}^{-i\cdot\Phi} \\ \beta^*\mathrm{e}^{-i\cdot\Phi} - \beta\mathrm{e}^{i\cdot\Phi} & 2 - \beta^*\mathrm{e}^{-i\cdot\Phi} - \beta\mathrm{e}^{i\cdot\Phi} \end{pmatrix}, \tag{2.33}$$

with

$$\hat{H} = \frac{1}{\sqrt{2}}\begin{pmatrix} 1 & 1 \\ 1 & -1 \end{pmatrix}. \tag{2.34}$$

The detection probability is now located in the diagonal elements. With $\alpha = 0.063$ and $\beta = 0.998$, the visibility reduces to 0.998. This leads to a negligible reduction of the enhancement of 0.998.

Furthermore, we can calculate the ellipticity by transforming the Jones matrix $\hat{J}_{\mathrm{WSWP}}$ into the corresponding Mueller-Jones matrix by the relation [151]

$$\hat{M}(\Theta) = \hat{A}(\hat{J}(\Theta) \otimes \hat{J}^*(\Theta))\hat{A}^T. \tag{2.35}$$

Here * indicates the complex conjugate and ^{T} the transpose, with

$$\hat{A} = \begin{pmatrix} 1 & 0 & 0 & 1 \\ 1 & 0 & 0 & 1 \\ 0 & 1 & 1 & 0 \\ 0 & -i & i & 0 \end{pmatrix}. \tag{2.36}$$

With the resulting Mueller-Jones matrix ($\hat{M}_{\mathrm{WSWP}}(\Theta)$) and the vertical polarized stokes vector

$$S_v = \begin{pmatrix} 1 \\ -1 \\ 0 \\ 0 \end{pmatrix}. \tag{2.37}$$

The resulting Stokes vector S_{WSWP} for a double passage can be calculated, using the relation $S_{\mathrm{WSWP}} = \hat{M}_{\mathrm{WSWP}}(-\Theta)\hat{M}_{\mathrm{WSWP}}(\Theta)S_v$

$$S_{\mathrm{WSWP}} = \begin{pmatrix} 4.000 \\ -3.968 \\ 0.000 \\ 0.501 \end{pmatrix}. \tag{2.38}$$

This vector resembles the three dimensions of a Poincaré sphere with a non-unity radius given by the first component of the vector. Thus it represents, when normalized to this first component:

$$S_{\mathrm{WSWP}} = \begin{pmatrix} -0.992 \\ 0.000 \\ 0.125 \end{pmatrix} \tag{2.39}$$

the three dimensions of the Poincaré sphere [51]. The first dimension of the Poincaré sphere gives the vertical, the second dimension the horizontal, and the third dimension the circularity of the polarization. For a perfectly vertical polarized photon, this vector would be

$$S_{\mathrm{WSWP}} = \begin{pmatrix} 1 \\ 0 \\ 0 \end{pmatrix}. \tag{2.40}$$

Note that the influence of tilting the WSWP with respect to the beam incidence below 10° of angle (red curve in Fig. 2.8a) shows a negligible effect on the retardance ($\pm 0.08\%$ @ 1023 nm and $\pm 0.5\%$ @ 1109 nm).
With this characterization, we concluded that the influence of the non-perfect retardance of the WSWP is small enough to use the commercially available multi-order waveplate from Thorlabs (WPMH05M-980). This waveplate thus meets the requirements to represent (for a double pass) a WWP for 1023 nm and a HWP for 1109 nm. The reduction of the visibility to 0.998 and a connected reduction of the enhancement factor to $0.998 \cdot \sqrt{2}$ is negligible. Additionally it could be shown, that a double

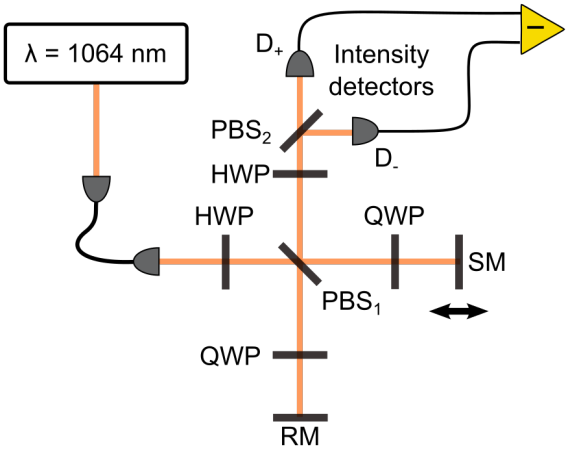

Figure 2.9: **Classical sensor.** The classical sensor resembles a simple Michelson interferometer. PBS = polarizing beam splitter, HWP = half-wave plate, QWP = quarter-wave plate, RM/SM = reference/sample mirror [1].

pass of the idler photon with a wavelength of 1023 nm leads to almost no change in the polarization (demonstrated with a polarization vector on the Poincaré sphere: $S_{\mathrm{WSWP}} \approx (-0.992 \pm 0.001 | 0.000 \pm 0.000 | 0.125 \pm 0.003)$.

2.2.3 Characterization

Due to the retro-reflection at both the sample mirror (SM) and the reference mirror (RM), our novel sensor is closest to a Michelson interferometer. Thus we naturally compared it with a similar classical Michelson interferometer (Fig. 2.9) driven by a laser with a center wavelength of 1064 nm (Roithner Laser Technik: RLT1064-50MGS). The beam is coupled into an optical fiber for spatial mode cleaning (Thorlabs P1-980A-FC) and subsequently collimated out of the fiber and split at the first polarizing beam splitter (PBS_1 – Thorlabs PBS203) into the two paths of the interferometer. Further, the beam is retro-reflected at the sample and reference mirror, respectively.
A quarter-wave plate (WPQ05M-1064) at 45° is placed in both paths. At the PBS_1 both path contributions are combined and leave the interferometer at the output port towards the detectors. Similar to the quantum sensor, a state analysis in the σ_x basis is performed using an achromatic half-wave plate (HWP – Thorlabs AHWP05M-980) and a polarizing beam-splitter (PBS – Thorlabs PBS203).
After the PBS, the beams are coupled into optical fibers (Corning SMF28e) and directed to superconducting intensity detectors (PhotonSpot, Inc.).
Note, that for both schemes, we defined as a resource the number of photons entering the interferometer; thus, challenges associated with the quantum strategy are explicitly not corrected for (loss inside the interferometer and non-perfect mode overlap inside the NLC). Further, it is essential to minimize parasitic noise from the intensity detectors to benchmark the sensing schemes at the purest and most fundamental level. This is why we used superconducting nanowire photon detectors (SNPDs) for this demonstration. However, the SNPDs are operated as low noise intensity detectors, and their single-photon detection capability is not required.

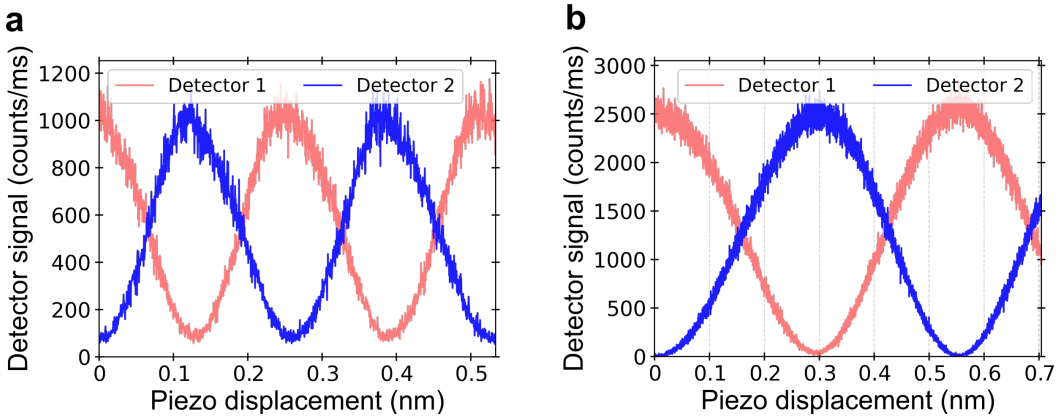

Figure 2.10: **Detector signals.** **a**, The raw data of both detectors (blue and red) of the quantum sensor. The visibility of both detectors (calculated from a sinusoidal fit) is 0.85 ± 0.02. **b**, Detector signals of the classical sensor. The visibility of both detectors is 0.98 ± 0.002 [1].

2.2.4 Visibility and detector signals

To benchmark our novel quantum sensor, we attached a piezoelectric actuator to the sample mirror (SM) in both setups and displaced this mirror by roughly 532 nm. The resulting interferometer signals gave access to the fringe visibility of both sensors (see Fig. 2.10).
To calculate the visibilities, a sinusoidal fit in the form of $f = N\cos^2(px + c) + d$, with N the amplitude (maximum photon number measured), p the spatial frequency, c an initial phase shift, and d the amplitude offset has been applied. To calculate the visibilities, the maximum and minimum values of the fit have been used and inserted into the standard equation: $\nu = (f_{\max} - f_{\min})/(f_{\max} + f_{\min})$. As a result the calculated visibilities resembled as $\nu_{\mathrm{qm}} = 0.85 \pm 0.02$ for both detectors of the quantum sensor and $\nu_{\mathrm{cl}} = 0.98 \pm 0.02$ for both detectors of the classical sensor.
In Fig. 2.11 the final interferometer signal (subtraction of both detector channels) of both sensors is shown.
For the same piezoelectric displacement, the resulting interferometer signal of the quantum sensor shows twice as many interference fringes, thus corroborating superresolution. As an indicating argument of the enhancement, the zero crossing of the signals of both sensors can be compared. At the zero crossing, both signals have roughly the same slope, but the quantum sensor shows merely half of the photon number compared to the classical sensor and thus exhibits less photonic shot noise.
However, superresolution alone is insufficient to demonstrate an exploitable quantum advantage [71]. The critical parameter to consider is the achievable phase sensitivity per photon sent to the interferometer.

2.2.5 Allan deviation of the phase noise spectral amplitude

An informative and still apparent overview of the enhancement as a function of the measurement speed or sampling rate is the presentation of the maximum phase sensitivity in an Allan deviation plot [152, 153]. The Allan deviation or Allan variance is a

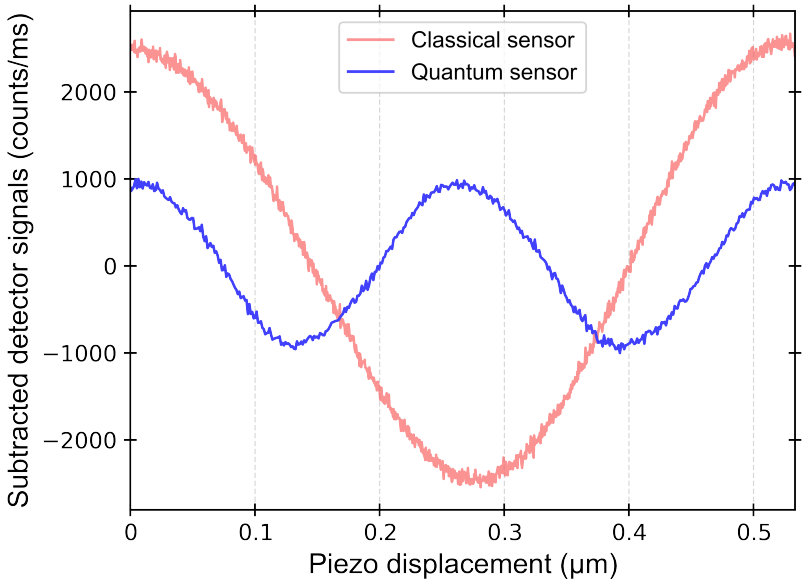

Figure 2.11: **Subtracted detector intensity signals.** For the same piezoelectric displacement, the quantum sensor presents twice as many fringes, thus corroborating phase sensing with super-resolution [1].

measure for uncorrelated noise processes. It is often used to illustrate the stability of clocks as well as to show the measurement sensitivity in interferometric systems [40]. The Allan deviation plot can be interpreted as a sensor's sampling rate or frequency-dependent sensitivity. If we take the phase sensitivity of a classical interferometer as an example (standard quantum limit: $\Delta\phi \geq 1/\sqrt{N}$), we can rewrite the sensitivity as

$$\Delta\phi \geq 1/\sqrt{t \cdot n}, \tag{2.41}$$

with n the number of photons per second and t the integration time. Thus the absolute phase sensitivity is dependent on the integration time.

- For high sampling rates, small t, the influence of external $1/f$ noise sources tends to be zero but also the product $t \cdot n$ and therefore the absolute phase sensitivity $\Delta\phi \propto \sqrt{t \cdot n}$ is low.
- For low sampling rates, large t, the influence of slow-changing noise sources like thermal drifts tends to be higher.
- But, for low sampling rates, large t, the product $t \cdot n$ increases and therefore the absolute phase sensitivity $\Delta\phi \propto \sqrt{t \cdot n}$.
- With external noise sources, for example thermal drifts, we expect that at some point the increasing sensitivity is influenced and reduced by these drifts. Thus, there exists an optimal point where the increasing external noise and the increasing sensitivity are balanced in the best way and thus form a global minimum. Based on this behavior the optimal point with the highest sensitivity to a phase shift is precisely at this minimum.

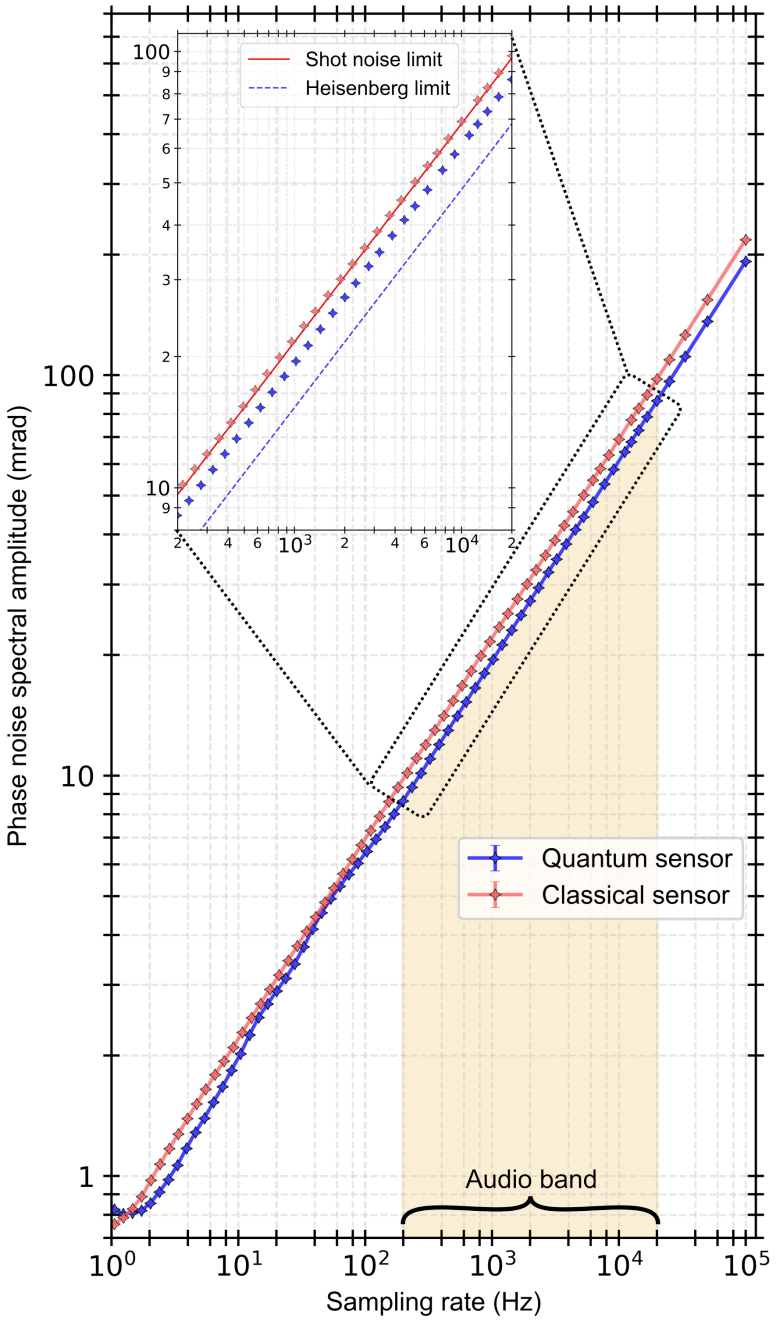

Figure 2.12: **Benchmarking the classical and quantum sensors.** Frequency-dependent phase noise spectral amplitudes of the classical (red) and quantum (blue) sensor. Both measurements are performed at identical photon fluxes before any loss inside the interferometer. Above 200 Hz, the quantum sensor surpasses the classical sensor by a factor of 1.13 ± 0.02. In the inset, the solid/dotted lines indicate the theoretical limits of both sensors at the used photon rate $R = 2.14 \cdot 10^6\,\mathrm{s}^{-1}$ [1].

Capitalizing on that, we decided to present the phase sensitivities of both sensors (classical and quantum) in an Allan deviation plot (Fig. 2.12). As described before, both sensors show for high sampling rates a square root behavior. In this double logarithmic plot, this is demonstrated as a linear curve with a slope of 0.5. At the very left side at approximately 1.25 Hz for the quantum sensor a local minimum of approximately $0.71\,\mathrm{mrad}/\sqrt{\mathrm{Hz}}$ appears. Note that the classical sensor is, as a consequence of the lower sensitivity, also less sensitive to external noise sources and thus more stable.
For sampling rates between 200 Hz up to values of 100 kHz the classical and the quantum sensors show sensitivities of approximately $0.70\,\mathrm{mrad}/\sqrt{\mathrm{Hz}}$ and $0.61\,\mathrm{mrad}/\sqrt{\mathrm{Hz}}$ respectively. In addition, the inset in Fig. 2.12 shows the standard quantum limit as a solid red line and the Heisenberg limit of a two-photon state as a dashed blue line. The classical sensor operates merely 1.5% above the standard quantum limit. Thus, the quantum sensor surpasses the standard quantum limit (for sampling rates of 200 Hz-100 kHz) by a factor of 1.13 ± 0.02, which is expected for our visibility (see chapter 4). Note, that the enhancement is sometimes defined as the squared ratio of signal-to-variance [52, 116, 139, 154]. However, the associated enhancement factor 1.28 ± 0.04 may be confusing as it does not directly reflect the phase sensitivity improvement.
A remarkable side result, which can be seen in Fig. 2.12, is that our multi-photon quantum sensing scheme shows sub-shot noise performance up to sampling rates of $f = 100\,\mathrm{kHz}$, which is at least four orders of magnitude higher than in previous approaches [31, 32, 64].
Note that the regime of a constant enhancement factor covers the entire audio band, where the human voice appears. Therefore, our quantum sensor can perform simultaneous measurements with an enhancement factor containing signals of all frequencies in the audio band.

2.2.6 Noise measurements for higher photon flux detection with commercially available InGaAs detectors

A recent publication [155] indicated that for specific sets of parameters, like the bandwidth of the generated photon pair, a high flux of still distinct photon pairs can be created, reaching levels of hundreds of nanowatts up to several microwatts. An increase of the absolute photon-pair flux can open the door to either higher absolute sensitivities ($\Delta\phi \propto 1/\sqrt{N}$) or even higher sampling rates.
The main problem at such power levels is the light detection, for which the optoelectrical signal conversion must be performed at a noise level that surpasses the photonic shot noise. In this sense, avalanche photodiodes or variable gain photoreceivers show intrinsic electronic noise way above the photonic shot noise.
We found a suitable solution in the form of commercially available InGaAs cameras. These camera modules exhibit essentially two noise sources; a dark current resulting in electronic shot noise and so-called read noise. With our subsequent measurements, we show that the overall noise of two commercially available camera modules is low enough to perform sub-shot noise quantum sensing [1].
We identified four suitable cameras which promised to meet these requirements: Wildcat 640 from Xenics, C14041-10U from Hamamatsu, MVCam from Princeton Infrared Technologies, and CL-008 TEC1 from Allied Vision. Two cameras were obtained for

in-house testing within the framework of a lend: Wildcat 640 from Xenics and C14041-10U from Hamamatsu.
We benchmarked both cameras in a scenario where both camera chips were initially illuminated with laser light at 1064 nm at 100 nW, with the beam diameter on the camera being carefully adjusted to maintain exposure below the full well capacity (FWC). After that, the laser power was adjusted with a neutral density filter wheel. For different power levels, we recorded a series of 300 images at a frame rate of 100 Hz with an exposure time of 5 ms. For a greater statistical significance, we considered an array of 11×11 pixels in the center of the beam, where we obtained a highly homogeneous intensity profile. An initial measurement was taken with the camera modules being blocked, which allowed us to infer the dark current per pixel. In all subsequent measurements, the dark current was subtracted. We then measured the frame-to-frame variance in the measured photon number for each pixel Δp_{tot} at these power levels. For perfect optoelectronic transduction, the cameras would induce no additional noise, Δp_{cam}, such that the variance should be entirely determined by photonic shot noise, Δp_{shot}. This expected shot noise equals the square root of the average detected photon number per pixel, $\bar{N}$ [1]. The relationship between these (independent) noise sources is:

$$(\Delta p_{\mathrm{tot}})^2 = (\Delta p_{\mathrm{cam}})^2 + (\Delta p_{\mathrm{shot}})^2 = (\Delta p_{\mathrm{cam}})^2 + \bar{N}. \tag{2.42}$$

We then attributed any deviation from perfect shot noise scaling to optoelectronic noise in the camera. We mention that additional intensity fluctuations may be due to laser noise; however, by attributing all noise to the camera electronics, we ensured that we give the most conservative estimate for the camera performance. At a pixel filling ratio of 77% (with respect to the FWC), the noise performance of the Xenics Wildcat 640 camera is merely 10.7% above the fundamental photonic shot noise (Fig. 2.13). This significantly surpasses the noise ratio between an ideal classical and ideal two-photon quantum sensor (41%). Thus, the camera can be used as an intensity detector for sub-shot noise quantum sensing. Due to the camera's additional noise Δp_{cam} the highest achievable phase sensitivity enhancement factor for the quantum sensor is reduced from $\mathrm{Enh}_{\mathrm{ideal}} = \sqrt{2}$ to:

$$\mathrm{Enh}_{\mathrm{real}} = \sqrt{\frac{(\Delta p_{\mathrm{shot}})^2 + (\Delta p_{\mathrm{cam}})^2}{\left(\frac{1}{2}\Delta p_{\mathrm{shot}}\right)^2 + (\Delta p_{\mathrm{cam}})^2}} \tag{2.43}$$

For the Xenics Wildcat 640 camera, this means that the maximum achievable enhancement factor with an ideal quantum sensor is $\mathrm{Enh}_{\mathrm{real}} = 1.300 = 0.919 \cdot \sqrt{2}$. The benchmarking of the Hamamatsu C14041-10U camera resulted in similar results. At a pixel filling ratio of 67% (FWC of 600 kcounts), the measured noise is 11.0% above the photonic shot noise limit; thus, quantum sensing with our scheme can still result in performances below the classical shot noise limit. The maximally-achievable quantum enhancement factor is then $\mathrm{Enh}_{\mathrm{real}} = 1.298 = 0.917 \cdot \sqrt{2}$ [1].

We, therefore, constitute that InGaAs cameras can be used for sub-shot noise quantum sensing, provided that pixel counts are in the range of $\sim 60 - 80\%$ of the FWC. After confirming that each pixel can perform sub-shot noise measurements, we estimated how many pixels have to be illuminated in a second step. First, we considered a photon-pair beam with a power of $P = 300$ at a center wavelength of $\lambda_0 = 1064\,\mathrm{nm}$. The photon

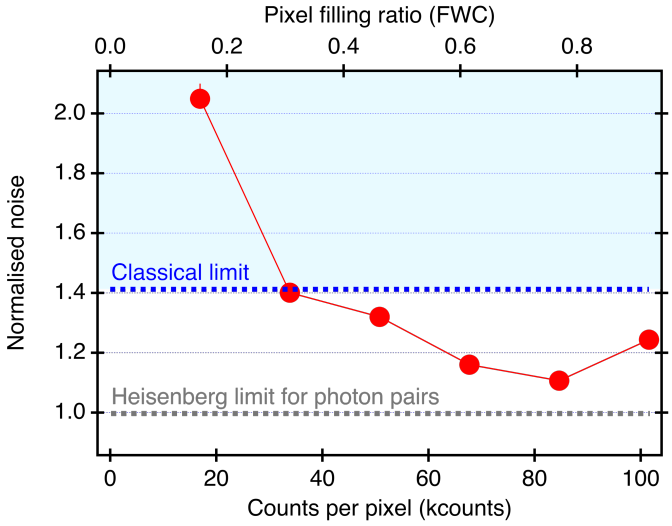

Figure 2.13: **Noise determination of the Xenics Wildcat 640.** Measured total noise normalized to the fundamental photonic shot noise as a function of the counts per pixel. The full well capacity (FWC) of the camera is 110 kcounts. At a pixel filling ratio of 77%, the measured noise is merely 10.7% above the photonic shot noise limit, which, for our sensing scheme, corresponds to the Heisenberg limit for two-photon phase sensing. An ideal classical sensor would have to measure twice as many photons to acquire the same phase information, thus leading to $\sqrt{2}\times$ higher noise. Red dots are data points, lines are a guide to the eyes. Adapted from [1].

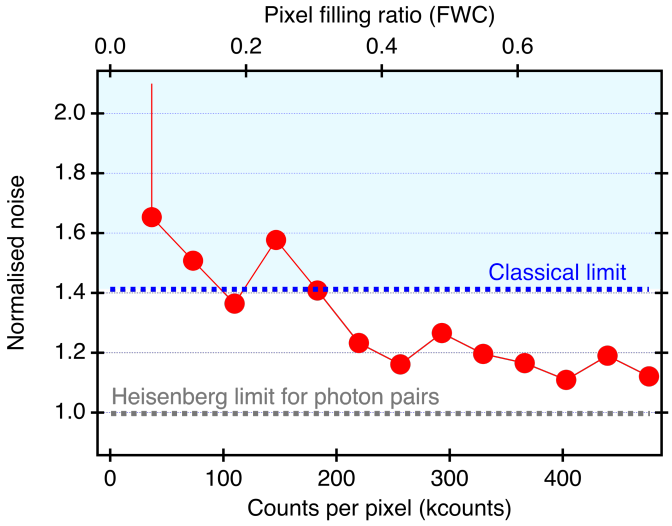

Figure 2.14: **Noise determination of the Hamamatsu C14041-10U.** Measured total noise normalized to the fundamental photonic shot noise as a function of the counts per pixel. The full well capacity (FWC) of the camera is 600 kcounts. At a pixel filling ratio of 67%, the measured noise is merely 11.0% above the photonic shot noise limit, which, for our sensing scheme, corresponds to the Heisenberg limit for two-photon phase sensing. An ideal classical sensor would have to measure twice as many photons to acquire the same phase information, thus leading to $\sqrt{2}\times$ higher noise. Red dots are data points, lines are a guide to the eyes.Adapted from [1].

rate is given by $R = \frac{P\,\lambda_0}{h\,c}$ in which $h = 6.62607 \cdot 10^{-34}\,\mathrm{Js}$ is Planck's constant and $c = 299792458\,\frac{\mathrm{m}}{\mathrm{s}}$ is the speed of light. We obtain then $R = 1.61 \cdot 10^{12}\,\mathrm{s}^{-1}$. Note, that in our sensing scheme, only half of the photons that interact with the sample are actually sent to the detectors. The remaining photons are split 50/50 between both detectors (camera). Thus, each camera receives, in average, $R_{\mathrm{cam}} = 4.02 \cdot 10^{11}\,\mathrm{s}^{-1}$ photons. At a frame rate of 100 Hz, this corresponds to $R_{\mathrm{frame}} = R_{\mathrm{cam}}/100\,\mathrm{Hz} = 4.02 \cdot 10^{9}\,\frac{\mathrm{photons}}{\mathrm{frame}}$. Due to the limited quantum efficiency of the cameras (about 60% for both cameras), the detected number of photons per frame is $R_{\mathrm{det}} = 0.6 \cdot R_{\mathrm{frame}} = 2.41 \cdot 10^{9}\,\frac{\mathrm{photons}}{\mathrm{frame}}$. These photons now need to be distributed across several pixels, such that the pixel counts fall in the range of $\sim 60 - 80\%$ of the FWC.
The best performance for the Xenics Wildcat 640 camera was shown for 77% FWC (110 kcounts); thus, in an ideal situation, 28,457 pixels are illuminated, corresponding to a circle with a diameter of 190 pixels. With a total sensor area of 640×512 pixels, a single Xenics Wildcat 640 camera could be conveniently used as the two intensity detectors.
The Hamamatsu C14041-10U performed best at 67% FWC (600 kcounts). Here, the ideal situation would thus be to illuminate 5996 pixels, or in other words, a circle with a diameter of 87 pixels. The Hamamatsu C14041-10U provides 320×256 pixels; therefore, this camera could also be used to replace two detectors.
Note that all pixels would have to be illuminated relatively homogeneously to achieve 60-80% filling of the FWC. This can be accomplished by beam-shaping optics that allow obtaining a flat top beam. Further, both tested cameras are additionally available with increased sampling rate capabilities (Wildcat 640: $220 - 500\,\mathrm{Hz}$; C14041-10U: 214 Hz). This would allow the development of a quantum-enhanced interference microscope in which images of biological samples could be obtained with pixel integration times down to 2 ms.

2.3 Conclusion and outlook

In this chapter, I introduced the basic working principle of our quantum sensor. It could be shown that the experimental setup is quite simple, and even highly sophisticated parts like the wavelength-selective waveplate or the adjustment of the temporal indistinguishability can be solved using simple commercially available optical elements. The here presented spectral filter scheme leads directly to two advantages. First, a noise reduction of a phase-sensitive measurement is possible, which results in a measured enhancement factor beyond the standard quantum limit of 1.13 ± 0.02, and second an independency to loss of the enhancement factor outside of the interferometer.
Further, we could demonstrate that the sensor can operate simultaneously over the broad sampling rate regime of 200 Hz up to 100 kHz, which is so far only limited by the photon-pair flux and a non-perfect decoupling from the environment and relating to that low-frequency drifts. Additionally, due to its single-photon characteristic, a similar detection scheme as in classical interferometry can be applied, allowing the same opportunity to cancel out common mode noise.

In a subsequent section, I introduced further measurements concerning a commercial solution to the sub-shot noise detection of photon-pair fluxes in the order of several 100 nW, which paves the way to higher absolute sensitivities and higher sampling rates. Finally, in the next chapter, we will build up on the demonstration of an enhancement over the entire audio band by developing a quantum optical microphone in the audio band. With the simultaneously enhanced sensitivity of signals of different frequencies (between 200 Hz and 20 kHz), I will present in the next chapter the superiority of recordings performed with the here presented quantum sensor directly compared with an almost perfect classical sensor. Here, I will not only show a higher signal-to-noise ratio (SNR) but also a better understandability of recorded words with the quantum sensor compared to its classical counterpart (evaluated by a medically approved speech recognition test).

Chapter 3

Quantum microphone in the audio band

In this chapter, I will present the development of a quantum optical microphone in the audio band. This example experiment shows the easy applicability of our nonlinear interferometry scheme. In the previous section, I could already show that the enhancement of the quantum sensor covers the complete audio band (200 Hz and 100 kHz), in which the human voice appears. Therefore, recording human language, requiring multiple frequency contingents at the same time, is possible.
Over this complete frequency regime, the quantum sensor possesses an almost constant enhancement factor of 1.13 ± 0.02 (beyond the standard quantum limit). Here, I present a nonlinear interferometer working (so far) up to 100 kHz and thus outperforming similar application relevant experimental realizations by more than four orders of magnitude [31, 32, 64]. Additionally I can demonstrate its easy applicability by the realization of a quantum optical microphone in the audio band, which shows an enhancement not only in the signal-to-noise ratio (SNR) of the recorded words but also a perceivable enhanced understandability of the recordings.
The first part of this chapter will cover the characterization of the used speaker and the mirror membrane. Here, I will first justify the choice of the used speaker and then introduce the final design of our mirror membrane, manufactured under collaboration with the Max Planck Institute for solid state research in Stuttgart. In the case of the mirror membrane, a characterization of the frequency response and the reproducibility of the membrane placement will be demonstrated.
Capitalizing on that, we introduce two medically approved speech recognition tests, the Freiburger speech test, and the Oldenburger sentence test. After a comparison, we will go into detail of how the Oldenburger sentence test (OLSA) is performed.
In the following chapter, the extraction of the signal-to-noise ratio from the recordings will be described. Here, an enhancement factor of 1.10 ± 0.04 can already be achieved, proving that the recordings obtained by the quantum sensor indeed show an enhanced signal-to-noise ratio compared to the classical sensor. With the results of the previous chapter, we calculated the minimum sample size needed to reach statistical significance with the OLSA.
Finally, we will present the raw results of the OLSA, and introduce the speech recog-

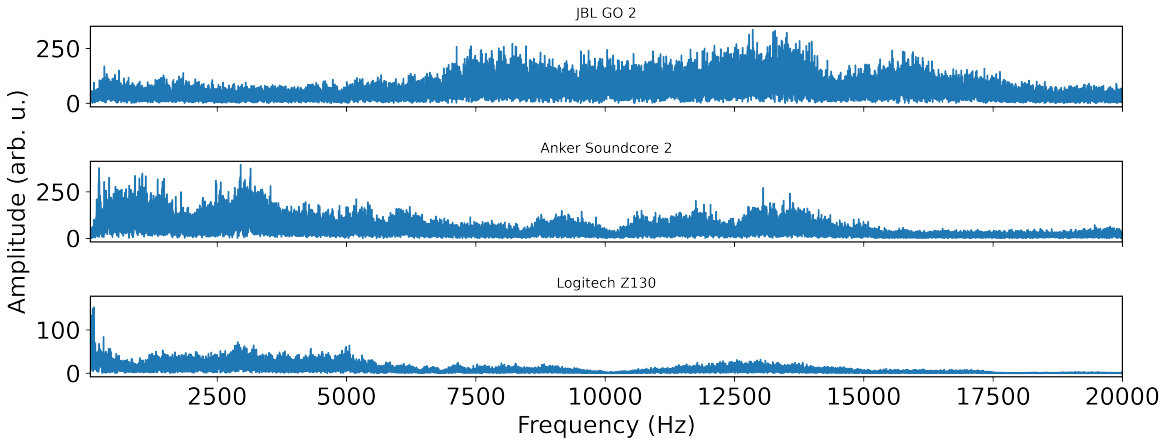

Figure 3.1: **Fourier spectrum of available speakers. a**, Fourier spectrum of the speaker JBL Go 2. **b**, Fourier spectrum of the speaker Anker Soundcore 2. **c**, Fourier spectrum of the speaker Logitech Z130.

nition threshold value and the the speech recognition test results. With these results we are able to present a reduction of the speech recognition threshold of $0.57\,\mathrm{dB_{SPL}}$ with a standard deviation under the square root law of $0.22\,\mathrm{dB_{SPL}}$. Furthermore, a standard statistical test, a one-sided t-test rejects the hypothesis: "The quantum microphone does not lead to an improvement."with a p-value below the common threshold of $p = 0.5$. Thus we can state confidently that we made the quantum effect perceivable by human beings. The here presented work was already published in [1].

3.1 Speaker analysis

A suitable speaker had to be found to play sounds and later words, that will be measured by our quantum sensor. As a framework condition, we targeted an as linear as possible frequency response over the entire audio band between 200 Hz and 20 kHz. As a selection of speakers, we chose three speakers from different manufacturers: JBL GO 2, Anker Soundcore 2, and Logitech Z130.
For measuring the Fourier spectrum of these speakers we used a calibrated measurement microphone (RG-20-PC) from Roga-Instruments, with a sufficient linear frequency response for frequencies between 50 Hz and 20 kHz of $\pm 1.5\,\mathrm{dB}$ [156]. With each speaker, we played white noise of frequencies between 50 Hz and 20 kHz at the same volume and recorded the resulting amplitude with the calibrated measuring microphone. Fig. 3.1 shows the Fourier spectrum of the three different speakers.
Due to its linear amplitude and especially its relatively high amplitude at high frequencies, we decided to use the JBL Go 2 for the measurements of the quantum and classical microphones. Note that we used an equalizer to adjust the combined frequency response of our microphone membrane and the speaker to be as linear as possible for a more precise analysis of the linearity.

3.2 Mirror membrane

To convert the quantum sensor to a quantum optical microphone, the primary change was the replacement of one of the retro-reflecting mirrors (sample mirror SM in Fig. 2.5) in the interferometer with a suitable mirror membrane. Our requirements for this mirror membrane have been, on the one hand, linearity of the response to soundwaves of different frequencies and amplitudes (frequency response) and, on the other hand, a high reflectivity to keep losses at a minimum level.
In this chapter, I will first present different strategies to design such a mirror membrane. In the second part, I present measurements of the longitudinal displacement to sound pressures of different amplitudes and frequencies to benchmark the mirror membrane.
In the last part, I present measurements concerning the reproducibility of the placement of the mirror membrane. The quantum and the classical sensor resemble two different experimental setups. To minimize further differences, the same mirror membrane was used for the recordings of both the classical and quantum sensors. Therefore, a verification was necessary, that the placement and replacement of the mirror membrane does not affect the recordings.

3.2.1 Membrane design

Designing a suitable mirror membrane proved to be more difficult than expected. In the search for a suitable mirror membrane, we underwent multiple collaborations with the glass workshop at the University of Stuttgart, Daniil Lukin of the group of Prof. Dr. Jelena Vučković from Stanford University, and Annette Zechmeister and Barbara Baum from the Max Planck Institute for Solid State Research.
A first approach, to grind down a standard dielectric mirror from Thorlabs (BB1-E03) at the glass workshop of the University of Stuttgart from the backside, proved unsuccessful. During the grinding process, the dielectric surface was compromised, leading to visible cracks and therefore impaired reflectivity.
Following the same approach, Annette Zechmeister and Barbara Baum from the Max Planck Institute for Solid State Research were able to preserve the coating. While still maintaining its high reflectivity, another effect occurred. Every dielectric mirror, which has been grinded down, showed a certain curvature impairing the unaffected retroreflection of the photon pair flux. While maintaining the high reflectivity, a proficient mode overlap could not be ensured. This curvature of the mirror membrane could be assigned to different lattice structures of the dielectric coating material and the underlying substrate. For the standard dimensions of the mirrors, the substrate proves to be strong enough to hinder the tension from deforming the surface. For several hundreds of micrometers thickness, the tension between these two layers leads to the observed curvature of the thin mirror membrane. Due to the irregularity of the bending, the adjustment of our sensor using these mirror membranes proved impossible.
A newly initiated collaboration with a Ph.D. student from the group of Prof. Dr. Jelena Vučković, experienced in crystal processing, led to new ideas and a new generation of grinded mirror membranes. Several approaches to flatten the thin mirror membranes have been taken to counteract the still occurring bending. But neither

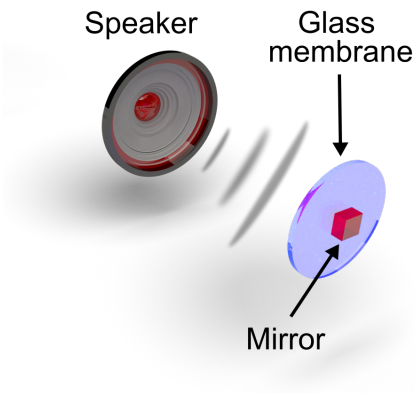

Figure 3.2: **Final design of the mirror membrane.** A glass membrane with 12.7 mm diameter and 70 µm thickness translates acoustic pressure waves into a physical displacement. Photons are reflected by a small dielectric mirror that is glued on the membrane (mirror size 2x2x0.5 mm^3). Adapted from [1]

gluing the mirror membrane to a flat surface nor clamping it in a suitable holder and stretching it proved to solve this issue.
Still facing these issues, we decided to try a completely different approach. The following design idea was to use a membrane and attach a small mirror piece onto it. The idea was to have an underlying substrate sensitive enough to sound waves and a mirror piece with a high reflectivity thick enough that it does not bend.
We again approached Annette Zechmeister and Barbara Baum from the Max Planck Institute for Solid State Research for the fabrication of the mirror pieces. The manufacturing of mirror pieces of different sizes (2x2x0.5 mm^3 and 2x2x1 mm^3) proved to be without further setbacks.
For the underlying substrate, we decided to try different approaches. Two ideas were tested first, the usage of the membrane of a commercially available microphone and second, a thin glass plate of some tens of micrometers. The microphone membrane proved too thin to handle the mirror piece's weight, resulting in an extremely challenging adjustment of the mode overlap. Finally, as a suitable mirror membrane, the design using a thin glass plate of 70 µm, which provides a compromise between responsiveness to sound waves and still a high enough stability to carry the attached mirror piece, has been found.
In Fig. 3.2 the ultimate design of the mirror membrane is presented. On a 70µm thick glass plate a 2x2x0.5 mm^3 is glued. The glass plate provides responsiveness to sound waves, while the mirror piece maintains its reflectivity. For the implementation into our sensor, we glued the mirror membrane onto a donut-shaped holder. This holder had an outer diameter of 25.4 mm and an inner diameter of 10.0 mm.

3.2.2 Frequency response of the mirror membrane

As a first characterization of the mirror membrane, we measured the longitudinal displacement as a function of the applied sound pressure level. To determine the displacement of the mirror membrane, a classical Michelson interferometer scheme has been used. To reduce the impact of noise, we used a standard photodiode (Thorlabs PDA10CS-EC) and 300 µW laser power, which was separated from a Coherent Verdi V18 at 532 nm running at full power (18 W).
To measure the longitudinal displacement, we applied sinusoidal signals at different frequencies and sound pressure levels to the mirror membrane. From the resulting change in the interferometer signal we then obtained the mirror membrane's displacement. We chose signals at frequencies between 200 Hz and 22 kHz. Up to 6578 Hz these frequency values are logarithmically scaled, followed by a linear scaling up to 22 kHz, avoiding multiples of the power line frequency of 50 Hz.
Each line in Fig. 3.6 corresponds to a measurement of the longitudinal displacement for different sound pressure levels in $\mathrm{dB_{SPL}}$ for a single sinusoidal frequency.
Up to $-9\,\mathrm{dB_{SPL}}$ the longitudinal displacement shows a linear behavior. Note that 97.8% of all SRT values of the OLSA of the quantum and 93.3% of the SRT values of the OLSA of the classical sensor lie below this sound pressure value (see section 3.7).
To define linearity, we fitted each curve with a linear fit. Measurements where this fit showed an average value of the absolute of the residuals larger than 0.25, were defined as not sufficiently linear. Note that outliers were mainly defined by their values above $-14\,\mathrm{dB_{SPL}}$, which proved to have little relevance for the audiology test. For measurements not fulfilling this linearity criterion, the fitting range was adjusted.
The linear fit up to $-9\,\mathrm{dB_{SPL}}$ (adjusted if non-linear) gave access to two interesting values. First, the offset/intercept shows the amplitude of the response for each frequency and, therefore shows the frequency response's linearity, which we already introduced in Chapter 3.1. As a second parameter the slope of each fit gives access in the linearity of the response as a function of the applied sound pressure level in $\mathrm{dB_{SPL}}$. For a perfect membrane, we expect no difference between the frequencies for the intercept, because the perfect membrane would respond with the same amplitude independent of the frequency with which the sound wave is applied. Furthermore, a perfect membrane would show a slope equal to unity, independent of the frequency.
In Fig. 3.4a the slope values of all fits are plotted as a function of the frequency. The average value of $\mu = 1.01 \pm 0.09$ is in excellent agreement with a perfect mirror membrane. In Fig. 3.4b, the intercept of each fit is plotted as a function of the frequency, showing non-perfect linearity of the response. Even though the response proved not perfectly linear, it is still comparable to the frequency response of commercially available microphones. Even more, recorded test samples proved to be understandable. Thus this mirror membrane shows sufficient linearity for recording human speech.
Even more test recordings with this design proved to be understandable (tested with commercially available headphones in an office environment), thus satisfying our requirements for a suitable mirror membrane.
With these findings, the chosen mirror membrane design met our requirements and could be implemented into our quantum sensor and the classical counterpart, respectively.

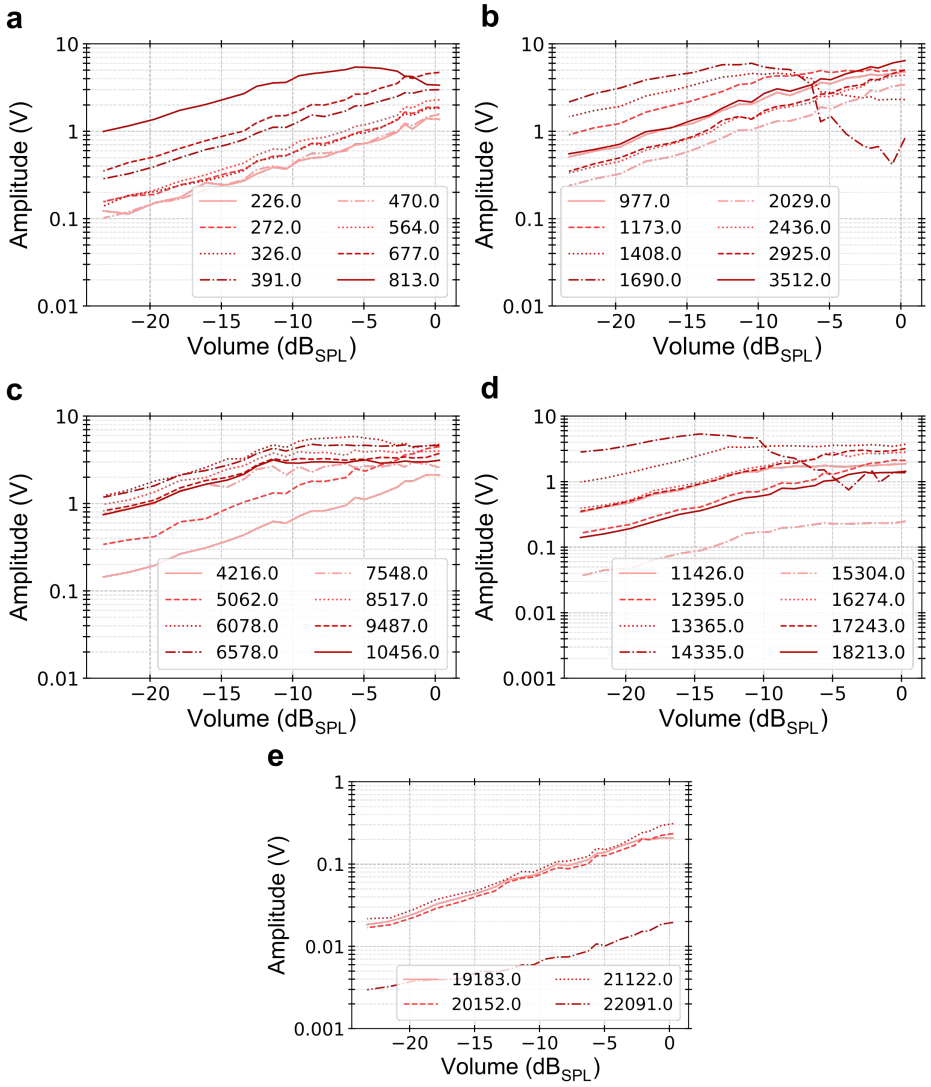

Figure 3.3: **Lateral displacement.** Lateral displacement measured with a classical interferometer. Each line represents a measurement of the displacement for different sound pressure levels (dB_{SPL}) for one single sinusoidal frequency. The frequency is up to 6578 Hz on a logarithmic scale, following a linear scaling up to 22091 Hz, avoiding multiples of the utility frequency of 50 Hz. Adapted from [1]

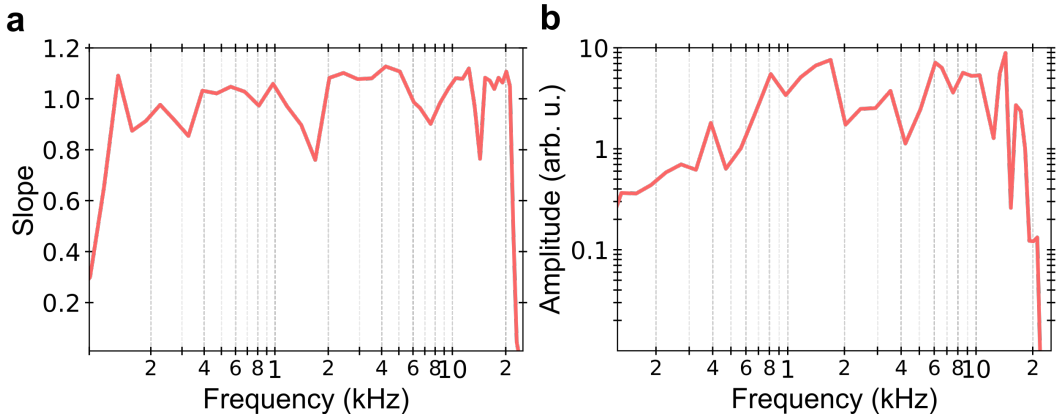

Figure 3.4: **Slope and intercept of the linear fit. a**, Shows responsiveness (slope) of the data shown in Fig. 3.6 in a logarithmic scale. The average over all frequencies is $\mu = 1.01 \pm 0.09$. **b**, Shows the strength of displacement (intercept) for each frequency, and thus a sufficient linear frequency response between 200 and 15,000 Hz almost up to 20,000 Hz. Adapted from [1]

3.2.3 Reproducibility of membrane placement

The same mirror membrane was used for the classical and the quantum sensor recordings. To ensure that the placement of the mirror membrane has no measurable effect we further characterized the mirror membrane placement reproducibility. For this, we placed and replaced the mirror membrane multiple times into the classical and the quantum sensor and measured the frequency response for single frequency sinusoidal signals between 50 Hz and 20,000 Hz (see Fig. 3.5a/b).
The experimental parameters (visibility, photon number, ...) have been kept identical for each measurement. For each sensor, we performed five iterations of mirror membrane (re)placement. Fig. 3.5a and b show the results of all five iterations. In Fig. 3.5c and d, the standard deviations between all five iterations for each frequency step are presented in percent for the classical (c) and the quantum sensor (d), respectively. It is visible that for the classical and the quantum sensor, the placement has little influence (1.26% (mean value of the standard deviations) for the classical and 3.49% for the quantum sensor; Fig. 3.5c/d). To further investigate the reason for the deviation between the iterations, we captured for each measurement and iteration the photon number for each sensor (Fig. 3.5e/f). For the photon numbers, the uncertainty (standard deviation) between the iterations is 0.65% for the classical and 3.37% for the quantum sensor. We assign these uncertainties mainly to thermal fluctuations in both sensors, which was not completely avoidable. A manual adjustment of the setup after the (re)placement of the mirror membrane has been necessary to achieve reproducible visibilities and photon numbers. The quantum sensor's complexity and accompanying longer adjustment time introduced more thermal induction, which is reflected in the higher uncertainty in the photon number.
With this in mind, we can calculate the (re)placement effect by taking the photon number uncertainty into account. To calculate this corrected uncertainty (for two

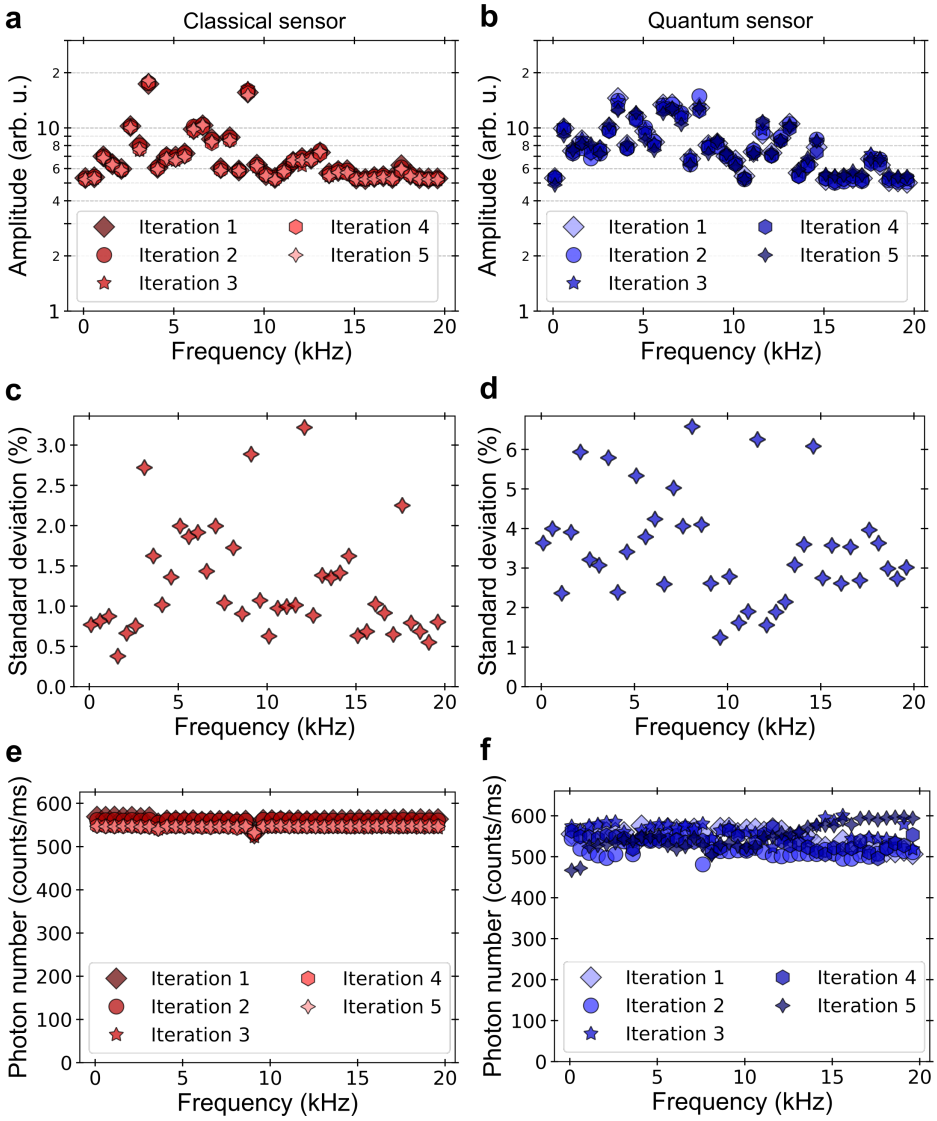

Figure 3.5: **Mirror membrane placement reproducibility.** **a**, Measurement of the longitudinal amplitude for repeated placement of the mirror membrane for **a** the classical and **b**, the quantum sensor. **c**/**d**, The standard deviation for each frequency step in percent (classical sensor **c**, mean value = 1.26% and quantum sensor **d** mean value = 3.49%). **e**, Photon number for each frequency and (re)placement step for the classical sensor (mean standard deviation: std = 0.65%) and **f** for the quantum sensor (standard deviation: std = 3.37%). Adapted from [1]

independent uncertainties with normal distributions), the formula [53]:

$$\Delta_{\text{corr}} = \sqrt{\Delta_{\text{total}}^2 - \Delta N^2} \tag{3.1}$$

with ΔN the fluctuation in the photon number, Δ_{total} the total noise and Δ_{corr} the corrected uncertainty, can be used. This leads to a value of $\Delta_{\text{corr, quantum}} = 0.91\%$ and $\Delta_{\text{corr, classical}} = 1.08\%$.
All together, for either the uncorrected or the corrected values, the uncertainty of replacing the mirror membrane and its holder proves to be well below the expected enhancement of approximately 13%.

3.3 Speech recognition tests

Audiometry is the field of investigating and evaluating parameters concerning the ability to hear sound or understand words and sentences. Often these tests are used to identify hearing loss or diseases.
There are active and passive tests, where for the active, contrary to the passive case, the cooperation of the test subject is required.
In the following, we will focus solely on the active audiometry tests. Additionally to active and passive tests, there is also a discrimination between tests solely measuring the ability to hear sound and so-called speech recognition tests, which try to be closer to reality and measure the ability to understand words or sentences in a noisy environment. An example of the first case is the pure tone audiometry test, in which a certain range of single frequency signals are played at different sound pressure levels, and the hearing threshold of the test subject is recorded.
For the second case, speech recognition tests, there are many different examples, so we solely focus here on two tests that are certified for the use in German healthcare [157], namely the Freiburger Sprachtest (Freiburger speech test) and the Oldenburger Satztest (OLSA; Oldenburger sentence test).

3.3.1 Freiburger speech test

To find the most informative test for the understandability of words, Karl-Heinz Hahlbrock invented the Freiburger speech test [158]. The Freiburger speech test consists of two different tests, the number test (Freiburger Zahlentest) and the monosyllabic test (Freiburger Einsilbertest). The number test consists of ten groups containing ten double-digit numbers with two or more syllables [158, 159].
The monosyllabic test consists of 400 monosyllabic substantives chosen by their general comprehensibility and occurrence in the German language [158, 159]. Additionally, the words of each group were chosen to minimize the phonetic difference between the groups [159, 160].
Since 1995 this test has been embedded in the DIN Standard [161], a voluntary national, European and international standard for material and immaterial objects [162]. DIN Standards are defined by manufacturers, consumers, businesses, research institutes, public authorities and testing bodies and are regularly reviewed at least every five years [162].

Even though this test is still a medical standard, it is not entirely undisputed and is perceived by some sources as partially inhomogeneous, or even imprecise [163–166].

3.3.2 Oldenburger sentence test

The Oldenburger Sentence Test (OLSA) is an audiometric test using whole sentences instead of single words [167–169]. Its goal is to determine the so-called speech recognition threshold (SRT) in a quiet or noisy environment. The speech recognition threshold (SRT) is defined as a sound pressure level in decibel at which 50% of a speech material is understood correctly.
As speech material for the OLSA, 120 sentences of the sequence
Name – Verb – Number – Adjective – Subject are used. These sentences consist of a random combination of 50 different words (Table 3.1). These words were carefully chosen for their phonetic homogeneity. The standard deviation for the SRT between all 120 sentences is only $0.16\,\mathrm{dB_{SPL}}$ [169]. The OLSA was specifically designed so that the training effect of the memorization of the already heard words for multiple repetitions is between 1 and $2\,\mathrm{dB_{SPL}}$. If a single OLSA test is carried out beforehand, this value can be further reduced below $1\,\mathrm{dB_{SPL}}$. Another advantage of the OLSA is its high precision leading to a slope of $17.1\,\%/\mathrm{dB_{SPL}} \pm 1.6\,\%/\mathrm{dB_{SPL}}$, here % is defined as the percentage of understood words. Due to this calibration, the precision of the OLSA test concerning the SRT is estimated as $1\,\mathrm{dB_{SPL}}$. With a measured enhancement in the sensitivity of $1.13 \mathrel{\widehat{=}} 1.06\,\mathrm{dB_{SPL}}$, slightly higher than the estimated precision of $1\,\mathrm{dB_{SPL}}$, the OLSA is a suitable test to demonstrate the superiority of our quantum optical microphone. Although this factor is only slightly higher than the precision of the OLSA, we still expect to be able to resolve the enhancement. Even if we cannot measure a better microphone performance for every single OLSA, we still expect to see the average enhancement over a couple of OLSA tests. Furthermore, we will prove the significance of this enhancement by a standard statistical test (see section 3.9)
Even though the OLSA is a matrix test adapted to German native speakers, derivates are available for other languages [170].

Table 3.1: **OLSA word matrix.** Word matrix with which the 120 sentences of the OLSA are formed. For creating a sentence one word out of each column is randomly chosen and the resulting words assembled. Example sentence: Peter Gibt Acht Weiße Bilder (Peter gives eight white pictures).

Britta	Bekommt	Zwei	Alte	Autos
Doris	Gewann	Drei	Große	Bilder
Kerstin	Gibt	Vier	Grüne	Blumen
Nina	Hat	Fünf	Kleine	Dosen
Peter	Kauft	Sieben	Nasse	Messer
Stefan	Malt	Acht	Rote	Ringe
Tanja	Nahm	Neun	Schöne	Schuhe
Thomas	Schenkt	Elf	Schwere	Sessel
Ulrich	Sieht	Zwölf	Teure	Steine
Wolfgang	Verleiht	Achtzehn	Weiße	Tassen

3.3.3 Execution of the OLSA.

Prior to the OLSA test, each test subject had to verify a normal hearing. We ensured this by performing prior to the OLSA test a pure tone audiometry test in a special soundproof room at the Department of Pediatric Audiology and Neurotology of the Olgahospital in Stuttgart, by the kind permission of Dr. Rüdiger Boppert.
After the confirmation of a normal hearing of each test subject, two OLSA tests were performed in the same location, one using the recordings of the classical and the other using the recordings of the quantum optical microphone.
The standard procedure of the OLSA is to play a sentence containing five words to a test subject, who has to repeat the sentence. Dependent on the targeted precision, this procedure is repeated several times [167–169]. The measurement of the OLSA is done adaptively. This means after each sentence, the sound pressure level (in the OLSA expressed in dB_{SPL} of the signal-to-noise-ratio) will be adapted, dependent on the number of understood words. After 30 repetitions (for a precision of $1\,dB_{SPL}$) the last 20 values of the SNR are averaged [167–169]. The resulting value represents the so-called speech recognition threshold (SRT). The SRT defines the SNR value at which the test subject can understand 50 percent of all the played words.
In the standard case, the noise level is set constant, and the signal level is adapted as defined in (Table S3.2). There are two ways to carry out the OLSA. In the first version (the open test), the test subject has no knowledge of the words forming the sentences, and in the second version (closed test), the test subject has access to all 50 words but not the possible sentences formed out of them. These test methods mainly differ in the test duration [171].
For the determination of the SRT after the completion of the OLSA, the average of the last 20 measured SNR levels is calculated and the noise floor subtracted. This noise floor consists of the superposition of all used words [167–169]. To avoid the influence of a learning effect, the order in which the different OLSA tests were performed was randomized.

Table 3.2: **SNR adaption of the original OLSA.** Level change of the signal to noise ratio (SNR) dependent on the number of correctly understood words of the previous sentence of the original OLSA.

Correctly understood words of the previous sentence	Sentence 2 to 5	Sentence 6 to 31
5	$-3\,\mathrm{dB_{SPL}}$	$-2\,\mathrm{dB_{SPL}}$
4	$-2\,\mathrm{dB_{SPL}}$	$-1\,\mathrm{dB_{SPL}}$
3	$-1\,\mathrm{dB_{SPL}}$	$0\,\mathrm{dB_{SPL}}$
2	$+1\,\mathrm{dB_{SPL}}$	$0\,\mathrm{dB_{SPL}}$
1	$+2\,\mathrm{dB_{SPL}}$	$+1\,\mathrm{dB_{SPL}}$
0	$+3\,\mathrm{dB_{SPL}}$	$+2\,\mathrm{dB_{SPL}}$

3.3.4 Changes in the OLSA.

To help the test subjects to become familiar with the words used in the OLSA, the closed version of the OLSA has been performed. Further, to carry out the OLSA with the recorded words of the classical and quantum sensor, an adaption of the initial OLSA has been necessary. The records of the classical and quantum sensor, contain intrinsic noise (photonic shot noise), which is planned to replace the noise signal of the original OLSA.
We, therefore, developed a python script following the same procedure as the original OLSA in terms of conduction but exchanging the original sound files with the files recorded with the classical or the quantum sensor for different sound pressure levels. To still guarantee performance as close to the original OLSA as possible, we chose a four-stage adaption of the SNR dividing the second step (see 'Sentence 6-31' in Table 3.2) into three steps slightly higher and lower than the original step size (Table 3.3), defined by the discrete step size of the digital signal output of the speaker and thus the SNR. The adjusted step sizes (Table 3.3) deviate barely from the original values (Table 3.2).

Table 3.3: **SNR adaption of the original OLSA.** Level change of the signal to noise ratio (SNR) dependent on the number of correctly understood words of the previous sentence of the original OLSA.

Correctly understood words of the previous sentence	Sentence 2 to 5	Sentence 6 to 9	Sentence 10-19	Sentence 20-30
5	$-4.25\,\mathrm{dB_{SPL}}$	$-2.50\,\mathrm{dB_{SPL}}$	$-1.50\,\mathrm{dB_{SPL}}$	$-1.00\,\mathrm{dB_{SPL}}$
4	$-3.25\,\mathrm{dB_{SPL}}$	$-2.00\,\mathrm{dB_{SPL}}$	$-1.00\,\mathrm{dB_{SPL}}$	$-0.50\,\mathrm{dB_{SPL}}$
3	$-1.50\,\mathrm{dB_{SPL}}$	$1.00\,\mathrm{dB_{SPL}}$	$-0.50\,\mathrm{dB_{SPL}}$	$0.00\,\mathrm{dB_{SPL}}$
2	$+1.50\,\mathrm{dB_{SPL}}$	$1.00\,\mathrm{dB_{SPL}}$	$+0.50\,\mathrm{dB_{SPL}}$	$0.00\,\mathrm{dB_{SPL}}$
1	$+3.25\,\mathrm{dB_{SPL}}$	$+2.00\,\mathrm{dB_{SPL}}$	$+1.00\,\mathrm{dB_{SPL}}$	$+0.50\,\mathrm{dB_{SPL}}$
0	$+4.25\,\mathrm{dB_{SPL}}$	$+2.50\,\mathrm{dB_{SPL}}$	$+1.50\,\mathrm{dB_{SPL}}$	$+1.00\,\mathrm{dB_{SPL}}$

3.3.5 Photon number

The maximal sensitivity of the measurement of a phase difference between two paths of an interferometer is proportional to the square root of the photon number (and by a factor of the square root of two higher for a perfect quantum sensor; $1/\sqrt{N}$ and $1/\sqrt{2N}$ respectively). To exclude that the measured enhancement factor between the classical and quantum recordings is due to a difference in the photon numbers, we tracked the photon number for each of the 13,200 recorded words (see Fig. 3.6).
As in chapter 2 shown, our novel nonlinear interferometer contains a wavelength-dependent filter to filter out one of each photon of the, in the nonlinear crystal generated, photon pair. Thus without any losses and differences between the classical and the quantum sensor, we would expect to measure twice as many photons for the classical sensor. Furthermore, we presume that the classical sensor, used as a reference, resembles a perfect interferometer. This means adding to the factor of two, every loss inside of the quantum sensor further decreases the number of photons arriving at the detectors. As a result, we measured a mean photon number for all recorded words for the classical sensor of $2,579 \pm 36$ and for the quantum sensor $1,090 \pm 55$ photons per millisecond (see Fig. 3.6). In Fig. 3.6 it is well illustrated that the overall photon number stability (standard deviation) of the two measurements is different (1.4% for the classical and 5.0% for the quantum sensor).
As mentioned before, considering the number of photons measured for the classical sensor as a starting point, we expect to measure a lower photon number for the quantum sensor due to the implemented filter and losses. Taking the values of the filter (a factor of 2) and the in section 4 evaluated maximum value for losses of $1 - \eta = 0.26$ into account ($N_{qm} = (1 + \eta)/4 \cdot N_{cl}$), $1,122 \pm 16$ photons per ms are expected. This value differs only by 2.5% from the measured photon number of $1,094 \pm 55$ photons per ms and lies well within the error bars. The single outliers visible in Fig. 3.6 are mainly due to a not completely avoidable temperature change in the laboratory caused by a cycling air-conditioning system. Even though we avoided times of high-temperature fluctuations, some single measurements seem to be still affected. Due to the small number of outliers and the small deviation, we can exclude that the intensity deviation is the sole factor of the presented enhancement in the SNR.
These measurements confirm that the measured quantum enhancement is not due to an effective higher photon number in the quantum sensor.

3.3.6 Saturation of superconducting detectors

As discussed in section 4 twice the amount of photons hit the detectors in the case of the classical sensor. To exclude that saturation effects of the superconducting nanowire single-photon detectors (SNSPD, Photon Spot Inc. optimized for 1550 nm) influence the experiment, a short calibration was performed to investigate the linearity. Suppose both detectors show the same linearity in the measured photon number as a function of the pump power in the here presented photon number regime (0 to 2,579 for the classical and 0 to 1,122 photons per millisecond for the quantum sensor). In that case there is no parasitic influence of the detector efficiency, because a rise or drop in the photon number would correspond to the same input power change and therefore the same phase shift.

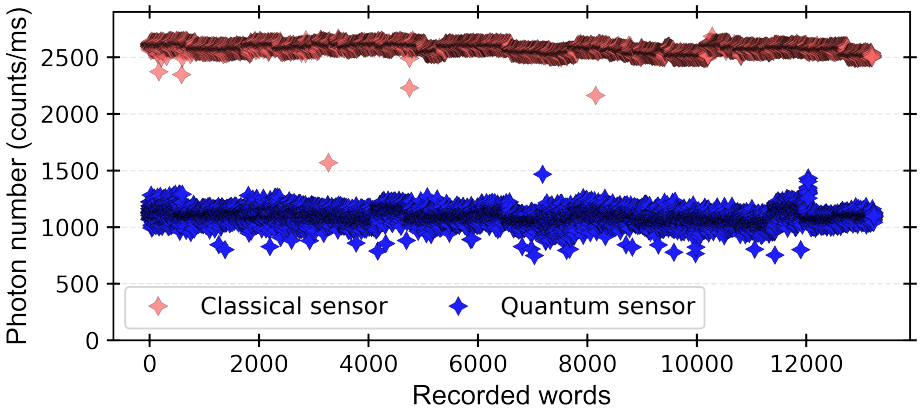

Figure 3.6: **Photon number stability.** The photon numbers for each recorded word for both measurements, the classical sensor (red), and the quantum sensor (blue). The standard deviations of the photon numbers are $\mathrm{std_c} = 1.4\%$ for the classical and $\mathrm{std_q} = 5.0\%$ for the quantum sensor. Adapted from [1].

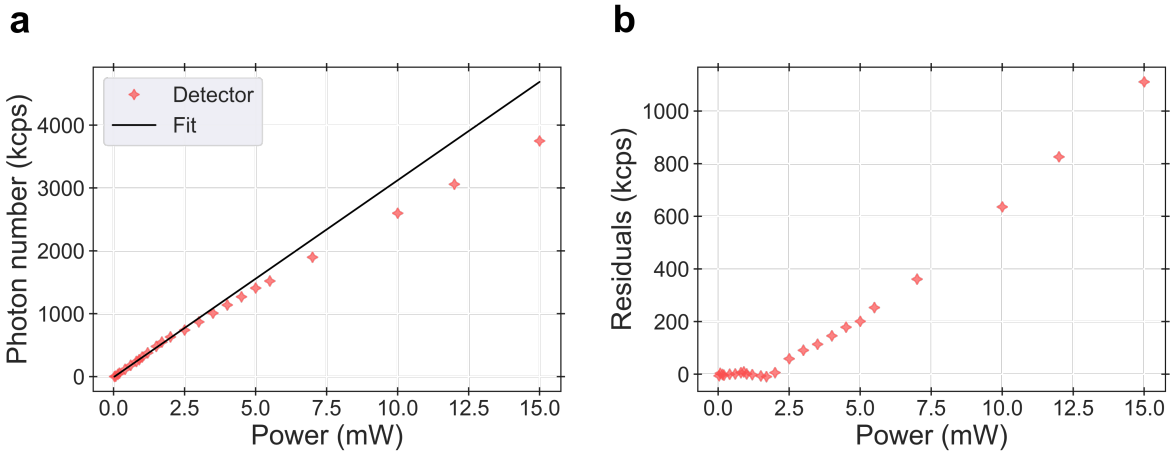

Figure 3.7: **SNSPD count rate as a function of pump power.** **a**, The count rate of the in this work used SNSPDs as a function of the pump power. To visualize linearity the first eight values were fitted by a linear fit function. **b**, The residuals of the fit applied in **a**. Up to approximately 630 kcps the SNSPD count rate shows a linear behavior (defined as residuals below 40 kcps).

To investigate the linearity as a function of the photon number, we measured the photon number of the SNSPDs as a function of the input (pump) power. For this measurement, we used the, in the experiment utilized, pump laser with a wavelength of 532 nm which was damped down to a single photon flux between zero and four million photons per second by neutral density filters.
The results of this measurement can be seen in Fig. 3.7a and b. Figure Fig. 3.7a shows the count rate of the SNSPD as a function of the pump power. Additionally, we applied a linear fit to the first eight data points. In Fig. 3.7b the residuals of this fit are presented. From both figures a linearity (defined as residuals below 40 kcps) up to 630 kcps can be demonstrated. Originally, for both sensor types, only two detectors with balanced illumination have been planned, thus resulting in photon count rates for the quantum sensor around 545 kcps and for the classical sensor around 1,290 kcps.
Capitalizing on these measurements, we splitted each detector of the classical sensor into two separate ones. Thus maximally 645 photons per millisecond hit each classical detector. For this count rate, a detection efficiency of 98.6% can still be reached (estimated with linear interpolation). Therefore, the difference for the detection efficiency with approximately 1% is negligible.
So by doubling the detector number for the classical sensor, we can exclude that the detection efficiency for different photon numbers of the SNSPDs will affect the enhancement factor.

3.3.7 Signal-to-noise extraction

To gain access to the recorded word's signal-to-noise ratio, we developed a process to extract the pure signal from the underlying noise. Extracting the signal from the underlying noise in the recordings taken by the quantum or classical microphone is a two-step procedure. In particular, the recordings consist of a part only containing the photonic shot noise, where no signal was applied, and a second part where the signal is overlying the noise (see Fig. 3.8). In the first step, we extract the recording part where only noise appeared. Here we take the temporal length of the original sound file (t_{original}) into account to obtain the exact time length of the recording. We then use the equation:

$$S_{\text{power}} = \frac{t_{\text{audio}}}{t_{\text{original}}} S_{\text{audio}} - \frac{t_{\text{audio}} - t_{\text{original}}}{t_{\text{original}}} S_{\text{noise}} \tag{3.2}$$

to extract the exact part of the recording which contains the signal with the underlying noise. Here t_{audio} is the total time of the recording and t_{original} the actual time of the recorded word (see Fig. 3.8). S_{audio} represents the root-mean-square (RMS) of the complete recording and S_{noise} the RMS of the part of the signal where no soundwave was applied (t_{noise}). Thus, this equation shows the full signal strength weighted with the length of the original audio file and recording length, and a subtracted part. Additionally, it is weighted with the length of the recording at which just noise is expected ($t_{\text{audio}} - t_{\text{original}}$). The result of this equation gives the RMS of the recorded word without the additional recorded noise.
Note that in this value still the noise and signal amplitude are superposed.

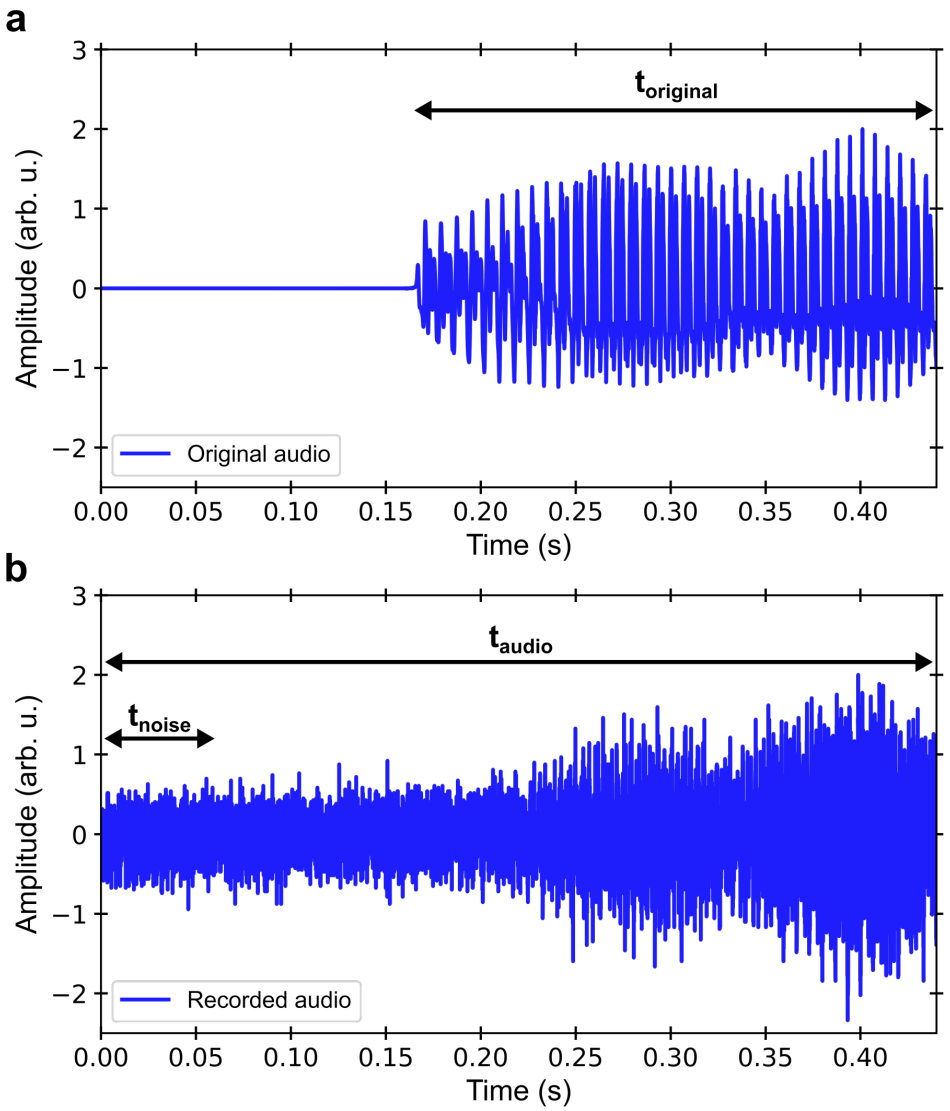

Figure 3.8: **Calculation of signal to noise ratio.** **a**, The original sound file with a sampling rate of 44, 100 Hz. t_{original} depicts the length of the signal. **b**, Recording of the quantum sensor sampled with 20, 000 Hz. Preceding to the actual recorded word the recordings with the quantum/classical sensor contain additionally a sequence with no applied signal, which is used to estimate the photonic shot noise. The length of the total recording is given by t_{audio}. Adapted from [1]

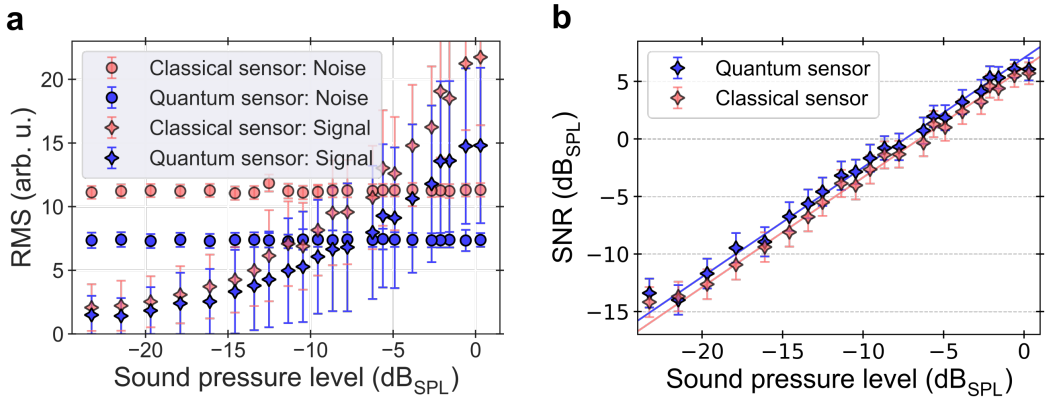

Figure 3.9: **Signal strength, noise and SNR.** **a**, The signal strength and the noise level for both sensors (blue: quantum sensor; red: classical sensor). For both sensors the horizontal data points depict the noise level averaged over all 600 recorded words for different signal strengths. The error bars are given by the standard deviation of all 600 recorded words. **b**, Calculated SNR for both detectors, using the data from a. The SNR of the quantum sensor is 1.10 ± 0.04 times higher than the SNR of the classical sensor. The fit function is a simple linear function of the form $\mathrm{SNR}_i = \alpha_i V_\mathrm{A} + \beta_i$, where α_i is the proportionality factor and β_i is the SNR at $V_\mathrm{A} = 0\,\mathrm{dB_{SPL}}$. Note that the values are fitted in $\mathrm{dB_{SPL}}$. The error bars in both plots are calculated using error propagation. Adapted from [1].

As a second step, we can access the pure RMS of the signal via the equation:

$$S_\mathrm{signal} = \sqrt{S^2_\mathrm{power} - S^2_\mathrm{noise}} \tag{3.3}$$

With the extracted signal (S_signal) and noise (S_noise) the calculation of the signal to noise ratio has been made possible (Fig. 3.9a,b). Fig. 3.9a shows both the noise and the signal strength for different sound pressure levels, and Fig. 3.9b the calculated SNR for both sensors. The error bars are the standard deviation over all 600 words.
Note that by the variety of the human language, each word consists of different compositions of rising or declining amplitudes. Thus the RMS of different words can show very diverse values, even though the understandability between the words is uniform.
The data in Fig. 3.9b was fitted by a linear function $\mathrm{SNR}_i = \alpha_i V_\mathrm{A} + \beta_i$, in which the subscript $i = \mathrm{c,q}$ denotes the classical and quantum microphone, α_i is the proportionality factor and β_i is the SNR at $V_\mathrm{A} = 0\,\mathrm{dB_{SPL}}$. The slopes of the sensors are $\alpha_\mathrm{c} = 0.95 \pm 0.02, \alpha_\mathrm{q} = 0.95 \pm 0.02$, confirming the same responsiveness of both sensors. However, the quantum microphones baseline SNR is higher, i.e., $\beta_\mathrm{c} = 6.20 \pm 0.22\,\mathrm{dB_{SPL}}$ and $\beta_\mathrm{q} = 7.04 \pm 0.20\,\mathrm{dB_{SPL}}$. This leads to an enhancement factor of $0.84 \pm 0.29\,\mathrm{dB_{SPL}}$ (equivalent to a factor of 1.10 ± 0.04) of the sensitivity of the quantum microphone compared to its classical counterpart.
As already shown in section 3.2.3 for single frequencies, these measurements show a linear dependency between the sound pressure level in $\mathrm{dB_{SPL}}$ and the SNR. Additionally, in Fig. 3.9 the enhancement of the quantum sensor is already visible as an offset in the SNR of the quantum sensor.
At this point, we could already state that our quantum optical microphone leads to an

enhanced recording of words by a factor of 1.10 ± 0.04 or by $0.84 \pm 0.29\,\mathrm{dB_{SPL}}$. Thus these results already prove the superiority of our quantum sensor in recording words or sentences.
Remarkably this enhancement is not only visible in the raw data of the recordings but also perceptible in a standard speech recognition test. In the following sections, the results of this test will be presented and an enhancement in the understandability will be verified by standard statistical testing.

3.4 Sample size

To ensure that we reach statistical significance, prior to conducting the OLSA, we performed a sample size determination calculation. As a first step, we determined the Cohen's d effect size using [3]

$$d = \frac{\bar{x}_1}{s}, \tag{3.4}$$

where $\bar{x}_1 = 0.84\,\mathrm{dB_{SPL}}$ is the mean value of enhancement in SNR of the recordings (see 5.3 Calculation of the SNR) and s the expected precision of the OLSA of $s = 1.41\,\mathrm{dB_{SPL}}$ [167–169]. The value of s was prior calculated using the equation [53]:

$$s = \sqrt{s_1^2 + s_2^2} \tag{3.5}$$

and taking the precision for a single measurement of the SRT of $1\,\mathrm{dB_{SPL}}$ into account [169].
With an aimed p-value of $p = 0.05$, a power of $P = 0.80$ and the resulting Cohen's d effect size $d = 0.60$, the minimum sample size assembled as 19 (calculated using the pwr package of the software environment for statistical computing R [172]). To increase the certainty of the speech recognition testing, we increased the sample size to 45, which was mainly limited by restrictions during the global coronavirus pandemic.

3.5 Recordings

After concluding that the OLSA was suitable to resolve the quantum enhancement, we recorded all 120 sentences, containing five words each, with both microphones at 22 different SNR values.
In Fig. 3.6 an example recording of the word 'Britta' with the classical and quantum sensor is shown. As all recorded words, this recording was sampled with 20 kHz. Due to losses inside the quantum sensor, the signal amplitude and noise amplitude are smaller than the classical sensor's. Note, that the SNR is still higher for the quantum sensor (see section 3.3.7).

3.6 Speech recognition threshold extraction

As a result of the OLSA test a simple one-dimensional value is generated. The so-called speech recognition threshold (SRT) resembles an average over the last 20 SNR values of the recordings played. In Fig. 3.11 an example measurement of a single

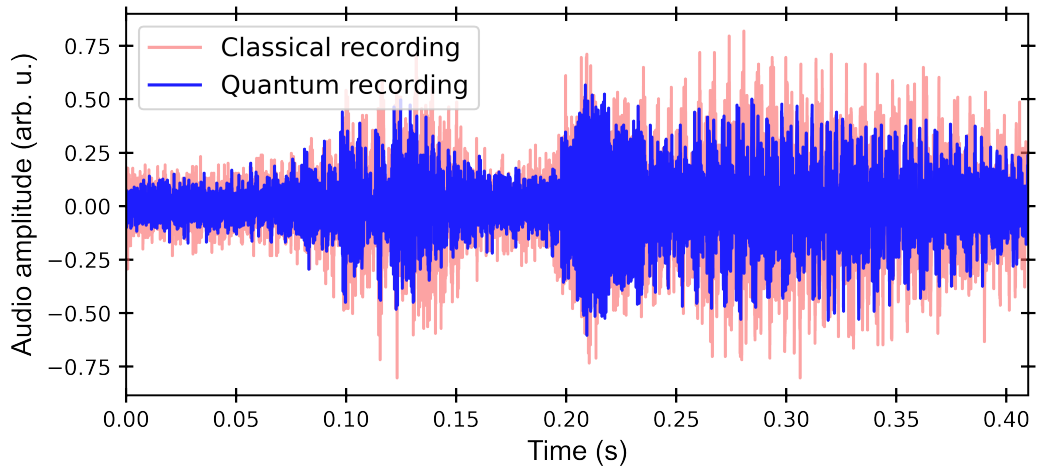

Figure 3.10: **Example audio file.** The quantum (blue) and classical (red) recordings of the word "Britta". The quantum sensor shows lower noise and a smaller signal amplitude compared to the classical sensor, while containing a higher signal to noise ratio (SNR). Adapted from [1].

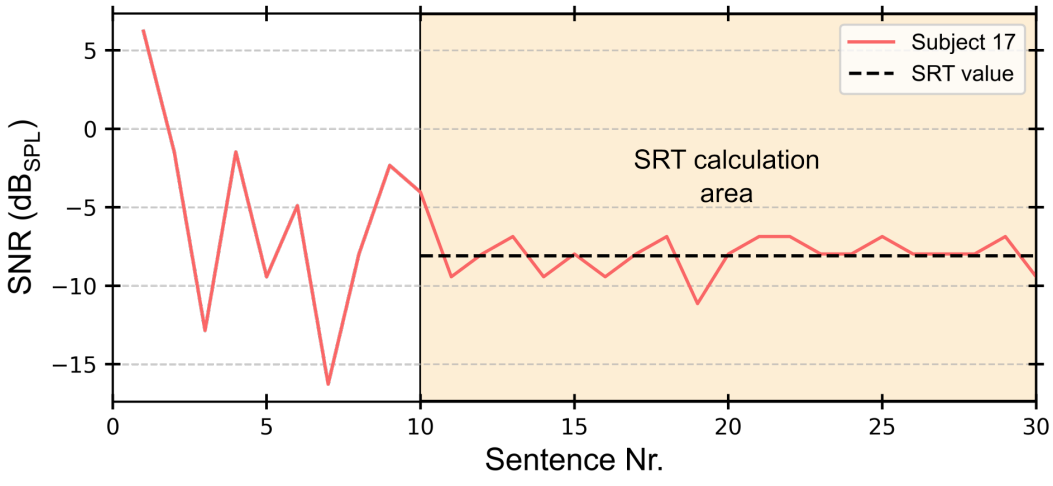

Figure 3.11: **Example measurement.** The applied SNR in dB_{SPL} following Table S3 is shown. The mean value of the last 20 data points determines the SRT. Adapted from [1].

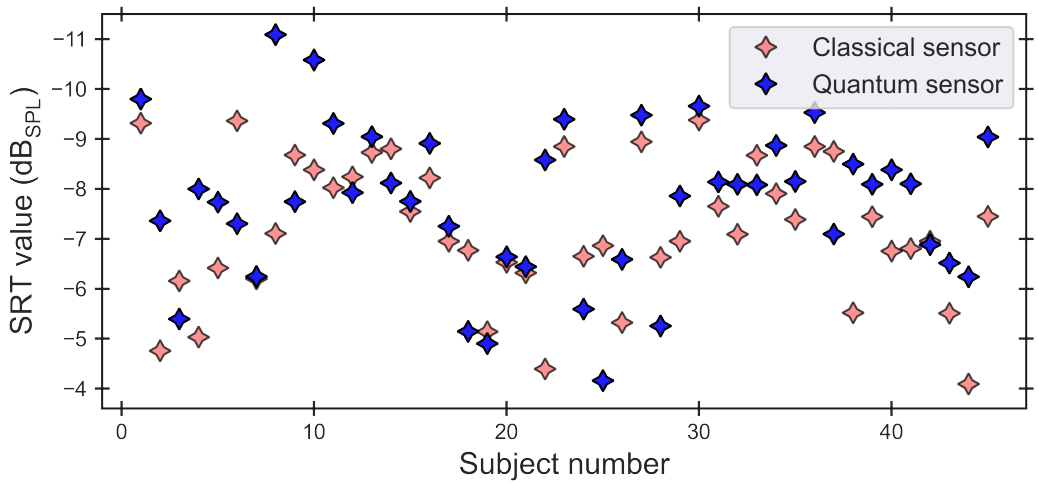

Figure 3.12: **Raw data of the OLSA.** Shows the raw data of both OLSAs for each test subject ($\mu_q = -7.76\,\mathrm{dB_{SPL}}$, $\mathrm{std_q} = 1.51\,\mathrm{dB_{SPL}}$; $\mu_c = -7.19\,\mathrm{dB_{SPL}}$, $\mathrm{std_c} = 1.38\,\mathrm{dB_{SPL}}$. Adapted from [1].

OLSA run is shown. After each played sentence, the test subject repeats the sentence, and dependent on how many words the test subject can repeat, the SNR is adjusted to higher or lower values. The SNR adaption step size is reduced with increasing sentence number following table 3.3. Thus the last 20 scarcely varying SNR values are averaged and define the single SRT value. To compare the understandability of different recordings, we compared these SRT thresholds with each other.

3.7 Raw data

In total, 45 times 2 OLSA tests were performed. Each of the 45 test subjects underwent two times the OLSA test, once with the recordings of the quantum and once with the classical sensor. Each performance results in a single value SRT. In Fig. 3.12 the results are plotted for each test subject. The results resemble two different single values for the SRT belonging to either the OLSA with the quantum sensor recordings or its classical counterpart. Hence the absolute value of the SRT can differ from test subject to test subject quite considerably (see Fig. 3.12); the precision of the SRT value for each test subject is still preserved. Thus, comparing both SRT values for each test subject separately leads to a reliable outcome.
Therefore, a simplified representation of these raw results will be presented in the next section. Consequently, the single SRT value of the classical recordings will be subtracted from the SRT value of the quantum recordings for each test subject separately. This results in a single difference SRT value which solely resembles the improvement in understanding of our quantum optical microphone's recordings per test subject.

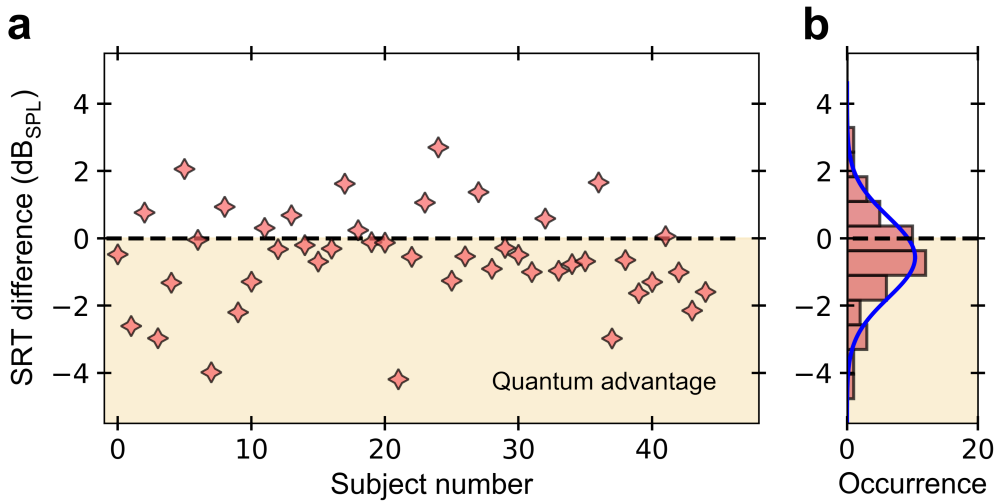

Figure 3.13: **Results of the speech recognition test on $n = 45$ individuals. a**, Each individual's difference in SRT for speech snippets recorded with the classical and quantum microphone, respectively. Data below the dashed line represent a quantum improvement. **b**, Histogram of all data points. The quantum microphone reduces the volume level required to achieve the SRT by $-0.57\,\mathrm{dB_{SPL}}$ with a standard deviation under the square root law of $\pm 0.22\,\mathrm{dB_{SPL}}$ [2]. Adapted from [1].

3.8 OLSA results

In Fig. 3.13 the difference SRT value for each test subject is shown. On the right side, a histogram of the results with a binning of $0.3\,\mathrm{dB_{SPL}}$ is created. To guide the eye, a Gaussian fit is applied as a blue curve.
As a result of the subtraction of the classical from the quantum SRT values, markers below zero show an enhanced understandability of the recorded words of the quantum optical microphone.
The average of the difference SRT value resembles as $-0.57\,\mathrm{dB_{SPL}}$ with a standard deviation under the square root law [2] of $0.22\,\mathrm{dB_{SPL}}$. This proves already that our quantum optical microphone leads to a better understanding of recorded words and thus makes the quantum optical enhancement perceivable by humans.
As a second argument, we will further prove the statistical significance of our findings using a standard statistical one-sided t-test.

3.9 Statistical test

Additionally to the evaluation in the previous section, we performed a state-of-the-art statistical analysis. As a first step, we confirmed using the Kolmogorov-Smirnov test that the data set follows a standard normal distribution (2.2% significance level).
Based on this performance, a subsequent one-sided t-test has been performed.
The principle of the one-sided t-test is the comparison of normal distributions. Therefore a study containing N probabilistic measurements with an uncertainty $\sigma/\sqrt{N}$ is presumed. The measured distribution is compared with the expected value of the null

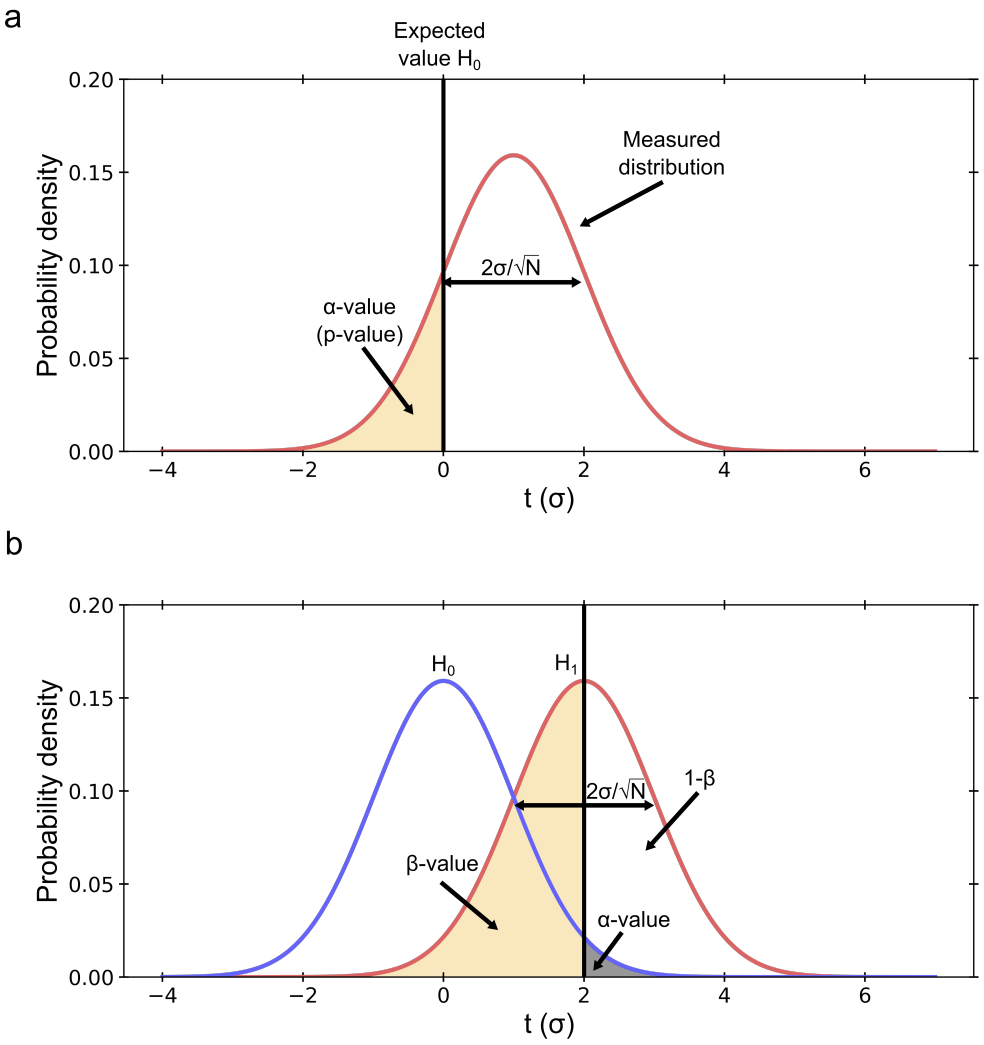

Figure 3.14: **Schematic of the t-test. a**, To investigate the significance of a deviation from the mean value of the null hypothesis H_0 the t-test in principle resembles a normal distribution around the measured mean value with a variance under the square root law ($\sigma/\sqrt{N}$) [3]. The overlap of this function with the expected value of the null hypothesis H_0 defines an alpha value (α). If this value is below a certain threshold (common values are $p = 0.5$) statistical significance is achieved. **b**, To further strengthen the argument the so called power P of the measurement can be calculated. Following the same step as in (**a**) both distributions (H_0 and H_1) are plotted into the same graph. For a given p-value (p) or alpha (α) threshold of the null hypothesis distribution H_0 the overlap of H_1 beyond this value is calculated. The inverse ($1-\beta$) of this value resembles the power P of the measurement. A standard threshold for the power p is given by $P = 0.80$.

hypothesis H_0 (see Fig. 3.14a). The probability of the measured distribution to show values beyond the expected value of the null hypothesis H_0 gives access to a so-called alpha-value (α). If this value surpasses a certain p-value threshold the result is assumed to be significant (see Fig. 3.14a).
In our experiment, a study of 45 test subjects (performing two OLSA tests) is compared to the null hypothesis "The quantum microphone does not lead to an improvement.". Thus the mean value of the null hypothesis H_0 is expected to be zero. The normal distribution of our study is given by a mean value of $-0.57\,\mathrm{dB_{SPL}}$ and a standard deviation of under the square root law [2] of $0.22\,\mathrm{dB_{SPL}}$. In our case, the alpha value (α) shows the probability to be still above zero.
The probability that after 45 measurements, the null hypothesis is correct results in our study to a value of $p/\alpha = 0.006$. This value surpasses by almost two orders of magnitude the common threshold of $p = 0.5$. The p-value prevents type 1 errors, which would result in a false rejection of the null hypothesis even though this hypothesis is correct.
Furthermore, to give an even stronger argument, we investigated the power of the performed t-test. The power P of a statistical test resembles the probability, assuming that the alternative hypothesis H_1 is correct, that the correct result emerges. For calculating the power, the same normal distribution is also presumed for the null hypothesis. The beta-value (β) resembles the probability to show results beyond the defined p-value threshold of the null hypothesis (common threshold $p/\alpha = 0.5$; see Fig. 3.14b). The inverse of this beta-value (β) is then defined as the power P of the test.
For our experiment, the power of the one-sided t-test results in a value of $P = 0.83$, which is above the common threshold for the power of $P = 0.80$.
The investigation of the power of a test prevents type 2 errors. Type 2 errors resemble falsely rejecting the alternative hypothesis even though it might be correct.
Combining both arguments, it is clear, that the sample size was chosen large enough and that the visible enhancement is statistically significant. We thus can confidently state that the quantum optical microphone indeed leads to a better understandability of recorded words compared to a classical counterpart.

3.10 Conclusion and outlook

To highlight quantum sensing scheme's reliability and applicability, we presented a quantum optical microphone for recording human speech in this chapter. We used our collaborations with the glass workshop at our university, the Max Planck Institute for solid state research in Stuttgart, and the group of Jelena Vučković at Stanford university to design a suitable mirror membrane, which showed a high reflectivity as well as an excellent frequency response.
Comparing classical and quantum microphones at identical photon numbers, showed that the quantum microphone records sound at a significantly reduced baseline noise level. We proved this by calculating an improvement in the SNR as $0.84 \pm 0.29\,\mathrm{dB_{SPL}}$ and confirmed this in a medical speech recognition test on $n = 45$ subjects. The results of this speech recognition test showed that the speech recognition threshold was improved by $0.57\,\mathrm{dB_{SPL}}$ on average, thus confirming that humans could hear the quantum advantage. Furthermore, we confirmed the results of the speech recognition test

by performing a standard statistical one-sided t-test, which resulted in a p-value/α-value of $p/\alpha = 0.006$ and a statistical power of the test of $P = 0.83$, which are well below/above the common threshold of $p/\alpha = 0.5/P = 0.80$. We thus could prove that recordings performed with our quantum optical microphone lead to an enhanced SNR and a better understandability of recorded words compared to a classical counterpart. Even though the here introduced quantum optical microphone at its current state cannot contend with modern classical microphones, the development shows how easy this nonlinear interferometry scheme can be implemented in various fields. I want to especially highlight that to record human voices, the enhancement simultaneously over the complete audio band has been necessary from low to high frequencies, i.e., a large dynamic range.

Building upon the last two chapters, the presented sensing scheme could be employed in applications involving biological samples, chemical reactions, or atomic spin ensembles, which are sensitive to light exposure and short wavelength photons [32, 44–48]. In this sense, our quantum light source operates already within the favorable second biological window BW-II ($1000 - 1350\,\mathrm{nm}$) [173]. To show exploitable quantum advantage, the light flux of our source would have to be increased to the level of a few $100\,\mathrm{nW}$. In that regard, a previous work demonstrated already photon pair beams at power levels of $0.3\,\mu\mathrm{W}$, while still operating in the distinct photon pair regime [155].

At that point, intensity detectors need to show superior performance in optoelectronic conversion with noise figures of merit below the photonic shot noise. In section 2.2.6 I pathed the way to sub-shot noise detection in this power level regime, thus putting quantum bio-imaging within realistic reach.

Another interesting study could be the escape of the distinct photon pair regime towards the parametric amplified regime to use the effect of stimulated emission similar as in the SU(1,1) interferometry [113–115]. On the one hand, higher power levels may further increase the quantum sensing enhancement factor. On the other hand, path-polarization state engineering may provide a pathway to introduce common mode noise suppression in these schemes.

In chapter 4 we investigate this regime further and show how the loss sensitivity and enhancement behave for higher squeezing parameters r.

Chapter 4

Theoretical framework

In this chapter, I will present a theoretical framework for our novel quantum sensor. The main work was performed together with Dr. Charles Babin during his Ph.D. in our group. These calculation results have already been partly published in the works [7] and [1]. The theory presented here, mainly covers two regimes of our experiment. The first regime covers small squeezing parameters $r \ll 1$, which resembles the current experimental realization, and a second regime $r \gg 1$, which gives an outlook on a possible extension of our quantum sensor.
For both cases, we will address how the visibility and losses inside of the interferometer are intertwined. With the results presented in section 2.2.3, an upper limit to the losses inside of the interferometer part can be estimated.

4.1 The Heisenberg picture

In contrast to the Schrödinger picture, where the time dependency is integrated into the state vectors, in the Heisenberg picture, the time dependency is solely incorporated into the operators. In the following, a recap of some general features will be given.
In general, time dependent operators $\hat{O}(t)$ in the Heisenberg picture (with $\hat{H}$ the Hamilton operator) follow the equation of motion:

$$\frac{\mathrm{d}\hat{O}_{\mathrm{H}}(t)}{\mathrm{d}t} = \frac{1}{i\hbar}\left[\,\hat{O}_{\mathrm{H}}(t), \hat{H}_{\mathrm{H}}\,\right] + \frac{\partial \hat{O}_{\mathrm{S}}(t)}{\partial t}. \tag{4.1}$$

Furthermore, any operator in the Schrödinger picture $\hat{A}_{\mathrm{S}}$ can be transformed into the Heisenberg picture ($\hat{A}_{\mathrm{H}}$) by the following equation:

$$\hat{A}_{\mathrm{H}}(t) = \exp(iH_{\mathrm{S}}t/\hbar)\, A_{\mathrm{S}}\, \exp(-iH_{\mathrm{S}}t/\hbar) \tag{4.2}$$

For developing a theoretical framework of our experimental setup, we first introduce the creation ($\hat{a}^\dagger$) and annihilation ($\hat{a}$) operators. These operators resemble a reduction or an increase of the number of particles in a given mode or state by one and is defined as the following [52]:

$$\hat{a}^\dagger \left|n\right\rangle = (n+1)^{1/2} \left|n+1\right\rangle, \tag{4.3}$$

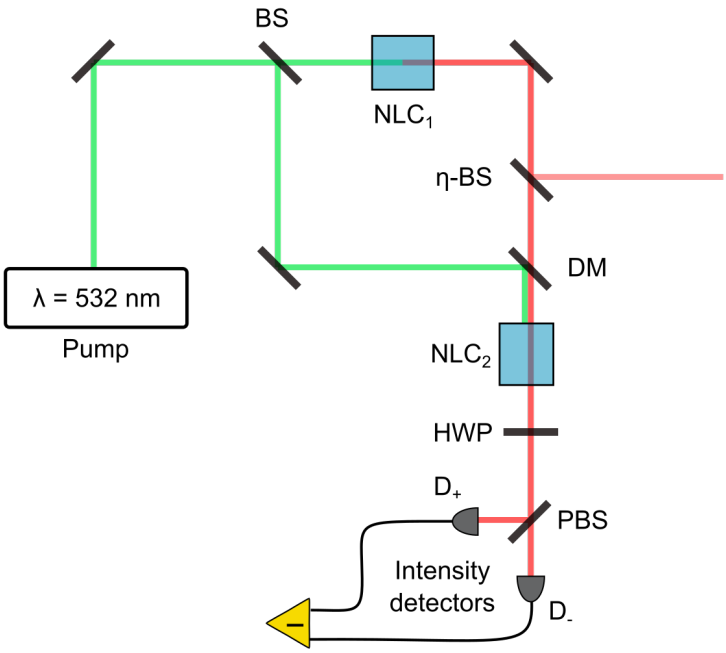

Figure 4.1: **Equivalent schematic of the quantum sensor.** The virtual beam splitter η-BS simulates losses inside the interferometer. Filter = spectral filter, DM = dichroic mirror, HWP = half-wave plate, BS = beam splitter, η-BS = beam splitter with transmissivity *eta*, PBS = polarizing beam splitter, D = intensity detector, NLC = PPKTP nonlinear crystal. [1]

where the creation operator $\hat{a}^\dagger$ creates one quantum of energy by raising the system from the state $|n\rangle$ to the state $|n+1\rangle$.
The annihilation operator $\hat{a}$ on the other hand destroys one quantum of energy by lowering the system from the state $|n\rangle$ to the state $|n-1\rangle$.

$$\hat{a}\,|n\rangle = (n)^{1/2}\,|n-1\rangle \tag{4.4}$$

The idea of this theoretical framework is to calculate the evolution of these annihilation and creation operators in the Heisenberg picture to combine the impact of the complete experimental setup in one single operator $\hat{O}_{\text{Qu.Sens.}}$.
Instead using a retro-reflecting approach as shown in section 2.2 using the indices f and b for forward and backward direction, we created an equivalent schematic which resembles our experimental setup but is easier to follow in Fig. 4.1. Here, instead of forward and backward contributions from a single nonlinear crystal (NLC), two separate NLCs are placed in the setup, creating the same photon pair contributions: $|\mathrm{H,s}\rangle|\mathrm{V,i}\rangle$ via type-II down-conversion in NLC_1 and $|\mathrm{V,s}\rangle|\mathrm{V,i}\rangle$ via type-0 down conversion in NLC_2. The result is the same state:

$$|\Psi\rangle = \frac{1}{\sqrt{2}}\left(\mathrm{e}^{i(\Phi_1+\Phi_2)}\,|\mathrm{H,s}\rangle|\mathrm{V,i}\rangle + |\mathrm{V,s}\rangle|\mathrm{V,i}\rangle\right) \tag{4.5}$$

as in the real setup (Fig. 2.5). For the calculation of the detector signals, only the modes $|\mathrm{H,s}\rangle$ and $|\mathrm{V,s}\rangle$ have been considered, thus being equivalent to implementing a filter eradicating photon $|\mathrm{V,i}\rangle$. To explore the effect of losses, we also placed loss

channels in form of virtual beam splitters (η-BS) at various locations. Losses usually come from a non-perfect mode overlap or optical elements that introduce losses by non-perfect reflectivity or transmissivity.

4.2 Matrix representation

In the following, we calculate the influence of the virtual beam splitter only inside of the interferometer itself. The placement of the virtual beam splitter in any other location outside the interferometer does affect neither the enhancement nor the single photon state. The loss of a $|H, s\rangle$ or $|V, s\rangle$ photon only results in a decrease of the measured number of photons and thus does not lead to decoherence as no "information" is leaked to the environment. Thus, for a comparison with a classical counterpart, losses outside of the interferometer are not taken into account.
Further, let $\hat{a}_i$, and $\hat{a}_i^\dagger$, denote the annihilation and creation operator for photons in mode i. Those operators satisfy the Boson commutation relations:

$$[\hat{a}_i, \hat{a}_j] = \left[\hat{a}_i^\dagger, \hat{a}_j^\dagger\right] = 0 \tag{4.6}$$

$$\left[\hat{a}_i, \hat{a}_j^\dagger\right] = \delta_{ij} \tag{4.7}$$

In the Heisenberg picture, we can describe each optical element by a linear operator acting on $\hat{a}_i$, and $\hat{a}_i^\dagger$. The operators can then be multiplied to find the operators describing the entire experimental setup. By utilizing the equations defining each optical element:

- ❖ BS with transmissivity η:
  - ➪ $\hat{a}_{1,\text{out}} = \sqrt{\eta}\,\hat{a}_{1,\text{in}} + \sqrt{1-\eta}\,\hat{a}_{2,\text{in}}$
  - ➪ $\hat{a}_{2,\text{out}} = -\sqrt{1-\eta}\,\hat{a}_{1,\text{in}} + \sqrt{\eta}\,\hat{a}_{2,\text{in}}$
- ❖ HWP:
  - ➪ $\hat{a}_{1,\text{out}} = \hat{a}_{1,\text{in}} - \hat{a}_{2,\text{in}}$
  - ➪ $\hat{a}_{2,\text{out}} = \hat{a}_{1,\text{in}} + \hat{a}_{2,\text{in}}$
- ❖ NLC:
  - ➪ $\hat{a}_{1,\text{out}} = \cosh(r)\,\hat{a}_{1,\text{in}} - \mathrm{e}^{i\Theta}\sinh(r)\,\hat{a}_{1,\text{in}}^\dagger$
  - ➪ $\hat{a}_{2,\text{out}} = \cosh(r)\,\hat{a}_{2,\text{in}} - \mathrm{e}^{i\Theta}\sinh(r)\,\hat{a}_{2,\text{in}}^\dagger$
- ❖ Phase object:
  - ➪ $\hat{a}_{1,\text{out}} = \mathrm{e}^{i\phi_1}\,\hat{a}_{1,\text{in}}$
  - ➪ $\hat{a}_{2,\text{out}} = \mathrm{e}^{i\phi_2}\,\hat{a}_{2,\text{in}}$

we can describe in the Heisenberg picture each optical element by a matrix as seen in Fig. 4.2a-d. The matrix representation can be understood by considering the simple

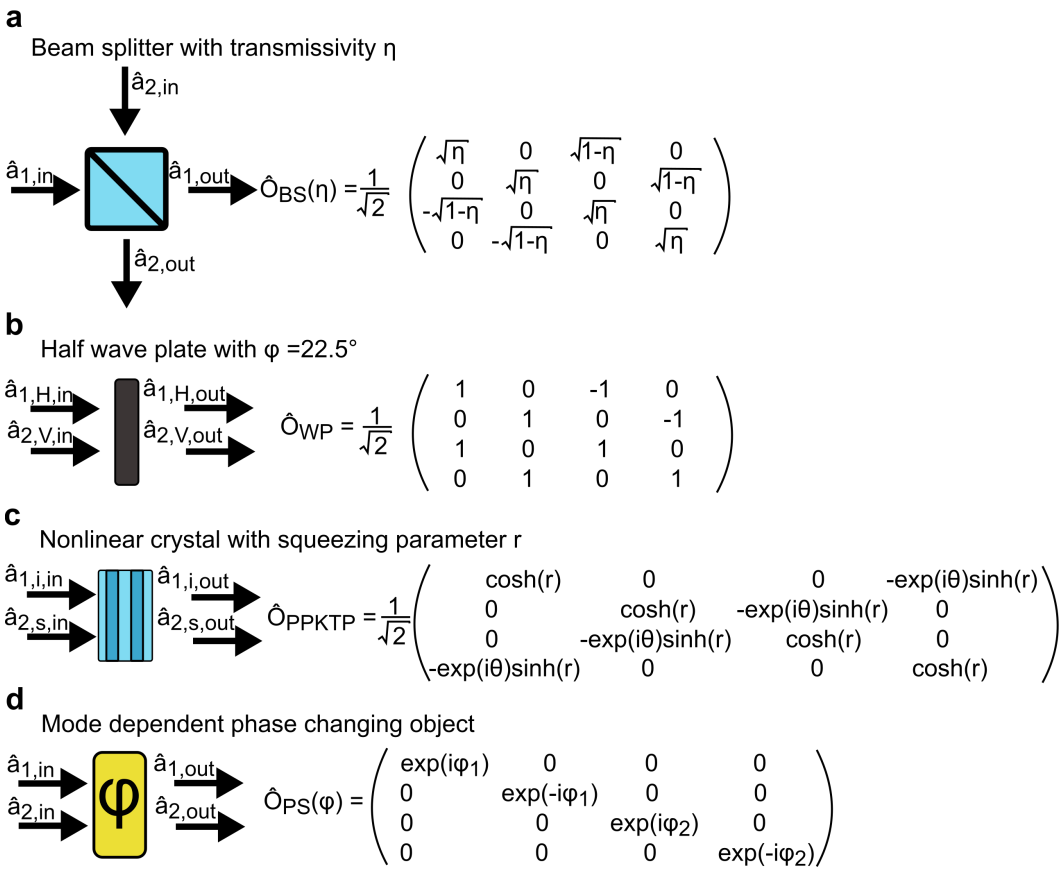

Figure 4.2: **Operators in the Heisenberg representation.** Utilized operators for the theoretical model. **a** represents an arbitrary beam splitter with transmissivity η, **b** a half wave plate, **c** a nonlinear crystal following equations (1.38) and (1.39) with a squeezing parameter r, a phase angle Θ and **d** a phase object introducing a wavelength dependent phase shift Φ. [1]

case of a BS with two input modes. To satisfy the above equations, one can define an input $\hat{A}_{\text{in}}$ and output vector $\hat{A}_{\text{out}}$:

$$\hat{A}_{\text{in}} = \begin{pmatrix} \hat{a}_{1,\text{in}} \\ \hat{a}^{\dagger}_{1,\text{in}} \\ \hat{a}_{2,\text{in}} \\ \hat{a}^{\dagger}_{2,\text{in}} \end{pmatrix}. \tag{4.8}$$

$$\hat{A}_{\text{out}} = \begin{pmatrix} \hat{a}_{1,\text{out}} \\ \hat{a}^{\dagger}_{1,\text{out}} \\ \hat{a}_{2,\text{out}} \\ \hat{a}^{\dagger}_{2,\text{out}} \end{pmatrix}. \tag{4.9}$$

and further define a matrix $\hat{U}$ transforming the input operator $\hat{A}_{\text{in}}$ into the output operator $\hat{A}_{\text{out}}$ satisfying the above equations via $\hat{A}_{\text{out}} = \hat{U}\hat{A}_{\text{in}}$ In Fig. 4.2 the matrices realizing the above shown equations for the input and output vector operators $\hat{A}_{\text{in}}$ and $\hat{A}_{\text{out}}$ are shown.
For our quantum sensor we need to consider all the modes present: $|\text{V}, \text{s}\rangle$, $|\text{H}, \text{s}\rangle$ and $|\text{V}, \text{i}\rangle$ and the modes introduced by the virtual beam splitter $|\text{V}, \text{s}\rangle_{\text{L}}$, $|\text{H}, \text{s}\rangle_{\text{L}}$ and $|\text{V}, \text{i}\rangle_{\text{L}}$. This forms a six-dimensional Hilbert space leading us to consider 12-dimensional vectors comprising all creation and annihilation operators. The four-dimensional transfer matrices of the optical elements shown in Fig. 4.2 are also expanded to 12x12 dimensions indicating non-interacting modes with unit matrices.
The total transfer matrix modeling the quantum sensor is defined as a linear combination of the nonlinear crystal operator $\hat{O}_{\text{PPKTP}}$, the phase changing operator $\hat{O}_{\text{PS}}$, the beam splitter operator $\hat{O}_{\text{BS}(\eta)}$ and the waveplate operator $\hat{O}_{\text{WP}}$:

$$\hat{A}_{\text{out}} = \hat{O}_{\text{WP}} \cdot \hat{O}_{\text{PPKTP}} \cdot \hat{O}_{\text{BS}(\eta)} \cdot \hat{O}_{\text{PS}} \cdot \hat{O}_{\text{PPKTP}} \cdot \hat{A}_{\text{in}} \tag{4.10}$$

or

$$\hat{A}_{\text{out}} = \hat{O}_{\text{Qu.Sens.}} \hat{A}_{\text{in}}. \tag{4.11}$$

In our case, we define the initial state as a coherent state, thus a laser. For an arbitrary operator $\hat{U}$, the variance can be calculated as $\Delta\hat{U}^2 = \langle\hat{U}^2\rangle - \langle\hat{U}\rangle^2$.
Using the variance and the signal strength of an infinitesimal phase change $|\partial_{\Phi}\langle\hat{U}\rangle|$ additionally the maximum sensitivity to a relative phase change can be calculated as $\Delta\Phi = \Delta\hat{U}/|\partial_{\Phi}\langle\hat{U}\rangle|$.
Following the experimental setup represented in Fig. 4.1 (or Fig. 2.5) we consider the intensity detection operator at each output as $\hat{I}_1 = \hat{a}^{\dagger}_{H,\text{out}}\hat{a}_{H,\text{out}}$ and $\hat{I}_2 = \hat{a}^{\dagger}_{V,\text{out}}\hat{a}_{V,\text{out}}$. Here the subscripts H and V depict the vertical and horizontal polarization of the signal photon. This gives access to the difference operator $\hat{S} = \hat{I}_1 - \hat{I}_2$.
Following the calculations of the intensity detection operator, the resulting signal is:

$$S(r, \eta, \phi_1, \phi_2) = \alpha \cos(\phi_1 + \phi_2) \tag{4.12}$$

with

$$\alpha = 2 \cdot \eta \cosh(r) \sinh^2(r) = \eta \cosh(r) N, \tag{4.13}$$

r the squeezing parameter, η the transmissivity, N the photon number and ϕ_1 and ϕ_2 the wavelength dependent collected phase difference between the sample path and the reference path. The variance of the signal operator $\hat{S}$ results in:

$$\Delta S^2(r,\eta,\phi_1,\phi_2) = \frac{\alpha^2}{2}\,\cos(\,2(\phi_1+\phi_2)\,) + \beta \tag{4.14}$$

with

$$\begin{aligned}\beta = \sinh^2(r)\Big(&\cosh^4(r)\,\eta^2 + 2\cosh^2(r)\,\eta\,(1-\eta)\\ &+\cosh^2(r)\,\eta + \sinh^4(r)\,\eta^2 + (1-\eta)^2\Big).\end{aligned} \tag{4.15}$$

The difference signal and the variance as functions of the squeezing parameter r, the transmissivity η and the wavelength dependent phase shifts ϕ_1 and ϕ_2 will enable the calculation of the phase estimation sensitivity ($\Delta\Phi = \Delta\hat{S}/|\partial_\Phi\langle\hat{S}\rangle|$) for various sets of parameters.
The sensitivity and the intertwinement between visibility and losses inside of the interferometer will be discussed in the next two chapters. Next, I will focus mainly on two extreme cases of a small squeezing parameter $r \ll 1$, which resembles our approach best, and for $r \gg 1$ in which the assumption of a flux of distinct photon pairs collapses and the regime of parametric amplification is reached.

4.3 Small squeezing parameter r

4.3.1 Experimentally realized photon pair flux

To gain access to the generated photon pair rate per mode and coherence time, we followed the strategy described in reference [174]. Note that this reference describes the efficiency in a waveguide but this approach can be, without loss of generality, directly translated into a free space experiment. To measure the photon pair flux generated in the nonlinear crystal, we adjusted the pump laser (532 nm) to an optical power of 10 mW and replaced the interferometer itself by a 50:50 beam splitter. We measured the single photon count rate at both output ports of this beam splitter to access both the single photon rates and the coincidence rate.
The count rates on both detectors D_1 and D_2 are given by:

$$D_1 = \frac{1}{2}\,\mu_1\,\eta_1\,N_{\text{pair}} \tag{4.16}$$

$$D_2 = \frac{1}{2}\,\mu_2\,\eta_2\,N_{\text{pair}}. \tag{4.17}$$

Here, μ_i and η_i denote propagation losses and the detector efficiencies ($i = 1, 2$ for detectors 1 and 2), and N_{pair} is the photon pair rate generated in the PPKTP crystal. The maximum coincidence rate is then given by

$$R_{\text{c}} = \frac{1}{2}\,\mu_1\,\eta_1\,\mu_2\,\eta_2\,N_{\text{pair}}. \tag{4.18}$$

Due to the use of a 50:50 beam splitter, the probability for a coincidence is reduced by 50%, leading to the prefactor of 1/2 in R_c. Finally, by combining equations (4.16), (4.17) and (4.18) we get a formula for the estimation of the generated photon flux.

$$N_{\text{pair}} = \frac{2D_1D_2}{R_c}. \tag{4.19}$$

Note that all quantities in this equation are directly accessible in an experiment. The single photon rates measured in our experiment are $D_1 = 1.27 \cdot 10^6\,\text{s}^{-1}$ and $D_2 = 1.16 \cdot 10^6\,\text{s}^{-1}$. The measured coincidence rate is $R_c = 71.10 \cdot 10^3\,\text{s}^{-1}$ leading to a photon pair rate of $N_{\text{pair}} = 41.44 \cdot 10^6\,\text{s}^{-1}$.
To estimate whether the photon pair flux at the rate N_{pair} is still composed of separated photon pairs, we have to consider the single-photon coherence time Δt. We obtain Δt via the spectral bandwidth, as measured in section 2.2.1. In wavelength units, we measured $\Delta\lambda_1 = 10.8\,\text{nm}$ at 1022.6 nm and $\Delta\lambda_2 = 12.6\,\text{nm}$ at 1109.3 nm. In frequency units, this converts to $\Delta f_1 = 3.10\,\text{THz}$ and $\Delta f_2 = 3.07\,\text{THz}$. In the following, we use the average value of both measurements, i.e., $\Delta f = \frac{\Delta f_1 + \Delta f_2}{2} = 3.09\,\text{THz}$. Assuming a Gaussian-shaped spectrum, we can now convert the frequency bandwidth into a temporal bandwidth:

$$\Delta t \approx \frac{0.44}{\Delta f} = 0.142\,\text{ps} \tag{4.20}$$

With this, a photon-pair flux can be still considered as consisting out of distinct photon pairs if it satisfies the following equation:

$$\Delta t \cdot N_{\text{pair}} \ll 1. \tag{4.21}$$

With a value of $\Delta t \cdot N_{\text{pair}} = 6 \cdot 10^{-6} \ll 1$, for the parameters chosen in our experiment, we validated two things: first, we confirmed that the photon pair flux indeed consists of distinct photon pairs, and second, that the quantum sensor works well in the regime of a small squeezing parameter $r \ll 1$.
Note that using a spectral filter does not change the product $\Delta t \cdot N_{\text{pair}}$. For instance, with the 2 nm bandpass filter used in the quantum microphone experiments, the single photon coherence time Δt is increased by approximately 6 times, however, the effective photon pair flux N_{pair} is reduced by the same factor.

4.3.2 Loss dependency and visibility

Building upon the findings of the last section, a realistic representation of our quantum sensor is in the regime of small squeezing parameters. For $r \ll 1$ the highest sensitivity to a phase difference between the two paths of the nonlinear interferometer ($\Delta\Phi = \Delta\hat{S}/|\partial_\Phi\langle\hat{S}\rangle|$) reduces to:

$$\Delta\phi_{\text{qm}}(r \ll 1, \phi \approx \frac{\pi}{4}) = \frac{\cosh^2(r)\,\eta + 1}{2\cosh(r)\,\eta\,\sqrt{(1+\eta)N}}, \tag{4.22}$$

where N represents the number of photons entering the interferometer. Further, the visibility of an interferometer is defined as:

$$\text{vis} = \frac{I_{\text{max}} - I_{\text{min}}}{I_{\text{max}} - I_{\text{min}}} \tag{4.23}$$

with $I_{\max}$ and $I_{\min}$ maximum and minimum number of photons measured. Additionally, we can express the visibility as

$$\text{vis} = \frac{2\cosh(r)\,\eta}{\cosh^2(r)\,\eta + 1}, \tag{4.24}$$

where η is the transmissivity of a fictitious beam splitter (η-BS in Fig. 4.1) representing the losses $(1-\eta)$ inside of the quantum sensor. Together this reduces equation (4.22) to:

$$\Delta\phi_{\text{qm}}(r \ll 1, \phi \approx \frac{\pi}{4}) = \frac{1}{\text{vis}\sqrt{(1+\eta)N}}. \tag{4.25}$$

The advantage of this calculation is the experimental accessibility of the visibility in our sensor. For example, we can use equation (4.24) to calculate the loss inside of the interferometer by rearranging the equation to:

$$1 - \eta = \frac{1 - \text{vis}}{1 - \text{vis}/2}. \tag{4.26}$$

For the determination of the visibilities a piezo actuator has been used to displace one of the retroreflecting mirrors over several interferometer fringes. We performed this measurement for the quantum sensor and the classical sensor (Fig. 2.10 in section 2.2.4).
The visibilities were calculated from a sinusoidal fit of the form $f = N\cos^2(px+c)+d$, with N the amplitude (maximum photon number measured), p the spatial frequency, c an initial phase shift and d an offset value. The visibilities were calculated following $(f_{\max} - f_{\min})/(f_{\max} + f_{\min})$. The visibilities are $\text{vis}_{\text{qm}} = 0.85 \pm 0.02$ for both detectors of the quantum sensor and $\text{vis}_{\text{cl}} = 0.98 \pm 0.002$ for both detectors of the classical sensor. Thus, following equation (4.26) we can determine an upper limit of losses of $1-\eta = 0.26$. As an additional step, also using the data from our classical counterpart, it is possible to calculate an expected enhancement factor of the quantum sensor. To reach this, we first calculate the sensitivity of a perfect Michelson Interferometer with the same amount of photons entering the interferometer:

$$\Delta\phi = \frac{1}{\sqrt{N}}. \tag{4.27}$$

Adding experimental imperfections in form of a non-perfect visibility the equation (4.27) changes to

$$\Delta\phi = \frac{1}{\text{vis}_{\text{cl}}\sqrt{N}}. \tag{4.28}$$

With equation (4.25) and (4.28) we can thus calculate directly the expected enhancement factor f by simply dividing these two equations:

$$f = \frac{\Delta\phi_{\text{cl}}}{\Delta\phi_{\text{qm}}} = \frac{\text{vis}_{\text{qm}}}{\text{vis}_{\text{cl}}}\sqrt{1+\eta}. \tag{4.29}$$

With the measured visibilities from Fig. 2.10 this equation leads to an expected enhancement factor over the non-ideal classical sensor of:

$$f = \frac{\Delta\phi_{\text{cl}}}{\Delta\phi_{\text{qm}}} = \frac{\text{vis}_{\text{qm}}}{\text{vis}_{\text{cl}}}\sqrt{1+\eta} = 1.14 \pm 0.01. \tag{4.30}$$

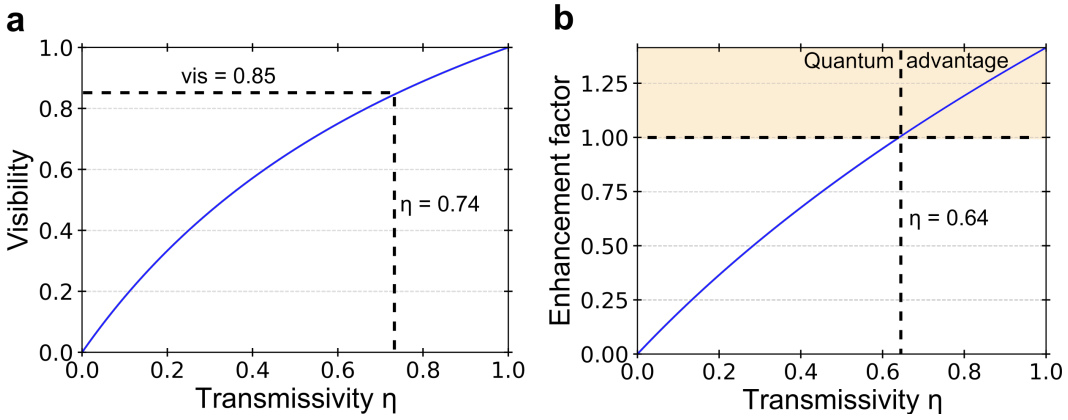

Figure 4.3: **Dependency of the visibility and the enhancement factor from the transmissivity η.** **a**, The visibility shows a dependency as shown in equation (4.24). The quantum sensor shows a visibility of $\text{vis}_{\text{qm}} = 0.85 \pm 0.01$ and thus a transmissivity of $\eta = 0.74$ is to be expected. **b**, The enhancement factor to a perfect classical sensor with a visibility equal to one. Note that the enhancement factor still surpasses one for transmissivities above 0.64. Adapted from [1].

For an ideal classical sensor the quantum sensor still shows an enhancement factor of $f = 1.12 \pm 0.01$. These results fit quite well the experimentally measured value of 1.13 ± 0.02 , (see section 2.2.5), thus demonstrating the validity of our model.
To not only prove the model's validity, but extend it to a broader set of parameters, Fig. 4.3a shows the visibility as a function of the transmissivity η. With this data, the calculation of the expected enhancement factor as a function of the transmissivity is possible. An exciting feature is that even for losses up to $1 - \eta = 36\%$, our novel quantum sensor still outperforms a perfect classical counterpart without losses inside of the interferometer and perfect visibility (see Fig. 4.3b).

4.4 Large squeezing parameter r

Additionally to the experimentally realized case of small squeezing parameters r we expanded our theoretical framework to the case of large squeezing parameters. Due to the lack of our current setup to reach high values of r this will only represent a short journey to possible extensions of our quantum sensor.

4.4.1 Loss dependency

If we follow the same approach as in section 4.3.2, calculating the highest sensitivity to a phase difference ($\Delta\Phi = \Delta\hat{S}/|\partial_\Phi\langle\hat{S}\rangle|$), for $r \gg 1$, we end up with:

$$\Delta\phi_{\text{qm}}(r \gg 1, \phi \approx \frac{\pi}{4}) = \frac{1}{2\sqrt{N}}\frac{3-2\eta}{2\eta} \tag{4.31}$$

In Fig. 4.4a for both cases $r \gg 1$ and $r \ll 1$ the enhancement factor compared to a classical interferometer of the same built and the same losses are plotted against the

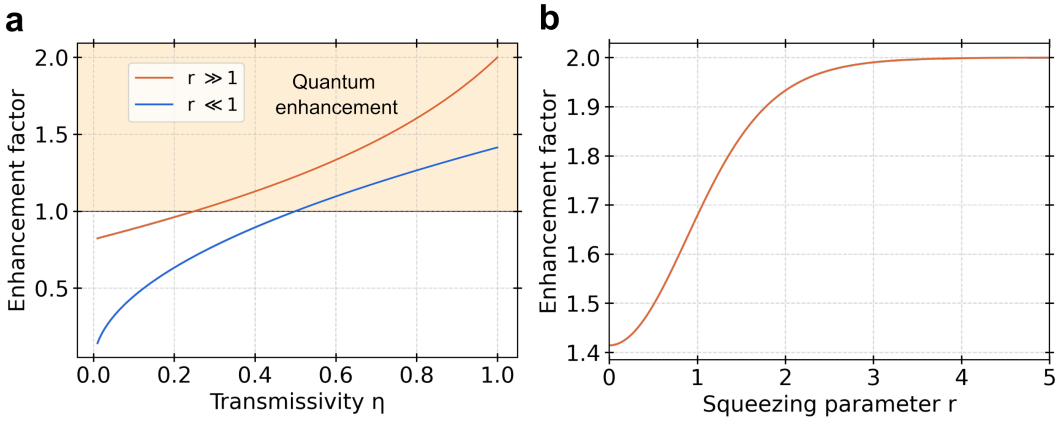

Figure 4.4: **Comparison of different squeezing parameters.** **a**, Comparison of the enhancement factor as a function of the transmissivity η. The enhancement is defined as the enhanced sensitivity over a classical sensor of the same built sharing the same amount of loss. **b**, The enhancement factor as a function of the squeezing parameter r. One can observe that for small squeezing parameters the enhancement factor shows a limit of $\sqrt{2}$, while for large squeezing parameters (above $r = 4$) the enhancement factor saturates to a value of two. [1]

transmissivity η. While for $r \ll 1$ above $\eta = 0.5$ an enhancement is visible, for large squeezing parameters $r \gg 1$ even down to $\eta \approx 0.25$ our quantum sensor outperforms its classical counterpart. Furthermore, while the case $r \ll 1$ can reach a maximum value of the enhancement factor of $f = \sqrt{2}$ the case of $r \gg 1$ shows values up to $f = 2$. This effect is again shown in Fig. 4.4b, where the enhancement factor is shown as a function of the squeezing parameter r. Here, an increase of the squeezing parameter r up to values of around $r = 1$ leads to a significant improvement of the enhancement factor to $f \approx 1.68$. Building upon this, above $r = 4$, the enhancement factor asymptotically approaches a new limit ($f_{\text{enh.}} \approx 2$).

4.4.2 Conclusion and outlook

In this chapter, we introduced a theoretical framework of our quantum sensor. We defined a quantum sensor operator $\hat{O}_{\text{Qu.Sens.}}$ in the Heisenberg picture and calculated the expected signal and variance. Based on this, we investigated the influence of losses, the visibility, and the squeezing parameter on the enhancement factor. Furthermore, we found a correlation between the losses and the visibility of our quantum sensor, with which we were able to set an upper limit to the losses inside of the quantum interferometer. Capitalizing on that, we calculated an expected enhancement factor of 1.12 ± 0.01 compared to an ideal classical sensor, which resembles the experimentally determined value of 1.13 ± 0.02 quite well. Additionally, we identified that even for losses of 36% our quantum sensor still outperforms a perfect classical counterpart.
As a short extension, we investigated the regime of large squeezing parameters $r \gg 1$. Here we could see an improvement in the loss dependency of the quantum sensor as well as in the absolute enhancement factor. Further, even if not yet supported by an

experimental realization, our theory indicates a reduced loss dependency and an even increased enhancement factor by entering the parametric amplification regime. Thus an investigation of this sensor in the regime of high squeezing parameters r might prove promising.

Chapter 5

Nanophotonic tapered-fiber-tapered-waveguide interface

This chapter investigates fiber-coupled nanophotonic interfaces. As the primary goal of this interface will be the collection of photons from implanted single color centers in silicon carbide, this chapter starts with a short introduction to the silicon carbide platform. Here, the chemical structure of silicon carbide (SiC) and the optical properties of certain defects in SiC will be explained.
In a second section, a theoretical description of nanophotonic waveguides is presented. Starting with the fundamentals of electromagnetic wave propagation in dielectric media, we will introduce the origin of waveguide modes and waveguide-specific parameters as the effective index or the TE and TM modes. Next, the algorithm used in this work, Yee's finite difference algorithm, is explained. In the last subsection, we will shortly motivate the waveguide grating couplers.
Based on the findings of the last two sections, different strategies to increase the coupling efficiency between an optical fiber and a nanophotonic waveguide are presented in the third section. This section will mainly treat the diffraction grating, edge (or butt) coupling, and tapered fiber coupling. Following this, I will introduce different fabrication processes to manufacture tapered optical fibers. Three different approaches will be shortly introduced; CO_2 laser or thermal heating and HF etching.
The following section treats the simulation of the waveguides and the nanophotonic interface using the commercially available software Lumerical. First, the used waveguide design will be motivated, showing the single-mode behavior of a waveguide of the width $w = 500\,\mathrm{nm}$, an etch angle of 45° and the wavelength of interest $\lambda = 917\,\mathrm{nm}$. Secondly, I will give a short introduction to the theoretical fiber coupling process, explaining the role of the effective index for the coupling efficiency, the term "beat length", and finally, the slow variation criterion.
Based on the findings of the previous sections, I will present the overlap dependency of the transmission of the tapered-fiber-tapered-waveguide interface. Here, a distinction between the case of light coupled into the waveguide and light coupled out of the waveguide will be given. The coupling efficiency's dependency on the final tip diameter

is also investigated. As before, a distinction between in- and outcoupling is made.
Based on the findings of the simulations of the previous sections, a set of parameters for the waveguide and tapered fiber production is found.
In the next section, the tapered-fiber-tapered-waveguide interface is characterized. First, the etching process in the Max Planck Institute for Solid State Research in Stuttgart is introduced directly, followed by an investigation of the fiber tip using a simple optical and a scanning electron microscope.
In the second part, the coupling efficiency of the nanophotonic interface is characterized. This subsection introduces the measurement process for determining the coupling efficiency, followed by the coupling efficiency characterization for a single wavelength of $\lambda = 878.8\,\mathrm{nm}$ for different waveguides; different waveguide taper length and support structure number. These measurements are followed by an investigation of the overlap-dependent coupling efficiency at the same wavelength. In the last part, the frequency-dependent coupling efficiency will be presented, showing a large wavelength regime, where a high coupling efficiency (above 80%) can be reached.
The last section introduces a conversion of our setup to a confocal system, with excitation from the top and a collection via the tapered-fiber-tapered-waveguide interface. This section gives an outlook on possible investigations of single defects in waveguides with a high collection efficiency of the emitted photons.

5.1 The silicon carbide platform

The discovery of point defects in solid crystal structures such as the nitrogen vacancy center in diamond in the last decade [175–177] has sparked the interest in the realization of solid-state based quantum technologies [178]. Now over 20 years later a variety of different spin defect centers in solids have been discovered and investigated with intriguing spin and optical properties [179–181].
In the following, I will focus on silicon carbide (SiC) as a host crystal of such defects and shortly introduce its properties, making this platform unique and some challenges that still need to be tackled. SiC is a wide bandgap semiconductor, and a complementary metal-oxide-semiconductor (CMOS) compatible material. In recent years SiC has become increasingly important for the high-power and high-temperature electronics industry, mainly due to its high thermal conductivity [182, 183]. Because of this increasing interest in the industry, high-quality crystal growth techniques for SiC and the overall large-scale availability are widely established. Furthermore, SiC is a nanofabrication-friendly material that is easy to implement in existing process structures, which promises high-quality nanophotonic structures for scalable quantum applications.
silicon carbide exists in equal measures out of silicon and carbon atoms, which can be arranged in over 250 different polytypes [184]. Contrary to this amount of different polytypes, there exist only three different crystal structures, cubic, hexagonal and rhombohedral [184]. The three different crystal structures are, in the usual nomenclature, indicated by the capital letters C, H, and R. Furthermore, there can occur different stacking orders in SiC, which means different 2-layers (cubic, hexagonal or rhombohedral) can be packed in different ways leading to different SiC double layers in the unit cell. Thus, as a second nomenclature, the number of double layers stacked

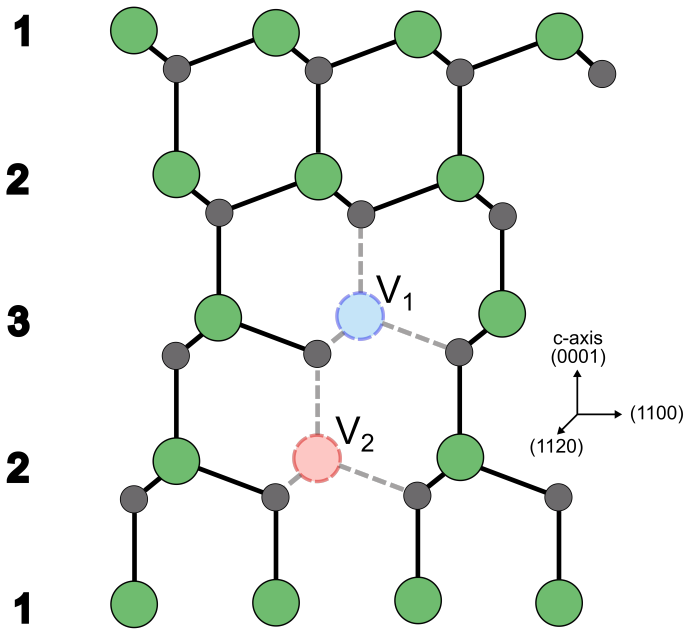

Figure 5.1: **SiC vacancy in 4H-SiC** Location of to different vacancy centers in 4H-SiC. A V_1 center results from a missing Si atom in the cubic k lattice site. A V_2 center emerges when a Si atom in the hexagonal h lattice site is missing [4].

onto each other in one unit cell is defined. In the case of hexagonal SiC there are three ways to achieve the closest packing (which we will label here 1, 2, and 3 [184]). For example, the unit cell of the polytype 2H-SiC consists of a stacking 1-2, 4H-SiC of 1-2-3-2 (see Fig. 5.1), and 6H-SiC of 1-2-3-1-3-2. So far, mostly the polytypes 4H, 6H, and 3C have been experimentally investigated as a host of optically-active spin defects [185, 186]. In the following, we will focus on the 4H-SiC polytype.

5.1.1 Optically active defects in silicon carbide

Wide bandgap semiconductors like silicon carbide promise, due to their large bandgap (between $2.3-3.3\,\mathrm{eV}$ depending on the crystal structure of SiC [187, 188]), to be excellent host materials for optically addressable spin defects. This wide bandgap ($3.2\,\mathrm{eV}$ for 4H-SiC) promises to protect the system from decoherence [189]. Additionally, the broadband transparency of $0.37-5.6\,\mu\mathrm{m}$ makes it an especially interesting material for optical interactions. Like single atom systems, color centers in solid-state materials can have unique properties like spin, energy levels, and coherence times. As aforementioned, I will focus solely on 4H-SiC, which can show various color centers such as monovacancy (V_C, V_{Si}, ...), divacancy (V_CV_{Si}), nitrogen vacancy centers, etc. [190].
In this section, I focus on the silicon vacancy (V_{Si}) as this defect system is a promising candidate for quantum information applications as shown in recent scientific publications [191–193].
The missing silicon atom leaves four dangling covalent bonds from the four nearest neighboring carbon atoms pointing to the vacant site [5], which evolves into a five-electron system if a free charge is trapped in the vacant site. This five-electron systems forms two orbitals with a_1-symmetry and one e orbital (see Fig. 5.2a). Calculations

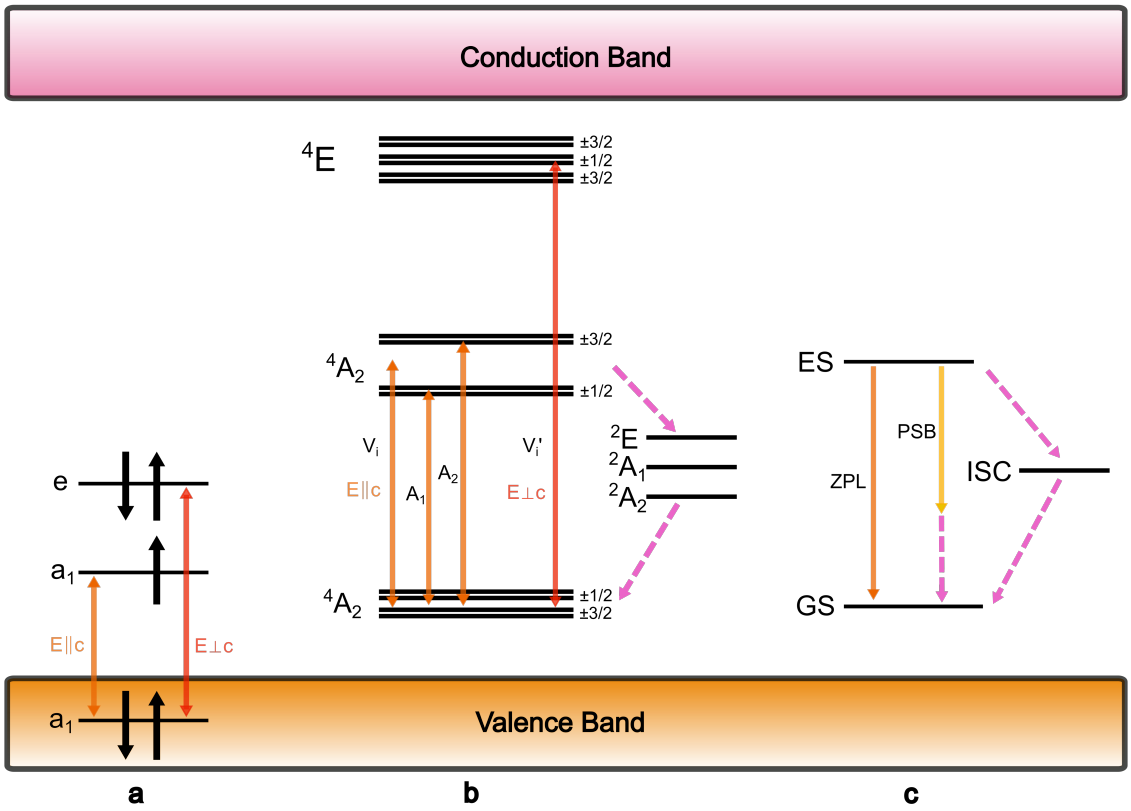

Figure 5.2: **Level structure of the negatively charged silicon monovacancy in silicon carbide** **a** Electronic orbital configuration of the negatively charged silicon mono-vacancy in 4H-SiC. The presented electron distribution is presumed to be the ground state. To excitation paths (V and V') can be optically addressed by electric fields either perpendicular or parallel to the c-axis of 4H-SiC [5]. **b** This electron configuration can be assigned to a three level system ($^4A_2(1)(a_1^2a_1^1e^2)$, $^4A_2(2)(a_1^1a_1^2e^2)$, $^4E_2(a_1^1a_1^1e^3)$) and a coupled intersystem crossing (^{2}E,^{2} A$_1$,^{2} A$_2$) [6]. **c** A highly simplified illustration of the lower two states gives rise to the designation of the purely optical decay channel as "zero phonon line" (ZPL) and the "phonon side band" (PSB).

based on group theory predict that the ground state configuration of this five electron system is presumed to be a double population of the lower a_1 orbital, a population with one electron of the upper a_1 orbital and again two electrons in the e orbital [5] (see Fig. 5.2a). While the lower a_1 level is still in the valence band the upper a_1 and the e level are located in the wide bandgap (see Fig. 5.2a). This ground state population can be written as $a_1^2a_1^1e^2$. There are two predicted excitation paths inside of the bandgap, exciting one electron from the lower a_1 to the upper a_1 level or from the lower a_1 to the e level. While an excitation from the ground state into the e orbital is only possible with an electric field perpendicular to the c-axis (Fig. 5.1) the transition between the a_1 orbitals takes place only under parallel polarization of the electric field in respect to the c-axis [5].
A representation of this orbital or energy level scheme is shown in Fig. 5.2b. Here the excitation scheme is represented as a three-level system with an additional inter-system crossing. These states consist out of an ground state $^4A_2(1)(a_1^2a_1^1e^2)$, a first

excited state $^4A_2(2)(a_1^1a_1^2e^2)$, a second excited state $^4E_2(a_1^1a_1^1e^3)$ and an ensemble of intermediate optically not addressable states ^2E, $^2A_1$ and $^2A_2$ [6]. The general nomenclature assigns the excitation path between the ground state $^4A_2(1)(a_1^2a_1^1e^2)$ and the excited state $^4A_2(a_1^1a_1^2e^2)$ the name V_i (with $i = 1, 2$ dependent on the location of the vacancy) and the transition between the ground state and the second excited state $^4E_2(a_1^1a_1^1e^3)$ as V_i'. While the investigation of the V_i and V_1' transition is part of recent research [5,191,193–198] the V_2' transition has been theoretically predicted but not yet observed experimentally.

This system possesses a total spin of $S = 3/2$, which is a quartet consisting of two Kramer's degenerate doublets with $ms = \pm 1/2$ and $ms = \pm 3/2$ [195]. The optical transitions are spin-conserving and assigned as A_1 and A_2 corresponding to each spin sub-level.

A simplified scheme can be drawn for an easier description of the fluorescence spectrum of the vacancy centers (Fig. 5.2c). Here only the V_i transitions are taken into account, and furthermore, any multi-particle fine structure splitting is ignored. Thus, the system can be considered as an optical two-level system with an additional intersystem crossing linked to metastable-state manifolds. In principal, three different decay processes can take place.

The first decay process is, most likely desired for quantum network applications, a direct optical spin conserving decay from the excited state (ES) down to the ground state (GS) by emitting a photon that corresponds directly to the energy gap between the lowest vibrational levels of the ES and GS.

A second type of decay can happen by emitting a photon with accompanying phonons of varying energy. In the latter case, the energy of the emitted photon depends on the energy dissipated into phonon modes of the lattice surrounding.

As a third decay channel, a decay via the intersystem crossing (ISC) can occur without the emission of photons but of phonons.

In the general nomenclature, the first decay channel is assigned as the "zero phonon line" (ZPL) and the second decay channel as the "phonon sideband" (PSB) [196]. As the energy of the ZPL is only dependent on the energy gap between the ES and the GS, this line appears in a spectral study of the fluorescence as a sharp peak, while the energy of the PSB shows a variety of different energies, which results in a spectral analysis as a broad emission spectrum towards lower energies (frequencies) than the ZPL [196].

The fluorescence of the ZPL appears for the V_1 center at 861 nm and for the V_2 center at 917 nm [197,199,200]. For both the V_1 and V_2 center, the Debye-Waller factor, which resembles the ratio between the ZPL and the entire emission spectrum (sum over ZPL and PSBs) at low temperatures, has been experimentally determined to be approximately $6-9\%$ [193,196,201]. Furthermore investigations using Hahn-echo experiments showed that the system exhibits long spin coherence times of up to 1.4 ms [191,196,202]. Another compelling advantage of the V_2 center is spectral stability up to 20 K: Up to this temperature, the photoluminescence (PL) spectrum still shows optical transitions with narrow PL linewidths [198]. The lifetime of the V_1 excited state(s) is approximately $5-6$ ns [193, 195, 199] (dependent on the excitation path A_1 or A_2, see Fig. 5.2b) and for the V_2 excited state(s) approximately $6-7$ ns [191, 194].

While the SiC platform promises several advantages as industrial scale availability,

excellent spin properties, and optical addressability, there is one remaining challenge: the small ratio of emission into the ZPL (Debye-Waller factor of $6-9\%$ [193, 201]). While the ZPL is a spin-conserving transition a photon from the PSB is not suitable for spin-photon interaction experiments in quantum information processing. Additionally, small collection efficiencies in standard confocal setups of about 1% decrease the detection rates. Here, the high refractive index of SiC (approximately $n = 2.6$ for 4H-SiC at 917 nm) benefits total internal reflection at smaller entry angles as other materials and thus leads combined with the emission of a dipole in a spatial angle of 4π to low collection efficiencies.
A variety of different concepts exist to tackle this challenge. Most of these approaches can be summarized into two major concepts. The first concept is to increase the overall collection efficiency and the second is to increase the emission into the ZPL by relatively decreasing other decay channels. While increasing the coupling efficiency is a straightforward (almost geometric) process, the suppression of other decay channels proves to be more complex. In the first half of the 20th century, Edward M. Purcell proved that spontaneous emission is dependent on the environment of the emitter [203].[1]
The transition rates of an atomic (or other) emitter are dependent on the density of final states [205, 206]. Thus, the presence of a cavity or other guiding systems like waveguides can alter these rates by changing the density of states [207–209]. The fractional increase in the total emission rate is defined as the Purcell factor. Often in literature, this effect is referred to as the Purcell enhancement. An elegant way to combine both concepts for solid state emitters is the location inside nanophotonic structures (like photonic crystal cavities) with a highly efficient fiber interface. As a step towards realizing such nanophotonic structures and interfaces, I will present in the following the development of a tapered-waveguide-to-tapered-fiber interface.

5.2 Theoretical description of nanophotonic structures

In this section, the basic theory of light propagation with macroscopic regions of different homogeneous dielectric media will be discussed. In the first part, I will briefly introduce the guiding of light in a dielectric medium using a comparison with quantum mechanics. As a next step the guidance of light in waveguides will be detailed by using simple ray optics. In this section, the existence of distinct modes and the single-mode behavior of waveguides will be explained. Subsequently, for more complex structures a numerical approach, Yee's finite difference algorithm, to solve Maxwell's equation in complex geometries is introduced. This algorithm was used for all simulations in this thesis. As a small additional section the basic principle of grating coupling is motivated.

[1] Edward M. Purcell received, together with Felix Bloch, the Nobel Prize in Physics, in 1952, not for the Purcell enhancement but "for their development of new methods for nuclear magnetic precision measurements and discoveries in connection therewith" [204].

5.2.1 Fundamental wave propagation in dielectric media

The fundamental description of electromagnetic wave propagation in any media is based on the four macroscopic Maxwell's equations [9, 10]:

$$\nabla \cdot \vec{D}(r,t) = \rho, \tag{5.1}$$

$$\nabla \cdot \vec{B}(r,t) = 0, \tag{5.2}$$

$$\nabla \times \vec{E}(r,t) = -\frac{\partial \vec{B}(r,t)}{\partial t}, \tag{5.3}$$

$$\nabla \times \vec{H}(r,t) = \vec{j} + \frac{\partial \vec{D}(r,t)}{\partial t}, \tag{5.4}$$

which reduce in the absence of free carriers and currents to their reduced form:

$$\nabla \cdot \vec{D}(r,t) = 0, \tag{5.5}$$

$$\nabla \cdot \vec{B}(r,t) = 0, \tag{5.6}$$

$$\nabla \times \vec{E}(r,t) = -\frac{\partial \vec{B}(r,t)}{\partial t}, \tag{5.7}$$

$$\nabla \times \vec{H}(r,t) = \frac{\partial \vec{D}(r,t)}{\partial t}. \tag{5.8}$$

In this introductory section, we perform some further reasonable assumptions [210]. We assume a macroscopic and isotropic medium, so $\vec{D}(r,t)$ is dependent on the electric field $\vec{E}(r,t)$ and the product of the vacuum permittivity ϵ_0 and the relative permittivity $\epsilon_r(\vec{r},\omega)$. Additionally, we assume a transparent media, so the relative permittivity ϵ_r is real and positive. Further small enough field strengths are assumed so that higher order terms of the electric susceptibility χ_{E} can be neglected. As a last assumption, we ignore for the moment any dispersion of the relative permittivity, so $\epsilon_r(\vec{r})$ is frequency independent.
Using the assumptions above, the magnetic field strength $\vec{H}$ and the electric displacement field $\vec{D}$ can be written as:

$$\vec{H}(r,t) = \frac{1}{\mu_0 \mu_r}\, \vec{B}(r,t), \tag{5.9}$$

$$\vec{D}(r,t) = \epsilon_0\, \epsilon_r(\vec{r})\, \vec{E}(r,t), \tag{5.10}$$

with μ_r the vacuum permeability in medium.
Furthermore we use a common "trick" to write electromagnetic fields as a real part multiplied by a complex-valued field [210]:

$$\vec{H}(r,t) = \mathrm{Real}\{\vec{H}(r)\}\, e^{i\omega t}, \tag{5.11}$$

$$\vec{E}(r,t) = \mathrm{Real}\{\vec{E}(r)\}\, e^{i\omega t}. \tag{5.12}$$

With this approach inserted in equation (5.7) and (5.8) we can eliminate the electric field $\vec{E}(r)$ ending up in:

$$\nabla \times \left(\frac{1}{\epsilon_r(r)} \nabla \times \vec{H}(r) \right) = \left(\frac{\omega}{c} \right)^2 \vec{H}(r), \tag{5.13}$$

with $c = 1/\sqrt{\epsilon_0 \mu_0}$ the vacuum speed of light. An interesting aspect of this equation, is its comparability to the Hamilton operator in quantum mechanics.
If we take a closer look onto equation (5.13) it is comparable to an eigenvalue problem:

$$\hat{O}\vec{H}(r) = \left(\frac{\omega}{c}\right)^2 \vec{H}(r), \tag{5.14}$$

where $\hat{O}$ is an operator which takes the curl, then divides by $\epsilon_r(r)$ and as a last step again takes the curl.
As a result of a direct comparison with quantum mechanics an interesting consequence can be drawn [210]:

	Quantum Mechanics	Electrodynamics
Field	$\vec{\Psi}(r,t)e^{iEt/\hbar}$	$\vec{H}(r)e^{i\omega t}$
Eigenvalue equation	$\hat{H}\Psi = E\Psi$	$\hat{O}\vec{H} = (\frac{\omega}{c})^2\vec{H}$
Hermitian operator	$\hat{H} = -\frac{\hbar}{2m}\nabla^2 + V(r)$	$\hat{O} = \nabla \times \frac{1}{\epsilon_r(r)}\nabla\times$

In quantum mechanics, the lowest eigenstates typically resemble regions of low potentials. Compared to that in electrodynamics the lowest modes have their electric energy concentrated in regions of high relative permittivity $\epsilon_r(r)$ [210]. Thus issuing an outlook on the propagation of light in dielectric media, electromagnetic waves tend to concentrate in regions of high refractive index ($n = \sqrt{\epsilon_r \mu_r}$). This effect can be used to design waveguides of high refractive index material surrounded by a lower refractive index material.

5.2.2 Ray optics

The following will discuss the propagation of light in such waveguides. Before that, I will introduce a standard nomenclature of two different mode types, the transverse-electric mode (TE mode) and the transverse-magnetic mode (TM mode). For the TE mode, the electric field is perpendicular to the plane of incidence (for example, xy-plane), while the magnetic field is parallel (Hx, Hy, Ez). In the case of the TM mode, the magnetic field is perpendicular to the plane of incidence (for example, xy-plane), while the electric field is parallel to it (Ex, Ey, Hz).
Using simple ray optics is an intuitive approach to the guidance of light in waveguides. An optical waveguide can be considered as a region of high refractive index, which is surrounded by a low refractive material. Thus according to Snell's law (see Fig. 5.3):

$$\frac{\sin(\theta_1)}{\sin(\theta_2)} = \frac{n_2}{n_1}, \tag{5.15}$$

for $n_1 > n_2$ the angle θ_2 is larger than θ_1. If θ_2 approaches $\pi/2$ total internal reflection occurs ($\theta_1 = \theta_{\text{tot.refl.}}$) under the condition:

$$\sin(\theta_{\text{tot.refl.}}) = \frac{n_2}{n_1}. \tag{5.16}$$

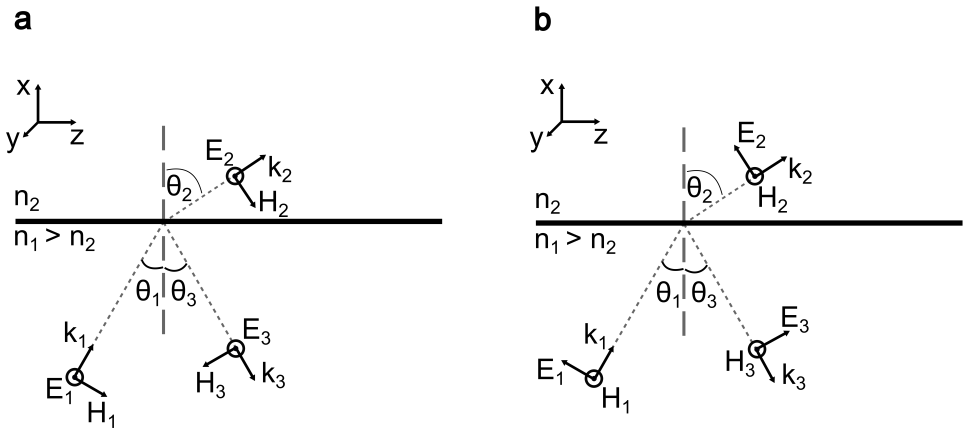

Figure 5.3: **Snell's law.** **a**, Propagation of the transverse-electric and **b**, transverse-magnetic modes on a dielectric boundary in yz-plane.

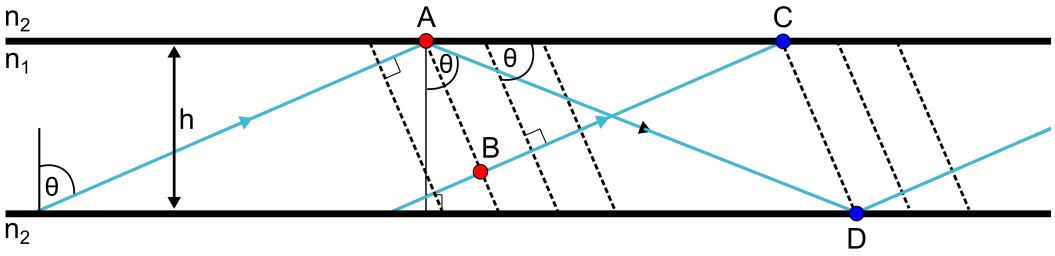

Figure 5.4: **Schematic of a two-dimensional slab waveguide.** Each colored line indicates a plane wave propagating through the slab waveguide of height h. Dashed lines indicate wave fronts with the same phase. The point pairs A and B, and C and D present a common phase front. While a ray traveling from B to C ($\overline{BC}$) is not reflected a beam traveling from A to D ($\overline{AD}$) is reflected twice. Thus, the wavefront accumulated along $\overline{BC}$ and $\overline{AD}$ have to differ by a multiple of 2π.

To understand the underlying process let us consider the longitudinal components of the wave vectors (see Fig. 5.3):

$$k_{2z} = k_{1z} = n_1 \, k_0 \, \sin(\theta_1) > n_2 k_0. \tag{5.17}$$

Since $k_{2x}^2 + k_{2z}^2 = n_2^2 k_0^2$, the transverse vector component k_{2x} has to be purely imaginary and thus the evanescent transverse field decays exponentially [211].
Furthermore, it is worth noticing that due to the Goos-Hähnchen-effect [212] the reflected field experiences a phase shift:

$$\phi_p = 2 \arctan\left(\sigma_p \frac{\sqrt{n_1^2 \sin(\theta_1)^2 - n_2^2}}{n_1 \cos(\theta_1)} \right), \quad \sigma_p = \begin{cases} 1 & \text{TE} \\ \frac{n_1^2}{n_2^2} & \text{TM} \end{cases} \tag{5.18}$$

So far, the assumption that each wave in a waveguide, provided the requirement $\theta > \theta_{\text{tot.refl.}}$ is fulfilled, will be a guided mode seems to be realistic. However, to

the requirement of internal reflection, guided modes have to satisfy a certain phase relation. In Fig. 5.4 the easiest case of a two-dimensional slab waveguide is illustrated. This figure represents two plane waves traveling through a waveguide of height (width) h. The dashed lines correspond to phase fronts and the point pairs A and B, and C and D have a common phase. Thus the phase difference of the paths $\overline{BC}$ and $\overline{AD}$ have to differ by a multiple of 2π:

$$-n_1\, k_0\, \overline{BC} = -n_1\, k_0\, \overline{AD} + 2\phi_p + m\, 2\pi, \quad m \in \mathbb{N} \tag{5.19}$$

From Fig. 5.4 the expressions $\overline{BC} = (h\tan(\theta) - h/\tan(\theta))\sin(\theta)$ and $\overline{AD} = h/\cos(\theta)$ can be derived. Thus, equation (5.19) can be reduced to:

$$2h\, n_1\, k_0\, \cos(\theta) = 2\phi_p + m\, 2\pi, \quad m \in \mathbb{N}. \tag{5.20}$$

This equation can be solved for discrete values of m only. This means, that only a discrete number of angles are allowed, each representing a so-called waveguide mode. In reality the situation is far more complex, especially for including the third dimension or nonuniform refractive indices [211]. Thus different numerical methods are commonly used to design waveguides and calculate their properties.
In general, numerical algorithms rely on the discretization of the refractive index within a finite computational domain (mesh grid). At the respective mesh points, Maxwell's equations or the corresponding wave equations can be approximated by a set of linear equations, which then can be solved numerically.

5.2.3 Yee's finite difference algorithm

The algorithm for the simulation presented in this work is based on Yee's finite difference algorithm [213]. This algorithm takes the vector from the equations (5.7) and (5.8), representing a set of six scalar equations:

$$\frac{\partial H_x}{\partial t} = \frac{1}{\mu}\left(\frac{\partial E_y}{\partial z} - \frac{\partial E_z}{\partial y}\right), \tag{5.21}$$

$$\frac{\partial H_y}{\partial t} = \frac{1}{\mu}\left(\frac{\partial E_z}{\partial x} - \frac{\partial E_x}{\partial z}\right), \tag{5.22}$$

$$\frac{\partial H_z}{\partial t} = \frac{1}{\mu}\left(\frac{\partial E_x}{\partial y} - \frac{\partial E_x}{\partial y}\right), \tag{5.23}$$

$$\frac{\partial E_x}{\partial t} = \frac{1}{\epsilon}\left(\frac{\partial H_z}{\partial y} - \frac{\partial H_y}{\partial z}\right), \tag{5.24}$$

$$\frac{\partial E_y}{\partial t} = \frac{1}{\epsilon}\left(\frac{\partial H_x}{\partial z} - \frac{\partial H_z}{\partial x}\right), \tag{5.25}$$

$$\frac{\partial E_z}{\partial t} = \frac{1}{\epsilon}\left(\frac{\partial H_y}{\partial x} - \frac{\partial H_x}{\partial y}\right). \tag{5.26}$$

with $\epsilon = \epsilon_0\, \epsilon_r$ and $\mu = \mu_0\, \mu_r$. Further, a so-called Yee cell is defined, which introduces a grid point, following Yee's notation [213], of:

$$(i,\ j,\ k) \equiv (i\,\Delta x,\ j\,\Delta y,\ k\,\Delta z). \tag{5.27}$$

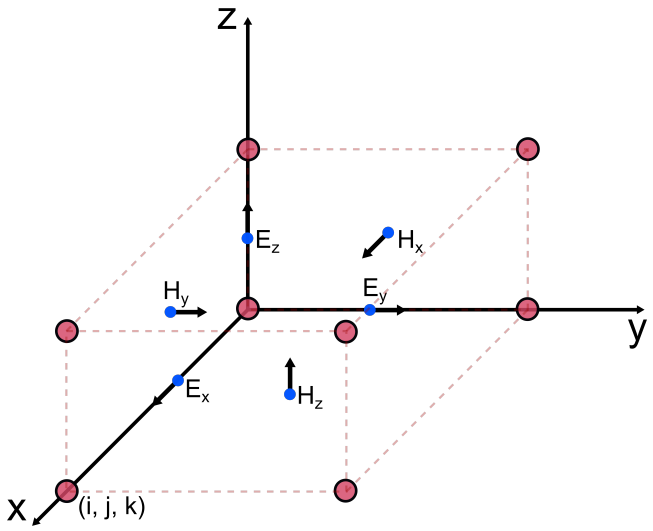

Figure 5.5: **Yee-cell.** Schematic representation of a yee-cell and calculated electric and magnetic field parameters of the TM and TE modes.

With time as a fourth dimension $(i\,\Delta x,\ j\,\Delta y,\ k\,\Delta z,\ n\,\Delta t)$ the components of $\vec{E}$ and $\vec{H}$ are evaluated at alternating half-time steps (see Fig. 5.5). Here we make use of the central finite difference approximation (CFDA) [214], where the derivative of a function f'(x) is approximated by an infinitesimal small half step before and after the point of interest, resulting in:

$$f'(x) = \lim_{h\to 0} \frac{f(x+h/2) - f(x-h/2)}{h}. \tag{5.28}$$

Thus equations (5.21-5.26) can be approximated as (exemplary shown for equation (5.21)):

$$\frac{B_x^{n+1/2}(i,j+\frac{1}{2},k+\frac{1}{2}) - B_x^{n-1/2}(i,j+\frac{1}{2},k+\frac{1}{2})}{\Delta t} = \tag{5.29}$$

$$\frac{E_y^n(i,j+\frac{1}{2},k+1) - E_y^n(i,j+\frac{1}{2},k)}{\Delta z} - \tag{5.30}$$

$$\frac{E_z^n(i,j+1,k+\frac{1}{2}) - E_z^n(i,j,k+\frac{1}{2})}{\Delta y}. \tag{5.31}$$

With this approximation and the introduced four dimensional Yee-cell $(i\,\Delta x,\ j\,\Delta y,\ k\,\Delta z,\ n\,\Delta t)$, the electric and magnetic field components can be calculated via linear equations. This gives rise to a numerical solution to calculate macroscopic problems by dividing space and time into small cubes (Yee-cells), which are solved using CFDA. Therefore, by step wise solving these equations the time evolution of electromagnetic fields in any media and geometry can be calculated avoiding complex computation techniques like derivatives or integrals.
To ensure the stability of the algorithm the temporal step size has to be chosen small enough, such that the electromagnetic wave does not propagate in one time step Δt

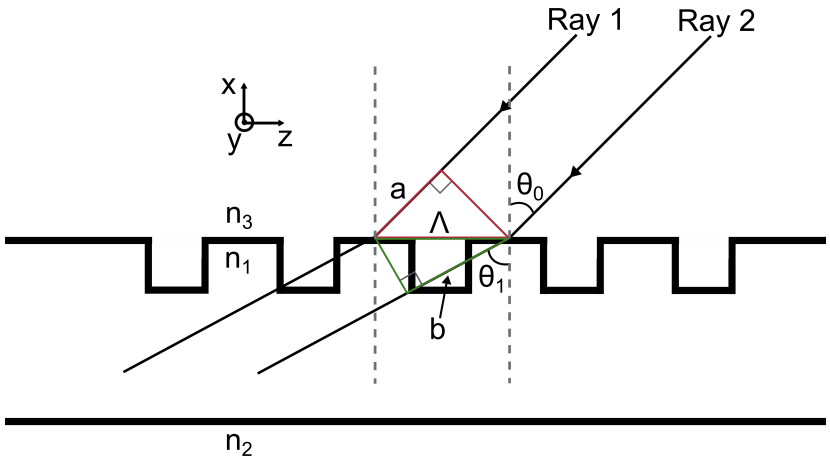

Figure 5.6: **Waveguide grating.** Principle of coupling modes by periodic perturbation.

out of the Yee-cell. The electromagnetic wave will travel in each time increment Δt maximally the distance $\Delta x = c\,\Delta t$ (with the maximal velocity of speed of light in vacuum c). Extended to three dimensions the spatial increment ($\Delta s = \Delta x = \Delta y = \Delta z$) and the time increment Δt has to satisfy the so called Courant condition [215, 216]:

$$\frac{u_{\max}\,\Delta t}{\Delta s} \leq \frac{1}{\sqrt{n}}, \tag{5.32}$$

with $u_{\max}$ the maximum phase velocity and n the number of space dimensions (alternatively $u_{\max}$ can be replaced by the speed of light in vacuum c).

5.2.4 Waveguide grating

A common way to couple light in or out of a waveguide is to introduce periodic structures along the waveguide. An intuitive approach is given by the grating equation or Bragg condition. Consider the case of the already introduced slab waveguide in section 5.2.2. In Fig. 5.6, we added rectangular corrugations with a periodicity of Λ. Without loss of generality, we cover solely the case of light entering the waveguide. In this figure, two rays (Ray 1 and Ray 2) shine from a medium of refractive index n_3 onto the waveguide with periodic corrugations (with refractive index n_1). The optical path length difference between these two rays is, therefore:

$$n_1 b - n_3 a = \Lambda\, n_1\, \sin(\theta_1) - \Lambda\, n_3\, \sin(\theta_0). \tag{5.33}$$

To achieve constructive interference the optical path length difference has to be equal to multiples of the wavelength λ of the rays. Thus, this equation can be written as:

$$\Lambda\,(\,n_1\,\sin(\theta_1) - n_3\,\sin(\theta_0)\,) = m\,\lambda, \quad m \in \mathbb{N}. \tag{5.34}$$

Furthermore, equation (5.34) can be derived in a more general way in terms of the

wavevector $\vec{k}$. Using the coordinate system from Fig. 5.6 yields:

$$k_{1,z} = k_{0,z} + m\,\frac{2\pi}{\Lambda}, \quad m \in \mathbb{N}., \tag{5.35}$$

$$k_{1,y} = k_{0,y}, \tag{5.36}$$

with the indices $k_{i,j}$, $i = 0, 1$ denote the incoming and diffracted beam and $j = y, z$ the direction in space. A common nomenclature is to call the term $K = m\frac{2\pi}{\Lambda}$ the grating vector. Since the absolute value of the wavevector $\vec{k}$ can be expressed as $|\vec{k}| = n\frac{2\pi}{\lambda}$ the component of k_z can be expressed as $k_z = n\frac{2\pi}{\lambda}\sin(\theta)$. Thus, equations (5.34) and (5.35) are equivalent. Using $|\vec{k}| = n\frac{2\pi}{\lambda} = k_z^2 + k_x^2$ the component k_x can be calculated as:

$$k_x = \sqrt{n^2\,\frac{2\pi}{\lambda} - k_z^2} = n\,\frac{2\pi}{\lambda}\cos(\theta_1). \tag{5.37}$$

Equations (5.34) and (5.35) are only satisfied for angles $-1 < \sin(\theta_1) \leq 1$. Satisfying this restriction leads to a plane wave propagating along the direction $\vec{k}$. For angles not satisfying $-1 < \sin(\theta_1) \leq 1$ the diffracted wave in $\vec{k}$ direction is decreasing by a factor of:

$$\exp\left(-i\vec{k}\vec{r}\right) = \exp(-ik_x x)\,\exp(-ik_z z). \tag{5.38}$$

These orders are commonly named evanescent orders. Thus for certain sets of parameters and geometries a periodic change of a waveguide can lead to an injection or ejection of light inside or outside of a waveguide.

5.3 Strategies to increase the collection efficiency

As described in section 5.1, solid-state emitters, despite offering excellent spin-optical properties, suffer from low collection efficiencies when investigated in bulk material. To overcome this challenge, a guidance of the emitted light and, therefore, a reduction of the spatial emission angle is favorable. A straightforward approach is the confinement in cavity or waveguide setups, both promising to increase the emission in one direction in space. Due to the tight mode confinement of light in space and the scalability in nanophotonic quantum systems, the development of nanophotonic structures is particularly appealing. While waveguides themselves mainly promise the guidance of light and thus an increased emission in one direction in space, cavity approaches promise to increase the photon spin interaction by the Purcell effect [203].
Due to their size, nanophotonic structures promise the realization of complete quantum optical setups in narrow space and thus a straightforward way to scalability. An essential step toward realizing such quantum systems on a chip is the increase in the efficiency of the insertion or extraction of single photons from these nanostructures into optical fibers.
To path the way for the integration of single defects into waveguides and dramatically increase the collection efficiency, I will present in the following sections a nanophotonic-waveguide-to-fiber interface with a high collection efficiency for both the insertion and extraction of light into and out of nanophotonic waveguides.
In the next section, I will briefly recap existing concepts to extract light from nanostructures into optical fibers (and vice versa). As a second step, I will go into more

detail in the case of the tapered fiber interface and introduce different manufacturing techniques.

5.3.1 Diffraction grating, edge coupling and tapered fibers.

In the past recent years a variety of approaches for interfaces between nanophotonic structures (mostly waveguides) and optical fibers emerged. The difference in size between nanophotonic waveguides and optical fibers is the main challenge of interconnecting nanophotonic structures and optical fibers. While nanophotonic structures usually show features in size between several tens of nanometers up to a few micrometers, the size of a standard single-mode optical fiber is around 125 µm with core sizes of several micrometers up to tens of micrometers. Therefore, the pure geometrical interconnection between nanophotonics and optical fibers proves to be challenging even more if multiple channels need to be addressed on a single chip.
To tackle this challenge, a couple of concepts emerged in the past. I will focus mainly on the three concepts edge [217–219] or butt coupling [220, 221], grating coupling [222, 223] and coupling with tapered single-mode fibers [224, 225].
The term edge (or butt) coupling refers to the in-plane coupling, where the optical fiber is usually placed on the facet of the chip, horizontally aligned with the waveguides [226]. While edge couplers promise high coupling efficiencies [227] relatively polarization independency and a broad bandwidth [226] they also come with some drawbacks. The very concept of edge coupling already geometrically limits its applicability. Due to its placement on the chip's edge, it limits the location of the nanophotonic structures and the number of couplers per chip.
A geometrically more convenient way to interface nanophotonic structures and optical fibers is the concept of grating coupling. Here, a periodic Bragg grating is applied at the end of the waveguide. This allows, dependent on the effective indices of the waveguide and the refractive index of the surrounding material, wave vectors with non-zero elements perpendicular to the waveguide plane (see section 5.2.4, [228]). A significant advantage is a relatively space-saving design and compact size, in addition to the freedom of the relative placement on the chip. However, without complex underlying layer structures, the symmetry of the Bragg reflection limits the coupling efficiency into the optical fiber. Even though, in theory, using highly sophisticated metastructures, almost unity coupling efficiency can be reached [222], experimental values stay so far well below this theoretical limit [223, 229–231].
As a third approach, the coupling between tapered waveguides and tapered fibers exists, with a subdivision between tapered fibers with tapered tips [224, 225], and tapered fibers with a biconical fiber taper [232]. Nanophotonic interfacing using tapered fibers promises polarization insensitive, highly efficient coupling by simply changing the width or diameter of the fiber and the waveguide. The slowly varying width or diameter introduces so-called super modes, which couple both structures with almost unity efficiency [211]. Thus this concept promises a relatively simple fabrication process compared to the prior approaches by at the same time almost unity coupling efficiency [211]. As a sign of its easy applicability, the gap between theoretically predicted and experimentally demonstrated coupling efficiency values is only in the percentage range [224, 225, 232].

In the following, I will focus solely on the approach using tapered fibers.

5.3.2 Tapered fiber production: CO_2-laser heating, thermal heating and HF etching

There are two main fabrication techniques for tapered optical fibers, thermal heating [233–235] and chemical etching [236, 237]. In the first case, an optical fiber is fixed on both sides. While a fiber segment is heated up, either by a high-power laser [234, 235], or a heater [233]. A pull is applied to expand the fiber slowly and thus creating a tapered area. This fabrication process leads at the outer rim of the tapered region to an exponential decrease of the fiber diameter [234].
The second fabrication process is based on the chemical etching of the optical fiber material with corrosive acid. Often, an aqueous solution of fluorhydric acid (HF) is used for the fabrication of tapered optical fibers [224, 225, 237]. The process is pretty straightforward; the optical fiber is stripped down to the (often 125 µm wide) cladding, dipped into the aqueous solution of fluorhydric acid (24-50%), and is, with a constant or varying velocity, pulled out. A thin layer of oil (in many cases o-Xylene) on top of the solution prevents further etching of surfacing fiber parts. Different taper angles or shapes can be realized depending on the velocity and the acceleration or deceleration (see Fig. 5.7).

5.4 Simulations

In the following, I will introduce the preceding simulations that motivated the used waveguide geometry. In the second section, the coupled tapered-waveguide-to-tapered-fiber interface is introduced, presenting the variable parameters of the tapered fiber and a motivation of the adiabatic regime using the effective index of the resulting supermodes.
Finally, two sections follow, presenting the simulations concerning:

- The taper angle β,
- The waveguide taper length,

for the in- and outcoupling, respectively, in the first section and simulations for varying tapered fiber tip diameters in the second section.
Together, this section presents a stable nanophotonic interface for

- Waveguide taper lengths $> 5\,\mu m$,
- Taper angles $1.2° < \beta < 5°$,
- Fiber tip diameters $\varnothing < 500\,\mu m$,

reaching coupling efficiencies above 96% and constant coupling for an overlap region of more than 5 µm. These results promise a stable and highly efficient interface with easy fabrication and adjustment. The following simulations have been performed by the Master student Lukas Niechziol under my supervision.

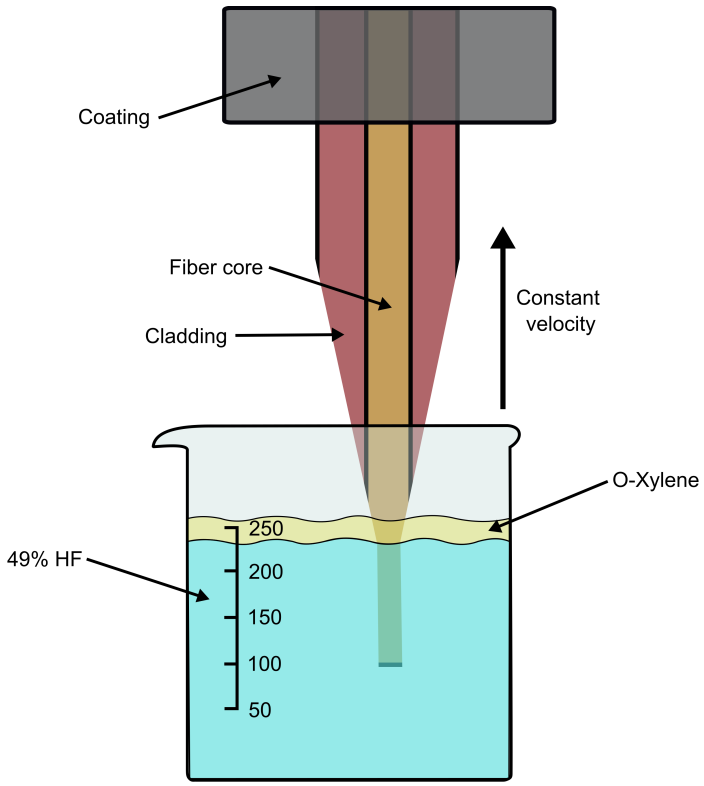

Figure 5.7: **Schematic of the taper etching process performed for this work.** The single-mode optical fiber is dipped into a 49% aqueous solution of fluorhydric acid with a thin layer of o-Xylene on top. A motorized actuator pulls the fiber with a constant velocity of 2.8 µm/s out of the acid bath, resulting in a linear decrease of the fiber diameter.

5.4.1 Simulation of single-mode waveguides using Lumerical

This section will theoretically investigate the properties of the waveguides fabricated for this experiment.
All simulations presented in this work have been done using the commercially available software Lumerical of the company Ansys based on Yee's algorithm (see section 5.2.3). For the simulation of waveguides, and later the coupling efficiency between tapered optical single-mode fibers and tapered waveguides, we used the Finite-Difference Time-Domain (FDTD) method, introduced in section 5.2.3 [213, 215, 238–240]. These sets of equations are usually solved separately for the two different transversal modes TE (Hx, Hy, Ez) and TM (Ex, Ey, Hz).
Due to their relatively easy production, we chose free-standing waveguides with a triangular cross-section for the beginning of the simulations. This waveguide design has already been well investigated and used in several successful experimental realizations [191, 225, 241–243].
We targeted a single-mode behavior at 917 nm for the free-standing waveguides with a triangular cross-section. Two parameters have been used for the simulations to define the cross-section of the waveguides; The waveguide width (w) and the etching angle (α; see Fig. 5.8). With both parameters, the cross-section is well defined. Therefore

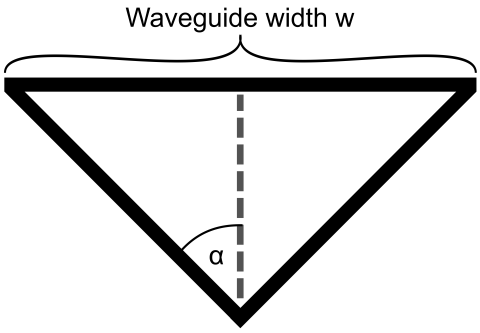

Figure 5.8: **Waveguide cross-section.** Schematic of the waveguide cross-section. The cross-section is defined by two parameters, the waveguide width w and the etching angle α.

we decided to simulate the possible guided modes for waveguides with different widths (w). Note that the etching angle has been kept constant at 45°.
All possible modes of each waveguide were excited to simulate which modes are guided in different waveguides. After several micrometers, the intensity in each mode was compared with the initial intensity. The resulting values are presented in Fig. 5.9a. Here, the relative intensity in each mode compared to the total transmitted intensity is presented as a function of the waveguide width w for modes between one and five. For up to 600 nm close to 100% of the transmitted light is completely located in the fundamental TE mode, confirming a single-mode behavior ($w = 400\,\text{nm} : 99.5\%$, $w = 500\,\text{nm} : 100\%$ and $w = 600\,\text{nm} : 90.0\%$). Note that only five modes are shown, so a population of higher order modes is possible for waveguides with a larger width above 600 nm. As an example of two different modes in Fig. 5.9b and c, the fundamental and the second mode of a waveguide with an etching angle of 45° and a width of 500 nm are presented. While for the fundamental mode, the electric field is mainly located in the center of the waveguide, the electric field distribution of the second mode shows large proportions outside of the waveguide, which already indicates, that this mode does not represent a guided mode.
As a result of these simulations, it was decided to use waveguides with a triangular cross-section, an etching angle of 45° and a width of 500 nm. In all following measurements and calculations, only this waveguide type was used.

5.4.2 Fiber coupled nanophotonic interface

With a suitable design for a single-mode waveguide, as a next step, the design of suitable tapered optical single-mode fibers remained. As discussed before, the waveguides used for all simulations are parameterized by an etch angle of 45° and a waveguide width of $w = 500\,\text{nm}$. For the tapered fiber, solely two important free parameters are left: the tip diameter of the taper ending and the taper angle β (see Fig. 5.10a and b). In the following simulations, the parameters:

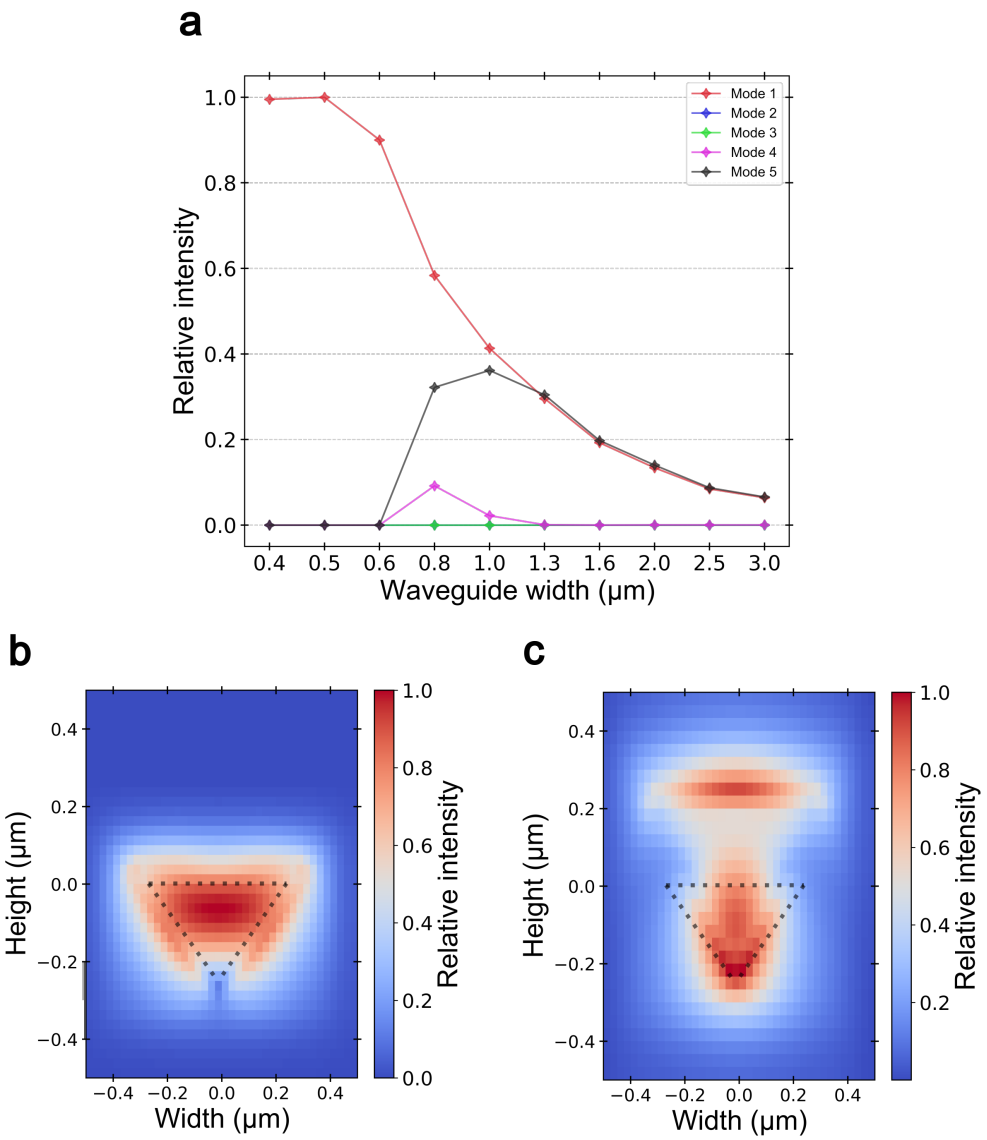

Figure 5.9: **Waveguide mode behavior.** **a**, Relative transmission for different waveguide modes of a waveguide with a triangular cross-section as a function of the waveguide width w. The angle for all waveguides had been chosen to be 45°. Up to a width of 600 nm waveguides with a triangular cross-section prove to show single-mode behavior. For wider waveguides also other modes are populated. Note, that mode 2 and 3 in this figure are equally populated so that the data points are located on top of each other.
b, Example of the fundamental TE mode of a waveguide with a triangular cross-section, an etching angle of 45° and a waveguide width of 500 nm. The dashed gray lines indicate the location of the triangular cross-section. **c**, Electric field distribution of the second TE mode of a waveguide with a triangular cross-section, an etching angle of 45° and a waveguide width of 500 nm.

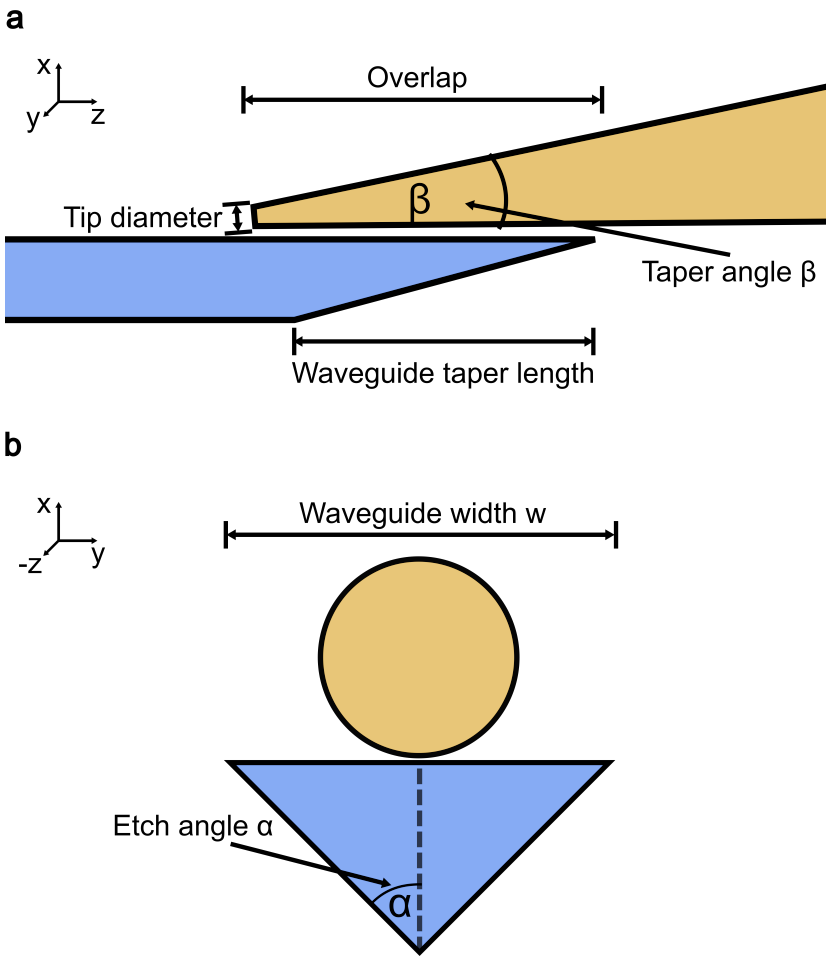

Figure 5.10: **Fiber coupled nanophotonic interface.** **a**, xz-plane of the fiber coupled nanophotonic interface. The tapered fiber is mainly defined by two characteristic lengths: the tip diameter and the taper angle β. For the waveguides a single free parameter is left: the waveguide taper length.
b, xy-plane of the fiber coupled nanophotonic interface. The waveguide (blue) is defined by an etch angle of 45° and a waveguide width of w = 500 nm.

- ❖ Taper angle β,
- ❖ Taper tip diameter,
- ❖ Waveguide taper length,

are varied. Furthermore the in- and outcoupling is simulated separately.
An interesting consequence of guided light in waveguides, as motivated in section 5.2, is, that the guided light modes show due to internal reflection a lower group velocity than in bulk. Therefore, a new parameter the effective group velocity is introduced, resulting in a more convenient value. Based on this considerations another parameter the effective index can be defined. While in optics the refractive index is defined as the speed of light in vacuum divided by the speed of light in a dielectric media $n = c/\nu$ [52], in nanophotonic structures, the effective index is the ratio of the speed of light in vacuum and of a mode for a given polarization in the direction of propagation

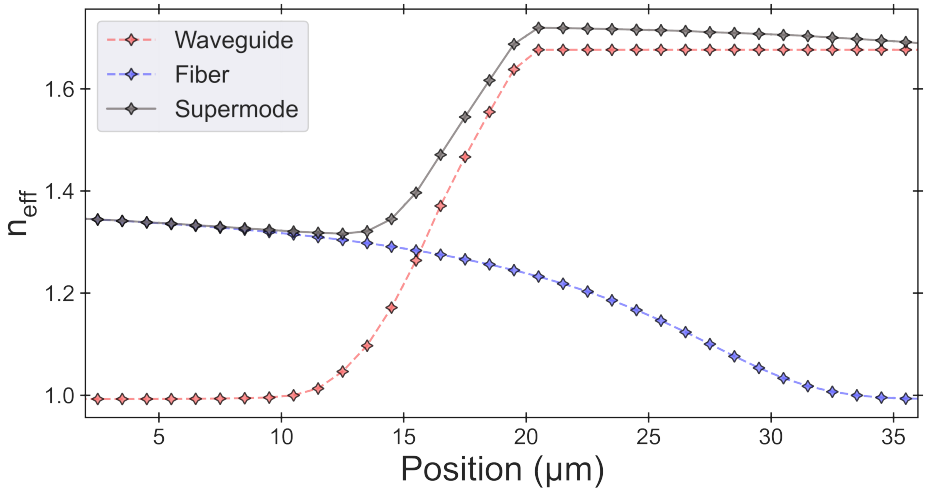

Figure 5.11: **Simulation of the effective index n_{eff}.** The blue and red lines are the simulated values of the effective index n_{eff} for the fiber and the waveguide, respectively. The waveguide tip is located at 0 µm and the fiber tip at 40 µm, creating a 40 µm overlap region. In gray the effective index of the coupled system is shown.

in the guiding structure [211]. This can be written as:

$$n_{\text{eff.,p,tm}} = \frac{c}{\nu_{\text{z,p,tm}}} = \frac{k_{\text{p,tm}}}{k_0}. \tag{5.39}$$

Here, the indices p and tm stand for polarization and transversal mode (TM, TE), respectively.
Intuitively, guided modes can only exist for effective indices greater than the refractive index of the surrounding material (in this case, air $n \approx 1$). In Fig. 5.11 the effective index of the combined system (seen in Fig. 5.10a) is shown. Here, in blue and red, the effective index n_{eff} for the fiber and the waveguide are calculated separately. The waveguide tip is located at 0 µm and the fiber tip at 40 µm, creating a 40 µm overlap region. The effective indices of the tapered waveguide and the tapered fiber approach effective index values below $n_{\text{eff}} < 1$. Thus, following the sections 5.2.1 and 5.2.2, no guided modes are obtained at a certain distance for the separated treatment. However, if we consider the combined system the effective index n_{eff} is always greater than $n_{\text{eff}} > 1.31$. Therefore, for the combined system, a guiding supermode exists.
For certain parameters, this combined system can show almost unity transmission efficiency. The key idea is to slowly change the cross-section of the waveguide along the light mode's propagation direction. The light initially in the fundamental mode of the waveguide is transferred into a supermode of the tapered-waveguide-tapered-fiber interface and further transferred adiabatically into the fundamental mode of the single-mode fiber [211, 224].
Introducing the power transfer between two parallel single-mode waveguides can give a more general overview. As a first step towards that, we present the propagation constant. For this, we imagine a translational invariant waveguide (for example, cylindrical

symmetry). For such a waveguide, the modal fields can be expressed as [211]:

$$\vec{E}_k(x,y,z) = \vec{e}_k \, \exp(i\,\beta_k\,z), \tag{5.40}$$

$$\vec{H}_k(x,y,z) = \vec{h}_k \, \exp(i\,\beta_k\,z), \tag{5.41}$$

with $\vec{e}_k$ and $\vec{h}_k$ the transversal modes, $\beta_k = 2\pi n_{\text{eff.}}/\lambda$ the propagation constant and λ the wavelength in vacuum.
With the obtained propagation constant, the so-called coupling line equations can be derived. By neglecting the possibility of coupling to counter-propagating modes and any losses, these equations for two degenerate modes can be written as [244]:

$$\frac{\mathrm{d}\Psi_1}{\mathrm{d}z} = -\,i\,\beta\,\Psi_1 + c_1\,\Psi_2, \tag{5.42}$$

$$\frac{\mathrm{d}\Psi_2}{\mathrm{d}z} = -\,i\,\beta\,\Psi_2 + c_2\,\Psi_1, \tag{5.43}$$

with β the propagation constant, Ψ_1 and Ψ_2 the amplitudes of the fundamental mode in two separated single-mode waveguides and c_1 and c_2 the associated coupling constants. This equation is an excellent approximation even for a more general view of multimode waveguides as only modes with equal phase velocity can exchange energy significantly [245].
For constant values of β, c_1 and c_2 this coupled differential equation system can be solved by:

$$\Psi_1(z) = \frac{1}{2}\left(\Psi_{1,0}(\,\mathrm{e}^{-i\Delta\beta} + \mathrm{e}^{i\Delta\beta}\,) + \sqrt{\frac{c_1}{c_2}}\,\Psi_{2,0}\,(\,\mathrm{e}^{-i\Delta\beta} - \mathrm{e}^{i\Delta\beta}\,)\right)\mathrm{e}^{-i\beta z}, \tag{5.44}$$

$$\Psi_2(z) = \frac{1}{2}\left(\Psi_{2,0}\,(\,e^{-i\Delta\beta} + e^{i\Delta\beta}\,) + \sqrt{\frac{c_2}{c_1}}\,\Psi_{1,0}\,(\,e^{-i\Delta\beta} - e^{i\Delta\beta}\,)\right)e^{-i\beta z}, \tag{5.45}$$

with $\Delta\beta = i\sqrt{c_1 c_2}$, and $\Psi_{1,0}$ and $\Psi_{2,0}$ the field amplitudes at $z = 0$. It is apparent, that these solutions show two new modes propagating with new propagation constants $\beta_1 = \beta + \Delta\beta$ and $\beta_2 = \beta - \Delta\beta$. If we assume the lossless case and further that the total energy is initially stored in mode Ψ_1 ($\Psi_{2,0} = 0$), the solutions reduce to:

$$\Psi_1(z) = \Psi_{1,0}\,\cos(\Delta\beta z)\,\mathrm{e}^{-i\beta z}, \tag{5.46}$$

$$\Psi_2(z) = -\,i\,\sqrt{\frac{c_2}{c_1}}\,\Psi_{1,0}\,\sin(\Delta\beta z)\,\mathrm{e}^{-i\beta z}. \tag{5.47}$$

There are several exciting features visible in this equation. The cross-talk between both fibers leads to an oscillating exchange of energy between both fibers. Secondly, the energy is entirely conserved, and finally, we can introduce the value of a beat length z_b, as a distance at which the total power is transferred from one fiber to the other [245]:

$$z_\mathrm{b} = \frac{\pi}{2\Delta\beta} = \frac{\pi}{\beta_1 - \beta_2}. \tag{5.48}$$

Similar to that case, the coupling can be described not only for two parallel cylindrical fibers but also for two fibers with the same taper angle β_{taper} (see Fig. 5.12). Even

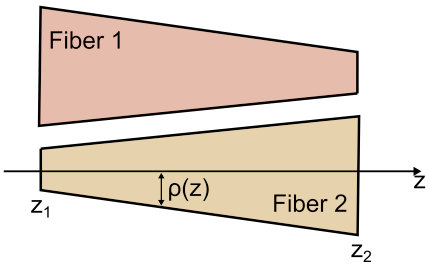

Figure 5.12: **Tapered waveguide coupler.** Two tapered fibers with reversed radii $\rho(z)$. z_1 and z_2 denote two symmetrical points of the coupler.

though this case is more complicated, it shows similar results [211]. Interestingly, contrary to the case of two cylindrical fibers, for $z \to \infty$ also $\vec{\Psi}_1 \to \vec{\Psi}_2$ is satisfied, meaning a complete energy transfer from $\vec{\Psi}_1$ to $\vec{\Psi}_2$. Even more, this derivation gives access to the conclusion that only a long enough region around the point, where both fibers have virtually identical diameters, has to vary slow enough to transfer essentially 100% of the optical power [211]. To reach this high coupling efficiencies, a slow variation criterion has to be satisfied.

Slow variation criterion

An illustrative way to explain this criterion is that the total power can be transferred over one beat length. Thus, the region of variation (we will name it characteristic length $z_{\text{ch.}}$) has to be at least equal to the beat length $z_{\text{ch.}} \leq z_{\text{b}}$ [211, 224].
This characteristic length scale $z_{\text{ch.}}$ is defined by the height of the circular cone and the apex angle equal to the local taper angle $\beta_{\text{taper}}(z) = \tan^{-1}(|\mathrm{d}\rho/\mathrm{d}z|)$ [246], with $\rho = \rho(z)$ is the local core radius. In our case, the taper angle has been, by purpose, kept constant, so $\beta_{\text{taper}}(z) = \text{const}$. Further, usually the angle β_{taper} is small ($\beta_{\text{taper}} \ll 1$), and thus:

$$z_{\text{ch.}} \approx \frac{\rho}{\beta_{\text{taper}}}. \tag{5.49}$$

Based on the findings above, it is intuitive that for $z_{\text{ch.}} \gg z_{\text{b}}$ everywhere along the fiber, negligible coupling will occur, and the fundamental mode will propagate approximately adiabatically with little loss [246]. For $z_{\text{ch.}} \ll z_{\text{b}}$ there will be a significant coupling but not long enough for a complete transfer of energy.
Analogous to the definition of the beat length using the propagation constants, also the effective indices of the two local modes can be used. Here, the beat length can be defined as:

$$z_{\text{b}} = \frac{\lambda}{n_k - n_l}, \tag{5.50}$$

Therefore, the inequality resembles as:

$$z_{\text{b}} \ll z_{\text{ch.}}, \tag{5.51}$$

$$\frac{\lambda}{n_k - n_l} \ll \frac{\rho}{\beta_{\text{taper}}}, \tag{5.52}$$

$$\beta_{\text{taper}} \ll \frac{\rho\,(n_k - n_l)}{\lambda}, \tag{5.53}$$

with n_k and n_l the effective indices of neighboring modes and λ the wavelength in vacuum. For a single-mode fiber, which only has one fundamental mode the vacuum radiation mode $n_l = n_{\text{vac.}} = 1$ can be used as n_l [224].
In our case, the effective index of the system is always above $n_{\text{eff.}} > 1.31$. Thus the beat length can be calculated (at 917 nm) as $z_b = 2.96\,\mu\text{m}$. Thus the coupling region or the tapered area has to be significantly larger than this value.
With this prediction, we could start simulations with intuitive values for the taper angle β and the waveguide taper length. In the following section, the results of this simulation are presented.

5.4.3 Overlap dependency of the transmission efficiency of tapered fibers and tapered waveguides

All following simulations consist of two separate parts. First, we simulate the incoupling into a waveguide, meaning the transmission efficiency of the fundamental mode of a single-mode fiber propagating through a tapered-fiber-tapered-waveguide interface. Second, we simulate the outcoupling, the transmission of the fundamental mode of the waveguide propagating through the tapered-fiber-tapered-waveguide interface. For both simulations, we start by exciting the fundamental mode of the fiber(waveguide) and calculate the transmission through the tapered-fiber-tapered-waveguide interface (see Fig. 5.10). We define the coupling efficiency as the ratio of the total transmission into the fundamental mode of the waveguide(fiber) and the total power initially excited in the fundamental mode of the fiber(waveguide).

Incoupling

As a first step we simulated the single-sided incoupling efficiency of a 780HP fiber ($n_{\text{fiber}} \approx 1.45$ at 830 nm) with a waveguide of triangular cross-section, a width of 500 nm and an etch angle of $\alpha = 45°$. In a first step, we assumed a perfect single-mode fiber with an infinitesimal small tip diameter (see Fig. 5.10a). Without a finite tip diameter, there are two primary geometrical parameters which define the tapered region of the single-mode fiber:

- Taper angle β,
- Waveguide taper length.

In Fig. 5.13a, the results of the single-sided incoupling efficiency as a function of the taper overlap for different waveguide taper lengths are illustrated (see Fig. 5.10a). Here, above 5 µm waveguide taper length almost unity ($> 96\%$) incoupling efficiencies are reachable. Interestingly, there exists a plateau of equal transmission, which reduces from over 16 µm for a 30 µm waveguide taper to 6 µm for a taper length of 5 µm. Thus for a stable large overlap region in which the incoupling efficiency is constant, longer waveguide tapers are favorable.
In Fig. 5.13b, the taper angle β has been varied between 1.2° and 5°. The single-sided incoupling efficiency for different taper angles has been simulated again as a function of the taper-taper overlap. Here, the same behavior as in Fig. 5.13a can be seen. For an

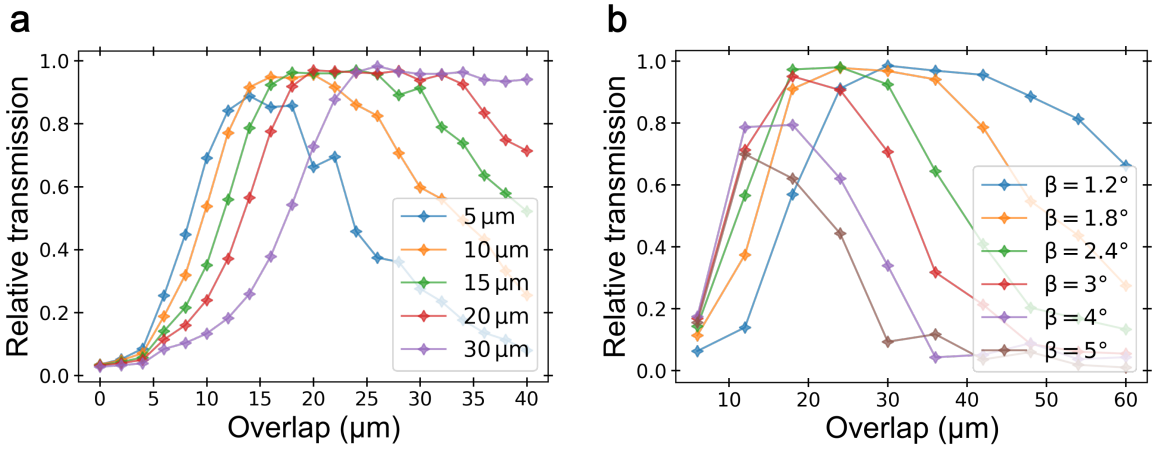

Figure 5.13: **Relative incoupling efficiency.** **a**, Relative transmission as a function of the taper-taper overlap for different waveguide taper lengths between 5 µm and 30 µm. The single-mode fiber taper angle has been kept constant at 1.8°. **b**, Relative transmission as a function of the taper-taper overlap for different single-mode fiber taper angles between 1.2° and 5°. The waveguide taper length has been kept constant at 20 µm.

increasing taper angle, the plateau of constant coupling efficiency reduces from 14 µm for a taper angle of 1.2° to below 5 µm for 5°. Furthermore, the incoupling efficiency drops from almost 100% (> 97%) to below 70% for an angle of 5°. Up to an angle of 3° the coupling efficiency can still reach values above 95%.
Thus similar to the waveguide taper, for the fiber, a smaller angle (below 3°) is favorable.
Both findings confirm the considerations presented in section 5.4.2 since both parameters, the waveguide taper length as well as the taper angle of the single-mode fiber, are in direct relation to the characteristic length $z_{\mathrm{ch.}}$.

Outcoupling

In analogy to the previous section, we performed the same simulations for the outcoupling efficiency of the excited fundamental mode of the waveguide into the fundamental mode of the single-mode fiber. The results are presented in Fig. 5.14.
In Fig. 5.14a the single-sided outcoupling efficiency for different waveguide taper lengths is shown as a function of the overlap. Here, compared to the incoupling there is no visible decrease for larger overlap values, so the coupling efficiency stays constant over the entire simulation region up to 60 µm. Even though there seems to be no decrease in the coupling efficiency for large overlap values, there is still a decrease in the absolute transmission for waveguide taper lengths shorter than 10 µm to values below 96%. Furthermore, for waveguide taper lengths longer or equal to 10 µm, the simulation shows almost unity coupling efficiency (above 98%).
A comparable result shows the variation of the single-mode fiber taper angle β in Fig. 5.14b. Here for values above 1.2° almost unity coupling efficiency can be reached (over 97%). Only for taper angles below 1.2° the outcoupling efficiency reduces below 94%. As for the variation of the waveguide taper length, a variation of the single-mode fiber

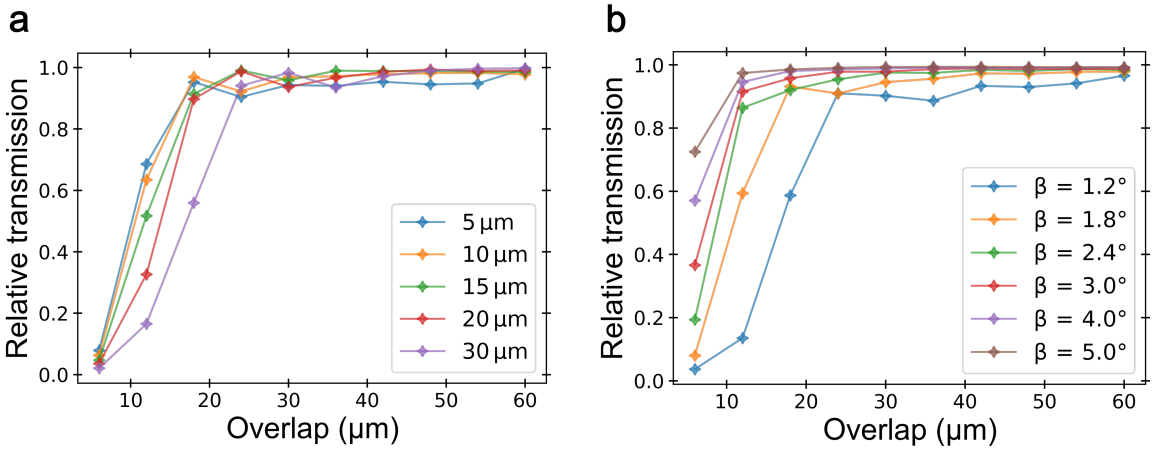

Figure 5.14: **Relative outcoupling efficiency.** **a**, Relative transmission as a function of the taper-taper overlap for different waveguide taper lengths between 5 µm and 30 µm. The single-mode fiber taper angle has been kept constant at 1.8°. **b**, Relative transmission as a function of the taper-taper overlap for different single-mode fiber taper angles between 1.2° and 5°. The waveguide taper length has been kept constant at 20 µm.

taper does not show the characteristic plateau of the incoupling (see Fig. 5.13) but stays constant over the entire simulation region up to 60 µm. Note, that in this work the utilized waveguide dimensions (waveguide lengths up to a maximum value of 120 µm) make simulations for larger overlap values obsolete.

5.4.4 Tip diameter dependency of the transmission efficiency of tapered fibers and tapered waveguides

So far, only ideal infinitesimal small fiber tip diameters, have been simulated. In reality the fiber tip (see Fig. 5.10) has a finite diameter. To investigate the influence of finite fiber tip diameters we simulated the in- and outcoupling efficiency as a function of the taper-taper overlap for fiber tip diameters ranging from 0 to 500 nm. Following the same procedure as in the last section, we performed the simulations for the incoupling and the outcoupling separately.
For an increasing fiber tip diameter, the value of the overlap changes (see Fig. 5.10a). Therefore we present in the following two separate simulations, one with the overlap measured at the end of the fiber tip with a finite diameter and second as a function of the overlap measured at the location where the ideal fiber would have ended. For these simulations, a waveguide taper length of 15 µm and a single-mode fiber taper angle of 2.4° has been used.

Incoupling

In Fig. 5.15a, the incoupling efficiency is shown as a function of the taper-taper overlap. The overlap is measured in this figure as the actual overlap of the fiber tip with the waveguide taper. In Fig. 5.15b, the overlap has been calculated as the corrected overlap of an ideal tapered fiber with a perfect infinitesimal taper tip diameter. Both

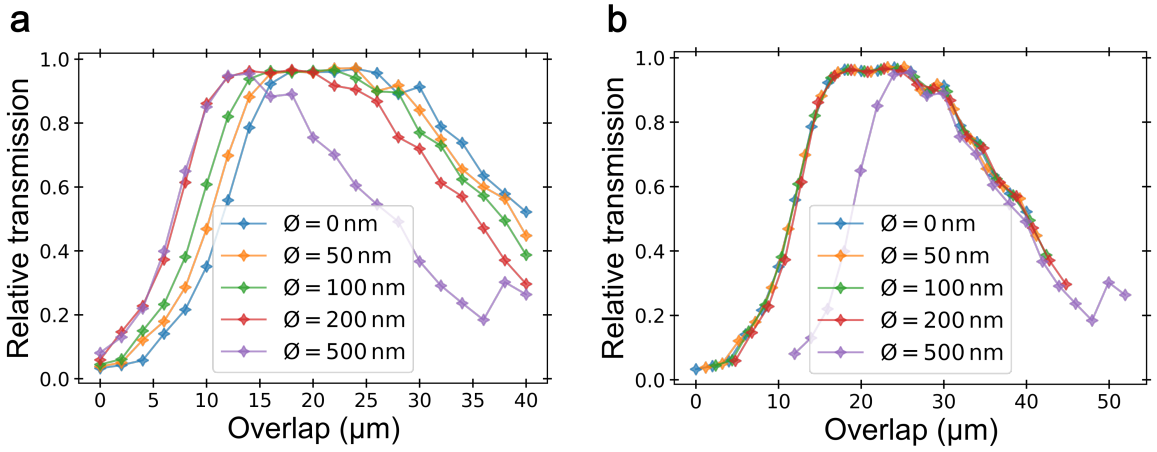

Figure 5.15: **Relative incoupling efficiency.** **a**, Incoupling efficiency as a function of the overlap for different fiber tip diameter, ranging from 0 to 500 nm. **b**, Incoupling efficiency as a function of the overlap for different fiber tip diameter, ranging from 0 to 500 nm. Here, the overlap is defined as the corrected overlap of an ideal fiber with infinitesimal fiber tip diameter.

simulations show that a fiber tip diameter up to 500 nm does not influence the almost unity coupling efficiency (above 96%). At 500 nm the characteristic plateau decreases in width from values of around 10 µm down to only 2 µm. Thus single-mode fibers with tip diameters above 500 nm lead to a reduced coupling efficiency (approximately below 95%) and a narrower coupling plateau.

Outcoupling

For the outcoupling the same simulations with a real overlap (Fig. 5.16a) and the corrected overlap (Fig. 5.16b) have been performed. Both illustrations show no reduction of the coupling efficiency up to 500 nm (above 99%). As seen in the previous section for the outcoupling the plateau ranges over the entire simulation region up to 40 µm (50 µm for the corrected overlap). Surprisingly, even for a taper tip diameter of 500 nm almost unity coupling efficiency can be reached only requiring by approximately 7 µm larger overlap.

5.4.5 Conclusion

In this section, I briefly introduced the fundamental wave propagation in dielectric media, emerging in the finite difference time domain (FDTD) approach for solving a set of linear Maxwell's equations. With the commercially available software Lumerical FDTD solver, we first characterized waveguides with a triangular cross-section and an etch angle of 45°. Here, we developed a waveguide design with a single fundamental guided mode for a design wavelength of 917 nm. As a last step, I presented simulations for the in- and outcoupling between tapered waveguides and tapered optical single-mode fibers. We investigated the effects of the parameters: Waveguide taper length, taper angle β, and the fiber tip diameter. For the incoupling an emerging plateau of constant coupling efficiency could be seen, while still for values of:

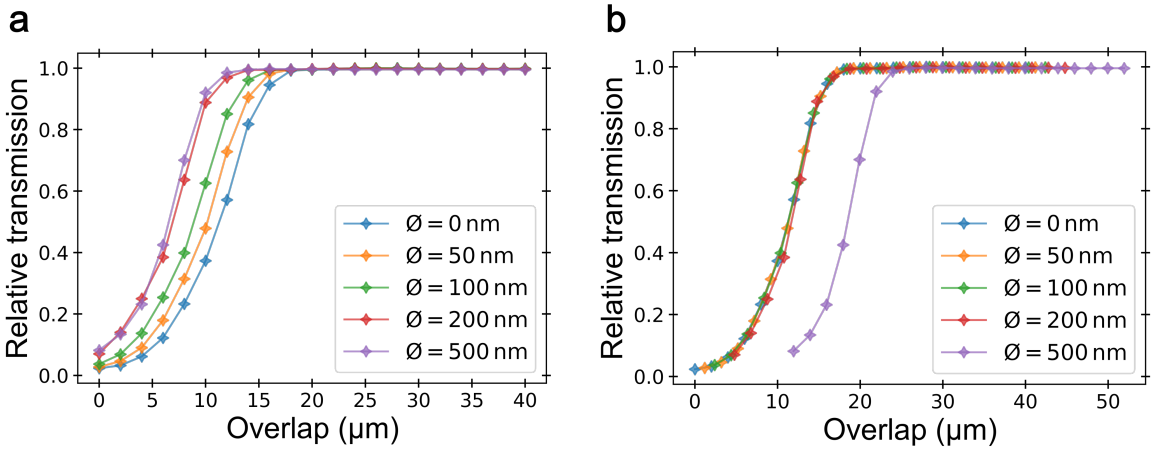

Figure 5.16: **Relative outcoupling efficiency for finite taper diameter for finite taper diameter.** **a**, Outcoupling efficiency as a function of the overlap for different fiber tip diameter, ranging from 0 to 500 nm. **b**, Outcoupling efficiency as a function of the overlap for different fiber tip diameter, ranging from 0 to 500 nm. Here, the overlap is defined as the overlap of an ideal fiber with infinitesimal fiber tip diameter.

Incoupling

- ❖ Waveguide taper length $> 5\,\mu m$,
- ❖ Taper angle $\beta < 3°$,
- ❖ Fiber tip diameter $\varnothing < 500\,\mu m$,

coupling efficiencies above 96% and plateaus larger than 5 µm could be reached. Furthermore, the outcoupling shows coupling efficiencies above 97% for

Outcoupling

- ❖ Waveguide taper length $> 5\,\mu m$,
- ❖ Taper angle $1.2° < \beta < 5°$,
- ❖ Fiber tip diameter $\varnothing < 500\,\mu m$.

The outcoupling does not develop the characteristic plateaus and therefore proves to be less prone to imperfections than the incoupling. For the same parameters as for the incoupling, coupling efficiencies above 98% can be reached.
These simulations prove the robustness of this nanophotonic interface to various fabrication errors or parameter mismatches. Furthermore, unity in- and outcoupling efficiency can be reached for a broad parameter spectrum. In the following section, I will introduce the fabrication of such tapered single-mode fibers and a complete characterization of the taper angle and coupling efficiencies for different waveguide parameters and wavelengths.

5.5 Characterization of the tapered optical fibers

In this section, I will present the characterization of the tapered-fiber-tapered-waveguide interface. The first section presents the fabrication process of tapered fibers using an aqueous solution of fluorhydric acid at the Max Planck Institute for Solid State Research. In the second section, the taper angle will be investigated using optical and scanning electron microscopy. After ensuring reproducible taper angles well below 3° the characterization of the single frequency single-sided coupling efficiency for various waveguide designs, the overlap dependency between tapered fiber and tapered waveguide and a spectral transmission will be investigated. Our measurements show a high coupling efficiency of approximately 80% at 878.8 nm, a broad stable overlap plateau of 10 µm, a broadband spectral coupling efficiency over several hundreds of nanometers and a coupling efficiency of above 80% at 917 nm, the design wavelength of the waveguide.

5.5.1 Etching process at the Max Planck Institute for Solid State Research

The tapered optical fibers described below were produced by chemical etching in an aqueous solution of fluorhydric acid. The fabrication took place at the Max Planck Institute for Solid State Research in Stuttgart. Our collaborator Marion Hagel used a setup consisting of a motorized actuator (Thorlabs Z825B) and a translation stage provided by us. For the optical single-mode fiber we used standard 780HP single-mode optical fiber (Thorlabs 780HP) with a single-mode operation wavelength of 780−970 nm a mode field diameter of 5.0 ± 0.5 µm at 850 nm, a cladding of 125 ± 1 µm, a coating of 245 ± 15 µm and a cut-off wavelength at 730 ± 30 nm. After dipping the fiber over a length of $20 - 25$ mm into the 49% aqueous solution of fluorhydric acid, the motorized actuator pulls the fiber with a constant velocity of 2.8 µm/s out; resulting in a linear decrease of the fiber diameter. On top of the acid solution, a thin layer of o-Xylene is added, which stops the etching process when surfacing (Fig. 5.7). After roughly one hour, the optical fiber is etched through the complete cladding diameter leaving a sharp tapered fiber tip. To remove residuals of the o-Xylene and dust particles (Fig. 5.17c), the tapered fibers have been cleaned in a propanole-2-ol bath.

5.5.2 Scanning electron and optical microscope investigation

For investigating the tapered fibers, two separate methods were used: a standard optical microscope with varying magnifications (Fig. 5.17) and a scanning electron microscope (SEM, Fig. 5.18).
Several goals were pursued with these two investigation methods. The surface roughness of the etching process has been investigated with the SEM. By help of the optical microscopy and SEM images, we determined the angle of the tapered fiber tip and fed this value into our simulations (see section 5.4.3) estimating the coupling efficiency that is theoretically achievable. As a last point the minimum reachable tip diameter could be determined, which also influences the coupling efficiency (see section 5.4.4).
The visible surface roughness in Fig. 5.18b is assumed to be mainly a result of the

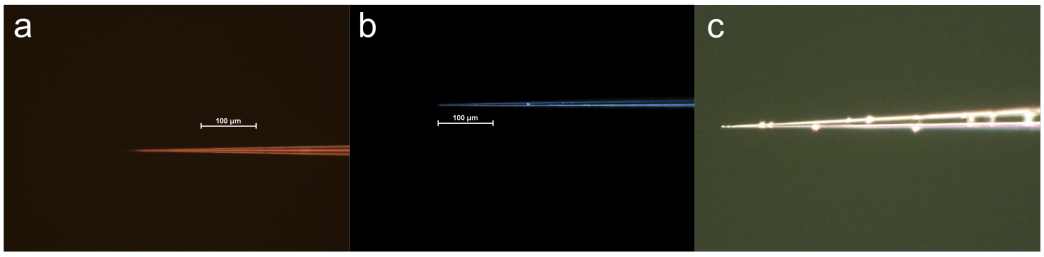

Figure 5.17: **Optical microscope pictures of the fiber taper.** **a** Bright field image with a magnification of 50. **b** Dark field image with a magnification of 50. **c** Visible contamination of the tapered fiber.

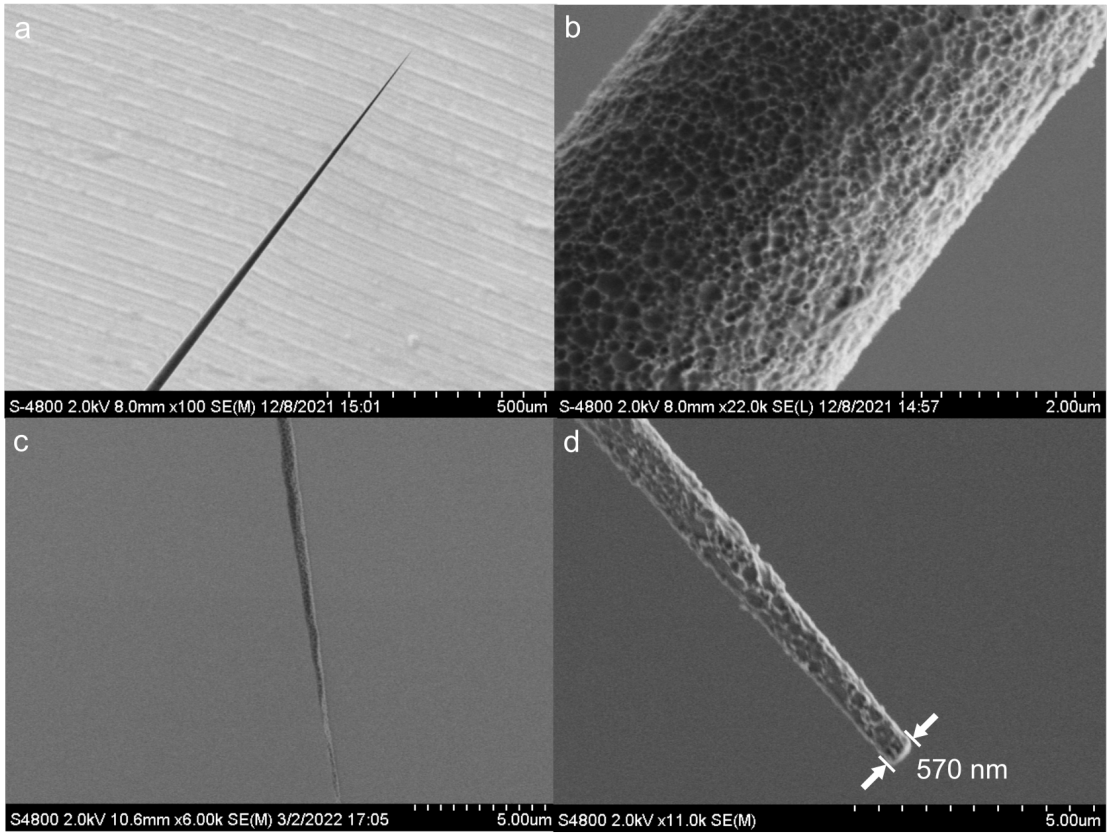

Figure 5.18: **Scanning electron microscope (SEM) pictures of the fiber taper.** **a** SEM image of the complete fiber tip. **b** Close up of the surface structure of the tapered fiber. **c** Close-up of a sharp tapered fiber tip. **d** Close-up of a broken tapered fiber with a tip diameter of approximately 570 nm.

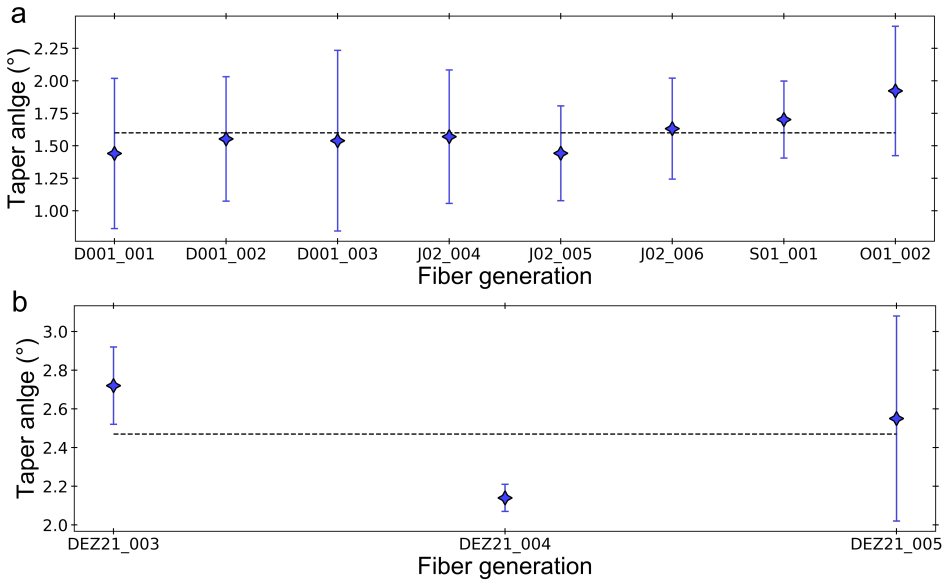

Figure 5.19: **Calculated taper angles.** **a** Calculated taper angles using the optical microscope. In average an angle of $1.60° \pm 0.48°$ is reached. **b** Calculated taper angles using the SEM. The measurements with the SEM result in an average taper tip angle of $2.47° \pm 0.27°$. The errorbars are calculated by using the Gaussian error propagation of the fitting parameters m_1 and m_2 in equation (5.54).

initial surface topography of the original fiber. Additionally, scattering losses due to this surface roughness are assumed to be not detrimental to the final coupling efficiency [225].
To estimate the taper angle, images from both microscopes were used, and a fitting by two linear functions of the form $y = m_1 x + b_1$ and $y = m_2 x + b_2$ applied to the upper and lower edge of the tapered tip, has been performed.
By using the equation:

$$\tan(\theta_{\text{taper}}) = \frac{m_1 - m_2}{1 + m_1\, m_2}, \tag{5.54}$$

we gain access to the angle between both linear functions and, thus, the taper tip angle.

We calculated the resulting taper angles of the etching process for eleven different fibers. Eight fibers were measured with the optical microscope and three with the SEM. Note that the SEM investigation process leads to the fiber's corruption. For characterization with the SEM, the tip of the tapered fiber had to be removed prior to the implementation into the SEM. Thus only a couple of fibers have been measured using the SEM. Further, we expect to have access to more accurate but not necessarily more precise values using this method.
The results of the angle estimation measurements are shown in Fig. 5.19. The angle estimation using the optical microscope and the SEM is presented separately in Fig. 5.19a and b, respectively. The optical microscope measurements lead to an average taper angle of 1.60° with an average standard deviation of 0.48°. The SEM measurements yield an average angle of 2.47° with a standard deviation of 0.27°. The differences between both investigation methods can be mainly assigned to a higher magnification of

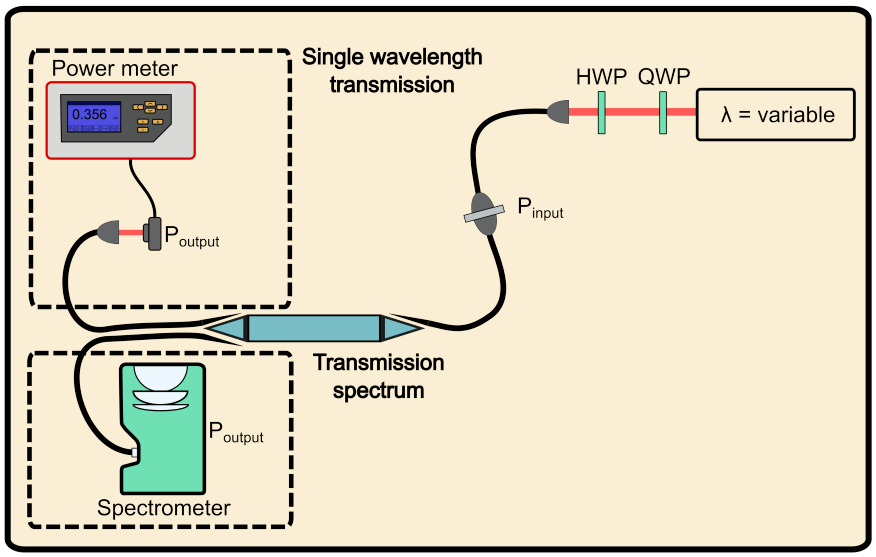

Figure 5.20: **Schematic of the coupling efficiency setup.** For a measurement of the coupling efficiency, we couple a light source into a single-mode optical fiber (780HP). This fiber is coupled to a single-mode tapered fiber (780HP) using a standard mating sleeve (Thorlabs). The optical light power before the tapered fiber defines the input power (P_{input}). This tapered fiber is used to couple to a triangular waveguide with a tapered termination. At the other side of the waveguide the same process leads to a coupling to a second tapered fiber (780HP). Depending on the sort of light source (single frequency laser or white light source) we either measure the output power (P_{output}) using a power meter (Thorlabs S120C) or a spectrometer from Ocean Insight (QE Pro NIR).

the SEM and a more precise horizontal placement, which avoids angle errors caused by a tilt outside the imaging plane.
With angles well below 3° coupling efficiencies of almost unity can still be achieved (see section 5.4.3).

5.5.3 Coupling efficiency measurements

Two different measurements were performed to investigate the coupling efficiency of the tapered optical fibers. First, we coupled single frequency light with a wavelength of 878.8 nm into an under-etched triangular waveguide with a width of 500 nm and an etching angle of approximately 45°. First, the input optical light power (P_{input}) right before an APC/APC mating sleeve from Thorlabs (ADAFC3) specified with an insertion loss below 0.5 dB has been measured. Directly after coupling the light from the waveguide into a second tapered optical fiber, we measured the output optical light power (P_{output}). Thus, the ratio between the input and output power is given by:

$$\frac{P_{output}}{P_{input}} = \eta_{mat.sl.}\,\eta_{in}\,\eta_{out}\,, \tag{5.55}$$

with P_{input} and P_{output} as the input and output power, respectively, $\eta_{mat.sl.}$ as losses at the mating sleeve and η_{in}, η_{out} the single sided coupling efficiencies for in- and outcoupling.
To estimate a lower limit of the single-sided coupling efficiency between the tapered optical fiber and the waveguide, we assumed an equal coupling efficiency for in- and outcoupling.
Thus, equation (5.55) reduces to:

$$\frac{P_{output}}{P_{input}} = \eta_{mat.sl.}\,\eta_{cp}^2, \tag{5.56}$$

with $\eta_{cp} = \eta_{in} = \eta_{out}$.
Therefore, the square root of the ratio between the input and output power resembles to

$$\sqrt{\frac{P_{output}}{P_{input}}} = \sqrt{\eta_{mat.sl.}}\,\eta_{cp}. \tag{5.57}$$

Because of the difficult accessibility of the coupling efficiency of the mating sleeve $\eta_{mat.sl.}$ a lower limit of the coupling efficiency is given by

$$\eta_{cp} \geq \sqrt{\frac{P_{output}}{P_{input}}}. \tag{5.58}$$

Note that here losses at the mating sleeve with $\sqrt{\eta_{mat.sl.}} \leq 0.25\,\mathrm{dB} \approx 5.9\%$ are neglected, such as all measurements presented are lower limits of the coupling efficiencies. Thus, the single-sided coupling efficiency's real value might be even higher. Furthermore, the assumption $\eta_{cp} = \eta_{in} = \eta_{out}$ likewise does not increase the expected single sided coupling efficiency but also is a worst case assessment, resembling the lowest possible single sided coupling efficiency. Also, we assume here that there are no transmission losses through the waveguides. Of course, this is not entirely true.
In a second experiment, the transmission spectrum of the tapered fibers was measured. Here, we coupled a white light source into the same experimental setup (Fig. 5.20) and instead of the optical light powers P_{input} and P_{output} measured the input and output spectrum.

Single wavelength transmission

To evaluate the tapered fibers' single-sided coupling efficiency, we performed multiple measurements on different waveguide parameters. All waveguides resembled triangular under-etched single-mode waveguides with a width of 500 nm and an etching angle of approximately 45° (see section 5.4.1). This design includes so-called support structures, which are approximately 7 µm long pillars, on which the free-standing waveguide is located (see also Fig. 5.21).
Furthermore, a self-constructed laser with a center wavelength of 878.8 nm has been used as a single frequency source. To exclude that fabrication errors influence the single-sided coupling efficiency, we attached the tapered fibers to waveguides with taper lengths between 15 µm and 30 µm and two to four support structures. Images of

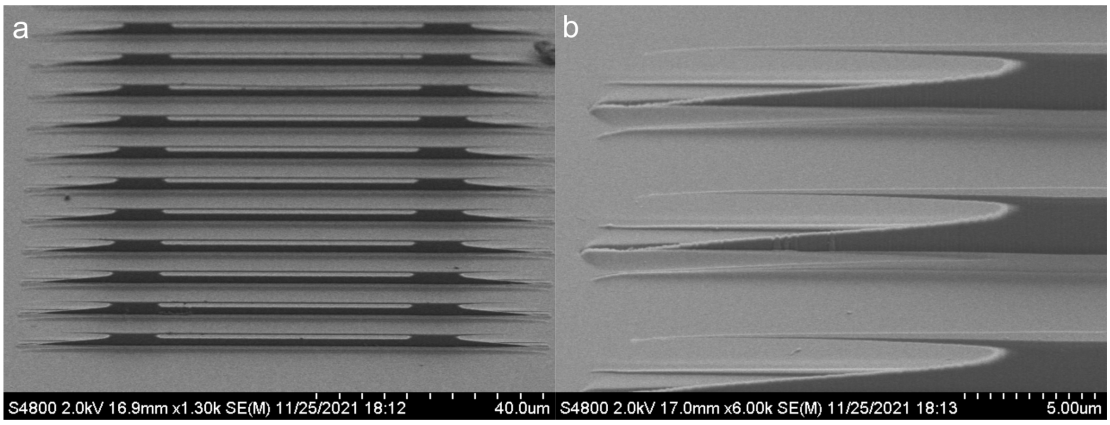

Figure 5.21: **Scanning electron microscope (SEM) pictures of the waveguides.** **a** SEM image of the entire waveguides. The freestanding waveguides, with a triangular cross-section is fabricated (in this case) on two support structures. **b** Close up of the taper region of the waveguide. The here presented waveguides have a design taper length of 15 µm.

the waveguide design are presented in Fig. 5.21 and the resulting transmission measurements are given in Fig. 5.22a and b.
For all measurements, the overlap between tapered fiber and tapered waveguide was adjusted for maximum transmission. For this purpose, we introduced a nomenclature of the waveguides in the scheme:
waveguide taper length_nr. of support structures_nr. of waveguide.
For example a waveguide with a taper length of 15 µm and two support structures would be named: 15_2_x (with x the xth waveguide).
According to section 5.4.3 we do not expect a significant influence of different taper lengths between 15 µm to 30 µm onto the maximum coupling efficiency. To further exclude that the support structures lead to a leakage of waveguide modes into the bulk, we also performed the coupling efficiency measurements for different quantities of support structures.
In Fig. 5.22a the results for the single-sided collection efficiency of waveguides with different taper lengths (15 µm, 20 µm, 25 µm and 30 µm) are shown. As expected from the simulations, the taper length has no major influence on the maximal reachable single-sided coupling efficiency.
In Fig. 5.22b, the results for different numbers of support structures (two, three, and four) are shown. For each quantity, five waveguides have been investigated. The single-sided coupling efficiencies resemble $79.62 \pm 1.53\%$ for two, $76.19 \pm 1.43\%$ for three, and $78.04 \pm 2.20\%$ for four support structures, respectively. Therefore a significant leakage of waveguide modes into the bulk can be excluded. Overall the lower bound for the single-sided coupling efficiency is highly reproducible and reaches approximately 80% ($78.97\,\% \pm 2.14\,\%$).

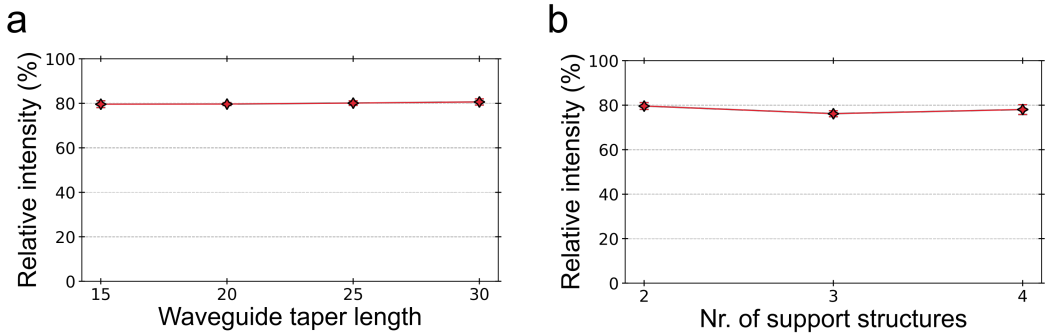

Figure 5.22: **Lower bound for the single sided coupling efficiency using equation (5.58) and a self build laser with a center wavelength of 878.8 nm.** Single sided coupling efficiency of a tapered optical fiber and a waveguide with a triangular cross-section. Single sided coupling efficiency as a function of **a** the waveguide taper length and **b** the number of support structures. For each point, five waveguides have been investigated. The errorbars are given by the standard deviation of all five measurements. The single-sided coupling efficiencies resemble $79.62 \pm 1.53\%$ for two, $76.19 \pm 1.43\%$ for three, and $78.04 \pm 2.20\%$ for four support structures, respectively. All measured single frequency single-sided coupling efficiency measurements are additionally presented in the appendix G in Fig. G.1a-f.

Overlap dependent coupling efficiency

Further, we investigated the overlap dependency of the tapered-fiber-tapered-waveguide interface. This measurement has been performed using piezoelectric actuators to adjust the overlap. For the following measurements, waveguides with a 20 µm taper length and two support structures were chosen. In this experiment only the coupling from an optical fiber into a waveguide was investigated, leaving the outcoupling efficiency of the tapered-fiber-tapered-waveguide interface constant.
Fig. 5.23 a-d shows the taper overlap-dependent single-sided coupling efficiency for four different waveguides. In Fig. 5.23e, all previous measurements are illustrated in a single figure.
The measurements show a plateau of approximately 10 µm at which the single-sided coupling efficiency is almost constant. For a smaller or larger overlap, the single-sided efficiency decreases. Note that we assign this decrease mainly to the taper length of the waveguide (Fig. 5.13a) and that an additional impact of a finite taper diameter can not be excluded (Fig. 5.15). Nevertheless, the measurements show a stable plateau of approximately 10 µm, over which the high coupling efficiency (of approximately 80%) is almost constant.

Transmission spectrum

To evaluate the spectral properties of the coupling efficiency, we used the same system as before. However, we exchanged the single frequency source for a white light source and the detector for a near-infrared spectrometer from Ocean Insight (QE Pro NIR). In Fig. 5.24 the spectrum of the white light source is shown. Even though not perfectly

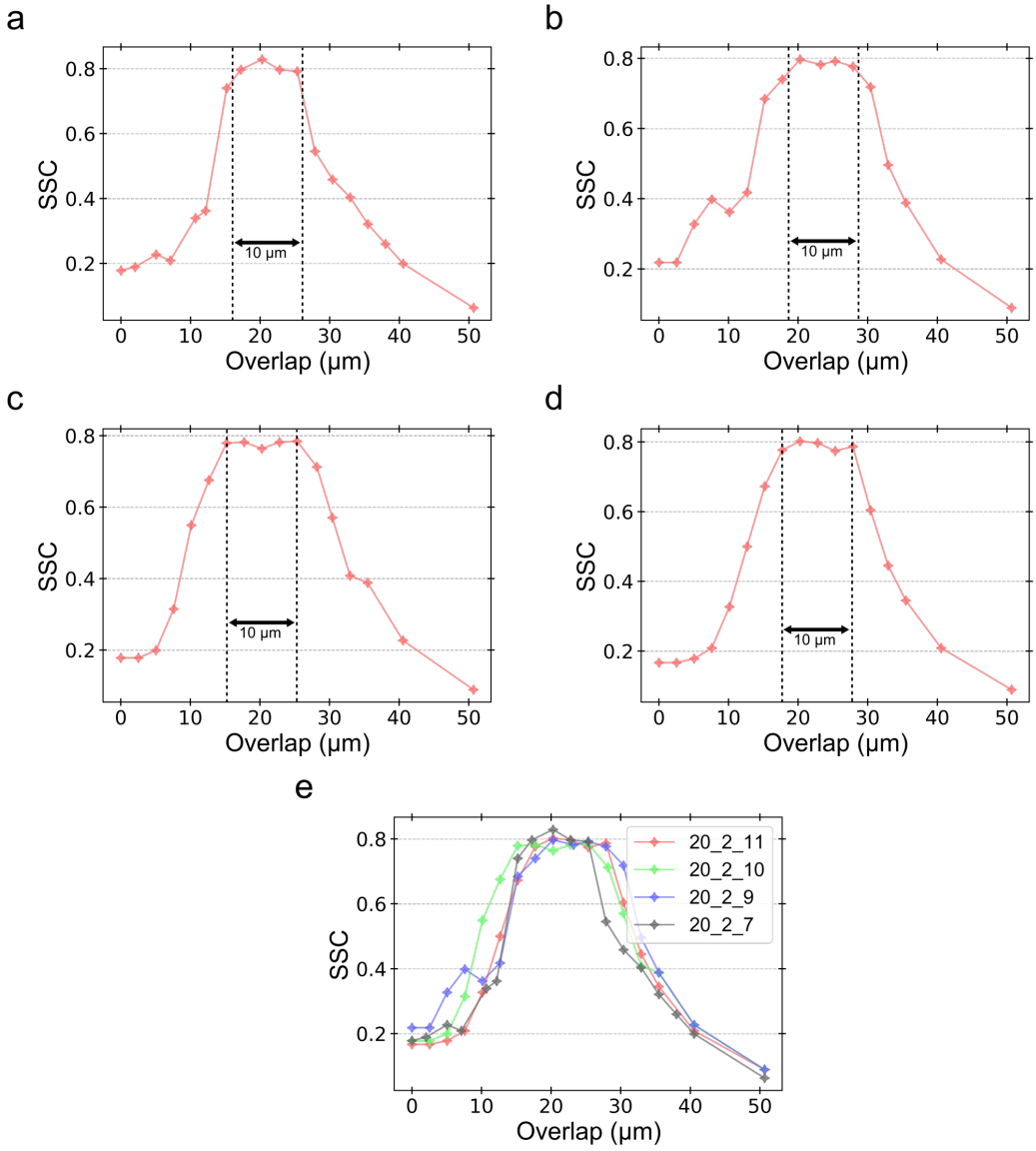

Figure 5.23: **Single sided coupling efficiency as a function of the taper overlap of multiple waveguides with a taper length of** 20 µm **and two support structures.** Single sided coupling efficiency of waveguide (**a**) 20_2_11, (**b**) 20_2_10, (**c**) 20_2_9 and (**d**) 20_2_7 as a function of the taper overlap. **e**, Combined plot of all waveguides. The coupling efficiency shows an almost constant plateau of approximately 10 µm.

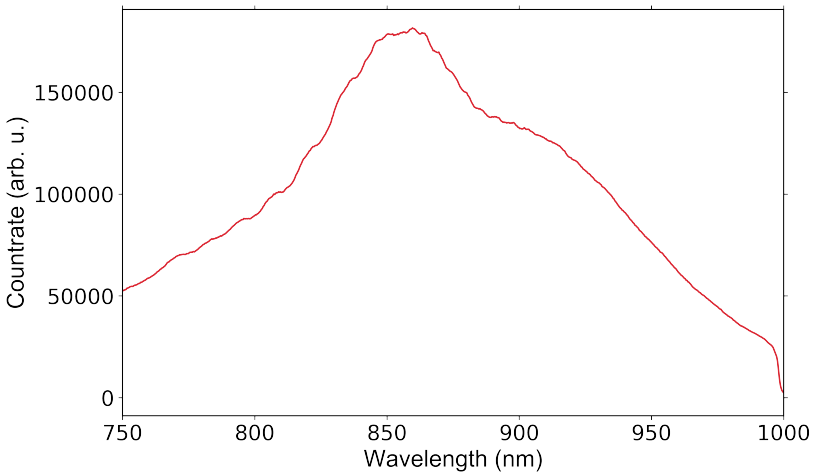

Figure 5.24: **Reference transmission spectrum measured at P_{input} in Fig. 5.20.** Reference spectrum of the white light source, which has been used for the wavelength dependent single sided coupling efficiency study.

flat, the different intensities for different wavelengths do not influence the calculation of the spectral single-sided coupling efficiencies.
The results of the transmission spectra analysis is shown in Fig. 5.25a-d. Note that the coupling efficiency adjustment is wavelength-dependent; thus, a maximum single-sided coupling efficiency can only be provided around this wavelength. We optimized the single-sided coupling efficiency for a wavelength of 917 nm, that is the design wavelength of the used waveguides.
The coupling efficiency at this wavelength can be seen in Fig. 5.26. Note that in this figure, more measurement points are seen than spectra in Fig. 5.25. Out of convenience the other figures were moved to appendix C).
This analysis reveals the broadband capacity of the tapered-fiber-tapered-waveguide interface. To cover the ZPL as well as the PSB of V_2 centers in SiC, the coupling efficiency must be high for the entire spectral range between 915 nm and 1000 nm [196]. Fig. 5.25 and C.1 show that over the entire spectral range between 915 nm and 1000 nm simultaneously a high coupling efficiency around 80% has been measured.
Furthermore, in case of the ZPL at 917 nm, an average coupling efficiency well above 80% ($83.45 \pm 1.63\%$) up to a maximum of 85% could be measured.

5.5.4 Conclusion

In this section, I presented the fabrication process of our tapered optical single-mode fibers at the Max Planck Institute for Solid State Research and the characterization of their geometrical properties like the roughness and the taper angle using optical and scanning electron microscopy. Here, taper angles in the range of $1 - 3°$ could be measured which should not affect the coupling efficiency (see section 5.4.3).
Further, we investigated the single-sided coupling efficiency using a single frequency laser source at a wavelength of 878.8 nm. We primarily focused on the coupling efficiency dependency on waveguide parameters like the waveguide taper length and the number of support structures. As a result, coupling efficiencies of approximately 80%

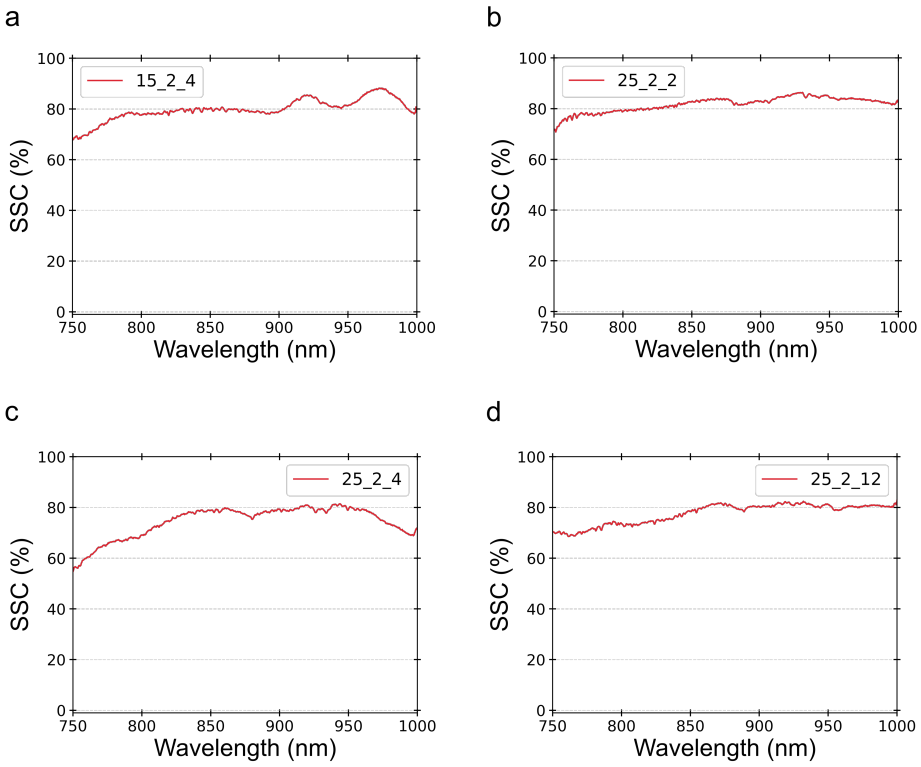

Figure 5.25: **Transmission spectra.** Single-sided coupling efficiency (SSC) spectrum of a waveguide with a taper length of **a**, 15 µm and two support structures, **b**, 25 µm and two support structures, **c**, 25 µm and two support structures and **d**, 25 µm and two support structures.

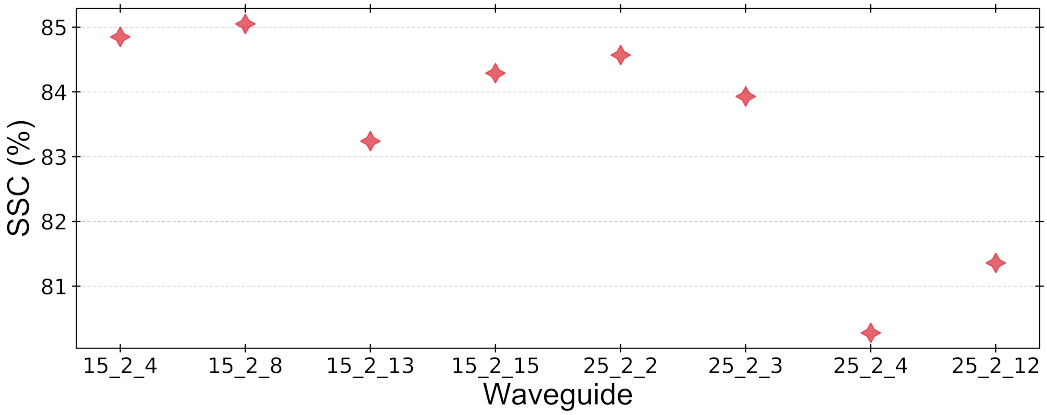

Figure 5.26: **Single sided coupling efficiency (SSC) at 917 nm.** The single sided coupling efficiency for a wavelength of 917 nm can reach values up to 85%. Average single sided coupling efficiency: $83.45 \pm 1.63\%$.

could be shown, independent of the above-mentioned waveguide parameters.
Furthermore, the dependency on the taper-taper overlap has been measured leading to an expected behavior (see section 5.4.3 and 5.4.4). Additionally, we were able to present a stable 10 µm plateau at which the single-sided coupling efficiency is almost constant.
As a last characterization measurement, we investigated the spectral properties by exchanging the single frequency laser for a white light source with a broadband spectrum between 750 nm and 1000 nm. For a spectral range covering the ZPL as well as a majority of the PSB, from 915 nm up to 1000 nm, a coupling efficiency around 80% could be measured. Further, the coupling efficiency at the design wavelength of the waveguide, representing the spectral properties of the ZPL at 917 nm, showed values above 80% ($83.45 \pm 1.63\%$) up to a maximum of 85%.
These measurements show that the tapered-fiber-tapered-waveguide interface not only shows highly reproducible coupling efficiencies of around 80% but also maintains this coupling efficiency simultaneously over a spectral range of several hundreds of nanometers. Thus, this interface proves to be a simple but highly efficient approach to guiding light in and out of nanophotonic structures.
Note that the values presented here are only lower bounds for the single-sided coupling efficiency. An imbalance between both fibers coupled to the same waveguide, losses of the mating sleeve ($\sqrt{\eta_{\text{mat.sl.}}} \leq 0.25\,\text{dB} \approx 5.9\%$), and transmission losses through the waveguide were not taken into account. Therefore the values presented here are a worst-case scenario estimation.

5.6 Expansion of the setup

5.6.1 Excitation from top and confocal imaging

Since a high coupling efficiency and high reproducibility could be demonstrated in the last section, we further developed our setup to excite single defects in waveguides and increase the collection efficiency compared to defects in bulk.
To achieve this, we extended our fiber characterization setup with a self-build imaging system and an excitation system from the top (see Fig. 5.27). We kept a single-frequency laser source path to adjust the coupling efficiency of our tapered-fiber-tapered-waveguide interface. Additionally, we added a single photon detection stage consisting of a long-pass filter at 900 nm (VersaChrome Edge TLP01-995-25x36 @50°), a bandpass filter at 950 nm with a FWHM of 50 nm (Edmund Optics GmbH #84-792) and two fiber-coupled single photon counting modules (SPCM-AQRH-14-FC). Further, we added an excitation and an imaging path on top of the setup. The excitation path consists of a 730 nm single frequency laser source with variable polarization adjustment, which is focused from the top onto the waveguide with a high NA objective (Objektiv LD EC EPN 100x/0,75 DIC Vak Carl Zeiss Microscopy GmbH). We further implemented an imaging path with a field of view (FOV) of around 120 µm with the same objective.
The general idea of this setup is a point-wise excitation of defects inside of the waveguide with an off-resonant laser at a center wavelength of 730 nm. At the same time, the detection takes place in the waveguide plane using one side of the tapered-fiber-

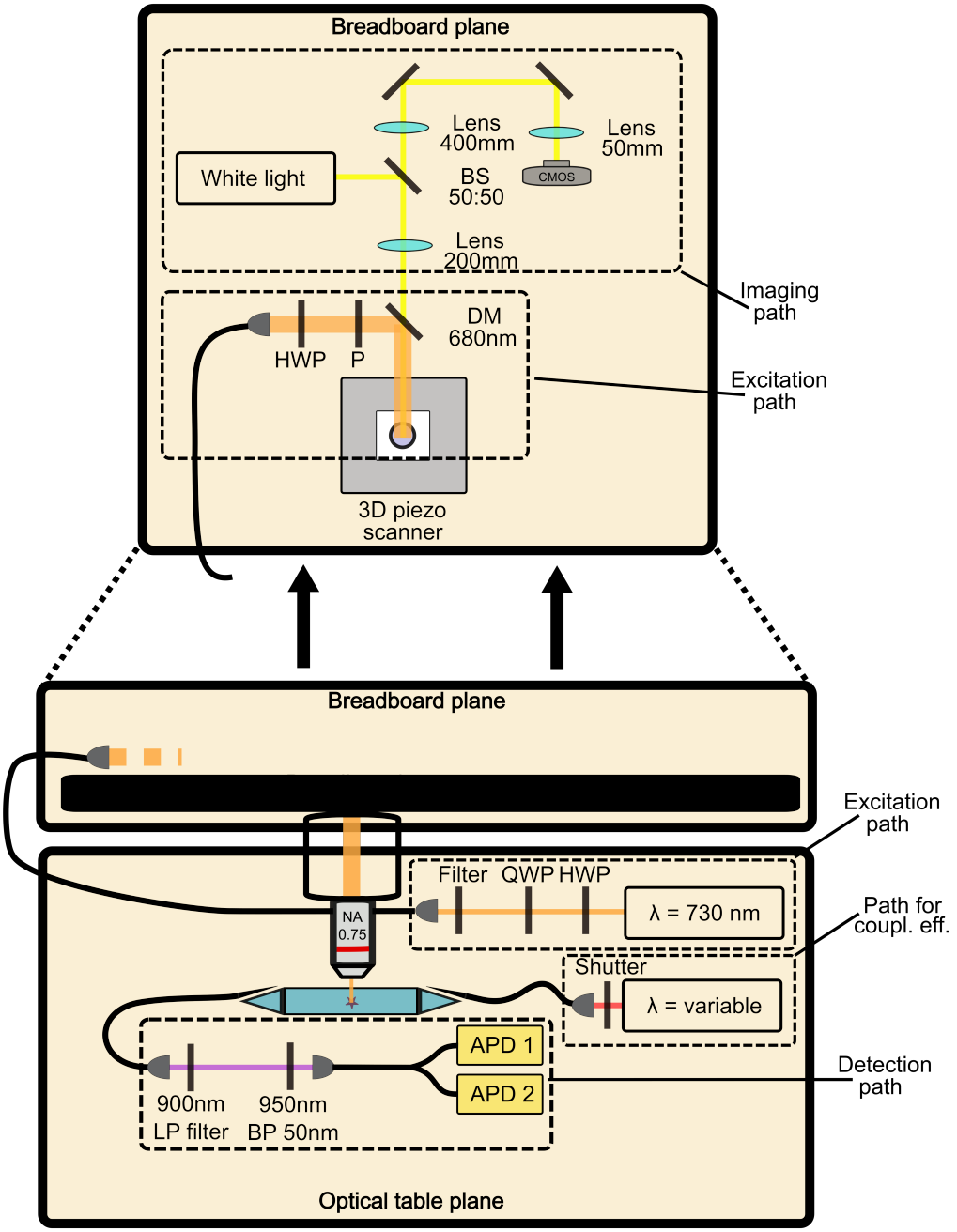

Figure 5.27: **Schematic of the excitation setup.** The expanded setup consists mainly out of four parts. The first parts is a leftover from the fiber characterization and consists out of a single frequency laser to adjust the coupling efficiency. As a second part, the detection path, a longpass filter at 900 nm (VersaChrome Edge TLP01-995-25x36 @50°), a bandpass filter at 950 nm with a FWHM of 50 nm (Edmund Optics GmbH #84-792) and two fiber coupled single photon counting modules (SPCM-AQRH-14-FC) are implemented. The third part is an off-resonant excitation path, which consists out of a 730 nm single frequency laser with adjustable polarization, which is focused down from top onto the waveguides with a high NA objective (Objektiv LD EC EPN 100x/0,75 DIC Vak Carl Zeiss Microscopy GmbH). The last part is an imaging system using the same objective for an imaging with a FOV of 120 µm.

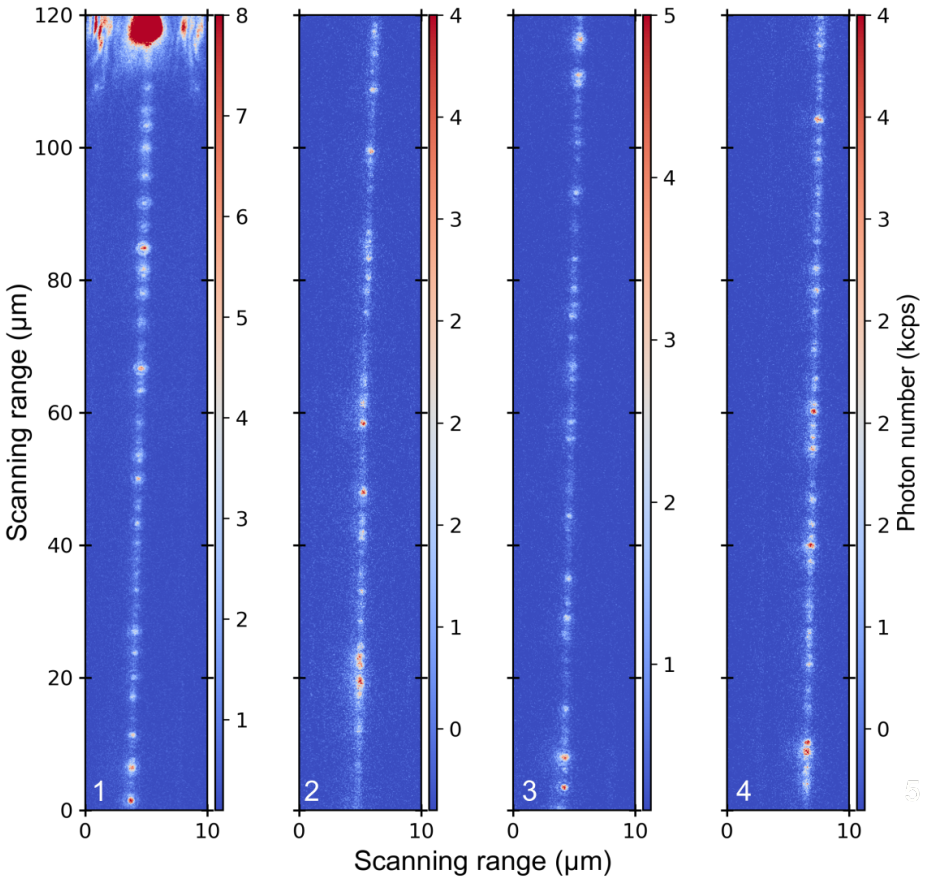

Figure 5.28: **Waveguide confocal scans.** Example measurements of different waveguides using an off-resonant excitation using a single frequency laser source of 730 nm from top and a detection scheme using the tapered fiber/tapered waveguide interface. The bright spot in the first measurement (1) results from a direct coupling of the laser coming from above into the tapered fiber piece at this location. The high count rate at this point does not belong to any emitter but to stray light of the excitation laser.

tapered-waveguide interface. The coupling to the waveguide can be adjusted using the imaging path and the path for adjusting the coupling efficiency introduced in Fig. 5.27. Using a piezoelectric actuator 3D-stage (PIMars P-561.3CD) the objective can be scanned with a resolution of 0.2 nm. Thus images similar to classical confocal scans can be realized.
Prior to the nanofabrication of waveguides, a SiC sample had been electron irradiated at 2 MeV with a dose of 2 kGy (with a fluence of approximately $5 \cdot 10^{11}\,\mathrm{cm}^{-1}$) to create randomly distributed V_2 centers. The electron radiation lead to a defect density of approximately $0.40\,\mu\mathrm{m}^{-3}$. To obtain different amounts of defects per waveguide, waveguides of different lengths were fabricated (between 12 µm and 120 µm).
As a test measurement to verify the correct performance of our setup, we investigated the waveguide sample with 0.40 defects per $\mu\mathrm{m}^3$ and different waveguide lengths. Here, we excited the waveguide sample from the top through the objective (Objektiv LD EC EPN 100x/0,75 DIC Vak Carl Zeiss Microscopy GmbH). The detection took place using one side of the tapered-fiber-tapered-waveguide interface. Fig. 5.28 shows an example measurement of five different waveguides (waveguide length: 120 µm). In this figure, the waveguides are distinguishable from the uncoupled background. Furthermore, there are several bright single spots visible in all four waveguides. This concludes that not only is the setup working and can be used for the location of single defects in waveguides, with a greatly enhanced coupling efficiency, but it also indicates the existence of (single) defects inside the waveguides.
A logical next step is to verify whether these bright spots originate from single defects or ensembles. A common approach to verify the singularity of emitters is the use of the second-order correlation function $g^{(2)}$ defined as [52]:

$$g^{(2)}(\tau) = \frac{\langle\, E^*(t)\, E^*(t+\tau)\, E(t) E(t+\tau)\,\rangle}{\langle\, E^*(t)\, E(t)\,\rangle\,\langle\, E^*(t+\tau)\, E(t+\tau)\,\rangle} = \frac{\langle\, I(t)\, I(t+\tau)\,\rangle}{\langle\, I(t)\,\rangle\,\langle\, I(t+\tau)\,\rangle}, \tag{5.59}$$

where E and I are the electric field and the intensity of a light beam at time t. In principle, this function introduces a value corresponding to the light field's statistics. In the Hanbury Brown-Twiss arrangement, where a photon flux is divided by a beam splitter and subsequently measured with two detectors (depicted by indices 1 and 2), the second-order correlation function can be written with respect to single photon events as [52]:

$$g^{(2)}(\tau) = \frac{\langle\, n_1(t)\, n_2(t+\tau)\,\rangle}{\langle\, n_1(t)\,\rangle\,\langle\, n_2(t+\tau)\,\rangle}. \tag{5.60}$$

For $\tau = 0$ the second correlation function of quantum mechanical fields can be calculated by [78]:

$$g^{(2)}(0) = \frac{\langle\, a^\dagger\, a^\dagger\, a\, a\,\rangle}{\langle\, a^\dagger\, a\,\rangle^2} = 1 + \frac{V(n) - \bar{n}}{\bar{n}^2}, \tag{5.61}$$

with $V(n) = \langle (a^\dagger a)^2 \rangle - \langle a^\dagger a \rangle^2$ and $\bar{n}$ the mean photon number. Thus for a coherent state defined as [52]:

$$|\alpha\rangle = \sum_{n=0}^{\infty} \frac{\alpha^n}{\sqrt{n!}}\, \mathrm{e}^{-|\alpha|^2/2}\, |n\rangle\,, \tag{5.62}$$

it shows a Poissonian distribution with $V(n) = n$. Subsequently, this leads for $\tau = 0$ to a second-order correlation function value of $g^{(2)}(0) = 1$.

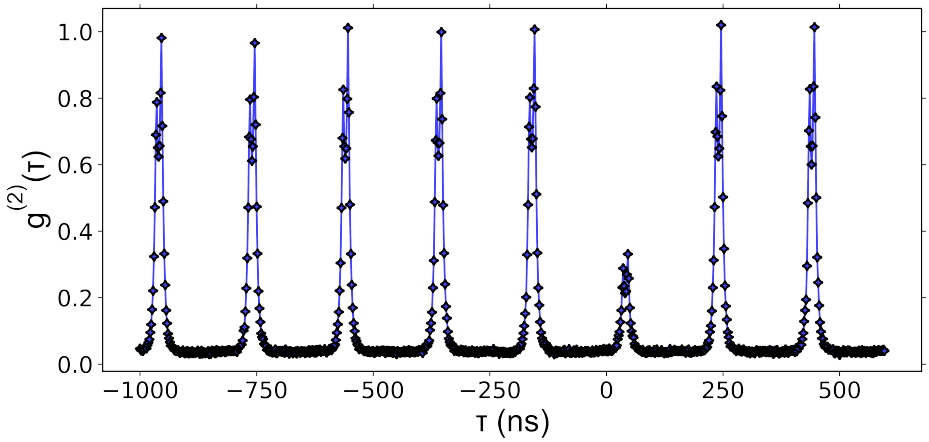

Figure 5.29: **$g^{(2)}$ measurement of a bright spot in the waveguide.** $g^{(2)}$ measurement on a bright spot of the waveguide. Instead of exciting with a continuous wave source, here, a pulsed laser with a frequency of 780 nm is used (PDL 800-B and LDH-P-C-780 from PicoQuant). The repetition rate of 5 MHz is clearly visible in the measurement. An initial path length difference between both detectors of approximately 46.5 ns has been introduced by insertion of a 10 m BNC cable. As expected the $g^{(2)}$ function drops at 46.5 ns below a value of 0.5, thus indicating a single emitter. Further measurements are available in appendix F Fig.F.1.

For any Fock state, however, $V(n) = 0$ is satisfied. Thus, for $\tau = 0$ this results in a second-order correlation function of [247]:

$$g^{(2)}_{\text{Fock}}(0) = 1 - \frac{1}{n}, \tag{5.63}$$

Based on the different second-order correlation function values for different light sources, in the literature, the second-order correlation function is often used to classify light into three distinct categories [51, 52, 78]:

- **bunched light**: $g^{(2)}(0) > 1$,
- **coherent light**: $g^{(2)}(0) = 1$,
- **antibunched light**: $g^{(2)}(0) < 1$.

Furthermore, the second-order correlation function can be used to characterize single-photon sources. For $\tau = 0$, using equation (5.63), a second-order correlation function value below $g^{(2)}_{\text{Fock}}(0) < 0.5$ verifies the existence of a single emitter (Fock state with $n = 1$).
For the second-order correlation function measurement, we decided to excite with an off-resonant laser at 780 nm from the top and collect via the tapered-fiber-tapered-waveguide interface in the waveguide plane. In contrast to the confocal measurements (Fig. 5.28) the excitation laser was pulsed with a repetition rate of 5 MHz and an average power of 100 µW. An initial path length difference between both detectors of approximately 46.5 ns has been introduced by inserting a 10 m BNC cable.
We inspected several bright spots in different waveguides. In each waveguide, we could find at least one bright spot, which proved to be, with $g^{(2)}_{\text{Fock}}(0) < 0.5$, a single emitter.

In Fig. 5.29, the results of this Hanbury Brown-Twiss experiment of an emitter in the waveguide and the detection via the tapered-fiber-tapered-waveguide interface are shown. To reduce the systematic uncertainty, we integrated over 17 hours, resulting in an average of 2,278 correlation events per peak. With a value of 0.24 ± 0.02 for the central peak at 46.5 ns, this measurement verifies the existence of a single emitter in the waveguide and the successful performance of the tapered-fiber-tapered-waveguide interface outside simple characterization measurements.
A logical next step would be the performance of an ODMR measurement that could verify whether the discovered single emitters are indeed V_2 centers. Following this confirmation, a saturation study could be performed to ultimately characterize the enhancement factor of the collection efficiency with our tapered-fiber-tapered-waveguide interface. Ph.D. student Marcel Krumrein will perform these future steps.

5.6.2 Conclusion and outlook

In this section, I introduced an expansion of our setup toward detecting single V_2 centers in SiC. Here, I presented an added self-built imaging system, allowing an excitation from the top. In this regard, the setup's performance has been motivated by a confocal scan of five different waveguides, showing distinct bright spots, which we assign to optically active defects in SiC. A subsequent study of the emission behavior showed that we were able to prove, with a value of $g^{(2)}(0) = 0.24 \pm 0.02$, that indeed single defects occur inside of the waveguides.
To verify that the single defects correspond to the emission of V_2 centers as a next step, the performance of an ODMR measurement would be necessary. Following this, a saturation study as in reference [248] could be undertaken to categorize the enhancement of the coupling efficiency.
Finally, even without clarifying the nature of the defects investigated, the tapered-fiber-tapered-waveguide interface could be implemented as a coupling enhancement tool into consisting quantum-optical experiments and make an essential contribution to future projects in SiC.

Chapter 6

General summary

Nonlinear optics

Not only in the past few years optical interferometry has proven the gold-standard for measuring small displacements [33], refractive indices [30, 34], and surface properties [35, 36]. At the latest, this became clear after LIGO observed a transient gravitational-wave signal [98]. In classical interferometry the best achievable phase sensitivity $\Delta\Phi$ with N uncorrelated photons is given by the shot noise limit (SNL) [71, 249, 250], $\Delta\Phi = 1/\sqrt{N}$. Since the field of quantum optics emerged, increasing this sensitivity was an early target. Thus, quantum optical sensors often promise to surpass the SNL by exploiting correlations and entanglement [71, 113, 250–254]. The first part of this thesis hits right into this notch: It introduces a novel concept of a quantum sensor based on nonlinear interferometry with a phase sensing sensitivity 1.13 ± 0.02 times beyond the SNL. Furthermore, this novel quantum sensor shows some unique features. For example, it comprises an independency of the enhancement factor to loss outside of the interferometer and an operation simultaneously over the broad sampling rate regime of 200 Hz up to 100 kHz, which is so far only limited by the photon-pair flux. Furthermore, a detection scheme similar to classical interferometry can be applied, and subsequently, common mode noise can be canceled out. None of the already realized approaches can fulfill all of these points simultaneously. To further prove its easy applicability, we presented a quantum optical microphone for recording human speech. Comparing classical and quantum microphones, at identical photon numbers, showed that the quantum microphone records sound at a significantly reduced baseline noise level, proved by an improvement in the SNR of $0.84 \pm 0.29\,\mathrm{dB_{SPL}}$. A subsequent medical speech recognition test confirmed these findings. A study on $n = 45$ human subjects showed an enhancement of $0.57 \pm 0.22\,\mathrm{dB_{SPL}}$ in the understandability of recorded words. Thus, it verified that even such a complex experiment, where the simultaneous enhancement over the entire audio band is vital, can be easily implemented.

Building upon these findings, this novel sensing scheme could be employed in applications involving biological samples, chemical reactions, or atomic spin ensembles, which are sensitive to light exposure and short wavelength photons [32, 44–48]. In this sense, our quantum light source already operates within the favorable second biological win-

dow BW-II ($1000 - 1350\,\mathrm{nm}$) [173]. To show the exploitable quantum advantage, the light flux of our source could be increased to the level of a few 100 nW. In that regard, previous work demonstrated already photon pair beams at power levels of $0.3\,\mu\mathrm{W}$ while still operating in the distinct photon pair regime [155].
All these reasons confirm that developing this new quantum sensor is an important step in the field of quantum optics.

Nanophotonic interfaces

Furthermore, optically active spins in solids are promising candidates for advanced quantum information processing and quantum metrology. Here, the existence of atom-like systems with properties like spin, decay rates, emission of photons, etc., represent a fascinating opportunity. In this regard, experimental realizations have been done among others on nitrogen-vacancy centers in diamond [175–178].
A more recent platform to host such defects is SiC. In 4H-SiC, for the V_2 center, the ZPL appears at 917 nm [197, 199, 200]. For both the V_1 and the V_2 center, the Debye-Waller factor, which resembles the ratio between the ZPL and the entire emission spectrum (sum over ZPL and PSBs) at low temperatures, has been experimentally determined as approximately $6 - 9\%$ [193, 196, 201]. Furthermore, investigations using Hahn-echo experiments showed that the system exhibits long spin coherence times of up to 1.4 ms [191, 196, 202].
Another compelling advantage of the V_2 center is thermal stability up to 20 K. Up to this temperature, the photoluminescence (PL) spectrum still shows optical transitions with narrow PL linewidths [198]. The lifetime of the V_1 excited state(s) is approximately $5 - 6\,\mathrm{ns}$ [193, 195, 199] (dependent on the excitation path A_1 or A_2, see Fig. 5.2b) and for the V_2 excited state(s) approximately $6 - 7\,\mathrm{ns}$ [191, 194].
While the SiC platform promises several advantages, such as industrial-scale availability, excellent spin properties, and optical addressability, one remaining challenge is the small emission ratio in the ZPL (Debye-Waller factor of $6 - 9\%$ [193, 201]), limiting the applicability in quantum information processing. Additionally, in standard confocal setups, due to the high refractive index of SiC (approximately $n = 2.6$ for 4H-SiC at 917 nm), which leads to total internal reflection at smaller entry angles, the collection efficiency is as low as about 1% or less of the total emission.
In this regard, an increase in the coupling efficiency between SiC and the environment, for example, optical single-mode fibers, plays a crucial role in the future of this platform. In the second part of my work, I presented a tapered-fiber-tapered-waveguide nanophotonic interface, which promises to significantly increase the coupling efficiency into optical single-mode fibers. Here, the fabrication of such tapered fibers was introduced and compared to equivalent concepts. Subsequently, simulations using FDTD were introduced, which showed possible coupling efficiencies of almost unity. Characterization measurements showed here, for a spectral range covering the ZPL and most of the PSB, from 915 nm up to 1000 nm, a coupling efficiency of around 80%. Further, the coupling efficiency at the design wavelength of the waveguide, representing the spectral properties of the ZPL at 917 nm, showed values well above 80% ($83.45 \pm 1.63\%$) up to a maximum of 85%. Thus, we significantly increased the coupling efficiencies for the V_2 center in 4H-SiC in waveguides. Furthermore, we demonstrated the exis-

tence of single emitters in waveguides with a second order correlation function value of $g^{(2)}(0) = 0.24$ and the associated proof-of-principle demonstration of collecting light from a single emitter with the tapered-fiber-tapered-waveguide interface. Both results fit perfectly into the current research direction in these fields and thus contribute to current research.

Appendix A

List of Symbols

^{13}C	Carbon 13 isotope
^{29}Si	Silicon 29 isotope
$\hat{a}$	annihilation operator
$\hat{a}^\dagger$	creation operator
$\mathbb{1}$	Identity matrix
$\hat{H}$	Hamiltonian
$\hbar$	Reduced Planck contant, 1.054 571...10^{-34} J·s
$\hat{S}(\xi)$	Squeeze operator
χ_{M}	Magnetic susceptibility
χ_{E}	Electric susceptibility
Λ	Pole spacing
$\hat{J}$	Jones matrix
ν	Visibility
η	Transmissivity
c	Vacuum speed of light $c = 299792458\,\mathrm{m/s}$
d	Cohens d effect size
r	Squeezing parameter
$\hat{O}_{\mathrm{Qu.Sens.}}$	Quantum sensor operator
u_{max}	Maximum phase velocity
β	Taper angle
$\beta_{\mathrm{prop.}}$	Propagation constant
z_{b}	Beat length
$z_{\mathrm{ch.}}$	Characteristic length

n	Refractive index
n_{eff}	Effective index
cps	Counts per second
μ_0	Vacuum permeability, $4\pi\ 10^{7}$ T·m·A^{-1}
μ_B	Bohr magneton, $9.274009994\ 10^{-24}$ J·T^{-1}
$\mathbf{S}$	Electron spin angular momentum operator (here: spin 3/2)
$\hat{S}_i$	i-component of $\mathbf{S}$ (here: spin 3/2)

Appendix B

List of Abbreviations

LIGO	Laser Interferometer Gravitational-Wave Observatory
SQL	Standard quantum limit
D	Detector
FWHM	Full width at half maximum
PDC	Parametric down-conversion
OPO	Optical parametric oscillation
PD	Photodiode
LO	Local oscillator
PA	Parametric amplifier
WSWP	Wavelength-selective waveplate
SPDC	Spontaneous parametric down-conversion
PPKTP	periodically poled potassium titanyl phosphate
HWP	half waveplate
QWP	Quarter waveplate
PBS	Polarizing beam splitter
SM	Sample mirror
RM	Reference mirror
NLC	Nonlinear crystal
L	Lens
DM	Dichroic mirror
F	Filter
KTP	potassium titanyl phosphate
R	Rate

FWC	Full well capacity
SNR	Signal-to-noise ratio
OLSA	Oldenburger sentence test
Ph.D.	Doctor of Philosophy
SRT	Speech recognition threshold
SPL	Sound pressure level
DIN	German Institute for Standardization Registered Association
SNSPD	Superconducting nanowire single-photon detectors
RMS	Root-mean-square
BS	Beam splitter
r	squeezing parameter
SiC	Silicon carbide
HF	Hydrogen fluoride
CO_2	Carbon dioxide
CMOS	Complementary metal-oxide- semiconductor
ZPL	Zero phonon line
PSB	Phonon side band
GS	Ground state
ES	Excited state
ISC	Intersystem crossing
TE	Transverse-electric
TM	Transverse-magnetic
CFDA	Central finite difference approximation
FDTD	Finite-Difference Time-Domain
SEM	Scanning electron microscope
ODMR	Optically detected magnetic resonance
FOV	Field of view
NA	Numerical aperture

Appendix C

Transmission spectra

The missing transmission spectra from Fig.5.26:

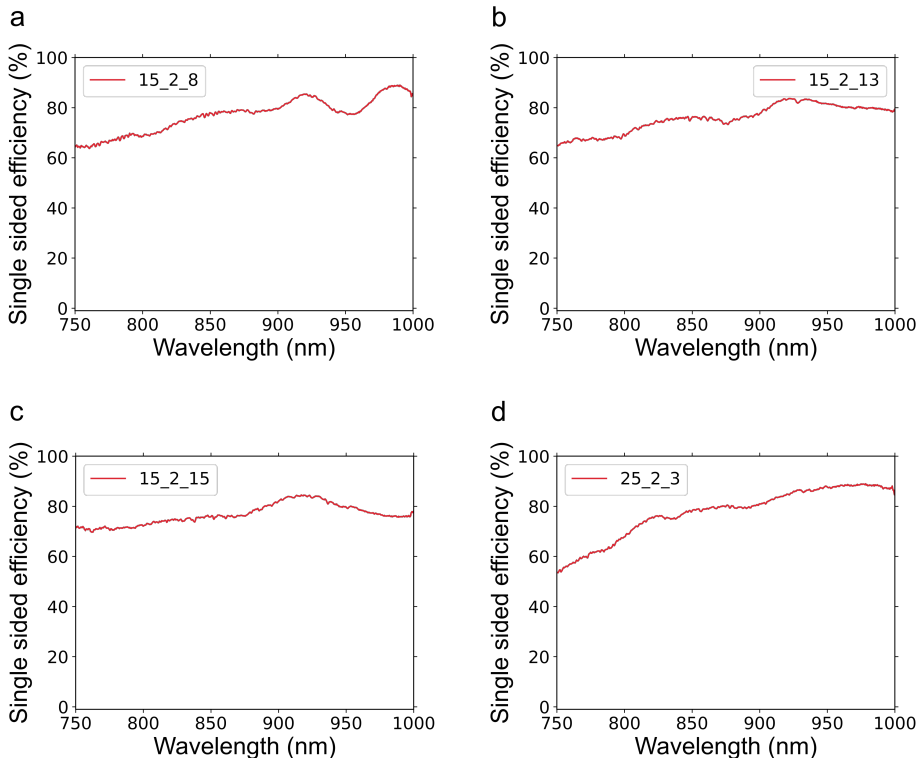

Figure C.1: **Transmission spectra.** Single sided coupling efficiency spectrum of a waveguide with **a** a taper length of 15 µm and two support structures, **b** a taper length of 15 µm and two support structures, **c** a taper length of 15 µm and two support structures and **d** a taper length of 25 µm and two support structures.

Appendix D

Parametric down-conversion

For a more detailed description of the down-converting process, I focus on solving the nonlinear Maxwell's equation [9, 10]. A standard approach to solve the linear as well as the nonlinear Maxwell equations is to take the curl of equation (2.3) and replace the magnetic field term $\nabla \times \frac{\partial \vec{B}(r,t)}{\partial t}$ with the Maxwell equation (2.4). Finally from using the vector identity $\nabla \times \nabla \times \vec{E}(r,t) = \nabla(\nabla \cdot \vec{E}(r,t)) - \nabla^2 \vec{E}(r,t)$ the general form of the wave equation in nonlinear optics [51]:

$$\left(\nabla^2 - \frac{n^2}{c^2} \frac{\partial^2}{\partial t^2} \right) \vec{E}(r,t) = \frac{1}{\epsilon_0 c^2} \frac{\partial^2}{\partial t^2} \vec{P}(r,t) \tag{D.1}$$

can be obtained [52].
If we assume a plane electromagnetic wave propagating in z-direction it is further possible to make the realistic assumption that the amplitude of the electromagnetic wave changes slowly compared to the wavelength so that the curvature of the amplitude is small compared to the curvature of the electromagnetic wave [51]:

$$\left| \frac{\partial^2 \vec{E}(z)}{\partial z^2} \right| \ll k \left| \frac{\partial \vec{E}(z)}{\partial z} \right| \tag{D.2}$$

Thus $\partial^2/\partial z^2 \, \vec{E}(z) \, \mathrm{e}^{i\,k\,z} \approx \mathrm{e}^{i\,k\,z}(2\,i\,k\frac{\partial}{\partial z} - k^2)\vec{E}(z)$ applies.
As a result the wave equation (D.1) reduces to:

$$\frac{d}{dz}\vec{E}(z) = \frac{\omega^2}{\epsilon_0 c^2} \frac{i}{2k} \vec{P}(\omega) \, \mathrm{e}^{-ikz} \tag{D.3}$$

It is already visible here that in addition to the in forward direction propagating wave, an in backward direction propagating wave is created. In principle, this equation can be used for any complex wave equation by replacing the polarization $\vec{P}$ by its explicit form [51].
For any three-wave mixing process the second order nonlinear susceptibility can be written as [51]:

$$P_i(\omega) \; = \; \epsilon_0 \sum_{jk} \sum_{mn} \chi^{(2)}_{\mathrm{E}}(\omega, \omega_m \omega_n) \, E_j(\omega_m) \, E_k(\omega_n), \tag{D.4}$$

were i, j, k can be any Cartesian coordinate.
Thus the second-order nonlinear susceptibility can also be portrayed in the three-dimensional polarization vector $\vec{P}(r,t)$:

$$\begin{pmatrix} P_x \\ P_y \\ P_z \end{pmatrix} = \begin{pmatrix} \epsilon_0\chi_{xxx} & \epsilon_0\chi_{xyy} & \epsilon_0\chi_{xxz} & \epsilon_0\chi_{xyz} & \epsilon_0\chi_{xzx} & \epsilon_0\chi_{xxy} \\ \epsilon_0\chi_{yxx} & \epsilon_0\chi_{yyy} & \epsilon_0\chi_{yxz} & \epsilon_0\chi_{yyz} & \epsilon_0\chi_{yzx} & \epsilon_0\chi_{yxy} \\ \epsilon_0\chi_{zxx} & \epsilon_0\chi_{zyy} & \epsilon_0\chi_{zxz} & \epsilon_0\chi_{zyz} & \epsilon_0\chi_{zzx} & \epsilon_0\chi_{zxy} \end{pmatrix} \begin{pmatrix} E_xE_x \\ E_yE_y \\ E_xE_z \\ 2E_yE_z \\ 2E_zE_x \\ 2E_xE_y \end{pmatrix}. \tag{D.5}$$

Here, the nonlinear susceptibility is given by a 3x6 matrix containing different values, dependent on the electric field polarization. Particularly in the literature (and in the specification sheets of nonlinear crystals) the second order nonlinear susceptibilities χ_{zyz} are often defined with the vacuum permittivity ϵ_0 to the nonlinear coefficients d ($d_{11} = \epsilon_0\chi_{xxx}$, $d_{21} = \epsilon_0\chi_{yxx}$, ...) [52, 143]. This reduces the equation (D.5) to the form:

$$\begin{pmatrix} P_x \\ P_y \\ P_z \end{pmatrix} = \begin{pmatrix} d_{11} & d_{12} & d_{13} & d_{14} & d_{15} & d_{16} \\ d_{21} & d_{22} & d_{23} & d_{24} & d_{25} & d_{26} \\ d_{31} & d_{32} & d_{33} & d_{34} & d_{35} & d_{36} \end{pmatrix} \begin{pmatrix} E_xE_x \\ E_yE_y \\ E_xE_z \\ 2E_yE_z \\ 2E_zE_x \\ 2E_xE_y \end{pmatrix}. \tag{D.6}$$

As a result, equation (D.1) in principle consists out of 18 different elements [51]. If we initially ignore the Cartesian dependency, require $\omega = \omega_1 + \omega_2$ with two electric waves and one polarization wave six products remain from equation (D.4):

$$\begin{array}{lll} \chi^{(2)}_{\mathrm{E}(r,t)}(\omega,\omega_1,\omega_2) & \chi^{(2)}_{\mathrm{E}(r,t)}(\omega_1,-\omega_2,\omega) & \chi^{(2)}_{\mathrm{E}(r,t)}(\omega_2,\omega,-\omega_1) \\ \chi^{(2)}_{\mathrm{E}(r,t)}(\omega,\omega_2,\omega_1) & \chi^{(2)}_{\mathrm{E}(r,t)}(\omega_1,\omega,-\omega_2) & \chi^{(2)}_{\mathrm{E}(r,t)}(\omega_2,-\omega_1,\omega), \end{array} \tag{D.7}$$

were further the upper and lower line are identical if the Cartesian coordinates (i,j) are reversed.
Thus in this case, equation (D.3) can be reduced to [51]:

$$\frac{d}{dz}E_1^*(\omega) = -\frac{2i\,d_{\text{eff}}\,\omega_1^2}{c\,n(\omega_1)}\,E_3^*\,E_2\,e^{-i\Delta kz} \tag{D.8}$$

$$\frac{d}{dz}E_2^*(\omega) = -\frac{2i\,d_{\text{eff}}\,\omega_2^2}{c\,n(\omega_2)}\,E_1\,E_3^*\,e^{-i\Delta kz} \tag{D.9}$$

$$\frac{d}{dz}E_3(\omega) = -\frac{2i\,d_{\text{eff}}\,\omega_3^2}{c\,n(\omega_3)}\,E_1\,E_2\,e^{-i\Delta kz}, \tag{D.10}$$

with$\Delta k = k - k_1 - k_2$.
In the special case of degenerate conversion ($\omega_1 = \omega_2$) these equations reduce to two equations:

$$\frac{d}{dz}E_1(2\omega) = \frac{2i\, d_{\text{eff}}\, \omega}{c\, n(2\omega)}\, E_2^2(\omega)\, e^{-i\Delta k z} \tag{D.11}$$

$$\frac{d}{dz}E_2(\omega) = \frac{2i\, d_{\text{eff}}\, \omega}{c\, n(\omega)}\, E_1(2\omega)\, E_2^*(\omega)\, e^{i\Delta k z} \tag{D.12}$$

For a nonlinear crystal of the length l and under the assumption of weak conversion ($E_2(\omega) \approx const$) the first equation can be solved as [51]:

$$E_1 = \frac{2d_{\text{eff}}}{c}\sqrt{\frac{\omega^3}{n(2\omega)\, n^2(\omega)}}\, l\, E_1^2\, \mathrm{e}^{i\Delta k l/2}\, \mathrm{sinc}(\Delta k l/2) \tag{D.13}$$

Following this equation the intensity I of a wave in a dielectric medium with refractive index n can be calculated:

$$I = \frac{n\, c\, \epsilon_0}{2}\, |E|^2 \tag{D.14}$$

$$I = \Gamma\, l^2\, I_1^2\, \mathrm{e}^{i\Delta k l/2}\, \mathrm{sinc}^2(\Delta k\, l/2) \tag{D.15}$$

with $\Gamma = \frac{4{d_{\text{eff}}}^2\omega^3}{c^3 n(2\omega) n^2(\omega) 2}$. With this simple representation, the most exciting part of nonlinear media is represented quite clearly; nonlinear media concede various frequency converters. This can be used to fairly easy generate laser light in wavelength regimes that are not covered by convenient laser transitions (frequency doubling in, for example, UV or near UV lasers [255–257]) or due to the coherent phase conversion for the generation of entangled photon pair states ([258–261]).

Appendix E

Degenerate parametric amplification

For the same parametric down-conversion process as aforementioned, namely satisfying the equations $k_p = k_i + k_s$ and $\omega_p = \omega_i + \omega_s = 2\omega$ equation (D.12) can be rewritten as:

$$\frac{d}{dz}E_2(\omega) = \frac{i}{2}\sqrt{\frac{\mu_0\,\epsilon_0}{\epsilon_r}}\,\omega\,\chi^{(2)}\,E_1(2\omega)\,E_2^*(\omega)\,e^{i\Delta k z}, \tag{E.1}$$

using the relations $n = \sqrt{\epsilon_r \mu_r}$ and $c = \frac{1}{\sqrt{\mu_0 \epsilon_0}}$. Considering $\delta k = 0$ and introducing the nonlinear coupling $g = \frac{1}{2}\sqrt{\frac{\mu_0 \epsilon_0}{\epsilon_r}}\omega\chi^{(2)} = \frac{\omega\chi^{(2)}}{2nc}$, this equation can be further simplified as [52]:

$$\frac{d}{dz}E_2(\omega) = i\,g\,E_1(2\omega)\,E_2^*(\omega). \tag{E.2}$$

The same equation can additionally be written as its complex conjugate:

$$\frac{d}{dz}E_2^*(\omega) = -i\,g\,E_1^*(2\omega)\,E_2(\omega). \tag{E.3}$$

An interesting approach is now to set the pump field as $E_1(2\omega) = E_0(2\omega)\mathrm{e}^{i\phi}$, where E_0 is a real amplitude and ϕ the phase [52].
By setting this phase $\phi = \pm\pi/2$ the term $E_1(2\omega)$ is real and thus the equations E.2 and E.3 reduce to:

$$\frac{d}{dz}E_2(\omega) = i\,g\,E_1(2\omega)\,E_2^*(\omega) \tag{E.4}$$

$$\frac{d}{dz}E_2^*(\omega) = i\,g\,E_1(2\omega)\,E_2(\omega) \tag{E.5}$$

By adding and subtracting these both equations a new equation pair is created:

$$\frac{d}{dz}(E_2(\omega) + E_2^*(\omega) = i\,g\,E_1(2\omega)\,(E_2^*(\omega) + E_2(\omega)) \tag{E.6}$$

$$\frac{d}{dz}(E_2^*(\omega) - E_2(\omega) = -\,i\,g\,E_1(2\omega)\,(E_2^*(\omega) - E_2(\omega)) \tag{E.7}$$

$$\tag{E.8}$$

By using the approach of putting $E^{\pm} = (E_2^*(\omega) \pm E_2(\omega))$ the following solutions can be found [52]:

$$E^+ = E_0^+ \, \mathrm{e}^{i\,g\,E_1(2\omega)\,z} \tag{E.9}$$

$$E^- = E_0^- \, \mathrm{e}^{-i\,g\,E_1(2\omega)\,z} \tag{E.10}$$

An interesting result of these solutions is the exponential growth (amplification) or decay (deamplification) of E^+ and E^-, respectively. These two fields are directly proportional to the field quadratures $\hat{X}$ and $\hat{Y}$ presented in section 1.3 [52]. As a consequence it is visible, that a nonlinear susceptibility leads in the process of degenerate parametric amplification to an amplification or deamplification of field quadratures. Furthermore, this (de)amplification is dependent on the phase of the pump photons. This means a degenerate parametric amplifier acts as an phase sensitive amplifier.

Appendix F

Complementary $g^{(2)}$ measurements

Further $g^{(2)}$ measurements of emitters in SiC waveguides excited from top with photon collection via the tapered-fiber-tapered-waveguide interface.

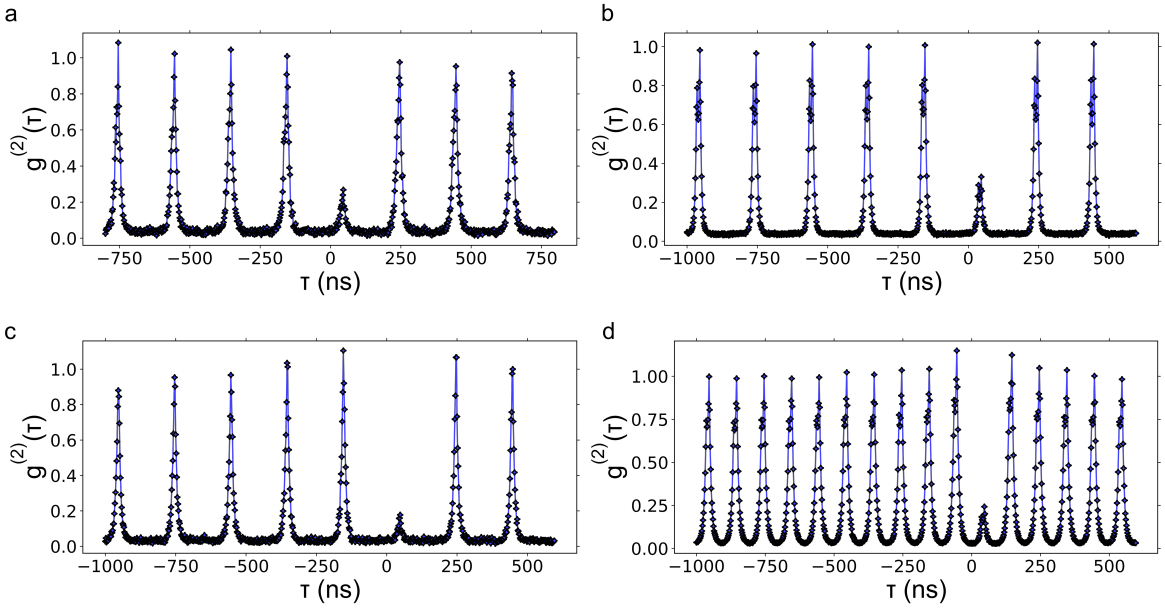

Figure F.1: **$g^{(2)}$ measurements of further bright spots in the waveguides.** $g^{(2)}$ measurement on a bright spot of the waveguide. The measurements where performed over a timescale of several hours resulting in an average of **a** 443, **b** 4508, **c** 602 and **d** 10845 correlation events per peak. With values of **a** 0.27, **b** 0.33, **c** 0.18 and **d** 0.24 these measurements confirm the existence of single emitters in the measured waveguides. Note, that the repetition rate for the last measurement was increased to 10 MHz.

Appendix G

Complementary SSC measurements

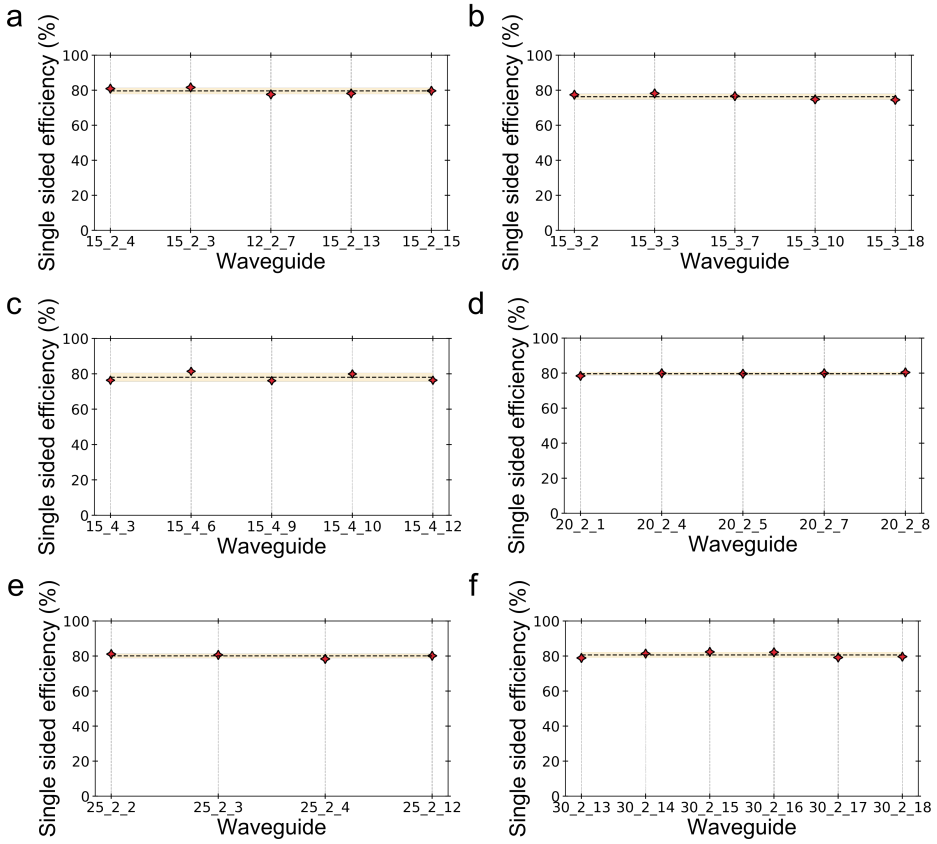

Figure G.1: **Lower bound for the single sided coupling efficiency (SSC) using equation (5.58) and a self build laser with a center wavelength of 878.8 nm.** Single sided coupling efficiency of a tapered optical fiber and a waveguide with a two sided taper length of **a**, 15 µm and two support structures, **b**, 15 µm and three support structures, **c**, 15 µm and four support structures, **d**, 20 µm and two support structures, **e**, 25 µm and two support structures and **f**, 30 µm and two support structures.
Average single sided coupling efficiencies: **a**, 79.62 ± 1.53%, **b**, 76.19 ± 1.43%, **c**, 78.04 ± 2.20%, **d**, 79.68 ± 0.67%, **e**, 80.11 ± 1.03% and **f**, 80.62 ± 1.40%.

Bibliography

[1] R. Nold, C. Babin, J. Schmidt, *et al.*: Quantum optical microphone in the audio band. *PRX Quantum*, **3**, 020358 (2022).

[2] D. Freedman: An empirical form of the square root law and the central limit theorem. *Math. Proc. Camb. Philos. Soc.*, **80**, 287–295 (1976).

[3] M. Eid, M., Gollwitzer, M. and Schmidt: Statistik und Forschungsmethoden. **2**, 204 (2013).

[4] V. Ivády, J. Davidsson, N. T. Son, T. Ohshima, I. A. Abrikosov, and A. Gali: Identification of si-vacancy related room-temperature qubits in 4 h silicon carbide. *Phys. Rev. B*, **96**, 16, 161114 (2017).

[5] E. Janzén, A. Gali, P. Carlsson, A. Gällström, B. Magnusson, and N. T. Son: The silicon vacancy in sic. *Physica B Condens. Matter*, **404**, 22, 4354–4358 (2009).

[6] Ö. Soykal, P. Dev, and S. E. Economou: Silicon vacancy center in 4 h-sic: Electronic structure and spin-photon interfaces. *Phys. Rev. B*, **93**, 8, 081207 (2016).

[7] P. Vergyris, C. Babin, R. Nold, E. Gouzien, H. Herrmann, C. Silberhorn, O. Alibart, S. Tanzilli, and F. Kaiser: Two-photon phase-sensing with single-photon detection. *App. Phys. Lett.*, **117**, 024001 (2020).

[8] M. Stecker, R. Nold, L.-M. Steinert, J. Grimmel, D. Petrosyan, J. Fortágh, and A. Günther: Controlling the dipole blockade and ionization rate of rydberg atoms in strong electric fields. *Phys. Rev. Lett.*, **125**, 10, 103602 (2020).

[9] J. C. Maxwell: Xliv. on physical lines of force. *Lond. Edinb. Dublin philos. mag. j. sci.*, **21**, 140, 281–291 (1861).

[10] J. C. Maxwell: Viii. a dynamical theory of the electromagnetic field. *Philos. Trans. R. Soc.*, , 155, 459–512 (1865).

[11] M. Planck: 1. über eine verbesserung der wienschen spektralgleichung. In *Quantentheorie*, 103–106 (De Gruyter2022).

[12] A. Einstein: Über einen die erzeugung und verwandlung des lichtes betreffenden heuristischen gesichtspunkt (1905).

[13] A. Einstein: Zum gegenwartigen stand des strahlungsproblems. *Phys. Zeits*, **10**, 185–193 (1909).

[14] P. A. M. Dirac: The quantum theory of the emission and absorption of radiation. *Proc. Math. Phys. Eng.*, **114**, 767, 243–265 (1927).

[15] R. J. Glauber: The quantum theory of optical coherence. *Phys. Rev.*, **130**, 6, 2529 (1963).

[16] R. J. Glauber: Photon correlations. *Phys. Rev. Lett.*, **10**, 3, 84 (1963).

[17] L. Mandel and E. Wolf: Coherence properties of optical fields. *Rev. Mod. Phys.*, **37**, 2, 231 (1965).

[18] E. Sudarshan: Equivalence of semiclassical and quantum mechanical descriptions of statistical light beams. *Phys. Rev. Lett.*, **10**, 7, 277 (1963).

[19] E. Sudarshan, P. Mathews, and J. Rau: Stochastic dynamics of quantum-mechanical systems. *Phys. Rev.*, **121**, 3, 920 (1961).

[20] R. H. Brown and R. Q. Twiss: 2. a test of a new type of stellar interferometer on sirius. In *A Source Book in Astronomy and Astrophysics, 1900–1975*, 8–12 (Harvard University Press2013).

[21] T. H. Maiman *et al.*: Stimulated optical radiation in ruby. *Nature*, **187**, 493–494 (1960).

[22] H. J. Kimble, M. Dagenais, and L. Mandel: Photon antibunching in resonance fluorescence. *Phys. Rev. Lett.*, **39**, 11, 691 (1977).

[23] R. Slusher, L. Hollberg, B. Yurke, J. Mertz, and J. Valley: Observation of squeezed states generated by four-wave mixing in an optical cavity. *Phys. Rev. Lett.*, **55**, 22, 2409 (1985).

[24] C. K. Hong, Z. Y. Ou, and L. Mandel: Measurement of Subpicosecond Time Intervals between Two Photons by Interference. *Phys. Rev. Lett.*, **59**, 2044 (1987).

[25] F. Arute, K. Arya, R. Babbush, *et al.*: Quantum supremacy using a programmable superconducting processor. *Nature*, **574**, 7779, 505–510 (2019).

[26] G. M. Harry: Advanced LIGO: The next generation of gravitational wave detectors. *Class. Quantum Gravity*, **27**, 084006 (2010).

[27] C. H. Bennett and G. Brassard: Quantum cryptography: Public key distribution and coin tossing. *Theoretical Computer Science*, **560**, 7–11 (2014).

[28] N. Gisin, G. Ribordy, W. Tittel, and H. Zbinden: Quantum cryptography. *Rev. Mod. Phys.*, **74**, 145–195 (2002).

[29] M. Dušek, N. Lütkenhaus, and M. Hendrych: Quantum cryptography. *Prog. in Optics*, **49**, 381–454 (2006).

[30] V. Cimini, M. Mellini, G. Rampioni, M. Sbroscia, L. Leoni, M. Barbieri, and I. Gianani: Adaptive tracking of enzymatic reactions with quantum light. *Opt. Express*, **27**, 35245–35256 (2019).

[31] T. Ono, R. Okamoto, and S. Takeuchi: An entanglement-enhanced microscope. *Nat. Commun.*, **4**, 2426 (2013).

[32] V. Cimini, I. Gianani, L. Ruggiero, T. Gasperi, M. Sbroscia, E. Roccia, D. Tofani, F. Bruni, M. Ricci, and M. Barbieri: Quantum sensing for dynamical tracking of chemical processes. *Phys. Rev. A*, **99**, 053817, 053817 (2019).

[33] I. Coddington, W. C. Swann, L. Nenadovic, and N. R. Newbury: Rapid and precise absolute distance measurements at long range. *Nat. Photonics*, **3**, 351–356 (2009).

[34] Y. J. Kim, P. M. Celliers, J. H. Eggert, A. Lazicki, and M. Millot: Interferometric measurements of refractive index and dispersion at high pressure. *Sci. Rep.*, **11**, 5610 (2021).

[35] B. R. Masters: Superresolution optical microscopy: the quest for enhanced resolution and contrast. *Springer*, **227**, 54–61 (2020).

[36] M. Conroy and D. Mansfield: Measuring microscale devices. *Nat. Photonics*, **2**, 661–663 (2008).

[37] M. B. Nasr, B. E. A. Saleh, A. V. Sergienko, and M. C. Teich: Dispersion-cancelled and dispersion-sensitive quantum optical coherence tomography. *Opt. Express*, **12**, 7, 1353–1362 (2004).

[38] F. Kaiser, P. Vergyris, D. Aktas, C. Babin, L. Labonté, and S. Tanzilli: Quantum enhancement of accuracy and precision in optical interferometry. *Light. Sci. Appl.*, **7**, 17163 (2018).

[39] C. A. Casacio, L. S. Madsen, A. Terrasson, M. Waleed, K. Barnscheidt, B. Hage, M. A. Taylor, and W. P. Bowen: Quantum-enhanced nonlinear microscopy. *Nature*, **594**, 201–206 (2021).

[40] H. Yu, L. McCuller, M. Tse, N. Kijbunchoo, L. Barsotti, and N. Mavalvala: Quantum correlations between light and the kilogram-mass mirrors of ligo. *Nature*, **583**, 7814, 43–47 (2020).

[41] S. W. Hell and J. Wichmann: Breaking the diffraction resolution limit by stimulated emission: stimulated-emission-depletion fluorescence microscopy. *Opt. Lett.*, **19**, 11, 780–782 (1994).

[42] E. Betzig and J. K. Trautman: Near-field optics: microscopy, spectroscopy, and surface modification beyond the diffraction limit. *Science*, **257**, 5067, 189–195 (1992).

[43] W. E. Moerner and L. Kador: Optical detection and spectroscopy of single molecules in a solid. *Phys. Rev. Lett.*, **62**, 21, 2535 (1989).

[44] F. Wolfgramm, A. Cerè, F. A. Beduini, A. Predojević, M. Koschorreck, and M. W. Mitchell: Squeezed-light optical magnetometry. *Phys. Rev. Lett.*, **105**, 053601 (2010).

[45] Y. Fu, H. Wang, R. Shi, and J. Cheng: Characterization of photodamage in coherent anti-stokes raman scattering microscopy. *Opt. Express*, **14**, 3942–3951 (2006).

[46] B. Li, C. Wu, M. Wang, K. Charan, and C. Xu: An adaptive excitation source for high-speed multiphoton microscopy. *Nat. Methods*, **17**, 163–166 (2020).

[47] L. Schermelleh, A. Ferrand, T. Huser, C. Eggeling, M. Sauer, O. Biehlmaier, and G. Drummen: An adaptive excitation source for high-speed multiphoton microscopy. *Nat. Cell Biol.*, **21**, 72–84 (2019).

[48] S. Wäldchen, J. Lehmann, T. Klein, S. van de Linde, and M. Sauer: Light-induced cell damage in live-cell super-resolution microscopy. *Sci. Rep.*, **5**, 15348 (2015).

[49] L. Zehnder: Ein neuer interferenzrefraktor. *Zeitschrift für Instrumentenkunde*, **11**, 275–285 (1891).

[50] L. Mach: Ueber einen interferenzrefraktor. *Zeitschrift für Instrumentenkunde*, **12**, 3, 89 (1892).

[51] D. Meschede: Optics, light and lasers: the practical approach to modern aspects of photonics and laser physics. **1**, 59–64 (2017).

[52] M. Fox: Quantum Optics an Introduction. *OUP Oxford*, **15**, 143–150 (2006).

[53] J. Taylor: Introduction to error analysis, the study of uncertainties in physical measurements. *USB*, **2**, 57–60 (1997).

[54] T. Kwaaitaal, B. Luymes, and G. Van Der Pijll: Noise limitations of michelson laser interferometers. *J. Phys. D*, **13**, 6, 1005 (1980).

[55] M. T. Jaekel and S. Reynaud: Quantum limits in interferometric measurements. *EPL*, **13**, 4, 301 (1990).

[56] B. C. Sanders and G. J. Milburn: Optimal quantum measurements for phase estimation. *Phys. Rev. Lett.*, **75**, 2944–2947 (1995).

[57] Z. Y. Ou: Complementarity and fundamental limit in precision phase measurement. *Phys. Rev. Lett.*, **77**, 2352–2355 (1996).

[58] N. D. Mermin: Extreme quantum entanglement in a superposition of macroscopically distinct states. *Phys. Rev. Lett.*, **65**, 1838–1840 (1990).

[59] J. J. . Bollinger, W. M. Itano, D. J. Wineland, and D. J. Heinzen: Optimal frequency measurements with maximally correlated states. *Phys. Rev. A*, **54**, R4649–R4652 (1996).

[60] G. Gilbert, M. Hamrick, and Y. S. Weinstein: Use of maximally entangled n-photon states for practical quantum interferometry. *JOSA B*, **25**, 8, 1336–1340 (2008).

[61] Z. Hradil: Phase measurement in quantum optics. *J. Eur. Opt. Soc.*, **4**, 2, 93 (1992).

[62] A. S. Lane, S. L. Braunstein, and C. M. Caves: Maximum-likelihood statistics of multiple quantum phase measurements. *Phys. Rev. A*, **47**, 3, 1667 (1993).

[63] H. Lee, P. Kok, and J. P. Dowling: A quantum rosetta stone for interferometry. *J. Mod. Opt.*, **49**, 14-15, 2325–2338 (2002).

[64] I. Afek, O. Ambar, and Y. Silberberg: High-NOON states by mixing quantum and classical light. *Science*, **328**, 879–881 (2010).

[65] A. N. Boto, P. Kok, D. S. Abrams, S. L. Braunstein, C. P. Williams, and J. P. Dowling: Quantum interferometric optical lithography: exploiting entanglement to beat the diffraction limit. *Phys. Rev. Lett.*, **85**, 13, 2733 (2000).

[66] M. W. Mitchell, J. S. Lundeen, and A. M. Steinberg: Super-resolving phase measurements with a multiphoton entangled state. *Nature*, **429**, 6988, 161–164 (2004).

[67] P. Walther, J.-W. Pan, M. Aspelmeyer, R. Ursin, S. Gasparoni, and A. Zeilinger: De broglie wavelength of a non-local four-photon state. *Nature*, **429**, 6988, 158–161 (2004).

[68] M. Malik, M. Erhard, M. Huber, M. Krenn, R. Fickler, and A. Zeilinger: Multi-photon entanglement in high dimensions. *Nat. Photonics*, **10**, 248–252 (2016).

[69] X. C. Yao, T. X. Wang, P. Xu, H. Lu, G. S. Pan, X. H. Bao, C. Z. Peng, C. Y. Lu, Y. A. Chen, and J. W. Pan: Observation of eight-photon entanglement. *Nat. Photonics*, **6**, 225–228 (2012).

[70] R. H. Hadfield: Single-photon detectors for optical quantum information applications. *Nat. Photonics*, **3**, 696–705 (2009).

[71] S. Slussarenko, M. M. Weston, H. M. Chrzanowski, L. K. Shalm, V. B. Verma, S. W. Nam, and G. J. Pryde: Unconditional violation of the shot-noise limit in photonic quantum metrology. *Nat. Photonics*, **11**, 700–703 (2017).

[72] S. F. Huelga, C. Macchiavello, T. Pellizzari, A. K. Ekert, M. B. Plenio, and J. I. Cirac: Improvement of frequency standards with quantum entanglement. *Phys. Rev. Lett.*, **79**, 3865–3868 (1997).

[73] M. W. Mitchell, J. S. Lundeen, and A. M. Steinberg: Super-resolving phase measurements with a multiphoton entangled state. *Nature*, **429**, 161–164 (2004).

[74] P. Walther, J.-W. Pan, M. Aspelmeyer, R. Ursin, S. Gasparoni, and A. Zeilinger: De broglie wavelength of a non-local four-photon state. *Nature*, **429**, 158–161 (2004).

[75] I. Afek, O. Ambar, and Y. Silberberg: High-noon states by mixing quantum and classical light. *Science*, **328**, 5980, 879–881 (2010).

[76] H. P. Yuen: Two-photon coherent states of the radiation field. *Phys. Rev. A*, **13**, 2226–2243 (1976).

[77] D. F. Walls: Squeezed states of light. *Nature*, **306**, 141–146 (1983).

[78] D. Walls and G. J. Milburn: Quantum optics. *Springer* (2008).

[79] R. Schnabel: Squeezed states of light and their applications in laser interferometers. *Phys. Rep.*, **684**, 1–51 (2017).

[80] C. Gerry, P. Knight, and P. L. Knight: Introductory quantum optics. *CUP* (2005).

[81] H. F. Baker: Alternants and continuous groups. *Proc. Lond. Math. Soc.*, **2**, 1, 24–47 (1905).

[82] J. E. Campbell: On a law of combination of operators (second paper). *Proc. London Math. Soc.*, **28**, 381 (1897).

[83] R. Gilmore: Baker-campbell-hausdorff formulas. *J. Math. Phys.*, **15**, 12, 2090–2092 (1974).

[84] F. Hausdorff: Die symbolische exponentialformel in der gruppentheorie. *Ber. Verh. Kgl. Sächs. Ges. Wiss. Leipzig. Math. phys. Kl.*, **58**, 19–48 (1906).

[85] E. Wigner: On the quantum correction for thermodynamic equilibrium. *Phys. Rev.*, **40**, 749–759 (1932).

[86] L. Mandel and E. Wolf: *Optical coherence and quantum optics* (CUP1995).

[87] M. Pysher, R. Bloomer, C. M. Kaleva, T. D. Roberts, P. Battle, and O. Pfister: Broadband amplitude squeezing in a periodically poled ktiopo 4 waveguide. *Opt. Lett.*, **34**, 3, 256–258 (2009).

[88] L.-A. Wu, H. Kimble, J. Hall, and H. Wu: Generation of squeezed states by parametric down conversion. *Phys. Rev. Lett.*, **57**, 20, 2520 (1986).

[89] U. L. Andersen, T. Gehring, C. Marquardt, and G. Leuchs: 30 Years of Squeezed Light Generation. *Phys. Scr.*, **91**, 053001 (2016).

[90] H. Vahlbruch, M. Mehmet, K. Danzmann, and R. Schnabel: Detection of 15 dB Squeezed States of Light and their Application for the Absolute Calibration of Photoelectric Quantum Efficiency. *Phys. Rev. Lett.*, **117**, 110801 (2016).

[91] B. J. Lawrie, P. D. Lett, A. M. Marino, and R. C. Pooser: Quantum sensing with squeezed light. *Acs Photonics*, **6**, 6, 1307–1318 (2019).

[92] P. Grangier, R. E. Slusher, B. Yurke, and A. LaPorta: Squeezed-light–enhanced polarization interferometer. *Phys. Rev. Lett.*, **59**, 2153–2156 (1987).

[93] M. Xiao, L.-A. Wu, and H. J. Kimble: Precision measurement beyond the shot-noise limit. *Phys. Rev. Lett.*, **59**, 278–281 (1987).

[94] K. Goda, O. Miyakawa, E. E. Mikhailov, S. Saraf, R. Adhikari, K. McKenzie, R. Ward, S. Vass, A. Weinstein, and N. Mavalvala: A quantum-enhanced prototype gravitational-wave detector. *Nat. Phys.*, **4**, 472–476 (2008).

[95] K. McKenzie, D. A. Shaddock, D. E. McClelland, B. C. Buchler, and P. K. Lam: Experimental demonstration of a squeezing-enhanced power-recycled michelson interferometer for gravitational wave detection. *Phys. Rev. Lett.*, **88**, 231102 (2002).

[96] M. Taylor, J. Janousek, V. Daria, J. Knittel, B. Hage, H.-A. Bachor, and W. Bowen: Biological measurement beyond the quantum limit. *Nat. Photonics*, **7**, 229–233 (2013).

[97] H. Vahlbruch, S. Chelkowski, B. Hage, A. Franzen, K. Danzmann, and R. Schnabel: Demonstration of a squeezed-light-enhanced power- and signal-recycled michelson interferometer. *Phys. Rev. Lett.*, **95**, 211102 (2005).

[98] B. P. Abbott, R. Abbott, T. D. Abbott, *et al.*: Observation of gravitational waves from a binary black hole merger. *Phys. Rev. Lett.*, **116**, 061102 (2016).

[99] T. L. S. Collaboration: A gravitational wave observatory operating beyond the quantum shot-noise limit. *Nat. Phys.*, **7**, 962–965 (2011).

[100] H. Grote, K. Danzmann, K. L. Dooley, R. Schnabel, J. Slutsky, and H. Vahlbruch: First long-term application of squeezed states of light in a gravitational-wave observatory. *Phys. Rev. Lett.*, **110**, 181101 (2013).

[101] M. Ast, S. Steinlechner, and R. Schnabel: Reduction of classical measurement noise via quantum-dense metrology. *Phys. Rev. Lett.*, **117**, 180801 (2016).

[102] S. Steinlecher, J. Bauchrowitz, M. Meinders, H. Müller-Eberhardt, K. Danzmann, and R. Schnabel: Quantum-dense metrology. *Nat. Photonics*, **7**, 626–630 (2013).

[103] C. A. Casacio, L. S. Madsen, A. Terrasson, M. Waleed, K. Barnscheidt, B. Hage, M. A. Taylor, and W. P. Bowen: Quantum-enhanced nonlinear microscopy. *Nature*, **594**, 201–206 (2021).

[104] V. Boyer, A. M. Marino, R. C. Pooser, and P. D. Lett: Entangled images from four-wave mixing. *Science*, **321**, 544–547 (2008).

[105] F. Kaiser, B. Fedrici, A. Zavatta, V. D'Auria, and S. Tanzilli: A fully guided-wave squeezing experiment for fiber quantum networks. *Optica*, **3**, 362 (2016).

[106] T. Kashiwazaki, N. Takanashi, T. Yamashima, T. Kazama, K. Enbutsu, R. Kasahara, T. Umeki, and A. Furusawa: Continuous-wave 6-dB-squeezed light with 2.5-THz-bandwidth from single-mode PPLN waveguide. *APL Photonics*, **5**, 036104 (2020).

[107] R. Demkowicz-Dobrzański, J. Kołodyński, and M. Guţa: The elusive Heisenberg limit in quantum-enhanced metrology. *Nat. Commun.*, **3**, 1063 (2012).

[108] T. Hirano, K. Kotani, T. Ishibashi, S. Okude, and T. Kuwamoto: 3 db squeezing by single-pass parametric amplification in a periodically poled ktiopo 4 crystal. *Opt. Lett.*, **30**, 13, 1722–1724 (2005).

[109] C. Kim and P. Kumar: Quadrature-squeezed light detection using a self-generated matched local oscillator. *Phys. Rev. Lett.*, **73**, 1605–1608 (1994).

[110] A. Eckstein, A. Christ, P. J. Mosley, and C. Silberhorn: Highly efficient single-pass source of pulsed single-mode twin beams of light. *Phys. Rev. Lett.*, **106**, 013603 (2011).

[111] R. E. Slusher, P. Grangier, A. LaPorta, B. Yurke, and M. J. Potasek: Pulsed Squeezed Light. *Phys. Rev. Lett.*, **59**, 2566–2569 (1987).

[112] Z. Y. Ou and X. Li: Quantum SU(1,1) interferometers: Basic principles and applications. *APL Photonics*, **5**, 080902 (2020).

[113] M. V. Chekhova and Z. Y. Ou: Nonlinear interferometers in quantum optics. *Adv. in Opt. and Phot.*, **8**, 104 (2016).

[114] B. Yurke, S. L. Mccall, and J. R. Klauder: SU(2) and SU(1,1) interferometers. *Phys. Rev. A*, **33**, 4033–4054 (1986).

[115] Z. Ou and X. Li: Quantum su(1,1) interferometers: Basic principles and applications. *APL Photonics*, **5**, 080902 (2020).

[116] F. Hudelist, J. Kong, C. Liu, J. Jing, Z. Y. Ou, and W. Zhang: Quantum metrology with parametric amplifier-based photon correlation interferometers. *Nat. Commun.*, **5**, 3049 (2014).

[117] J. Li, Y. Liu, L. Cui, N. Huo, S. M. Assad, X. Li, and Z. Ou: Joint measurement of multiple noncommuting parameters. *Phys. Rev. A*, **97**, 5, 052127 (2018).

[118] Z. Ou: Enhancement of the phase-measurement sensitivity beyond the standard quantum limit by a nonlinear interferometer. *Phys. Rev. A*, **85**, 2, 023815 (2012).

[119] W. N. Plick, J. P. Dowling, and G. S. Agarwal: Coherent-light-boosted, sub-shot noise, quantum interferometry. *New J. Phys.*, **12**, 8, 083014 (2010).

[120] A. M. Marino, N. C. Trejo, and P. D. Lett: Effect of losses on the performance of an su (1, 1) interferometer. *Phys. Rev. A*, **86**, 2, 023844 (2012).

[121] D. Li, C. H. Yuan, Z. Y. Ou, and W. Zhang: The phase sensitivity of an SU(1,1) interferometer with coherent and squeezed-vacuum light. *New J. Phys.*, **16**, 073020 (2014).

[122] B. E. Anderson, B. L. Schmittberger, P. Gupta, K. M. Jones, and P. D. Lett: Optimal phase measurements with bright- and vacuum-seeded su(1,1) interferometers. *Phys. Rev. A*, **95**, 063843 (2017).

[123] W. Du, J. F. Chen, Z. Y. Ou, and W. Zhang: Quantum dense metrology by an SU(2)-in-SU(1,1) nested interferometer. *App. Phys. Lett.*, **117**, 024003 (2020).

[124] Z. Ou, S. F. Pereira, H. Kimble, and K. Peng: Realization of the einstein-podolsky-rosen paradox for continuous variables. *Phys. Rev. Lett.*, **68**, 25, 3663 (1992).

[125] J. Kong, Z. Ou, W. Zhang, *et al.*: Phase-measurement sensitivity beyond the standard quantum limit in an interferometer consisting of a parametric amplifier and a beam splitter. *Phys. Rev. A*, **87**, 2, 023825 (2013).

[126] B. E. Anderson, P. Gupta, B. L. Schmittberger, T. Horrom, C. Hermann-Avigliano, K. M. Jones, and P. D. Lett: Phase sensing beyond the standard quantum limit with a variation on the su (1, 1) interferometer. *Optica*, **4**, 7, 752–756 (2017).

[127] P. Gupta, B. L. Schmittberger, B. E. Anderson, K. M. Jones, and P. D. Lett: Optimized phase sensing in a truncated su (1, 1) interferometer. *Opt. Express*, **26**, 1, 391–401 (2018).

[128] J. Li, Y. Liu, L. Cui, N. Huo, S. M. Assad, X. Li, and Z. Ou: Joint measurement of multiple noncommuting parameters. *Phys. Rev. A*, **97**, 5, 052127 (2018).

[129] Y. Liu, N. Huo, J. Li, L. Cui, X. Li, and Z. J. Ou: Optimum quantum resource distribution for phase measurement and quantum information tapping in a dual-beam su (1, 1) interferometer. *Opt. Express*, **27**, 8, 11292–11302 (2019).

[130] M. Gabbrielli, L. Pezze, and A. Smerzi: Spin-mixing interferometry with bose-einstein condensates. *Phys. Rev. Lett.*, **115**, 16, 163002 (2015).

[131] D. Linnemann, H. Strobel, W. Muessel, J. Schulz, R. J. Lewis-Swan, K. V. Kheruntsyan, and M. K. Oberthaler: Quantum-enhanced sensing based on time reversal of nonlinear dynamics. *Phys. Rev. Lett.*, **117**, 1, 013001 (2016).

[132] L. Pezze, A. Smerzi, M. K. Oberthaler, R. Schmied, and P. Treutlein: Quantum metrology with nonclassical states of atomic ensembles. *Rev. Mod. Phys.*, **90**, 3, 035005 (2018).

[133] E. Flurin, N. Roch, F. Mallet, M. H. Devoret, and B. Huard: Generating entangled microwave radiation over two transmission lines. *Phys. Rev. Lett.*, **109**, 18, 183901 (2012).

[134] Z. Y. Ou: Enhancement of the phase-measurement sensitivity beyond the standard quantum limit by a nonlinear interferometer. *Phys. Rev. A*, **85**, 023815 (2012).

[135] S. Adhikari, N. Bhusal, C. You, H. Lee, and J. P. Dowling: Phase estimation in an su (1, 1) interferometer with displaced squeezed states. *OSA Continuum*, **1**, 2, 438–450 (2018).

[136] D. Li, C.-H. Yuan, Z. Ou, and W. Zhang: The phase sensitivity of an su (1, 1) interferometer with coherent and squeezed-vacuum light. *New J. Phys.*, **16**, 7, 073020 (2014).

[137] D. Li, B. T. Gard, Y. Gao, C.-H. Yuan, W. Zhang, H. Lee, and J. P. Dowling: Phase sensitivity at the heisenberg limit in an su (1, 1) interferometer via parity detection. *Phys. Rev. A*, **94**, 6, 063840 (2016).

[138] W. Du, J. Jia, J. F. Chen, Z. Y. Ou, and W. Zhang: Absolute sensitivity of phase measurement in an su(1,1) type interferometer. *Opt. Lett.*, **43**, 5, 1051–1054 (2018).

[139] G. Frascella, E. Mikhailov, N. Takanashi, R. Zakharov, O. Tikhonova, and M. Chekhova: Wide-field su (1, 1) interferometer. *Optica*, **6**, 9, 1233–1236 (2019).

[140] S.-K. Choi, M. Vasilyev, and P. Kumar: Noiseless optical amplification of images. *Phys. Rev. Lett.*, **83**, 10, 1938 (1999).

[141] A. Mosset, F. Devaux, and E. Lantz: Spatially noiseless optical amplification of images. *Phys. Rev. Lett.*, **94**, 22, 223603 (2005).

[142] J. Aasi, B. P. Abbott, R. Abbott, *et al.*: Advanced LIGO. *Class. Quantum Gravity*, **32**, 074001 (2015).

[143] R. W. Boyd: Nonlinear optics. *Academic press* (2020).

[144] R. Harlander: Feynman diagrams. *Synthese*, **199**, 5, 15087–15111 (2021).

[145] M. Fiorentino, S. M. Spillane, R. G. Beausoleil, T. D. Roberts, P. Battle, and M. W. Munro: Spontaneous parametric down-conversion in periodically poled ktp waveguides and bulk crystals. *Opt. Express*, **15**, 12, 7479–7488 (2007).

[146] J. Armstrong, N. Bloembergen, J. Ducuing, and P. S. Pershan: Interactions between light waves in a nonlinear dielectric. *Phys. Rev.*, **127**, 6, 1918 (1962).

[147] G. Magel, M. Fejer, and R. Byer: Quasi-phase-matched second-harmonic generation of blue light in periodically poled linbo3. *Appl. Phys. Lett.*, **56**, 2, 108–110 (1990).

[148] H. U. Ahmed, A. Thwaini, I. S. Shergill, M. Y. Hammadeh, M. Arya, and A. V. Kaisary: Greenlight prostatectomy: a challenge to the gold standard?: a review of ktp photoselective vaporization of the prostate. *Surg. Laparosc. Endosc. Percutan. Tech.*, **17**, 3, 156–163 (2007).

[149] K. Kato and E. Takaoka: Sellmeier and thermo-optic dispersion formulas for ktp. *Appl. Opt.*, **41**, 24, 5040–5044 (2002).

[150] R. C. Jones: I . Description and Discussion of the Calculus. *J. Opt. Soc. Am.*, **31**, 488–493 (1941).

[151] P. S. Hauge, R. H. Muller, and C. G. Smith: Conventions and formulas for using the Mueller-Stokes calculus in ellipsometry. *Surf. Sci.*, **96**, 81–107 (1980).

[152] D. W. Allan: Statistics of atomic frequency standards. *Proc. IEEE*, **54**, 2, 221–230 (1966).

[153] Ieee standard definitions of physical quantities for fundamental frequency and time metrology-random instabilities. *IEEE Std 1139-1999*, 1–40 (1999).

[154] W. Du, J. F. Chen, Z. Y. Ou, and W. Zhang: Quantum dense metrology by an SU(2)-in-SU(1,1) nested interferometer. *App. Phys. Lett.*, **117**, 024003 (2020).

[155] B. Dayan, A. Pe'er, A. Friesem, and Y. Silberberg: Nonlinear interactions with an ultrahigh flux of broadband entangled photons. *Phys. Rev. Lett.*, **94**, 043602 (2005).

[156] Roga Instruments free field measurement microphone. https://www.datasheetarchive.com/whats_new/a0a00c16d562aef67225cd26cbc5b35c.html. Accessed: 2022-07-22.

[157] G. Bundesausschuss: Hilfsmittel-Richtlinie des Gemeinsamen Bundesausschusses. *https://www.g-ba.de/richtlinien/13/*, **Stand 17** (2020).

[158] K.-H. Hahlbrock: Sprachaudiometrie: Grundlagen und praktische anwendung einer sprachaudiometrie für das deutsche sprachgebiet; 157 abbildungen in 305 einzeldarstellungen 9 tabellen. *Thieme* (1970).

[159] S. Hoth: Der freiburger sprachtest. *HNO*, **64**, 8, 540–548 (2016).

[160] H. Feldmann: 200 jahre hörprüfungen mit sprache, 50 jahre deutsche sprachaudiometrie-ein rückblick. *Laryngo-rhino-otologie*, **83**, 11, 735–742 (2004).

[161] D. I. für Normung: DIN 45621- 1 Sprache für Gehörprüfung – Teil 1: Ein- und mehrsilbige Wörter. *Beuth* (1995).

[162] D. I. für Normung e.V.: What is a DIN Standard? *https://www.din.de/en/about-standards/din-standards* (2022).

[163] J. Kießling: Fehlerquellen in der audiometrie–grundlagen und abhilfe. *Praktische Arbeitsmedizin*, **6**, 12–16 (2006).

[164] H. von Wedel: Suitability of speech audiometry study procedures for current demands in clinical and general practice. *HNO*, **34**, 2, 71–74 (1986).

[165] G. Alich: Anmerkungen zum freiburger sprachverständnistest (fst). *Sprache, Stimme. Gehör*, **9**, 1, 1–6 (1985).

[166] H. Bangert: Probleme bei der ermittlung des diskriminationsverlustes nach dem freiburger sprachtest. *Audiol Akustik*, **19**, 5, 166–170 (1980).

[167] K. C. Wagener, V. Kuhnel, B. Kollmeier, T. Brand, and B. Kollmeier: Entwicklung und Evaluation eines Satztests für die deutsche Sprache I: Design des Oldenburger Satztests. *Z Audiol*, **38**, 1–32 (1999).

[168] K. C. Wagener, V. Kuhnel, B. Kollmeier, T. Brand, and B. Kollmeier: Entwicklung und Evaluation eines Satztests für die deutsche Sprache Teil II: Optimierung des Oldenburger Satztests. *Z Audiol*, **38**, 44–56 (1999).

[169] K. Wagener, T. Brand, and B. Kollmeier: Entwicklung und Evaluation eines Satztests für die deutsche Sprache Teil III: Optimierung des Oldenburger Satztests. *Z Audiol*, **38**, 86–95 (1999).

[170] B. Kollmeier, A. Warzybok, S. Hochmuth, M. A. Zokoll, V. Uslar, T. Brand, and K. C. Wagener: The multilingual matrix test: Principles, applications, and comparison across languages: A review. *Int. J. Audiol.*, **54**, 3–16 (2015).

[171] I. Holube, S. Blab, K. Fürsen, S. Gürtler, K. Meisenbacher, D. Nguyen, and S. Taesler: Einfluss des Maskierers und der Testmethode auf die Sprachverständlichkeitsschwelle von jüngeren und älteren Normalhörenden. *Zeitschrift für Audiologie*, **48**, 120–127 (2009).

[172] B. D. Ripley: The R Project in Statistical Computing. *MSOR Connections*, **1**, 23–25 (2001).

[173] B. del Rosal, I. Villa, D. Jaque, and F. Sanz-Rodríguez: In vivo autofluorescence in the biological windows: the role of pigmentation. *J. Biophoton*, **9**, 1059–1067 (2016).

[174] S. Tanzilli, H. De Riedmatten, W. Tittel, H. Zbinden, P. Baldi, M. De Micheli, D. B. Ostrowsky, and N. Gisin: Highly efficient photon-pair source using periodically poled lithium niobate waveguide. *Electron. Lett.*, **37**, 26–28 (2001).

[175] J. Wrachtrup, C. Von Borczyskowski, J. Bernard, M. Orrit, and R. Brown: Optically detected spin coherence of single molecules. *Phys. Rev. Lett.*, **71**, 21, 3565 (1993).

[176] J. Wrachtrup, C. Von Borczyskowski, J. Bernard, M. Orrit, and R. Brown: Optical detection of magnetic resonance in a single molecule. *Nature*, **363**, 6426, 244–245 (1993).

[177] A. Gruber, M. Vogel, J. Wrachtrup, and C. von Borczskowski: Magnetic resonance on single molecules in an external magnetic field. the zeeman effect of a single electron spin and determination of the orientation of individual molecules. *Chem. Phys. Lett.*, **242**, 4-5, 465–470 (1995).

[178] S. Pezzagna and J. Meijer: Quantum computer based on color centers in diamond. *Appl. Phys. Rev.*, **8**, 1, 011308 (2021).

[179] P. Siyushev, K. Xia, R. Reuter, *et al.*: Coherent properties of single rare-earth spin qubits. *Nat. Commun.*, **5**, 1, 3895 (2014).

[180] N. Zhao, S.-W. Ho, and R.-B. Liu: Decoherence and dynamical decoupling control of nitrogen vacancy center electron spins in nuclear spin baths. *Phys. Rev. B*, **85**, 11, 115303 (2012).

[181] L.-P. Yang, C. Burk, M. Widmann, S.-Y. Lee, J. Wrachtrup, and N. Zhao: Electron spin decoherence in silicon carbide nuclear spin bath. *Phys. Rev. B*, **90**, 24, 241203 (2014).

[182] T. Kimoto: Material science and device physics in sic technology for high-voltage power devices. *JJAP*, **54**, 4, 040103 (2015).

[183] H. Matsunami: Technological breakthroughs in growth control of silicon carbide for high power electronic devices. *JJAP*, **43**, 10R, 6835 (2004).

[184] R. Cheung: Silicon carbide microelectromechanical systems for harsh environments. *World Scientific* (2006).

[185] H. Itoh, M. Yoshikawa, I. Nashiyama, L. Wei, S. Tanigawa, S. Misawa, H. Okumura, and S. Yoshida: Defects in electron-irradiated 3c-sic epilayers observed by positron annihilation. *Hyperfine Interact.*, **79**, 1, 725–729 (1993).

[186] E. Sörman, N. Son, W. Chen, O. Kordina, C. Hallin, and E. Janzén: Silicon vacancy related defect in 4h and 6h sic. *Phys. Rev. B*, **61**, 4, 2613 (2000).

[187] J. Casady and R. W. Johnson: Status of silicon carbide (sic) as a wide-bandgap semiconductor for high-temperature applications: A review. *Solid State Electron. Lett.*, **39**, 10, 1409–1422 (1996).

[188] C. Haberstroh, R. Helbig, and R. Stein: Some new features of the photoluminescence of sic (6h), sic (4h), and sic (15r). *J. Appl. Phys.*, **76**, 1, 509–513 (1994).

[189] T. Van der Sar, Z. Wang, M. Blok, H. Bernien, T. Taminiau, D. Toyli, D. Lidar, D. Awschalom, R. Hanson, and V. Dobrovitski: Decoherence-protected quantum gates for a hybrid solid-state spin register. *Nature*, **484**, 7392, 82–86 (2012).

[190] S. Castelletto and A. Boretti: Silicon carbide color centers for quantum applications. *JPhys photonics*, **2**, 2, 022001 (2020).

[191] C. Babin, R. Stöhr, N. Morioka, *et al.*: Fabrication and nanophotonic waveguide integration of silicon carbide colour centres with preserved spin-optical coherence. *Nat. Mat.*, **21**, 1, 67–73 (2022).

[192] D. M. Lukin, C. Dory, M. A. Guidry, *et al.*: 4h-silicon-carbide-on-insulator for integrated quantum and nonlinear photonics. *Nat. Photonics*, **14**, 5, 330–334 (2020).

[193] R. Nagy, M. Widmann, M. Niethammer, *et al.*: Quantum properties of dichroic silicon vacancies in silicon carbide. *Phys. Rev. Appl.*, **9**, 3, 034022 (2018).

[194] F. Fuchs, B. Stender, M. Trupke, D. Simin, J. Pflaum, V. Dyakonov, and G. Astakhov: Engineering near-infrared single-photon emitters with optically active spins in ultrapure silicon carbide. *Nat. Commun.*, **6**, 1, 7578 (2015).

[195] N. Morioka, D. Liu, Ö. O. Soykal, *et al.*: Spin-optical dynamics and quantum efficiency of a single v1 center in silicon carbide. *Phys. Rev. Appl.*, **17**, 5, 054005 (2022).

[196] P. Udvarhelyi, G. Thiering, N. Morioka, *et al.*: Vibronic states and their effect on the temperature and strain dependence of silicon-vacancy qubits in 4 h-si c. *Phys. Rev. Appl.*, **13**, 5, 054017 (2020).

[197] P. G. Baranov, A. P. Bundakova, A. A. Soltamova, S. B. Orlinskii, I. V. Borovykh, R. Zondervan, R. Verberk, and J. Schmidt: Silicon vacancy in sic as a promising quantum system for single-defect and single-photon spectroscopy. *Phys. Rev. B*, **83**, 12, 125203 (2011).

[198] P. Udvarhelyi, G. Thiering, N. Morioka, *et al.*: Vibronic states and their effect on the temperature and strain dependence of silicon-vacancy qubits in 4 h-si c. *Phys. Rev. Appl.*, **13**, 5, 054017 (2020).

[199] T. Hain, F. Fuchs, V. Soltamov, P. Baranov, G. Astakhov, T. Hertel, and V. Dyakonov: Excitation and recombination dynamics of vacancy-related spin centers in silicon carbide. *J. Appl. Phys.*, **115**, 13, 133508 (2014).

[200] M. Widmann, S.-Y. Lee, T. Rendler, *et al.*: Coherent control of single spins in silicon carbide at room temperature. *Nat. Mat.*, **14**, 2, 164–168 (2015).

[201] Z. Shang, A. Hashemi, Y. Berencén, H.-P. Komsa, P. Erhart, S. Zhou, M. Helm, A. Krasheninnikov, and G. Astakhov: Local vibrational modes of si vacancy spin qubits in sic. *Physical Review B*, **101**, 14, 144109 (2020).

[202] R. Nagy, M. Niethammer, M. Widmann, *et al.*: High-fidelity spin and optical control of single silicon-vacancy centres in silicon carbide. *Nat. Commun.*, **10**, 1, 1954 (2019).

[203] E. M. Purcell, H. C. Torrey, and R. V. Pound: Resonance absorption by nuclear magnetic moments in a solid. *Physical review*, **69**, 1-2, 37 (1946).

[204] The Nobel Prize the nobel prize in physics 1952. https://www.nobelprize.org/prizes/physics/1952/summary/. Accessed: 2022-07-29.

[205] D. Kleppner: Inhibited spontaneous emission. *Phys. Rev. Lett.*, **47**, 4, 233 (1981).

[206] V. P. Bykov: Spontaneous emission from a medium with a band spectrum. *Sov. J. Quantum Electron.*, **4**, 7, 861 (1975).

[207] G. M. Akselrod, C. Argyropoulos, T. B. Hoang, C. Ciracì, C. Fang, J. Huang, D. R. Smith, and M. H. Mikkelsen: Probing the mechanisms of large purcell enhancement in plasmonic nanoantennas. *Nat. Photonics*, **8**, 11, 835–840 (2014).

[208] T. D. Barrett, T. H. Doherty, and A. Kuhn: Pushing purcell enhancement beyond its limits. *New J. Phys.*, **22**, 6, 063013 (2020).

[209] D. O. Bracher, X. Zhang, and E. L. Hu: Selective purcell enhancement of two closely linked zero-phonon transitions of a silicon carbide color center. *PNAS*, **114**, 16, 4060–4065 (2017).

[210] R. D. Meade, J. N. Winn, and J. Joannopoulos: Photonic crystals: Molding the flow of light. *Pinceton Univ. Press* (1995).

[211] A. W. Snyder and J. Love: Optical waveguide theory. *Springer Science & Business Media* (2012).

[212] F. Goos and H. Hänchen: Über das eindringen des totalreflektierten lichtes in das dünnere medium. *Ann. Phys.*, **435**, 5, 383–392 (1943).

[213] K. Yee: Numerical solution of initial boundary value problems involving maxwell's equations in isotropic media. *IEEE Trans. Antennas Propag.*, **14**, 3, 302–307 (1966).

[214] M. NO: Numerical techniques in electromagnetics with matlab®. *CRC Press* (2009).

[215] M. N. Sadiku: Numerical techniques in electromagnetics. *CRC press* (2000).

[216] R. Courant, K. Friedrichs, and H. Lewy: Über die partiellen differenzengleichungen der mathematischen physik. *Math. Ann.*, **100**, 1, 32–74 (1928).

[217] I. Krasnokutska, J.-L. J. Tambasco, and A. Peruzzo: Nanostructuring of lnoi for efficient edge coupling. *Opt. Express*, **27**, 12, 16578–16585 (2019).

[218] H. Melkonyan, K. Sloyan, K. Twayana, P. Moreira, and M. S. Dahlem: Efficient fiber-to-waveguide edge coupling using an optical fiber axicon lens fabricated by focused ion beam. *IEEE Photonics J.*, **9**, 4, 1–9 (2017).

[219] P. Ying, H. Tan, J. Zhang, M. He, M. Xu, X. Liu, R. Ge, Y. Zhu, C. Liu, and X. Cai: Low-loss edge-coupling thin-film lithium niobate modulator with an efficient phase shifter. *Opt. Lett.*, **46**, 6, 1478–1481 (2021).

[220] R. G. Hunsperger, A. Yariv, and A. Lee: Parallel end-butt coupling for optical integrated circuits. *Appl. Opt.*, **16**, 4, 1026–1032 (1977).

[221] D. Taillaert, W. Bogaerts, P. Bienstman, T. F. Krauss, P. Van Daele, I. Moerman, S. Verstuyft, K. De Mesel, and R. Baets: An out-of-plane grating coupler for efficient butt-coupling between compact planar waveguides and single-mode fibers. *IEEE J. Quantum Electron*, **38**, 7, 949–955 (2002).

[222] L. Zhu, W. Yang, and C. Chang-Hasnain: G efficiency optical coupler for silicon nanophotonic waveguide and single mode optical fiber. *Opt. Express*, **25**, 15, 18462–18473 (2017).

[223] G. Roelkens, D. Vermeulen, D. Van Thourhout, R. Baets, S. Brision, P. Lyan, P. Gautier, and J.-M. Fedeli: High efficiency diffractive grating couplers for interfacing a single mode optical fiber with a nanophotonic silicon-on-insulator waveguide circuit. *Appl. Phys. Lett.*, **92**, 13, 131101 (2008).

[224] T. Tiecke, K. Nayak, J. D. Thompson, T. Peyronel, N. P. de Leon, V. Vuletić, and M. Lukin: Efficient fiber-optical interface for nanophotonic devices. *Optica*, **2**, 2, 70–75 (2015).

[225] M. J. Burek, C. Meuwly, R. E. Evans, *et al.*: Fiber-coupled diamond quantum nanophotonic interface. *Phys. Rev. Appl.*, **8**, 2, 024026 (2017).

[226] X. Mu, S. Wu, L. Cheng, and H. Fu: Edge couplers in silicon photonic integrated circuits: A review. *Appl. Sci.*, **10**, 4, 1538 (2020).

[227] R. Takei, M. Suzuki, E. Omoda, S. Manako, T. Kamei, M. Mori, and Y. Sakakibara: Silicon knife-edge taper waveguide for ultralow-loss spot-size converter fabricated by photolithography. *Appl. Phys. Lett.*, **102**, 10, 101108 (2013).

[228] R. Osgood and X. Meng: Principles of photonic integrated circuits. *Principles of Photonic Integrated Circuits. Series: Graduate Texts in Physics* (2021).

[229] F. Van Laere, G. Roelkens, M. Ayre, J. Schrauwen, D. Taillaert, D. Van Thourhout, T. F. Krauss, and R. Baets: Compact and highly efficient grating couplers between optical fiber and nanophotonic waveguides. *J. Light. Technol.*, **25**, 1, 151–156 (2007).

[230] Y. Ding, C. Peucheret, H. Ou, and K. Yvind: Fully etched apodized grating coupler on the soi platform with- 0.58 db coupling efficiency. *Opt. Lett.*, **39**, 18, 5348–5350 (2014).

[231] C. Dory, D. Vercruysse, K. Y. Yang, *et al.*: Inverse-designed diamond photonics. *Nat. commun.*, **10**, 1, 1–7 (2019).

[232] S. Gröblacher, J. T. Hill, A. H. Safavi-Naeini, J. Chan, and O. Painter: Highly efficient coupling from an optical fiber to a nanoscale silicon optomechanical cavity. *Appl. Phys. Lett.*, **103**, 18, 181104 (2013).

[233] L. Ding, C. Belacel, S. Ducci, G. Leo, and I. Favero: Ultralow loss single-mode silica tapers manufactured by a microheater. *Appl. Opt.*, **49**, 13, 2441–2445 (2010).

[234] J. M. Ward, D. G. O'Shea, B. J. Shortt, M. J. Morrissey, K. Deasy, and S. G. Nic Chormaic: Heat-and-pull rig for fiber taper fabrication. *Rev. Sci. Instrum.*, **77**, 8, 083105 (2006).

[235] H. Yokota, E. Sugai, and Y. Sasaki: Optical irradiation method for fiber coupler fabrications. *Opt. Rev.*, **4**, 1A, 104–107 (1997).

[236] H. J. Kbashi: Fabrication of submicron-diameter and taper fibers using chemical etching. *J. Mater. Sci. Technol.*, **28**, 4, 308–312 (2012).

[237] P. Lambelet, A. Sayah, M. Pfeffer, C. Philipona, and F. Marquis-Weible: Chemically etched fiber tips for near-field optical microscopy: a process for smoother tips. *Appl. Opt.*, **37**, 31, 7289–7292 (1998).

[238] S. D. Gedney: Introduction to the finite-difference time-domain (fdtd) method for electromagnetics. *Synth. Lect. Electromagn.*, **6**, 1, 1–250 (2011).

[239] D. M. Sullivan: *Electromagnetic simulation using the FDTD method* (John Wiley & Sons2013).

[240] A. Taflove, S. C. Hagness, and M. Piket-May: Computational electromagnetics: the finite-difference time-domain method. *The Electrical Engineering Handbook*, **3**, 629–670 (2005).

[241] B. Lin, X. Wang, J. Lv, Y. Cao, Y. Yang, Y. Zhang, A. Zhang, Y. Yi, F. Wang, and D. Zhang: Low-power-consumption polymer mach–zehnder interferometer thermo-optic switch at 532 nm based on a triangular waveguide. *Opt. Lett.*, **45**, 16, 4448–4451 (2020).

[242] S. Majety, V. A. Norman, L. Li, M. Bell, P. Saha, and M. Radulaski: Quantum photonics in triangular-cross-section nanodevices in silicon carbide. *JPhys photonics*, **3**, 3, 034008 (2021).

[243] P. Overfelt and D. White: Te and tm modes of some triangular cross-section waveguides using superposition of plane waves (short paper). *IEEE Trans. Microw. Theory Techn.*, **34**, 1, 161–167 (1986).

[244] S. Miller: Coupled wave theory and waveguide applications. *Bell Syst. Tech. J.*, **33**, 3, 661–719 (1954).

[245] D. Marcuse: The coupling of degenerate modes in two parallel dielectric waveguides. *Bell Syst. Tech. J.*, **50**, 6, 1791–1816 (1971).

[246] J. D. Love, W. M. Henry, W. Stewart, R. J. Black, S. Lacroix, and F. Gonthier: Tapered single-mode fibres and devices. i. adiabaticity criteria. *IEE Optoelectron.*, **138**, 1, 343–354 (1991).

[247] P. Grünwald: Effective second-order correlation function and single-photon detection. *New J. Phys.*, **21**, 9, 093003 (2019).

[248] F. Sardi, T. Kornher, M. Widmann, R. Kolesov, F. Schiller, T. Reindl, M. Hagel, and J. Wrachtrup: Scalable production of solid-immersion lenses for quantum emitters in silicon carbide. *Appl. Phys. Lett.*, **117**, 2, 022105 (2020).

[249] V. Giovannetti, S. Lloyd, and L. MacCone: Quantum metrology. *Phys. Rev. Lett.*, **96**, 010401 (2006).

[250] R. Demkowicz-Dobrzański, M. Jarzyna, and J. Kołodyński: Quantum Limits in Optical Interferometry. *Prog. in Opt.*, **60**, 345–435 (2015).

[251] C. M. Caves: Quantum-mechanical noise in an interferometer. *Phys. Rev. D*, **23**, 1693–1708 (1981).

[252] J. W. Pan, Z. B. Chen, C. Y. Lu, H. Weinfurter, A. Zeilinger, and M. Zukowski: Multiphoton entanglement and interferometry. *Rev. Mod. Phys.*, **84**, 777 (2012).

[253] G. Brida, M. Genovese, and I. R. Berchera: Experimental realization of sub-shot-noise quantum imaging. *Nat. Photonics*, **4**, 227–230 (2010).

[254] A. E. Ulanov, I. A. Fedorov, D. Sychev, P. Grangier, and A. I. Lvovsky: Loss-tolerant state engineering for quantum-enhanced metrology via the reverse Hong-Ou-Mandel effect. *Nat. Commun.*, **7**, 11925 (2016).

[255] C. Dewey Jr, W. Cook Jr, R. Hodgson, and J. Wynne: Frequency doubling in kb5o8 4h2o and nh4b5o8 4h2o to 217.3 nm. *Appl. Phys. Lett.*, **26**, 12, 714–716 (1975).

[256] U. Eismann, M. Scholz, T. Paasch-Colberg, and J. Stuhler: Short, shorter, shortest: Diode lasers in the deep ultraviolet. *Laser Focus World*, **52**, 6, 39–44 (2016).

[257] V. Ruseva and J. Hald: Generation of uv light by frequency doubling in bibo. *Opt. Commun.*, **236**, 1-3, 219–223 (2004).

[258] K. Edamatsu, R. Shimizu, and T. Itoh: Measurement of the photonic de broglie wavelength of entangled photon pairs generated by spontaneous parametric down-conversion. *Phys. Rev. Lett.*, **89**, 21, 213601 (2002).

[259] C. Kurtsiefer, M. Oberparleiter, and H. Weinfurter: Generation of correlated photon pairs in type-ii parametric down conversion—revisited. *J. Mod. Opt.*, **48**, 13, 1997–2007 (2001).

[260] H. Weinfurter and M. Żukowski: Four-photon entanglement from down-conversion. *Phys. Rev. A*, **64**, 1, 010102 (2001).

[261] H.-S. Zhong, Y. Li, W. Li, *et al.*: 12-photon entanglement and scalable scattershot boson sampling with optimal entangled-photon pairs from parametric down-conversion. *Phys. Rev. Lett.*, **121**, 25, 250505 (2018).

Eidesstattliche Erklärung, Declaration on oath

Hiermit erkläre ich, Raphael Nold, geboren in Tübingen, dass die eingereichte Dissertation zum Thema "A quantum optical microphone in the audio band based on nonlinear interferometry and a fiber-optical interface for nanophotonic devices" meine eigenständig erbrachte Leistung darstellt. Ich habe ausschließlich die angegebenen Quellen und Hilfsmittel benutzt. Wörtlich oder inhaltlich aus anderen Werken übernommene Angaben habe ich als solche kenntlich gemacht. Die Richtigkeit der hier getätigten Angaben bestätige ich und versichere, nach bestem Wissen die Wahrheit erklärt zu haben.
Hiermit erkläre ich, Raphael Nold, dass das von mir eingereichte pdf-Dokument zur Dissertation mit dem Thema "A quantum optical microphone in the audio band based on nonlinear interferometry and a fiber-optical interface for nanophotonic devices" in Inhalt und Wortlaut der ebenfalls eingereichten Printversion meiner Dissertationsschrift entspricht.

I, Raphael Nold, born in Tübingen, hereby declare that the dissertation submitted on the topic "A quantum optical microphone in the audio band based on nonlinear interferometry and a fiber-optical interface for nanophotonic devices" constitutes my independent work. I have used only the sources and aids indicated. I have marked information taken over verbatim or in content from other works as such. I confirm the correctness of the information given here and assure that I have declared the truth to the best of my knowledge.
I, Raphael Nold, hereby declare that the pdf document I submitted for the dissertation with the topic "A quantum optical microphone in the audio band based on nonlinear interferometry and a fiber-optical interface for nanophotonic devices" is identical in content and wording to the print version of my dissertation paper that was also submitted.

Stuttgart, den (the) 15/10/2022

Unterschrift/Signature: Raphael Nold 

"Sometimes science is more art than science, Morty. Lot of people don't get that."
—Rick Sanchez

Abstract

We find ourselves in times of the second quantum revolution, where the research and development of applicable quantum systems or quantum sensors becomes more and more important. In our search for suitable quantum systems, separate approaches for two different topics are presented. First, a novel concept of a quantum sensor for phase-sensitive measurements that outperforms previous approaches in nonlinear interferometry in certain aspects, and second, a nanophotonic conical fiber-conical waveguide interface to increase the collection efficiency of photons for solid-state quantum systems was shown. Thus, this work paves the way for useful applications in the field of nonlinear interferometry and the integration of solid-state emitters into nanophotonic structures to overcome the inherently low light collection efficiency of optically active spins in the solid state.

Zusammenfassung

Wir befinden uns in Zeiten der zweiten Quantenrevolution, wo die Erforschung und Entwicklung von anwendbaren Quantensystemen oder Quantensensoren immer weiter an Bedeutung gewinnt. Auf der Suche nach geeigneten Quantensystemen werden in dieser Arbeit separate Ansätze für zwei unterschiedliche Themengebiete präsentiert. Zum einen für einen neuartigen Quantensensor für phasenempfindliche Messungen, der in bestimmten Aspekten bisherige Ansätze in der nichtlinearen Interferometrie übertrifft, und zum anderen eine nanophotonische, konische-Faser-konischer-Wellenleiter-Schnittstelle zur Steigerung der Sammeleffizienz von Photonen für Festkörper-Quantensysteme. Damit ebnet diese Arbeit den Weg für sinnvolle Anwendungen im Bereich der nichtlinearen Interferometrie und der Integration von Festkörper-Emittern in nanophotonische Strukturen, um die inhärent geringe Lichtsammeleffizienz optisch aktiver Spins im Festkörper zu überwinden.